UNIVERSITÉ DE STRASBOURG

UNIVERSITÉ DE STRASBOURG

ÉCOLE DOCTORALE

DOCTORAL SCHOOL MSII

ICube Laboratory (UMR 7357)

Research Group CAMMA

Computational Analysis and Modeling of Medical Activities

THESIS presented by

Nicolas Loy Rodas

Defended publicly on: **February 19, 2018**

For obtaining the degree of **Doctor of Philosophy**
from the **University of Strasbourg**

Field: **Medical Robotics**

Context-Aware Radiation Protection for the Hybrid Operating Room

Thesis Directors:

Prof. Dr. Michel de Mathelin	Professor, Université de Strasbourg
Dr. Nicolas Padoy	Associate Professor on a Chair of Excellence, Université de Strasbourg

Examiners:

Prof. Dr. Philippe Cattin	Professor, University of Basel
Prof. Dr. Pascal Fallavollita	Assistant Professor, University of Ottawa

Invited jury members:

Prof. Dr. Nassir Navab	Professor, Technische Universität München
Dr. Julien Bert	Research Engineer, CHRU Brest, LaTIM – INSERM

Abstract

Last decades have witnessed an important increase in the use of X-ray based imaging technologies during minimally invasive procedures. Consequently, the exposure to ionizing radiation of both clinical staff and patients has significantly increased. Even if the dose absorbed during a single procedure can be low, long-term exposure to radiation can lead to negative effects in the body such as skin damage, eye cataracts and even cancer. The inability to visually perceive X-rays and the lack of immediate effects to exposure hinder the optimal use of protective measures. Also, several patient, equipment and/or procedure dependent factors affect the magnitude and spatial distribution of radiation inside the Operating Room (OR), which makes irradiated areas and the amount of radiation hard to forecast. In this thesis, we therefore propose novel methods to improve the overall radiation safety during X-ray guided procedures, by acting in two complementary directions. First, we propose an approach for estimating and monitoring patient and staff radiation exposure, along with the propagation/intensity of scattered radiation for the current room context and imaging protocol. In-situ visual feedback of the ongoing radiation dose is then provided by means of Augmented Reality (AR) to increase the awareness of personnel to harmful radiation and reinforce the proper use of protective equipment. Second, we propose to act on the X-ray device positioning with an optimization approach for recommending an angulation reducing the dose deposited to both patient and clinical staff, while maintaining the clinical quality of the outcome image. Both approaches rely on the perception and modeling of the lay-out of the OR, which is achieved thanks to multiple ceiling-mounted Red-Green-Blue-Depth (RGBD) cameras. This information is then exploited by Monte Carlo-based simulation methods to compute in real-time the propagation of radiation and the dose to patient and staff. These simulation approaches have been validated experimentally using dosimeters and a real-time demonstrator of the AR visualization system has been implemented in an interventional room containing a robotized X-ray imaging device. We hope that the approaches presented in this thesis can contribute to reduce the overall radiation exposure during interventional procedures, increase the acceptance of X-ray imaging devices and make the benefits of image-guided procedures accessible to a wider population.

Acknowledgments

This thesis is the result of nearly four years of work at the *ICube Laboratory*. During this exciting time, I received help, support and teachings from numerous people without whom my PhD thesis would have never been completed. Acknowledgments to most of them are given below but also in footnotes spread across the upcoming pages of this dissertation.

I would like to start by thanking **Pr. Nassir Navab**, **Pr. Philippe Cattin** and **Pr. Pascal Fallavollita** for taking the time to read my dissertation and for being part of my defense committee. It is a great honor for me to have such esteemed and respected members of our research community to evaluate and give feedback of my work.

I would like to also thank **Pr. Pierre Renaud** for introducing me to the field of Medical Robotics. You were my first supervisor in the lab back then when I thought I would be building robots instead of software. Thanks for all your support.

I would like to particularly express my deepest gratitude to both of my thesis directors **Pr. Michel de Mathelin** and **Dr. Nicolas Padoy**. Thank you **Michel** for your continuous support and motivation; you are an example of non-stopping hard-work. Your enormous experience in the field and passion have very much motivated me over the years. Thank you **Nicolas** for introducing me to the field of Computer-Assisted Medical Interventions. Thanks for sharing your immense knowledge with me every day; I could not have imagined having a better mentor than you. To say that you have been patient with me would be an understatement. I am incredibly grateful for the large amount of time and energy you have taken to guide and help me. Everything you've taught me has profoundly marked the way I conduct my work. Thanks for all those interesting discussions, not only the scientific ones, but also the ones about books, movies, politics, career advice... I got the chance to join *Research Group CAMMA* at its very beginnings and to witness how our team was built by **Nicolas** from scratch, amazing.

I would also like to offer my thanks to the former and current members of the *CAMMA* group. I am particularly grateful with **Laurent Goffin**, **Dr. Rahim Kadkhodamohammadi**, **Dr. Andru Twinanda**, **Dr. Fernando Barrera** and **Dr. Antonio De Donno** for your technical contributions to my work and for helping me conducting my experiments. Thanks **Rahim**, **Andru** and **Fernando** for all those interesting and/or

funny discussions over a coffee or a beer. Thanks **Fernando** for the many hours we spent together in the interventional room doing recordings, calibrations, demos... Thanks **Andru** for your sense of humor and motivation, and for being the only one I could discuss pop culture with. Thanks **Rahim** for your patience, for sharing your wisdom with all of us and also for your immense help in the development of *XAware-Live*.

I cannot forget the help and inspiration from my colleagues at the Automatique Vision et Robotique (AVR) group from **ICube**, and from the personnel of **IRCAD** and **IHU** Strasbourg. Thank you all for your kindness, friendship and support, and for promoting a stimulating and welcoming environment to work in. Thanks also for all those interesting and/or funny discussions I could have with some of you during the past years.

I would like to thank **Dr. Julien Bert** and **Pr. Dimitris Vizvikis** who were instrumental in this work. Thank you both for collaborating with us in the radiation simulation part, and also for your feedback and helpful comments. Special thanks go to **Julien** for always promptly answering my emails filled with technical questions and for all his ideas that greatly contributed to my work.

I am deeply thankful to **Mourad Bouhadjar**, **Gaël Fouré** and all radiology staff from IHU Strasbourg for their patience and immense assistance during our many long-days of experiments in the experimental operating rooms. We couldn't have done any of our experimental validations, recordings or demonstrations without your help. Many thanks to **Pr. Afshin Gangi** and all the staff of the interventional radiology department of Strasbourg's University Hospital for collaborating with us and allowing us to install our cameras in your operating rooms. Special thanks to **Emile Reeb** for taking the time to educate me about interventional radiology and answering all my clinical questions. I also want to thank **Nicolas Clauss** for sharing his knowledge on radiation protection with us and for his insightful feedback about our radiation awareness system.

Special thanks go to **Dr. Konstanze Gunzert** and **Tim Horz** since they were instrumental in the development of our radiation awareness prototype system. Thank you **Konstanze** for always believing and supporting the project. Thank you **Tim** for all your technical assistance.

Finally, I would like to thank my parents, my brother and sisters for their limitless love and support since the day I was born. Thank you for giving me the chance of getting a higher education and pursue my goals even if it is far away from you and from my country of birth. Thank you for your constant encouragement and for always being there when I needed it. I am also deeply grateful with my girlfriend Julie for her immense love, support and for encouraging me every day to keep moving forward. It was through our PhDs that we found each other, and for that I am really grateful.

Last but not least, I gratefully acknowledge the financial support which funded my work, received from French state funds managed by the ANR within the Investissements d'Avenir program under references ANR-11-LABX-0004 (Labex CAMI), ANR-10-IDEX-0002-02 (IdEx Unistra), ANR-10-IAHU-02 (IHU Strasbourg) and ANR-11-INBS-0006 (FLI).

Table of Contents

I Introduction **1**

1 Clinical motivation and context **3**

1.1 X-ray imaging in today's medicine 5

1.1.1 Minimally invasive procedures 5

1.1.2 Interventional surgical procedures 6

1.1.3 X-ray imaging modalities 7

1.2 Exposure to ionizing radiation during X-ray guided procedures 9

1.2.1 Radiation exposure risks 9

1.2.1.1 Effects of ionizing radiation on living tissue 10

1.2.1.2 Risk to patients 10

1.2.1.3 Risk to healthcare providers 11

1.2.2 Factors affecting radiation propagation 12

1.3 Strategies to reduce radiation dose to patients and clinical staff 14

1.3.1 Radiation safety guidelines 15

1.3.2 Reduction of the imaging device's effective doses 15

1.3.3 Radiation exposure monitoring 15

1.3.4 Protective equipment 16

1.4 Summary and thesis overview 18

1.4.1 Summary of the medical context 18

1.4.2 Contributions 18

1.4.3 Outline 20

2 Systems for improving radiation safety: Related work **23**

2.1 Commercially available systems for monitoring and/or reducing radiation exposure 25

2.1.1 Patient's exposure 25

2.1.2 Occupational exposure 26

2.1.2.1 Real-time staff dose assessment 26

2.1.2.2 Staff exposure reduction . . . 27
2.2 Research projects for improving radiation safety . . . 29
2.2.1 Systems enabling an active reduction of radiation exposure . . . 29
2.2.1.1 Robotized surgical assistance . . . 29
2.2.1.2 Enhanced surgical guidance . . . 30
2.2.2 Systems to understand, teach and/or increase awareness to radiation exposure . . . 32
2.2.2.1 Assessing radiation through computer simulations . . . 32
2.2.2.2 Virtual training systems . . . 33
2.2.2.3 Computational systems for increasing radiation awareness 35
2.3 Thesis positioning . . . 37

II Context-aware radiation monitoring 41

3 OR context perception through a multi-RGBD camera system 43
3.1 Camera setup and calibration . . . 45
3.1.1 RGBD sensors . . . 45
3.1.2 Camera calibration . . . 46
3.1.3 Multi-camera system registration . . . 47
3.2 Visual perception of the room environment . . . 48
3.2.1 Room layout tracking . . . 49
3.2.2 Patient registration . . . 49
3.2.3 Clinicians tracking . . . 49
3.3 X-ray device configuration detection . . . 52
3.4 Conclusion . . . 54

4 Radiation simulation 57
4.1 X-ray imaging modeling . . . 59
4.1.1 Imaging process . . . 59
4.1.2 X-ray energy spectrum . . . 61
4.2 Monte Carlo simulations of X-ray transport with Geant4 . . . 62
4.2.1 Simulation approach . . . 62
4.2.2 Visualization of simulated radiation risk maps . . . 64
4.2.3 Experimental validation using dosimeters . . . 65
4.2.3.1 Validation methodology . . . 65
4.2.3.2 Results and discussion . . . 67
4.3 GPU-accelerated radiation simulation . . . 70
4.3.1 Simulation approach . . . 71
4.3.1.1 Patient exposure . . . 71
4.3.1.2 Staff exposure . . . 74
4.3.1.3 Scattered radiation propagation . . . 77
4.3.2 Experimental validation . . . 77

4.3.2.1 Clinician exposure validation . . . 77
4.3.2.2 Evaluation with experimental measurements . . . 79
4.4 Conclusions . . . 80

5 Intuitive visual feedback of ionizing radiation 83
5.1 Augmented reality visualization of ionizing radiation . . . 85
5.1.1 Benefits of X-ray radiation's AR visualization . . . 85
5.1.2 Visualization methods . . . 86
5.1.2.1 3D propagation of scattered radiation . . . 86
5.1.2.2 Patient exposure visualization . . . 89
5.1.2.3 Staff exposure visualization . . . 89
5.2 Augmented Reality visualization approaches . . . 90
5.2.1 Ceiling-view AR visualization . . . 91
5.2.2 Mobile AR using a hand-held screen . . . 91
5.2.3 Mobile AR using a HoloLens . . . 92
5.3 Conclusions . . . 96

6 Optimization of an X-ray imaging device's pose 99
6.1 C-arm positioning assistance . . . 101
6.1.1 Context . . . 101
6.1.2 Related work . . . 102
6.2 Imaging device's pose optimization . . . 103
6.2.1 Problem statement . . . 104
6.2.2 Fast computation of cost function . . . 105
6.2.2.1 Patient exposure term v . . . 106
6.2.2.2 Clinical staff exposure term h . . . 106
6.2.3 Optimization approach . . . 107
6.2.4 Imaging device's re-positioning in clinical application . . . 107
6.3 Experiments in a simulated environment . . . 109
6.3.1 Experimental setup . . . 110
6.3.2 Optimization algorithm evaluation . . . 111
6.3.3 Cost function weights trade-off analysis . . . 113
6.3.4 Evaluation of the cost function computation approach . . . 115
6.4 Evaluation with dose measurements . . . 117
6.4.1 Experimental setup . . . 117
6.4.2 Evaluation results . . . 119
6.5 Discussion and conclusions . . . 120

III Applications, conclusions and perspectives 123

7 Clinical applications 125
7.1 XAware-Live: a global radiation awareness system . . . 126

7.1.1 General description of the system . . . 126
7.1.2 System's features and visualizations modes . . . 128
7.1.3 Demonstrations and feedback about the system . . . 129
7.1.4 Future developments . . . 130
7.2 Potential clinical applications . . . 131
7.2.1 Intraoperative radiation awareness . . . 131
7.2.2 Clinical applications of a C-arm pose optimization approach . . . 133
7.3 Conclusions . . . 134

8 Conclusions and perspectives 135
8.1 Conclusions . . . 135
8.2 Perspectives . . . 138

List of Publications 143

IV Appendices 145

A Radiation dose information 147
A.1 Radiation dose measurements . . . 147
A.1.1 Conversions between radiation dose units . . . 147
A.2 Radiation dose values, thresholds and occupational limits . . . 148
A.2.1 Radiation dose values for common exams . . . 148
A.2.2 Radiation exposure thresholds . . . 148
A.2.3 Dose limits as recommended by the International Commission on Radiological Protection (ICRP) . . . 149
A.3 Radiation exposure metrics . . . 149

B xawAR16 dataset 151
B.1 A multi-RGBD camera dataset for camera relocalization evaluation in the operating room . . . 151
B.2 Dataset description . . . 152
B.3 Optical tracking system calibration . . . 153
B.4 Additional information . . . 153

C Camera relocalization approach for a markerless mobile AR 155
C.1 Introduction . . . 155
C.2 Method . . . 156
C.2.1 Overview . . . 156
C.2.2 Tracking approach . . . 157
C.2.2.1 Tracking initialization/relocalization . . . 157
C.2.2.2 Frame-to-frame tracking . . . 157
C.2.3 Equipment detection in the OR . . . 158
C.2.3.1 Template databases' generation . . . 158

C.2.3.2 Ceiling cameras template database . . . 159
C.2.3.3 Moving camera template database . . . 159
C.2.3.4 Occlusion handling . . . 159
C.2.4 Dynamic template database sub-sampling . . . 159
C.3 Evaluation with the xawAR16 dataset . . . 160
C.3.0.1 Evaluation metrics . . . 160
C.3.0.2 System settings . . . 161
C.4 Evaluation Results . . . 161
C.4.1 Equipment detection . . . 161
C.4.2 Moving camera tracking . . . 162
C.4.3 Relocalization . . . 163
C.5 Conclusions . . . 165

D Résumé en français **167**
D.1 Introduction . . . 168
D.2 Radioprotection réactive au contexte . . . 170
D.2.1 Perception de la salle opératoire par des caméras RGBD . . . 170
D.2.2 Méthodes de simulation des radiations . . . 170
D.2.3 Visualisations des radiations par réalité augmentée . . . 172
D.3 Optimisation de la pose d'un capteur plan . . . 175
D.4 Application clinique: *XAware-Live* . . . 176
D.5 Conclusions . . . 179
D.6 Perspectives . . . 180

References **181**

List of Figures

1.1 A century of technological improvements in X-ray imaging. 3
1.2 Frequency of Interventional Radiology (IR) procedures in 6 EU's hospitals reported in [Nikodemová 2011] (1.2a) and Strasbourg's University Hospital IR department (1.2b). 8
1.3 Effect of increasing patient abdomen thickness on operator exposure, courtesy of [Schueler 2006]. The drawings illustrate scattered radiation isodose curves calculated with a phantom simulating abdomen thicknesses. A 5 cm increase almost doubles staff exposure. 13
1.4 Use of radiation protection equipment in hospitals in Europe as reported by [Nikodemová 2011]. 17

2.1 Toshiba's Dose Tracking System [Rana 2013, Kuhls-Gilcrist 2017] for the visualization of the cumulative skin dose distribution overlaid over a patient's generic model during X-ray imaging. 23
2.2 Commercially available tele-operated navigation systems for interventional procedures. 28
2.3 Examples of systems providing an enhanced visualization to improve surgical guidance and reduce radiation exposure. 31
2.4 Examples of computer-based training systems to teach about C-arm operation and radiation exposure. 35
2.5 Systems for providing feedback of radiation exposure for increasing clinicians' awareness. 38

3.1 Views from a multi-RGBD camera system installed in an experimental interventional room at IHU Strasbourg, featuring an Artis Zeego X-ray imaging device (Siemens Healthcare, Forchheim, Germany). 43
3.2 Evaluation of the depth measurement error and of depth correction approaches. 47
3.3 Registered multi-camera system for performing a 3D reconstruction of an interventional room. 48

3.4 Background subtraction approach to track the 3D positions of clinicians in an interventional room and provide a visualization of their current full-body exposure. 50
3.5 Courtesy of [Kadkhodamohammadi 2017b]: (left) the detected clinician's upper-body poses on an image from an interventional room at Strasbourg's University Hospital and (right) the simulated radiation exposure per body joint (modeled as water spheres), where red indicates higher dose. 51
3.6 (Left) Real-time person pose estimation using the approach from [Cao 2017], and its usage for the visualization of the body radiation exposure of clinicians (right). 52
3.7 Automatic detection of the X-ray imaging device configuration from views of the ceiling-mounted multi-camera system. 54

4.1 Representation of the X-ray imaging process and simulated output radiography. 57
4.2 Visualization of the X-ray source position and nomenclature for imaging projections in the transverse plane (left) and in the sagittal plane (right). The position of the source is represented by the red circle with an arrow pointing in the direction of the X-ray beam. 60
4.3 Simulated X-ray spectrum (85 kV - 0.4 mm Al filtration) using the online X-ray spectra simulator from Siemens [Siemens Healthcare 2017b]. 62
4.4 Simulation model and setup of the experimental validation. 64
4.5 2D Isomaps obtained by summing the radiation risk maps along the x-axis for two imaging configurations (red indicates higher dose). 65
4.6 Position of the dosimeters with respect to the C-arm isocenter (S) for the two sets of experiments presented. 67
4.7 Patient's energy and dose maps simulated for an Anterior-Posterior (AP) X-ray projection, 70 kV tube tension, 0.4 mm Al spectrum 8° of aperture angle. 73
4.8 Generation of *scatter maps* and their use for a fast computation of a clinicians' radiation exposure. 75
4.9 Generation of *scatter maps* and their use for a fast computation of a clinicians' radiation exposure. 76
4.10 (Left) Results of the simulation of a clinician's energy for a full rotation of a C-arm in the Left Anterior Oblique (LAO)/Right Anterior Oblique (RAO) plane computed with a Monte Carlo (MC) simulation, using pre-computed Phase-Space File (PSF) or using *scatter maps*. (Right) Experimental setup for the experimental validation with measurements from dosimeters in an OR. 80

5.1 AR visualization of the 3D propagation of scattered radiation (left) and of a clinician's full-body exposure (right), during a RAO at 135° X-ray imaging projection. 83

5.2 AR visualization of the 3D diffusion of scattered radiation for two imaging projections: an RAO at 120° projection (left) and a Posterior-Anterior (PA) projection (right). Red indicates higher dose. 87

5.3 AR visualization of the propagation/intensities of scattered radiation for two C-arm angulations (AP and LAO at 90°), illustrating the effect of table- and ceiling-suspended protective shields for radiation protection. . 88

5.4 AR visualization overlaid a posteriori for visualization purposes, to show the scattered radiation that would be generated if the X-ray device was used in such a situation: no lead protective shields (left) and with a ceiling-suspended shield (right) (Strasbourg's University Hospital). . . . 89

5.5 Visualization of a patient radiation exposure (to skin and organs) on a virtual environment (left) or through a mobile AR (right), for an RAO at 135° C-arm projection. 90

5.6 (Left) Mobile AR visualization of a clinician's exposure during a PA projection. (Right) Ceiling-view AR visualization of the exposure of two clinicians for an AP projection. 91

5.7 Mobile AR visualization for radiation awareness using a hand-held screen. The user visualizes the propagation of scattered radiation for the current device configuration directly in his own view. 93

5.8 Using Microsoft's HoloLens to display radiation exposure information. . . 95

5.9 HoloLens visualization of a clinician's body-part exposure: the person's pose is computed in images from a ceiling-camera and transmitted wirelessly. 95

5.10 Virtual Reality (VR) radiation training application: a virtual interventional scene is displayed to the user with information related to radiation safety through a HoloLens for learning purposes. 96

6.1 X-ray imaging device's pose optimization concept: from an initial configuration, considering clinician, imaging and patient parameters, a recommended device's pose lowering patient/staff radiation exposure and maintaining the visibility of the targeted anatomical structure in the output image is computed through an optimization loop. 99

6.2 "Desired View" pipeline from [Fallavollita 2014]: the user chooses the desired outcome image and, based on simulated X-rays from pre-operative Computed Tomography (CT) data, the system computes the required positioning of the imaging device. 103

6.3 Parametrization of an angiographic C-arm: a projection is determined by the angles θ (right/left anterior oblique) and ϕ (caudal/cranial). Tube-to-isocenter distance (TID) (tube-to-isocenter distance) and Tube-to-detector distance (TDD) (tube-to-detector distance) determine the image's magnification. 104

6.4 Pose optimization pipeline: from an initial nominal projection C_{nom}, our approach suggests a close configuration C_{opt} for which the radiation exposure of staff and patient is reduced. A simulated X-ray image along with exposure reduction statistics are displayed to the operator for him/her to decide to adopt or not the recommendation. If the device's Application Programming Interface (API) is available, its re-positioning can be performed automatically through inverse kinematics. 109
6.5 Virtual setup illustrating the two clinicians' scenario for the experiments presented in sections 6.3.2 and 6.3.3. 112
6.6 Trade-off analysis when varying the weights (α, β) from cost function 6.1. 114
6.7 (Left) Setup for the dose measurements performed in a hybrid OR at IHU Strasbourg using a Siemens' Artis Zeego X-ray imaging device and RaySafe dosimeters. (Right) Four dosimeters taped to a drip rod used to obtain dose measurements over a "dummy" clinician's body. 118
6.8 Images captured by our ceiling-mounted multi-camera system during the dose measurements performed at IHU Strasbourg. The nominal configuration (C_{nom}) and the one recommended by our C-arm pose optimization approach (C_{opt}) are shown. 119

7.1 Graphical User Interface (Graphical User Interface (GUI)) of our radiation awareness prototype system *XAware-Live*. 125
7.2 Clinician tracking in *XAware-Live*: the 2D body-joints' positions are overlaid over the color image (left) and the persons' 3D positions are shown in a virtual environment (right). 127
7.3 Visualization of the patient's dose to the internal structures and to the skin for the current X-ray imaging device's projection and imaging protocol on *XAware-Live*. 128
7.4 AR visualization of the intensities and of the 3D propagation of scattered radiation for the current C-arm projection with *XAware-Live*. 129
7.5 AR visualization of the current personnel's body radiation exposure with *XAware-Live*. 130
7.6 Demonstrations of *XAware-Live* to our industrial partners (left) and to IHU Strasbourg's medical fellow staff (right). 130
7.7 Concept of a GUI for an intraoperative tool displaying the current scattered radiation and patient dose in a virtual environment. 132
7.8 Postoperative review of atypical dose events recorded by dosimeters during an X-ray guided procedure, with an AR visualization of the propagation of scattered radiation during such events. 133
7.9 Concept for a preoperative procedure planning application to determine the optimal C-arm poses yielding the lowest dose to the patient in an upcoming procedure. 134

B.1 Sample images from the xawAR16 dataset recorded with three RGBD cameras (two ceiling-mounted and a mobile one) in an OR, with ground-truth pose information of the mobile camera. 151
B.2 xawAR16 dataset recording setup: Two RGBD cameras are rigidly mounted to the ceiling ($\mathbf{C_1}$ and $\mathbf{C_2}$), a third one is fixed to a display ($\mathbf{M}$) held by a user. A reflective passive marker is attached to the moving camera and its ground-truth pose is obtained with the infiniTrack tracking system. . . 152

C.1 The two steps of our approach for markerless camera relocalization and tracking, applied for a mobile AR application. 155
C.2 Overview of our approach's workflow. In practice, the data streams from the cameras (C_1, C_2 and M) are processed simultanously by processes executed on separate threads. 157
C.3 Estimated mobile AR display 's trajectories with our tracking approach, compared to the ground-truth trajectories for two sequences of the dataset. 164

D.1 Chirurgie mini-invasive guidée par fluoroscopie au service de radiologie interventionnelle du Nouvel Hôpital Civil de Strasbourg. 169
D.2 Positions des trois caméras RGBD qui sont installées au plafond d'une salle opératoire expérimentale au IHU Strasbourg (en rouge). 171
D.3 Vues du système multi-caméra utilisé pour percevoir la salle opératoire. . 171
D.4 Méthodes de simulation Monte Carlo de la propagation 3D des radiations et des doses au patient et personnel médical. 172
D.5 Visualisation par AR de la propagation en 3D du rétrodiffusé de radiation, pour deux angulations différentes de l'imageur: pour une acquisition RAO à 120° (gauche) et une PA (droite). 173
D.6 Visualisation par AR de la propagation en 3D du rétrodiffusé de radiation, pour deux angulations différentes de l'imageur, avec un sans utilisation de protection plombées (suspension plafonnière et paravent plombé). 173
D.7 (Gauche) Visualisation par AR mobile de l'exposition aux radiations des cliniciens lors d'une acquisition PA. (Droite) Visualisation par AR effectuée avec les vues des caméras fixées au plafond de la salle, illustrant l'exposition de deux cliniciens lors d'une acquisition AP. 174
D.8 Visualisation de la dose aux organes et à la peau du patient calculée avec nos méthodes de simulation Monte Carlo. 174
D.9 Méthode d'optimisation de la pose d'un C-arm: à partir d'une configuration initiale et en prenant en compte les positions actuelles du staff, les paramètres de l'acquisition et du patient, notre méthode cherche la configuration optimale qui réduit la dose patient/staff tout en conservant la qualité clinique de l'image. 176
D.10 Concept pour l'interface utilisateur d'une application de planning préopératoire pour déterminer les configurations optimales de l'imageur qui minimisent la dose au patient. 177

D.11 Visualisation par réalité augmentée de la propagation et intensité du rétrodiffusé de radiation pour l'angle d'incidence courant du capteur plan, proposée par le système *XAware-Live*. 178
D.12 Visualisation de la dose à la peau et aux organes du patient pour l'angle d'incidence courant du capteur plan, proposée par le système *XAware-Live*.178
D.13 Estimation en temps réel de la pose des cliniciens présents dans la salle, grâce à l'intégration de l'approche de [Cao 2017] à *XAware-Live*. 179
D.14 Visualisation par réalité augmentée de la dose sur les différentes parties du corps des cliniciens présents dans la salle pour l'angle d'incidence courant du capteur plan, proposée par le système *XAware-Live*. 179

List of Tables

4.1 Simulation errors for the *configuration test* when using dosimeter 1 for calibration. 68

4.2 Mean simulation errors per validation dosimeter and per configuration for the *tube parameters' test*, when calibrating with dosimeter 6 and 8. 68

4.3 Mean simulation errors per irradiation protocol when calibrating with dosimeter 6 and 8 in the *tube parameters' test*. 69

4.4 Patient radiation exposure maps: simulation times and mean statistical uncertainty in function of the number of particles emitted. 74

4.5 Simulation times of clinician exposure with the three approaches evaluated: a full Monte Carlo simulation (MC) without approximations, with pre-computed PSF and *scatter maps*. 78

4.6 Mean relative difference of a clinician's exposure obtained with the PSF and *scatter maps* methods, compared with a full MC simulation and pre-computed PSF as references. 79

4.7 Mean simulation errors per irradiation protocol with two calibration dosimeters. 81

6.1 Imaging configurations typical in interventional radiology procedures evaluated with our approach along with the considered ranges for the sets S. 111

6.2 Optimization of the X-ray device's pose with two algorithms: greedy best-first search and gradient descent. A scenario with two clinicians is considered, where clinician #1 is at position $T_1 = [-1000, 0, 0]^T$ and #2 at $T_2 = [700, 0, 500]^T$. The recommended configuration C_{opt}, the relative exposure reduction of the patient (Δ_v) and of both clinicians (Δ_h), along with the optimization time are given. 113

6.3 Results of the optimized C-arm's pose for each S and comparison with the computation of function (6.1) with no approximations (*Full MC*). The absolute difference of *Ours* and *Full MC* (*Diff*), the recommended configuration C_{opt}, the achieved relative exposure reduction Δ_f and the execution times are provided. 116
6.4 Device's pose optimization with two clinicians in the scene, where clinician #1 is at position $T_1 = [-1000, 0, 0]^T$ and #2 at $T_2 = [700, 0, 500]^T$. The recommended configuration C_{opt}, the relative exposure reduction of the patient ($\Delta_v(\%)$) and of both of the clinicians' heads (Δ_{h_1} and Δ_{h_2}) are provided. 117
6.5 Evaluation of the C-arm pose optimization approach with real dose measurements: the evaluated configuration pairs (C_{nom}, C_{opt}), the relative clinician exposure reduction as computed from the dose measurements (Δ_h (measured)) and as predicted by the optimization approach (Δ_h (simulated)) along with the absolute difference (Diff.) between them are provided. 120

A.1 Typical organ radiation dose from various radiologic studies, as reported in [Brenner 2007], [FDA 2010] and [Conti 2014]. 148
A.2 Threshold doses for potential radiation exposure effects, as reported in [Miller 2005]. 148
A.3 Dose Limits Recommended by the ICRP in [ICRP 2017]. 149

B.1 Evaluation dataset: each sequence is categorized according to the side of the operating table where the mobile display was held, the type of sequence (*Smooth*, *Clinician*, *Challenging* or *Device rotation*) and the ongoing X-ray device projection. The average rotation velocity (deg/s) and translation velocity (m/s) is also provided. 154

C.1 Absolute Pose Error (APE) when relocalizing with different template databases. *Non-filtered*: templates generated from synthetic views covering the full sphere of viewpoints around the object. *Filtered*: sets where a priori information has been used to filter-out irrelevant views. *User tracking*: using the detected user's position to load the templates to match. The number of training views as well as the mean translation error (T) in mm, rotation error (R) in degrees, detection speed (S) in seconds and mean values for all the evaluated sequences are provided. 162
C.2 Evaluation of our full approach on all sequences from the dataset with the evaluation metrics described in C.3.0.1. The number of evaluated frames (*Ev. frames*) corresponds to the frames with ground-truth available. Mean errors per sequence type (*Smooth* AR display's trajectories or *Challenging* for sequences including occlusions, clinicians and/or large/sudden camera viewpoint changes) are provided. 163

C.3 Evaluation of our relocalization approach compared to Iterative Closest Point (ICP) with initialization: *Ev. Frames* is the number of frames per sequence where a relocalization was performed and which also has ground-truth available. We evaluate by computing APE on the relocalized frames (T for the translation error in mm and R for the rotation error in degrees). *%Rel* corresponds to the percentage of recovered frames (APE within 15 cm in translation and 7° in rotation). 165

List of Abbreviations

AEC Automatic Exposure Control. 13, 61

ALARA As Low As Reasonably Achievable. 15, 104

AP Anterior-Posterior. xii, xiii, xv, 8, 60, 65, 66, 68, 69, 72, 73, 87, 88, 90, 91, 96, 148, 153, 161, 174

APD Active Personal Dosimeter. 15, 26, 27, 69, 119

APE Absolute Pose Error. xviii, xix, 160, 162–165

API Application Programming Interface. xiv, 49, 52, 54, 55, 109, 126–128, 131, 137

AR Augmented Reality. i, vii, viii, xii–xv, xviii, 18, 19, 30, 35, 37, 39, 54, 83–92, 96, 97, 128–131, 133, 136, 138, 151, 153, 155–158, 160, 162–166, 168–170, 172–174, 177

CAT Computed Axial Tomography. 8

CAUD Caudal. 60, 79, 81, 104, 127

CBCT Cone-Beam Computed Tomography. 31

CRAN Cranial. 60, 79, 81, 104, 127

CT Computed Tomography. xiii, 3, 6–9, 15, 30, 59, 60, 72, 90, 101–103, 107, 110, 139, 148, 170

DAP Dose Area Product. 16, 25–27, 38, 139, 150

DICOM Digital Imaging and Communications in Medicine. 52

DRR Digitally Reconstructed Radiograph. 34, 57

ERCP Endoscopic Retrograde Cholangio-Pancreatography. 7

EVS Endovascular Surgical Neuroradiology. 7

FOV Field of View. 13, 52, 63, 66

GPU Graphics Processing Unit. 19, 32, 34, 36, 58, 70, 71, 73, 77, 78, 80–82, 105, 110, 127, 131, 136, 137, 139, 160, 161, 170, 172, 175

GUI Graphical User Interface. xiv, 125–128, 131, 132, 134

HMD Head-mounted Display. 93, 94, 96, 138

IC Interventional Cardiology. 7, 10, 12, 14, 16, 18, 27, 32, 35

ICP Iterative Closest Point. xix, 49, 53, 157–159, 163–165

ICRP International Commission on Radiological Protection. viii, xviii, 12, 16, 25, 149

II Image Intensifier. 49

IR Interventional Radiology. xi, 7, 8, 16–18, 32, 33, 88

LAO Left Anterior Oblique. xii, xiii, 60, 66, 68, 69, 78–81, 87, 88, 104, 127, 153

MC Monte Carlo. xii, xvii, 32–34, 39, 68, 70, 73, 74, 76, 78–80

MIS Minimally Invasive Surgery. 5, 6, 9, 18, 20, 30, 101

MRI Magnetic Resonance Imaging. 6, 7, 141

OR Operating Room. i, viii, xii, xiv, xv, 5, 19, 20, 24, 34, 38, 44, 47, 52, 54, 58, 62–64, 77, 80, 85, 86, 91, 92, 94, 95, 101, 103, 105, 117–121, 126, 127, 129, 131, 136–138, 141, 151, 158, 165

OST-HMD Optical See-Through Head-Mounted Display. 85, 93, 94, 96, 131

PA Posterior-Anterior. xiii, xv, 37, 60, 63, 65, 66, 68, 69, 80, 87, 90, 91, 94, 96, 148, 153, 161, 173, 174

PET Positron Emission Tomography. 7–9, 15

PSD Peak Skin Dose. 150

PSF Phase-Space File. xii, xvii, 74, 75, 77–80

PTA Percutaneous Transluminal Angioplasty. 6, 8, 14

RAK Reference Air Kerma. 25, 149, 150

RAO Right Anterior Oblique. xii, xiii, xv, 60, 66, 68, 69, 76, 78–81, 83, 85, 87, 89, 90, 104, 127, 153, 173

RGBD Red-Green-Blue-Depth. i, vi, ix, xi, xv, 19, 20, 30, 31, 37, 43–45, 48, 50–54, 62, 65, 70, 79, 84, 86, 91, 92, 94, 126, 132, 136, 151, 152, 156–158, 161, 165, 167, 168, 170–172, 176, 180

RPE Relative Pose Error. 160, 162, 163

SLAM Simultaneous Localization and Mapping. 151–153

SPECT Single Photon Emission Computed Tomography. 8

TDD Tube-to-detector distance. xiii, 104

TID Tube-to-isocenter distance. xiii, 104

TLD Thermoluminescent dosimeters. 15, 16, 26, 27, 70

VR Virtual Reality. xiii, 94, 96, 138

Introduction Part I

1 Clinical motivation and context

To keep the body in good health is a duty...
otherwise we shall not be able to keep our mind storing and clear.
– Gautama Buddha

(a) The first known X-ray image, taken from Röntgen's wife left hand [Reed 2011].

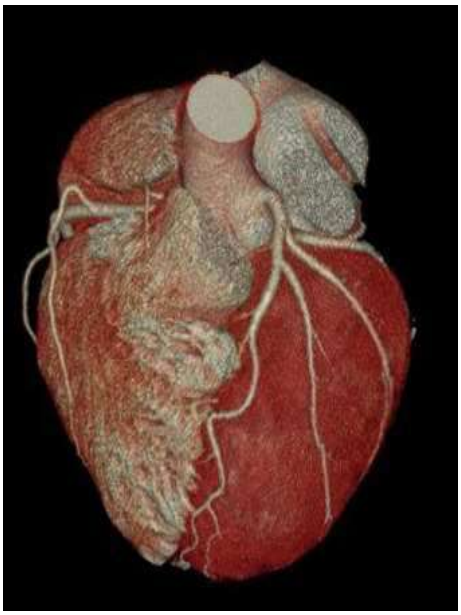

(b) Three-dimensional volume-rendered CT image depicting normal coronary arteries [Kuchynka 2015].

Figure 1.1: A century of technological improvements in X-ray imaging.

Chapter Summary

1.1 X-ray imaging in today's medicine 5
1.1.1 Minimally invasive procedures 5
1.1.2 Interventional surgical procedures 6
1.1.3 X-ray imaging modalities 7
1.2 Exposure to ionizing radiation during X-ray guided procedures 9
1.2.1 Radiation exposure risks 9
1.2.1.1 Effects of ionizing radiation on living tissue 10
1.2.1.2 Risk to patients 10
1.2.1.3 Risk to healthcare providers 11
1.2.2 Factors affecting radiation propagation 12
1.3 Strategies to reduce radiation dose to patients and clinical staff 14
1.3.1 Radiation safety guidelines 15
1.3.2 Reduction of the imaging device's effective doses 15
1.3.3 Radiation exposure monitoring 15
1.3.4 Protective equipment 16
1.4 Summary and thesis overview 18
1.4.1 Summary of the medical context 18
1.4.2 Contributions 18
1.4.3 Outline 20

The use of X-ray based medical imaging has revolutionized the diagnostic of diseases and the practice of numerous surgical treatments. It has also been a key factor in the paradigm shift from traditional to minimally invasive surgery. Nowadays, X-ray imaging is fundamental to several fields of medicine such as interventional radiology/cardiology, orthopedics, urology, neuroradiology and radiation therapy to name a few. Even if it is hard today to envision medicine without having the capacity to visualize internal structures and bones through X-ray imaging, X-rays were discovered just slightly more than a century ago. It was in 1895 that Wilhelm Conrad Röntgen performed the first radiography (shown in figure 1.1a) while working with a cathode-ray tube in his laboratory at Würzberg University in Germany [Reed 2011]. The discovery of this new kind of ray, which could penetrate the body and give the capability to record its inner structure without any visible damage, is considered one of the most momentous events in science and medicine. It was not hard for Röntgen's contemporaries to see the enormous potential of such a discovery. Only a month after, radiographs were being produced in the United States as well as in Europe; within 6 months after this discovery, they were being used at the frontline in battlefields to help locate bullets in wounded soldiers [Reed 2011]. Other advances came quickly such as the invention of the fluoroscope by Thomas Edison and the appearance of contrast agents to further look within body structures. Even though a sea

of technical developments has been made ever since Röntgen's first radiography, there is a core issue related to X-ray imaging which still remains the same even a century later. We refer to the risks associated with the exposure to the ionizing radiation generated during the image acquisition process. At first, there was understandably very little concern about the unintended consequences that could occur from the use of these invisible rays. But after some time, workers exposed to X-rays noted that repeated exposures seemed to make hair fall out, cause skin inflammations, sores, loss of limbs and even death [Linton 1995]. It took several years for scientists to realize that X-rays' shorter wavelength than light's along with their high energy could penetrate and break chemical bonds in living tissues, which results in the alteration of the structures and functions of cells [Reed 2011]. Indeed, much of the early collection of information related to radiation damage was gained at great personal expense. However, the large efforts of scientists to develop radiation safety protocols, to devise protection methodologies, to learn to control and assess X-ray production are also considered a major progress in this century of X-ray imaging history [Linton 1995].

In this dissertation, we propose methods to contribute to the effort that radiation scientists have performed throughout the past century to decrease the risks of exposure to ionizing radiation when X-rays are used for medical purposes. We focus on modern applications of X-ray imaging, namely on the use of X-rays for guidance during minimally invasive procedures. In the following sections, we discuss about minimally invasive X-ray guided interventions, including the different image modalities which are used. Then, we present the negative effects associated with the exposure to ionizing radiation, along with a description of the current radiation protection practices. The last section of this chapter provides an overview of the work carried out throughout this thesis to improve radiation safety in the operating room (OR) and also presents the outline of this dissertation.

1.1 X-ray imaging in today's medicine

In order to improve patient care, surgical procedures are evolving to become minimally invasive. As a consequence, medical imaging devices are now fundamental to the performance of today's procedures. In this section we first give an overview of the growth of minimally invasive surgery (MIS). Then, we introduce interventional procedures, a kind of MIS generally involving important doses of ionizing radiation. We close this section with a summary of the imaging modalities used in MIS and which cause radiation exposure.

1.1.1 Minimally invasive procedures

Driven by last decades' significant technological improvements in medical and imaging equipment, minimally invasive procedures (also known as MIS) are progressively replacing traditional open surgery procedures in today's hospitals [Nikodemová 2011]. Open surgery requires a large incision and can incur significant trauma to soft tissue, which can be painful for the patient, can take more time to heal and can lead to potential complications.

Minimally invasive surgery encompasses imaging and catheterization techniques that limit the size of the needed incisions. Reported benefits of MIS include less pain for the patient, reduced risk of infections, quick recovery time and reduced blood loss [Fuchs 2002]. Furthermore, MIS is also associated with decreased postoperative complication rates and shorter hospital stays, which can lead to reduced healthcare costs [Xu 2015]. Therefore, these kinds of procedures are used by a rapidly growing number of healthcare providers in a wide range of medical specialties.

MIS was pioneered in the 1960's by interventional radiologists. They introduced techniques such as injecting arteries with dye, visualizing these via X-ray imaging and introducing catheters to open up blockages, with the aim of finding safer and better ways to treat atherosclerotic vascular diseases [Lakhan 2009]. Such developments not only led to the replacement of conventional procedures with minimally invasive ones, but also stimulated surgeons to reevaluate conventional approaches. For instance, coronary artery stent insertion became rapidly a more popular alternative than the traditional coronary artery bypass, and from 1996 to 2000 its rate of performance doubled from 157 to 318 per 100,000 adults in the United States [Miller 2005]. In Europe, the number of interventional cardiovascular procedures increased from 350,000 in 1993 to more than 1 million in 2001 [Picano 2013].

The spectrum of minimally invasive procedures performed today is extremely large. They are typically classified according to the means used for guidance and visualization of the interior of the patient's body. On the one hand, endoscopic, laparoscopic and arthroscopic procedures rely on the use of a camera inserted through a small incision or through natural orifices, enabling to get live color images of the inside of the patient. On the other hand, interventional and several orthopedics procedures are performed using medical imaging devices such as fluoroscopic X-ray systems, Computed Tomography (CT) or Magnetic Resonance Imaging (MRI) scanners for guidance and visualization of internal anatomical structures. Interventional procedures, presented in the following section, are becoming more frequent and complex and are the focus of this thesis. This is due to the fact that several reports have documented that the dosage of ionizing radiation among interventional physicians is the highest registered by any medical staff using X-rays [Roguin 2013].

1.1.2 Interventional surgical procedures

Because of the many aforementioned benefits of minimally invasive procedures, both their popularity and complexity have increased in the past years. This is directly connected to the technological progress in highly sophisticated imaging equipment used for these purposes, which enables clearer visualizations of fine internal anatomical structures of the patient (see Figure 1.1b). Nowadays, in European countries more than 400 types of X-ray guided interventional procedures are identified, with a 12 % increase in the number of procedures performed every year [Nikodemová 2011]. Furthermore, 657,000 fluoroscopy guided percutaneous transluminal angioplasty (PTA) procedures were performed in adults in 2002 in the United States [Miller 2005], with a tendency to increase in the

following years.

Interventional practices are nowadays most common in the fields of interventional cardiology (IC), radiology (IR) and neuroradiology. IC is the specialized branch of cardiology performing conventional coronary angiography, stenting and other procedures on coronary arteries, along with various kinds of therapies to unblock clogged arteries supplying blood to the heart, to stop heart attacks and/or relieve chest pain [Lakhan 2009]. The duties of IR practitioners are more varied. These include the performance of angiographies on other peripheral arteries (renal, popliteal, femoral...) and the use of percutaneous access to treat diseases or perform biopsies [Lakhan 2009]. The results of a study on the frequency of IR procedures in six different EU countries (see Figure 1.2a) presented in [Nikodemová 2011], indicate that angiographies are just half of IR practitioners' workload; the other half corresponds to embolization and Endoscopic Retrograde Cholangiopancreatography (ERCP) procedures. Interventional neuroradiology (also known as Endovascular Surgical Neuroradiology (EVS)) is a subspecialty of radiology also making use of minimally invasive catheter-based technology and radiologic imaging to treat and diagnose diseases of the central nervous system, head, neck and spine [Lakhan 2009]. Common EVS interventions include treating carotid artery stenosis, intracranial/extracranial aneurysms and performing vertebroplasty/kyphoplasty procedures.

All interventional procedures hitherto mentioned rely on the use of medical imaging equipment for diagnosis or therapy delivery (X-ray devices, CT, MRI, Positron Emission Tomography (PET) scanners, and/or ultrasound probes). Several of these devices generate ionizing radiation during the imaging process, and, therefore, cause risks of radiation exposure to patients and clinicians. Such risks vary according to the complexity of the procedure. Hence, as the frequency, complexity and diversity of interventional procedures is increasing, so is the radiation dose to patients and healthcare personnel [Miller 2005]. Indeed, interventional practitioners are performing more procedures than ever, which usually last longer, resulting in more exposure to radiation than in the past [Roguin 2012]. Studies [Roguin 2013] have reported that the dosage of ionizing radiation among interventional practitioners are the highest registered for any medical staff using X-ray, especially since most of interventional procedures are performed under fluoroscopy guidance (continuous X-ray imaging). Additionally, staff is obliged to remain close to the patient during interventional procedures, therefore, their exposure to radiation cannot be fully avoided. This can be observed in Figure 1.2b, which shows an example of a fluoroscopy-guided interventional procedure performed by an interventional practitioner at Strasbourg's University Hospital.

1.1.3 X-ray imaging modalities

There exist many types of medical imaging modalities, each relying on different technologies and techniques. Ultrasound imaging makes use of high frequency sound waves to visualize soft tissues, such as muscles and internal organs. MRI relies on radio waves and magnetic fields to produce images. Unlike ultrasound and MRI, projection radiography

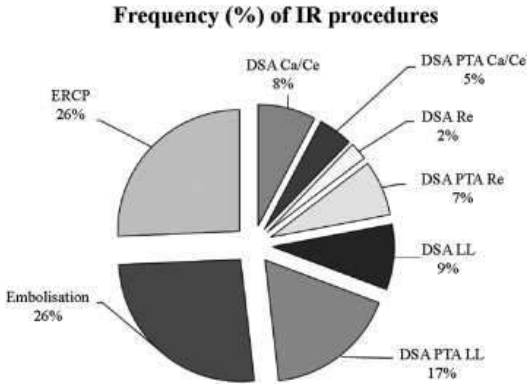

(a) Digital Subtraction Angiography (DSA), Percutaneous Transluminal Angioplasty (PTA), Carotid (Ca), brain (Ce), lower limbs (LL) and renal arteries (Re) angiographies.

(b) Interventional room at the Strasbourg's University Hospital during the execution of a fluoroscopy guided vertebroplasty.

Figure 1.2: Frequency of IR procedures in 6 EU's hospitals reported in [Nikodemová 2011] (1.2a) and Strasbourg's University Hospital IR department (1.2b).

(commonly called standard X-ray), CT, fluoroscopy, and nuclear medicine procedures all rely on ionizing radiation to generate images of the body [FDA 2010]. We discuss relevant facts about these imaging modalities below.

Projection radiography procedures, which include chest X-rays and mammography, involve relatively low amounts of radiation (a typical chest X-ray exposes the patient to 0.02 mSv[1] [Conti 2014]). During a CT scan (also called a CAT scan) a rotating source passes X-rays through a patient's body to produce several cross-sectional images of a particular area. These two-dimensional images can also be digitally combined to produce a single three-dimensional image for better visualization. Hence, organ doses from CT scanning are considerably larger than those from corresponding conventional radiography. For instance, a conventional anterior-posterior (AP) abdominal X-ray results in 0.25 mSv of equivalent dose, which is at least 50 times less than the corresponding stomach dose from an abdominal CT scan [Brenner 2007].

Continuous X-ray imaging or live fluoroscopy is the preferred modality among interventional practitioners since it allows to image the surgical site in real-time and gain a better 3D understanding. This is useful to observe the movement of an object or substance inside the patient's body. When fluoroscopy is continuous, around 30 X-ray images per second are obtained and as a consequence the amounts of radiation generated are significantly higher [Kaplan 2016]. Pulsed fluoroscopy obtains 1 to 6 images per second and can be a less irradiating alternative, yet, it does not allow clinicians to benefit from the same real-time feedback.

Other procedures involving radiation are nuclear medicine procedures, such as PET or Single Photon Emission Computed Tomography (SPECT) examinations. These are relevant imaging techniques that provide functional and quantitative information about

[1]For a detailed description of radiation dose units, see appendix A.1

the organ of interest for diagnostic and therapeutic applications. A patient is given a small amount of a radioactive substance, called a radiopharmaceutical or radiotracer, and a detector outside the body is then used to obtain an image of the radioactive material as it moves throughout the body [FDA 2010]. The extremity dose of workers in nuclear medicine can be a concern since the procedures require the handling of radiopharmaceuticals at contact and/or very close to the extremities (hands and fingers) [Vanhavere 2008]. According to the literature, technicians working in PET facilities receive slightly higher doses than those working in conventional diagnostic nuclear medicine departments, however, these doses are generally below the limits [Vanhavere 2008]. In general, the doses involved in nuclear medicine procedures are significantly smaller than during a fluoroscopic intervention or a CT scan [FDA 2010].

Because CT, fluoroscopy, and nuclear medicine procedures involve repeated or extended exposure to ionizing radiation, they are associated with a higher radiation dose than projection radiography. Among these modalities, interventional fluoroscopy is the one which causes the highest exposure to clinical staff and, for several kinds of procedures, to the patient too [FDA 2010]. Due to the excellent image quality of CT images, these are rather used for pretreatment imaging and treatment planning. Despite providing the ability to see structures in 3D, CT is not often used for direct guidance since its real-time performances are not as high as fluoroscopy's [Wong 2008]. Indeed, no post-processing or reconstruction is required for fluoroscopy, so users can see in real-time changes in the patient or the transit of tools and catheters inserted into the patient. Also, the CT scanner environment offers less work area that fluoroscopy because of the large gantry. Therefore, fluoroscopy is preferred for intraoperative guidance during interventional procedures, which highly exposes clinical staff and patients to ionizing radiation.

1.2 Exposure to ionizing radiation during X-ray guided procedures

The benefits of X-ray guided MIS come at a price: the exposure to ionizing radiation of staff and patient. While a patient's exposure can be justified by medical indication and usually happens in a single episode, medical staff providing patient care can be chronically exposed for many years on a daily basis. In this section, we discuss the risks of exposure to ionizing radiation for patient and clinical staff during X-ray guided procedures. We also describe the many factors that affect radiation's magnitude and propagation, which render the monitoring of exposure complex to achieve.

1.2.1 Radiation exposure risks

Recent studies have reaffirmed the hypothesis that any radiation dose carries with it an associated risk of negative biological effects and that such a risk increases with an increasing dose [Roguin 2013]. Indeed, it is generally accepted that there is no low dose threshold, namely no amount of ionizing radiation should be considered absolutely safe [Miller 2005]. Negative effects of radiation exposure are classified in two categories:

deterministic and stochastic. On the one hand, deterministic effects occur once a dose threshold has been exceeded and their severity increases with the magnitude of the dose. The most common are skin and eye injuries. Stochastic effects, on the other hand, come with no minimal threshold dosage and their adverse outcomes, such as cancer, can take up to several decades to manifest. The likelihood of stochastic effects increases with the total radiation energy accumulated over time, but the severity of such effects is independent of the dose [Kirkwood 2014].

Studies have reported the average dose of a patient in IC to range from 10 to 50 mSv per procedure [Morrish 2008]. On average, a coronary angiography exposes the patient to a dose equivalent to 300 chest X-rays, and a cardiac radiofrequency ablation to 750 chest X-rays [Picano 2013][2]. Effective staff/operators dose range from 0.02 to 30 μSv [Morrish 2008], and can reach higher values for complex procedures, such as up to 200 μSv in a single endovascular thoracoabdominal aneurysm repair [Picano 2013]. However, the repetitive nature of staff's exposure, even when the dose is low, increases the long-term risk of developing negative biological effects. The most active interventional cardiologists can have an annual exposure equivalent to around 5 mSv (under the lead apron) per year, which is two to three times higher than diagnostic radiologists' exposure [Picano 2013]. We discuss more thoroughly radiation exposure risks for patient and clinical staff below, after explaining radiation's effects on living tissue.

1.2.1.1 Effects of ionizing radiation on living tissue

X-rays are electromagnetic radiation of the same nature as light but with a much shorter wavelength. This shorter wavelength is what gives them the capability of penetrating materials that light cannot, such as living tissue [Reed 2011]. The damage caused by the exposure to ionizing radiation occurs at the cellular level and rapidly replicating cell components such as DNA and cell membranes are the most susceptible to be damaged [Kaplan 2016]. Since these electromagnetic waves are of high energy, they have the ability to break chemical bonds, which may incur in both direct and indirect damage. Direct damage occurs as energy is absorbed and molecular bonds are broken, which can result in cell necrosis or distorted replication (deterministic effects). Indirect damage occurs when water molecules are ionized into free radicals. This has the ability of disrupting bonds, and it is thought to be responsible for the long-term effects of radiation, namely stochastic effects [Kaplan 2016].

1.2.1.2 Risk to patients

In the case of patients, the benefits of a proper usage of X-ray devices (either for diagnosis or therapy), outweighs the experienced radiation risks, especially in the older age groups [Roguin 2014]. The patient is exposed to primary radiation, namely radiation between the X-ray source and the image intensifier. Short-term risks are radiation-

[2]More statistics about radiation doses for common X-ray examinations can be found in appendix A.2.1.

induced skin damages (erythema, epilation and even dermal necrosis)[3], which result from acute radiation doses beyond 2 Gy [Miller 2005]. The extent of the injury may not be apparent for weeks and repeated procedures increase the risk of skin damage, since previous exposures sensitize the skin. At lower dose, exposure to the eye lens can cause lens opacity and cataracts that can take years before manifesting. Long term effects include the potential risk of cancer, which for patients is less common since in most cases they are not exposed repetitively to radiation.

1.2.1.3 Risk to healthcare providers

During the X-ray imaging process, X-rays which are not absorbed or do not interact with any material on their path, are deflected and continue their trajectory with an attenuated energy. Such a pattern of deflection, known as scattered radiation or scatter, produces a field of radiation which is responsible for most of clinical staff's exposure [Kaplan 2016]. Therefore, occupational exposure is directly linked to patient dose since it results from this secondary scattered radiation that is produced. Moreover, the exposure of clinicians performing X-ray guided interventional procedures cannot be fully avoided due to the required proximity to the patient, the complexity of the procedure and the need for performing a large set of acquisitions with varying parameters [Schueler 2006]. As mentioned earlier, reports have documented the dosage of radiation among interventional physicians as the greatest registered among any medical staff working with X-rays [Roguin 2013]. As highlighted by [Picano 2013], cumulative doses after 30 years of working life are in the range of 50 to 200 mSv, corresponding to a whole-body dose equivalent of 2,500 to 10,000 chest X-rays.

Even if most of the clinicians' body is shielded with lead protective clothing (see section 1.3.4), studies have shown that the dose delivered to unprotected body parts such as hands, eyes and legs, can approach the maximum established limits [Nikodemová 2011]. Especially the hands are at danger since these remain close to the patient *i.e.* close to the radiation source. Indeed, skin doses to the hands can reach 1 mSv per procedure and can even be higher if bad practices are followed [Carinou 2011]. A rise in reported skin changes on the hands, and an expected increase in late effects such as lens injuries, cataracts and possibly cancer have been reported in [Miller 2005]. Additionally, results from a study of reported cases of brain cancers among interventional cardiologists have shown that in 85 % of the studied cases, the malignancy was located in the left side of the brain [Roguin 2013]. This is due to the usual layout of an interventional room where the practitioner operates from the right side of the patient, thus, the scatter radiation comes predominantly from the patient on his/her left side [Picano 2013]. Clinicians' heads can be at best incompletely protected and annual head exposure among interventional cardiologists has been reported to be nearly 10 to 20 times higher than the whole-body dose recorded below apron [Roguin 2013, Picano 2013]. Concerning eye exposure, studies have found a dose-dependent increased risk of posterior lens

[3]Reported dose thresholds before radiation-induced tissue damage can be found in appendix A.2.2.

opacities for interventional cardiologists and nurses during IC procedures [Roguin 2012]. Indeed, eye cataracts can be observed in one-third of staff after 30 years of work in IC departments [Picano 2013]. It was recently reported that exposure to the eye lens may induce lens opacities and cataracts at substantially lower adsorbed doses than previously considered. As a consequence, the threshold for radiation-induced cataracts has been revised from 2 to 0.5 Gy [Omar 2017]. Furthermore, the International Commission on Radiological Protection (ICRP) has recently recommended a reduction of the occupational dose limit for the eye lens from 150 mSv to 20 mSv, averaged over 5 years, with no single year exceeding 50 mSv [Principi 2016]. Ionization radiation exposure also affects the reproductive health of exposed clinicians. Reports highlight that the cumulative gonad dose (below the lead apron) for interventional cardiologists is in the range of 0.5-1 Sv over a professional lifetime of 30 years, and this can cause significant risks of reproductive health problems [Picano 2013].

The common radiation protection principles with regard to time, distance, and shielding are difficult for operators to fully implement in interventional procedures due to examination complexity, the required proximity between clinician and patient, and the need to maintain a sterile field [Schueler 2006]. Increases in interventional procedures' difficulty, volumes, and workload per clinician contribute to increase the risk of appearance of adverse outcomes for staff exposed to scattered radiation [Roguin 2012]. Therefore, exposure to ionizing radiation during such interventions is further becoming a concern for healthcare providers.

1.2.2 Factors affecting radiation propagation

The propagation of X-rays and their interactions with matter are complex phenomena. Hence, large-scale efforts have been performed to develop methodologies and tools for better understanding the factors affecting it, either through large dose measurement campaigns (e.g. ORAMED project[4] [Nikodemová 2011]) or by means of computer-based simulations [Koukorava 2011, Santos 2015, Principi 2016]. A patient is exposed to the primary X-ray beam, hence, his/her exposure depends on: the imaging parameters (tube voltage (kV), current (mA), collimation...), his/her own physical characteristics (sex, body weight, age...) and the irradiated region of the body. However, occupational exposure is more challenging to assess since staff is mostly exposed to the photons scattered by the patient, table and/or equipment, and also because the propagation and magnitude of such a scatter are affected by several simultaneously changing factors [Koukorava 2011]. Some of them, such as the patient's characteristics (e.g. abdominal thickness) or the complexity of the procedure, are beyond clinicians' control. For instance, complex procedures requiring long fluoroscopy time and higher tube current, such as complex endovascular procedures, incur in higher potential dose [Kirkwood 2014]. Also, it has been reported

[4]ORAMED was a large consortium-based collaborative project (2008-2011), supported by the European Commission within its 7th Framework Program, aiming at the development of methodologies for better assessing and reducing radiation exposure to medical staff performing interventional procedures [ORAMED 2011].

that operators' body height has a major impact on the amount of scatter radiation to different parts of their body [Picano 2013]. Other factors, such as the personnel's position with respect to the patient, the imaging parameters or the disposition of protective equipment can be partially controlled but are usually altered during the procedure. Indeed, many studies can be found in the literature on the influence of the different risk factors of staff/patient exposure. We discuss below some relevant examples:

Patient size For patients with a thicker layer of adipose tissue, the automatic exposure control (AEC) of modern X-ray equipment increases the tube's voltage in order to compensate for the increase of beam attenuation by the patient's body, with the aim of producing clinically useful images [Santos 2015]. Such an increase of the source's potential results in scattered X-rays with higher energy, and, as a consequence, in a significant increase in the levels of scattered radiation [Schueler 2006]. This can be observed in figure 1.3, where the scatter values at the level of the operator's legs are almost doubled for a 5 cm increase of a patient's abdominal thickness [Schueler 2006].

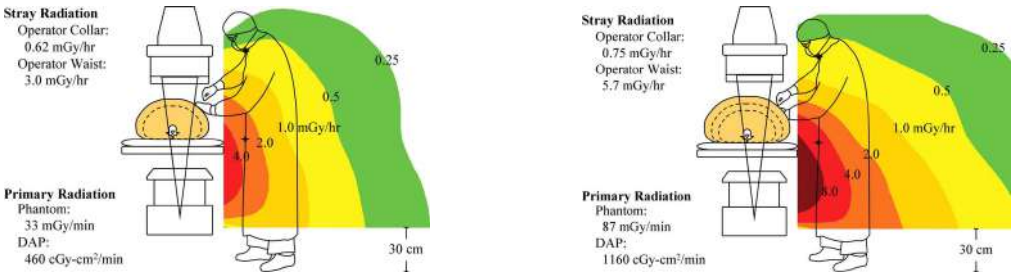

(a) Scatter levels calculated with a phantom of 29 cm of thickness.

(b) Scatter levels calculated with a phantom of 34 cm of thickness.

Figure 1.3: Effect of increasing patient abdomen thickness on operator exposure, courtesy of [Schueler 2006]. The drawings illustrate scattered radiation isodose curves calculated with a phantom simulating abdomen thicknesses. A 5 cm increase almost doubles staff exposure.

X-ray imaging parameters Parameters of the image acquisition protocol, such as the field-of-view (FOV) size, the tube tension (or kilovoltage) and the beam filtration, significantly affect radiation dose. A larger FOV enables to visualize a larger region of a patient's anatomy in the image. However, the doses are higher since more scatter is produced and a larger part of the patient is irradiated [Koukorava 2011]. Moreover, adding filtration (*e.g.* copper spectral beam filtration) to the X-ray beam reduces both the patient dose and the levels of scatter [Schueler 2006]. Yet, the use of copper filtration will reduce the proportion of low energy photons and can degrade image contrast.

X-ray source position During a procedure, a radiographer operates the X-ray imaging device according to instructions from the operating surgeon or the clinical radiologist, for acquiring the right image for navigation or therapy delivery. This is achieved

through changes in the X-ray beam projection (also known as angulation). Changing the angulation means changing the position of the X-ray source with respect to the patient, and thereby has a significant effect in both patient and staff dose. Indeed, studies have shown that the highest rate of scatter is always produced between the X-ray source and the patient (*i.e.* backscattering effect) [Carinou 2011]. Hence, it is commonly recommended to keep the X-ray source below the table (undercouch) since both the patient dose and scatter levels are lower. In such configurations, the patient's spine and the surgical table result in a beam filtration of low energy photons. This contributes to decrease the intensity of the transmitted radiation and to lower the energy values absorbed by the sensitive organs located in the patient's thoracic region [Santos 2015]. Operator dose is also significantly lowered as opposed to the case when the source is above the operating table (overcouch). Indeed, in overcouch configurations, the dose to the clinicians' eyes and hands can be up to 6 times higher [Koukorava 2011]. This is due to the fact that in such projections, X-rays are scattered above the table. If no ceiling-mounted shields are used, sensitive body-parts (head, thyroid, eyes...) of the attending personnel can be dangerously exposed. This is why many recommendations to avoid such configurations can be found in the literature [Carinou 2011].

Operator's position Staff must avoid standing close the X-ray source during the imaging process as the levels of scattered radiation are the highest [Carinou 2011]. In several IC procedures such as angiographies and PTA, radial access has become a more popular approach than femoral access since this approach has been shown to reduce complication rates and hospital stay [Ertel 2012]. However, radial access requires longer fluoroscopy times and a closer positioning of the operator to the X-ray source [Carinou 2011]. A comprehensive study reported the operator's doses to be 5-7 times higher than when standing in the position for femoral access [Nikodemová 2011]. In general, the operator's distance to the patient's skin entrance site is crucial because the level of scatter radiation is inversely proportional to the distance squared (inverse-square law) [Picano 2013].

1.3 Strategies to reduce radiation dose to patients and clinical staff

X-ray imaging has many important clinical uses and can provide significant benefits. This is why the healthcare professional community seeks to support the benefits of medical imaging while reducing the risks. To this end, several major strategies have been adopted and the most common ones are herein described[5].

[5]Other commercially available systems for reducing patient/staff dose are presented in section 2.1.

1.3.1 Radiation safety guidelines

For years, national and international radiation protection organizations have recommended the adoption of a non-threshold dose-response relationship for the purposes of radiation protection, such that radiation dose has to be kept at levels which are As Low As Reasonably Achievable (ALARA) [NCRP 1990]. Following such a principle, the procedures involving radiation must be medically indicated, justified and optimized by following defined dose protocols. Therefore, all examinations using ionizing radiation should be performed only when necessary to answer a medical question, help treat a disease, or guide a procedure, and by administering the lowest radiation dose that yields an image quality adequate for diagnosis or therapy [FDA 2010]. Furthermore, radiation protection organizations designate a certified radiation safety officer in any organization approved for the use of ionizing radiation. This person is in charge of identifying radiation safety problems, recommending or approving corrective actions, verifying the radiation safety program for adherence to ALARA, performing reviews of occupational exposures and dose levels, and organizing briefings and educational safety sessions.

1.3.2 Reduction of the imaging device's effective doses

Imaging devices' manufacturers work towards keeping the effective dose low while providing the best possible image quality. This is achieved through technical innovation and optimized design of the equipment. For instance, Philips' ClarityIQ low-dose X-ray imaging technology [Philips 2017a] combines image-processing with hardware to obtain patient dose reductions of up to 80 % while maintaining image quality. Similarly, while PET/CT scanning is usually accompanied by substantial radiation dose for the patient [Huang 2009], Siemens' Biograph mCT [Siemens Healthcare 2017a] achieves dose reductions of 60 % with technology reducing the scanning time. Toshiba's fluoroscopy devices now include a feature called Spot Fluoroscopy [Toshiba 2017], which enables fluoroscopy to be performed within a region of interest while holding the last image outside this region. This function reduces the patient input dose area and the scatter dose to the clinicians, and is particularly useful in applications requiring prolonged fluoroscopy. While technical innovation and optimization of the design of medical imaging equipment enable to reduce the patient dose during image acquisition, occupational exposure is affected by many dynamic factors and is thereby more challenging to monitor.

1.3.3 Radiation exposure monitoring

Three main types of recording devices are used to monitor radiation: film badges, Thermoluminescent dosimeters (TLD), and active personal dosimeters (APD). Film badges consist of a small sealed film packet inside a plastic holder than can be clipped to clothing; radiation striking the emulsion causes darkening, and the energy values can be measured afterwards with a densitometer [Singer 2005]. TLDs contain a chip of lithium fluoride, a crystal exhibiting thermoluminescence in response to ionizing radiation. Unlike film badges or TLDs, which measure accumulated exposure, APDs measure ongoing

levels of exposure (current dose and dose rate). Such dosimeters are usually calibrated to measure $H_p(10)$ dose, which is the individual equivalent dose penetrating a depth of 10 mm under the skin [Fardid 2011]. The standard method consists on wearing a TLD dosimeter usually at chest level. Yet, the placement of such a dosimeter can be controversial. First of all, for a person wearing it over the lead apron, the reported measure will be higher than the actual one, and inversely for someone wearing a dosimeter under the apron. Because of this, the ICRP actually recommends wearing two dosimeters: one over the apron to provide an assessment of the dose of the tissues that are not protected and the other under the apron, to provide an assessment of the dose of protected tissues [Fardid 2011]. Second, comprehensive dose measurement campaigns [Nikodemová 2011] have reported that the dose at the body extremities significantly varies during IC/IR procedures. This is due to the many parameters affecting radiation propagation. Such studies also highlight the fact that operators receive higher doses at the left side extremities, since these are closer to the X-ray source. In the same way, [Roguin 2012] reported that the left side of an operator's head is exposed twice as much as the right one. Since dosimeters can only measure personal dose at a single location on the body, they cannot provide a complete estimation of the full-body exposure. For this reason, wearing dosimeters on the eyes and wrists is recommended in the literature [Carinou 2011], yet, this can be unpractical. As highlighted by [Vanhavere 2008], extremity dose monitoring may impede the manipulations carried out by the staff, cause problems with the sterilizations and the wearing of gloves. The use of ring dosimeters is recommended in the literature too, yet, its placement is also difficult to choose since the type of procedure and the manipulations of the staff affect the dose distribution. For IR procedures, the recommended placement of a ring dosimeter is the little finger, however, during percutaneous procedures, the tips of the fourth and middle fingers may receive 20-30 % higher doses [Vanhavere 2008].

Imaging devices also provide an estimation of the dose during the imaging process estimations, such as the dose area product (DAP)[6], which is sometimes used as an estimation of the likely staff dose during the procedure. Nonetheless, recent studies have reported poor or even bad correlations between the DAP values and the actual measured staff exposure since such estimations do not consider the parameters affecting scattered radiation propagation, which are external to the device [Vanhavere 2008, Carinou 2011]. For instance, moving away from the operating table during an image acquisition decreases the staff dose significantly while the DAP is unaffected [Vanhavere 2008]. Therefore, operators cannot use such values as an indicator of their likely radiation exposure.

1.3.4 Protective equipment

Current practice to mitigate the risk of exposure to ionizing radiation consists in the use of room and personal protective equipment. This includes ceiling suspended shields for the protection of the upper part of the operator's body, the lateral shield for protection during lateral beam projections and the table shield for the protection of the legs

[6]For a detailed description of the most common radiation metrics, see appendix A.3.

[Nikodemová 2011]. Shielding drapes placed around the patient are also used to reduce scattered radiation [Ertel 2012]. Personal protective equipment includes aprons, thyroid collars and skirts which usually contain lead or similar light-weight materials that attenuate scattered X-rays. A lead-equivalent thickness of at least 0.5 mm is typically required, which attenuates over 95 % of scattered X-rays that strike it [Kaplan 2016]. Also, recognition of the sensitivity of the eyes to radiation damage has led to mandatory use of leaded eyewear [Roguin 2014]. Shielded gloves are also available for protecting the hands, yet, these can produce greater scatter and exposure to the hand within the glove if the hand is placed directly in the X-ray beam [Kaplan 2016].

Despite the use of personal protective equipment, the operators' legs, arms, neck, and head remain not fully protected [Nikodemová 2011]. However, as reported in [Carinou 2011], the proper use of a ceiling suspended shield reduces the doses to the hands by half and a table shield reduced the doses to the legs up to 5 times. Even though protective equipment can provide high protection, often its usage is not practical and can impede the operator's work. A large study across six different EU countries reported that in 23 % of the IR procedures performed in the hospitals concerned by the study, no room protective equipment was used [Nikodemová 2011]. The results of such a study can be seen in the graphs from figure 1.4. Wearing lead protective clothing can also be tiring for operators working standing and wearing them repeatedly over many years. Especially, those over the age of 35 can frequently develop orthopedic problems, such as aches and pains in the neck, back, hips, knees and ankles that range in severity [Roguin 2012]. As shown in figure 1.4b, 1 % of the personal did not use any kind of personal protective equipment and only 25 % used all protective means available, namely apron, collar and glasses [Nikodemová 2011].

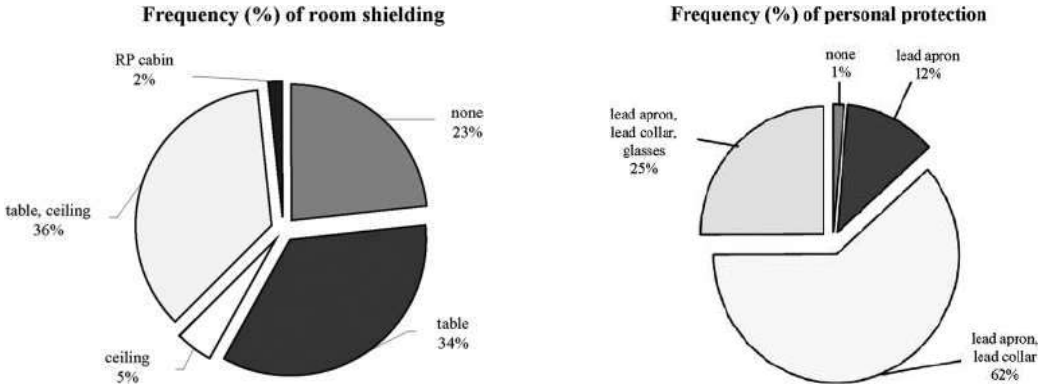

(a) Use of room protective equipment. (b) Use of personal protective equipment.

Figure 1.4: Use of radiation protection equipment in hospitals in Europe as reported by [Nikodemová 2011].

1.4 Summary and thesis overview

1.4.1 Summary of the medical context

Modern X-ray imaging systems greatly improve healthcare providers' abilities for diagnostic and performance precision during clinical procedures. They have become fundamental for MIS and for medical disciplines such as IR and IC, enabling to reduce the patient's risk and recovery time for several types of surgical procedures. However, the growing use and increasing complexity of X-ray guided procedures have been accompanied by a renewed focus on the monitoring and reduction of the ionizing radiation produced by X-ray imaging devices. Indeed, continuous exposure to ionizing radiation can lead to short- and long-term negative effects, ranging from cataracts to cancerous growths (section 1.2.1). Fluoroscopy-guided procedures incur high levels of patient exposure. This also results in a significant exposure for interventional practitioners who have to operate near the patient and are exposed to scattered radiation. The repetitive nature of this exposure, even when the dose is low, increases the risk of developing negative biological effects and such a risk increases with the dose accumulated over time [Kirkwood 2014].

Technical enhancements and the use of radiation protection equipment help reducing radiation exposure. The monitoring of staff's exposure is currently achieved by means of dosimeters usually worn at chest level. Still, dosimeters do not provide a measure of the exposure of other body-parts such as hands and head which can be highly exposed (section 1.3.3). Furthermore, no means currently exist to intraoperatively depict the 3D propagation and magnitude of radiation fields. Indeed, the many factors that affect radiation's magnitude and propagation render the monitoring of exposure complex to achieve and also make irradiated areas and the amount of radiation hard to forecast (section 1.2.2). Moreover, the inability to visually perceive X-rays and the lack of immediate adverse effects to X-ray exposure lead to reduced awareness and concern about the risks of long-term exposure. As reported in [Katz 2017a], a considerable proportion of unnecessary exposure results from a lack of awareness and poor knowledge about radiation propagation behavior.

1.4.2 Contributions

During this thesis, we have proposed new methods to improve the overall radiation safety during X-ray guided procedures in two complementary directions. (1) First, we have developed a system capable of estimating and monitoring the propagation of radiation in the current 3D environment in a non-disruptive fashion. Such a system can help increasing clinicians' awareness to radiation since it provides *in-situ* visual feedback of the current propagation of scattered radiation and of the exposure of staff and patient by means of augmented reality (AR). The system has been demonstrated in an interventional room containing a robotized X-ray imaging device at the IHU of Strasbourg [IHU 2017]. It renders the current diffusion of scattered radiation visible by means of AR, and the visualizations are updated in real-time as the C-arm parameters change. It can also show

a patient's 2D and 3D dose map and a visualization of the staff's radiation exposure. (2) Second, we have proposed to act on the X-ray device positioning with an optimization approach enabling to suggest a configuration reducing the dose deposited on both patient and clinical staff during image acquisition. We have proposed to formulate such a problem as the search for a configuration that minimizes a cost function modeling the different radiation exposures. An approach to perform the optimization of such a cost function in near real-time has also been introduced.

Furthermore, novel approaches in the fields of X-ray Simulation, Medical Robotics and Computer Vision have been developed to make the aforementioned output applications possible. The overall contributions of this thesis are summarized below:

- Two radiation simulation approaches applying Monte Carlo methods have been proposed. They enable to compute the 3D propagation of scattered radiation along with the patient and medical staff dose by taking into account the current imaging protocol and room layout. Our latest radiation simulation approach exploits the computing capabilities of GPUs to achieve quasi real-time performances. Also, novel simulation strategies based on approximations of the behavior of scattered radiation have been introduced to further reduce simulation time, while maintaining the simulation's accuracy.

- AR visualization methods to provide *in-situ* visual feedback about information related to radiation safety have been introduced. These can also be applied to teach intuitively about the diffusion effects of radiation. Our visualization approaches enable a user to visualize in an intuitive manner the current patient and staff dose, along with the 3D distribution and intensity of scattered radiation. To our knowledge, this is the first work demonstrating the use of augmented reality to make ionizing radiation visible in a hybrid OR.

- A mobile AR visualization system relying on a new camera relocalization approach based on multiple RGBD cameras has been proposed and evaluated in a clinical scenario. For such an evaluation, a large multi-RGBD camera dataset[7] providing the ground-truth pose of a camera moving inside an operating room was generated. To the best of our knowledge, this is the first dataset for mobile AR/camera relocalization evaluation recorded in an OR. This dataset has been made publicly available online.

- An approach to optimize the pose of an angiographic C-arm in order to reduce the exposure to radiation of staff and patient, while also preserving the visibility of the targeted anatomical structure in the outcome image has been introduced. It is based on the optimization of a cost function we have proposed to model the overall radiation exposure in the considered scenario.

[7] A complete description of this publicly available dataset can be found in appendix B.

- Validations of our radiation simulation approaches and of our C-arm pose optimization method have been performed through extensive dose measurements acquired in clinical conditions using a robotized X-ray imaging device. Such experimental results showed that the error between the dose measured under different irradiation protocols and the dose simulated with our approaches is in agreement with the intrinsic error of the dosimetric system we use. Moreover, dose measurements allowed us to verify that the C-arm poses recommended by our optimization approach achieve a real decrease in the potential exposure of a clinician in the scene.
- A prototype radiation awareness system for providing *in-situ* visual feedback of radiation inside a hybrid OR has been developed and has been demonstrated to our clinical and industrial partners. It relies on a framework for perceiving and modeling the lay-out of the OR, composed of multiple registered ceiling-mounted RGBD cameras. Such a framework is also used to keep track of the X-ray device configuration and/or of the positioning of equipment and clinicians in the room, since this is relevant information that must be considered in the computation of radiation propagation.

The work carried out in this thesis can contribute to improve the monitoring of the exposure of clinical staff and patient to ionizing radiation. Intraoperatively, these approaches can assist the radiographer in adjusting the positioning of the imaging device to reduce patient and staff dose. Postoperatively, they can help improving the understanding of radiation propagation and help making the workflow of X-ray guided procedures safer in terms of radiation exposure. This can be particularly useful for radiation safety officers, for helping them recommending corrective actions and identifying radiation safety problems in their organizations. Furthermore, several methods herein proposed can be applied to develop a tool to teach trainees about the effects of the different parameters affecting radiation propagation. We hope that the novel approaches proposed in this thesis can help increasing the acceptance of X-ray imaging devices and rendering the benefits of MIS accessible to a wider population.

1.4.3 Outline

This dissertation is organized in three parts. The first part introduces the medical context and motivations of this work (chapter 1). It also includes a literature review of both commercially available systems and works carried out by the research community to improve radiation safety in X-ray guided procedures (chapter 2).

The second part contains the main body of the dissertation. Chapter 3 describes the framework for perceiving and modeling the lay-out of the OR that we have developed, which relies on multiple registered ceiling-mounted RGBD cameras. Chapter 4 introduces our approaches for simulating with Monte Carlo methods the propagation/intensity of scattered radiation along with the dose to patients and medical staff. It also presents evaluations to assess their performances in terms of accuracy and speed. Then, chapter 5 describes the different visualization methods we have developed to provide *in-situ*

visual feedback about current radiation exposure. The combination of the approaches outlined in chapters 3, 4 and 5 has led to works published in [Loy Rodas 2014, Loy Rodas 2015a, Loy Rodas 2015b, Loy Rodas 2017a, Loy Rodas 2018a, Loy Rodas 2018b], to a book chapter submission [Loy Rodas 2018c] and to a patent application [Padoy 2014]. Furthermore, chapter 6 presents our X-ray imaging device's pose optimization approach for recommending a configuration reducing patient/staff dose while maintaining the clinical quality of the output image. Such an approach has been published in [Loy Rodas 2017b] and has also led to a recent patent application [Padoy 2017].

Finally, the third part of this thesis concludes this work by first discussing existing and potential clinical applications of the proposed approaches in chapter 7. Then, a summary of this dissertation is provided in chapter 8, along with discussions about directions for future work.

2 Systems for improving radiation safety: Related work

Learn as much as you can from those who know more than you do,
who do better than you, who see more clearly than you.
– Dwight Eisenhower

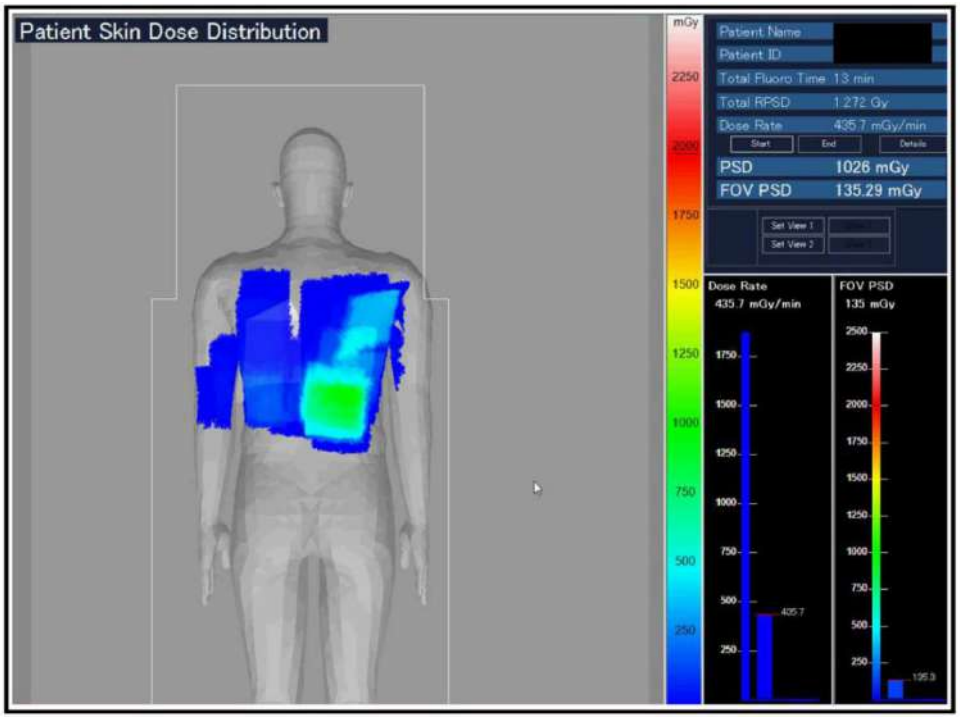

Figure 2.1: Toshiba's Dose Tracking System [Rana 2013, Kuhls-Gilcrist 2017] for the visualization of the cumulative skin dose distribution overlaid over a patient's generic model during X-ray imaging.

Chapter Summary

2.1 Commercially available systems for monitoring and/or reducing radiation exposure . . . 25
2.1.1 Patient's exposure . . . 25
2.1.2 Occupational exposure . . . 26
2.1.2.1 Real-time staff dose assessment . . . 26
2.1.2.2 Staff exposure reduction . . . 27
2.2 Research projects for improving radiation safety . . . 29
2.2.1 Systems enabling an active reduction of radiation exposure . . . 29
2.2.1.1 Robotized surgical assistance . . . 29
2.2.1.2 Enhanced surgical guidance . . . 30
2.2.2 Systems to understand, teach and/or increase awareness to radiation exposure . . . 32
2.2.2.1 Assessing radiation through computer simulations . . . 32
2.2.2.2 Virtual training systems . . . 33
2.2.2.3 Computational systems for increasing radiation awareness 35
2.3 Thesis positioning . . . 37

Radiation safety in X-ray guided interventions is crucial for patient care quality assurance as well as for the safety of physicians chronically exposed to scattered radiation on a daily basis. As presented in the previous chapter, exposure, even to low doses of radiation, is accompanied by a risk of negative biological effects that can lead to the appearance of cancers. Large-scale efforts have been made to develop methodologies for improving radiation safety standards, optimizing the working procedures with respect to radiation protection, improving the knowledge on radiation behavior, optimizing the use of conventional protective measures, and devising new kinds of measures to reduce the exposure of patient and staff. Therefore, a large variety of works can be found in the literature looking to contribute to the effort of improving radiation protection in the OR. In this section, we review the ones which are the most relevant in the context of this thesis. We first review systems developed by companies and which have been made commercially available or have been implemented in modern imaging devices (section 2.1) for monitoring and/or reducing radiation exposure. Then, in section 2.2, we discuss other works carried out by the research community showing potential to become future clinical applications.

2.1 Commercially available systems for monitoring and/or reducing radiation exposure

We hereby review several commercial systems for monitoring radiation doses and reduce the exposure of staff and patient. For assessing the patient's dose, besides the standard dose metrics provided by modern fluoroscopic imaging systems, other more comprehensive dose tracking solutions have been developed. To reduce occupational exposure, online dose monitoring systems are starting to gain popularity and to make their way into the interventional rooms. Moreover, robotized systems are now available enabling clinicians to perform some X-ray guided surgical tasks remotely, namely far from the irradiated areas.

2.1.1 Patient's exposure

International radiation protection commissions (e.g. ICRP) have emphasized the importance of monitoring patient skin dose during and after fluoroscopically guided interventions. This is important in order to predict the likelihood and severity of negative effects and also to identify which patients may require follow-up for the detection of possible skin injuries [Kwon 2011]. Historically, fluoroscopy time has been used as an indication for clinical radiation dose management, often in conjunction with a count of the number of performed acquisitions. Some interventional imaging equipment include a five-minute fluoroscopy timer that emits an audible alert for increasing awareness to the amount of fluoroscopy used during the course of a procedure [Kuhls-Gilcrist 2017]. Today's state-of-the art imaging devices provide a multitude of dosimetric indications, such as the reference air kerma (RAK[1]) or the DAP, to assess the current levels of ionizing radiation delivered. Both DAP and RAK are actually surrogate measures of the amount of energy/dose delivered to the patient in the current imaging conditions [Kwon 2011]. However, the accuracy of these metrics can be limited because of the following reasons. First, they consider radiation dose as if it occurred at a single point in space, hence, changes in the table's position and C-arm angulation, which tend to distribute the dose across the patient's skin surface, are not considered [Kuhls-Gilcrist 2017]. Second, RAK is computed at the patient's entrance reference, which is always considered to be 15 cm away from the X-ray source. Thus, such an estimation may not correspond to the actual position of the patient's skin. Third, these metrics are measured free-in-air, namely they do not take into account attenuation and scattering effects of the patient table and mattress or tissue absorption and backscatter effects [Kuhls-Gilcrist 2017].

Therefore, imaging device's manufacturers have proposed patient dose assessment systems to provide a more precise monitoring of the cumulated patient dose during a procedure. For instance, Toshiba's Dose Tracking System [Rana 2013,Kuhls-Gilcrist 2017] allows to visualize in real-time the estimated accumulated dose deposited on the patient's skin during image acquisition. Such a system calculates the intraoperative radiation dose

[1]More information about radiation dose metrics such as RAK and DAP can be found in appendix A.3.

to the patient's skin by acquiring exposure and geometry parameters (beam orientation, table height and position, tube tension...) directly from the imaging device. Then, a color-coded graphic representation of the cumulative skin dose distribution is overlaid over a patient's model (manually chosen from a set of generic human models). The visualization interface is shown in figure 2.1. The cumulative dose and dose rate are computed using the exposure parameters from the imaging device and an exposure calibration data file. The latter is generated beforehand through measurements performed with an ionization chamber [Rana 2013]. Each implementation of the system is thereby calibrated on-site, and the skin dose estimation under typical clinical conditions can be estimated within a range of ± 20 % [Kuhls-Gilcrist 2017]. Similarly, GE HealthCare's DoseMap [Bordier 2014] is a system integrated to GE's X-ray angiographic systems, for visualizing in real-time the estimated accumulated dose deposited on the patient's skin during an exam. The patient's shape is approximated as a cylindrical envelope computed from patient data input by the user. A ray tracing approach is applied to determine the points of the envelope intersecting with the X-ray beam. Then, the local dose is estimated using the air kerma value provided by the imaging device, by applying a distance correction factor (estimated X-ray source to patient distance) and a backscatter factor (to account for the backscatter from the patient and attenuation effects from the table). Such a backscatter factor is determined from experimental measurements performed beforehand on a phantom. As reported in [Bordier 2014], this method has been shown to have an accuracy within 25 %.

While such systems help assessing the patient's exposure and limiting overexposure risks, they do not provide precise skin and organ dose measurements. Indeed, the dose calculations do not consider the real room context, operators' positions and patient parameters. They are either based on estimations provided by the imaging device (*e.g.* DAP) or rely on calibration files generated experimentally beforehand.

2.1.2 Occupational exposure

2.1.2.1 Real-time staff dose assessment

The traditional film and TLD are passive dosimeters measuring the accumulated dose over time. Hence, they cannot provide an assessment of the ongoing exposure of staff during a procedure. This is why recently introduced active personal dosimeters (APD), which are capable of immediate dose measurement, have been received with great interest among clinicians. For instance, the RaySafe i2 [RaySafe 2017] personal dosimeters enable the monitoring of personal dose equivalent ($H_p(10)$) in real-time when worn by the staff during an intervention. Furthermore, in-room qualitative feedback of the current dose rate (dose/second) is provided through color-coded bars shown in a screen to give each user insight about his/her current exposure. The accumulated dose per user is also captured and displayed, and all measurements are saved with time-stamps for offline analysis. Through a partnership with Philips Healthcare, such a system has been integrated to the DoseWise Portal software [Philips 2017b], a web-based solution

that collects, analyzes and reports patient and staff radiation exposure. Such a system automatically registers patient and staff dose for each procedure by combining radiation dose structured reports from the X-ray system, containing data such as the DAP and acquisition type, with the real-time staff dose measurements from the APDs [Sailer 2017]. This enables a comprehensive dose analysis, which can help finding correlations between the patient/staff dose and the type of procedure for improving radiation safety practices.

Despite the possibility of assessing dose in real-time, the use of APDs for the legal dose record after interventional procedures is not recommended and the reference personal equivalent dose must still be given by a passive dosimeter [Clairand 2011]. Indeed, because of their semiconductor-based construction, active dosimeters are angle-dependent and measurements can vary up to ±30 % within a ±50° range. As a part of the ORAMED project [ORAMED 2011], the performance of APDs was evaluated against the traditionally used passive dosimeters under different clinical setups, and the results showed that the APD response is roughly within ±30 % of the TLD measurements [Struelens 2011]. Because of such a variability in the dose estimations, additional studies or new technical developments are recommended in the literature [Struelens 2011] before officially adopting APDs for assessing occupational exposure in clinical practice. Additionally, as mentioned in section 1.2.1.3, a clinician's exposure can significantly vary from one body-part to the other [Nikodemová 2011], especially for the body areas closer to the irradiation field. Hence, providing a complete picture of the full body exposure of a practitioner solely by means of dosimeters would be unpractical due to the need of wearing a multitude of them on various parts of the body.

2.1.2.2 Staff exposure reduction

Interventional practitioners cannot avoid being exposed to radiation since they are obliged to remain next to the patient while performing any X-ray guided surgical task. For this reason, tele-operated assistance systems have been introduced as an alternative to enable clinicians to remotely carry out parts of the procedure. By driving the clinician away from the patient, his/her exposure to scattered radiation is significantly reduced. We hereby present several commercially available systems for this purpose.

Catheter ablations are the standard IC procedures for treating various kinds of cardiac arrhythmias [Nguyen 2010]. Such procedures require a precise catheter manipulation inside the vascular system and cardiac chambers, which is performed under prolongated fluoroscopic guidance [Proietti 2013]. This results in significant X-ray exposure for both patients and medical staff. Therefore, remote navigation systems have been recently developed and some of them are commercially available. The use of such systems allows operators to maneuver the catheters inside the cardiovascular system with enhanced precision from a remote workstation [Nguyen 2010]. Hence, not only their exposure to radiation is dramatically reduced, but they can also be relieved from the orthopedic burden of wearing lead aprons. For instance, the Niobe system from Stereotaxis [Stereotaxis 2017] allows to remotely operate a magnetically-enabled catheter through magnetic forces generated by two large permanent magnets positioned on each side of the patient's

(a) Niobe system from Stereotaxis [Stereotaxis 2017].

(b) Magellan Robotic system [Hansen Medical 2017a].

Figure 2.2: Commercially available tele-operated navigation systems for interventional procedures.

body [Nguyen 2010]. These large magnets are visible in figure 2.2a. Using joysticks, the surgeon can manipulate the motion of the catheter tip thanks to variations in the orientations of the magnets altering the magnetic field. Studies have reported that the use of this system for electrophysiology procedures such as atrial fibrillation ablation, significantly reduces the incidence of surgical complications and decreases the time the patient is exposed to fluoroscopy [Proietti 2013]. Similarly, the Sensei Robotic System [Hansen Medical 2017b] from Hansen Medical is a robotic navigation device which also allows an operator to precisely manipulate a catheter while being comfortably seated at a remote workstation [Kaplan 2013]. The system performs catheter navigation through steerable sheaths, where any conventional catheter can be inserted, and these are manipulated via a pull-wire mechanism by a robotic arm fixed at the operating table [Nguyen 2010]. Hospital trials have reported a 35 % reduction in radiation time when using the Sensei system in electrophysiology procedures and also a decrease in procedure time [Kaplan 2013]. With a similar construction, Hansen Medical also introduced the Magellan Robotic system [Hansen Medical 2017a] intended for tele-operated catheter navigation in peripheral vessels for endovascular procedures. Its remote-control panel is shown in Figure 2.2b. Besides electrophysiology and endovascular procedures, robot assistance systems for Percutaneous Coronary Interventions have also been developed and are now commercially available. Indeed, the CorPath GRX system by Corindus Vascular Robotics [Corindus 2017] enables a robotic-assisted control of coronary guide wires, balloons and stents with millimetric precision. As the devices mentioned before, the CorPath GRX is composed of a bedside unit, consisting of an articulated arm, the robotic drive, and a single-use cassette in which wires, balloons, and stents are loaded, and a remote workspace surrounded by a radiation shield [Maor 2017]. From there, the operator can control and manipulate guide wires, balloon, and stents using a set of joysticks and touch screens, while being protected from scattered radiation.

2.2 Research projects for improving radiation safety

The research community has also proposed a large variety of methodologies and systems for better understanding, assessing and decreasing medical ionizing radiation. We dedicate this section to review relevant works on this topic. For the clarity of the presentation, we classify them into two categories. We make a separation between the works looking to reduce radiation exposure in an active way, namely lowering the doses by having some influence on the imaging process, from others addressing this issue in a passive manner, *i.e.* by helping to improve the awareness and/or understanding of radiation propagation.

2.2.1 Systems enabling an active reduction of radiation exposure

We hereby present research projects proposing systems for reducing radiation exposure by actively influencing the X-ray guided procedure. Indeed, enabling surgical staff to perform an X-ray guided gesture away from the patient (thus far from scattered radiation) is an example of an active influence on the procedure's execution allowing to decrease radiation dose. Some examples of research prototypes developed for this purpose are discussed below. Moreover, a second example of an action during a procedure that yields a decrease in radiation dose is the reduction of the needed amount of X-ray acquisitions or fluoroscopy time. Hence, in section 2.2.1.2, we study systems which aim at achieving this by improving the visualization and guidance during an intervention.

2.2.1.1 Robotized surgical assistance

Similarly to the systems presented in section 2.1.2.2, the medical robotics research community has been actively working on robotized assistance devices enabling clinicians to carry out complex surgical tasks, which are usually performed under X-ray guidance, in a remote manner. The design of such devices targets a particular task, and, this is why a multitude of such robotic assistance systems can be found in the literature. For instance, vertebroplasty is the standard interventional procedure to treat vertebral fractures by injecting bone cement into the vertebral body. The cement injection phase is a crucial part and is carefully performed under fluoroscopic guidance in order to avoid cement leakage, damage to the vertebrae and other complications. Therefore, in order to lower the exposure of radiologists performing such procedures, a tele-operated cement injection device was proposed in [Lepoutre 2016], enabling them to carry out the procedure from a console outside the irradiated area. A key aspect of the system is that force feedback is provided through the master console, allowing the clinician performing the injection to supervise the viscosity of the cement and to minimize the risk of leakage. In the same way, percutaneous needle insertion is also a complex surgical task performed under fluoroscopic guidance. Whereas a commercially available system enabling to perform needle grasping, insertion and manipulation in a tele-operated way cannot be found yet, a prototype system for achieving such tasks has been proposed by [Piccin 2016]. Such a system has not yet been demonstrated in clinical practice, still, it is a promising advance towards enabling surgeons to perform percutaneous needle insertion and manipulation

while avoiding radiation exposure. Similarly, in orthopedic surgery, minimally invasive joint fracture treatment requires a careful fracture manipulation which is performed under fluoroscopy. Robotized fracture manipulators have been developed [Dagnino 2017] to enable surgeons to perform fracture reduction procedures from a workstation, which can be placed away from the irradiated area.

The development of complex tele-operated robotized devices targeting specific surgical gestures is a possible path in order to decrease radiation exposure. However, this is technically complex and may not be possible to achieve in a near future for all kinds of tasks performed today under X-ray guidance.

2.2.1.2 Enhanced surgical guidance

X-ray imaging and fluoroscopy provide a visualization of the body's inner anatomy, which is crucial for properly guiding a catheter or a needle to a target in MIS. However, nowadays AR can also be used to provide an enhanced visualization of a patient's inner anatomical structure. Several works can be found in the literature where, by facilitating the surgical navigation through an enhanced non-irradiating visualization, the amount of performed X-ray shots and/or the fluoroscopy time are reduced. As a consequence, the exposure to radiation of both patient and staff can be significantly lowered. For instance, [Müller 2013] and [Seitel 2016] propose to use AR to facilitate the navigation during percutaneous needle insertion. They rely on a registration of a preoperative patient's CT model to the user's viewpoint, which is achieved either by means of fiducial markers [Müller 2013] or by using the depth data from an RGBD camera and surface matching algorithms [Seitel 2016]. Information such as the insertion trajectory or the target's position can be overlaid onto a video stream serving as guidance visualization during the needle insertion. Figure 2.3a shows the setup from [Seitel 2016], where the navigation system is used for a percutaneous needle insertion during a porcine trial. Similarly, fluoroscopy guidance is crucial during orthopedic and trauma surgery to guide joint replacements or for the treatment of fractures. To facilitate guidance during such procedures, [Navab 2010] propose to augment a mobile angiographic C-arm with a video camera and mirror construction, since this enables to have a direct overlay of the X-ray images over the video stream. After a calibration procedure [Chen 2013], such a design enables both the camera and the X-ray source centers to be virtually aligned, and therefore to provide a precise X-ray and video overlay to perform AR-guided fluoroscopy. The system setup and examples of augmented clinical images can be seen in figure 2.3b. Augmenting X-ray images with coregistered live video helps surgeons to intuitively depict the spatial relations between patients and medical images. Studies have reported that such an intuitive intraoperative overlay allows surgeons to reduce the number of X-ray acquisitions performed, and thereby radiation exposure, for orthopedic and trauma procedures and for several clinical tasks such as skin incision, entry point localization and X-ray device positioning [Navab 2012, Chen 2013]. Also, clinicians can see in the augmented image whether their hands are directly in the imaging area, so that they can move them away during the X-ray or fluoroscopic image acquisition and

thereby avoid being exposed to primary radiation. However, since the video camera and the X-ray source are placed on the same side and the optical view of the real scene must be captured from the top in order to see the patient and the surgical site, the system requires the X-ray source to be positioned above the patient table. As explained in section 1.2.2, such a configuration highly exposes surgical staff to scattered radiation. To cope with this, [Wang 2016] propose to mount an RGBD camera to the image intensifier of the C-arm instead. Then, after a calibration procedure, an inverse visualization approach is applied to visualize the X-ray images over the reconstructed 3D data from the camera when the device is in undercouch position. Augmenting a C-arm with an RGBD camera was also proven to be useful to improve the quality of Cone-Beam Computed Tomography (CBCT) by capturing and incorporating surface information from the patient into the reconstruction process [Fotouhi 2017]. The RGBD sensor is also used to track and correct the reconstruction from any rigid movement in the scene. As reported in [Fotouhi 2017], such an approach enables to perform CBCT reconstructions with fewer X-ray projections and to avoid repeated scans by correcting accidental patient movements, hence contributing to reduce radiation exposure.

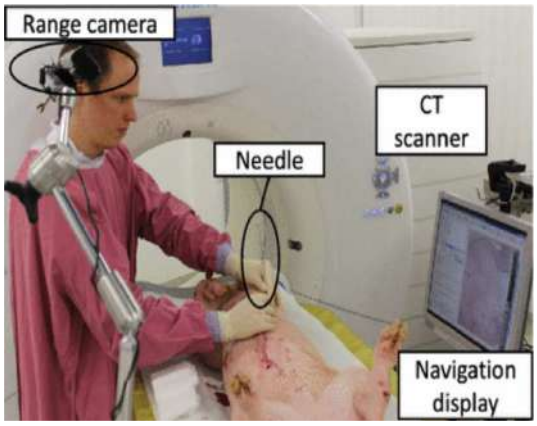

(a) Navigation system for guiding percutaneous needle insertions proposed in [Seitel 2016] during a porcine trial.

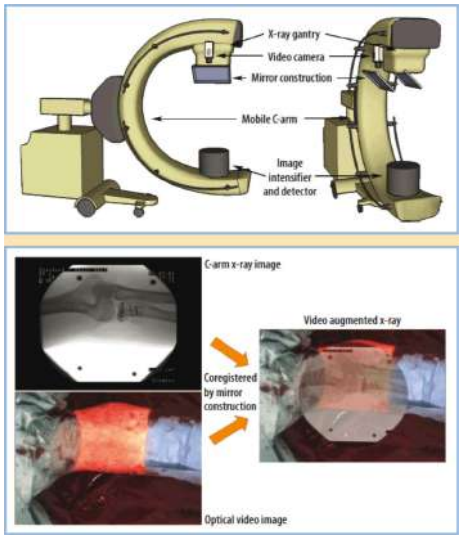

(b) CamC: the upper images show the system's setup and the lower ones the augmented visualization [Navab 2012].

Figure 2.3: Examples of systems providing an enhanced visualization to improve surgical guidance and reduce radiation exposure.

2.2.2 Systems to understand, teach and/or increase awareness to radiation exposure

2.2.2.1 Assessing radiation through computer simulations

In clinical practice, dose levels are affected by a large number of parameters that change simultaneously. Assessing the influence of each of them separately cannot be achieved solely by means of dose measurements [Koukorava 2011]. Also, modeling of X-ray photon propagation and interaction with matter is heavily complex and not possible to achieve analytically. Therefore, computer simulations are a valuable tool to describe the transport of ionizing radiation since they are inexpensive, safe and can provide information that would be almost impossible to measure experimentally.

The theoretical study of radiation transport problems is based on the Boltzmann Transport Equation, equation devised in 1872 initially to describe the diffusion of gases from a statistical mechanics viewpoint. X-ray particle transport can be considered as a special linear variant of the Boltzmann equation [Razani 1972]. Essentially, it is an integrodifferential equation that is a restatement of the equation of continuity in terms of radiation transport and can only be solved analytically in simple and semi-finite geometries. However, probabilistic (stochastic) solutions can be found to approximate the radiation transport problem, and there is general agreement that the Monte Carlo (MC) method is the most accurate computational approach currently available for this purpose [Razani 1972, Badal-Soler 2008]. The physical process of particle transport is described by the Boltzmann equation and the MC methods are used to describe random walks of particles [Razani 1972]. A detailed Monte Carlo simulation can in fact yield the exact solution to the transport equation for a given interaction model and within the statistical uncertainty inherent to the method [Badal-Soler 2008]. Such a simulation is based on a random sampling of a large number of independent particle tracks (or histories) and in the subsequent estimation of certain quantities of interest obtained by averaging the contribution from each history. For a sufficiently large number of histories, the statistical uncertainty of the approximation is significantly reduced, and for this reason MC simulations typically require the computation of a huge number of histories and, thus, long execution times. Several general-purpose Monte Carlo codes have been developed and have been extensively applied for medical physics' applications, such as PENELOPE [Baró 1995], MCNPX [Pelowitz 2005] and Geant4 [Agostinelli 2003] (further described in chapter 4). To cope with the long computational times associated with MC methods, frameworks relying on GPU-accelerated computations such as MC-GPU [Badal 2009] and GGEMS [Lemaréchal 2015, GGEMS 2017] (further described in chapter 4) have also been introduced.

MC simulations have been largely applied in the last decades in the fields of radiation therapy, dosimetry and radiation protection. In radiation therapy, MC simulations enable to compute the optimal positioning of radioactive seeds in order to treat tumors while sparing healthy tissue [Lemaréchal 2015]. Furthermore, even though the ORAMED project [ORAMED 2011] gathered extensive dose data during various types of IR/IC

procedures in several hospitals in Europe, it was only through MC simulations that a thorough study of the influence of the many parameters affecting radiation dose could be performed. In [Koukorava 2011], extensive simulations using the MCNPX [Pelowitz 2005] framework were carried out while varying parameters such as the imaging device's angulation and the operators' positions (modeled as anthropomorphic phantoms). Such a study enabled the authors to provide specific guidelines concerning the radiation protection of the occupationally involved personnel in interventional procedures. A similar setup is applied by [Principi 2016] to study the variation of eye lens exposure for changing operator position, height and body orientation with respect to the patient and the X-ray tube. The results were applied to devise practical recommendations to reduce eye lens dose for interventional practitioners, such as the statement that a rotation of the head of 30° away from the tube can reduce the eye lens dose by approximately 50 %. In the same way, [Santos 2015] study the effect of the beam angulation and the use of lead protections on the exposure of patient and staff through MC simulations. The reported results highlight the fact that when the X-ray source is located above the table, more scattered radiation reaches the middle and upper portions of a physician's trunk, where most of the radiosensitive organs are located. Recently, [Alnewaini 2017] proposed an approach to simulate the distribution of scattered radiation by using MC methods to compute the scatter generated by the patient, table, ceiling and floor. The exposure of a clinician to such a scatter is simulated by projecting the scattered particles into a cylinder placed at different positions around the table. To speed-up the computations, the scattered particles' properties are pre-computed and saved into files for a given room setup. As expected, the results consistently show that a clinician is highly exposed when standing close to the X-ray source.

Computer-based simulations are indeed an important tool to provide useful information regarding radiation safety in a safe manner. While such recommendations can be useful for clinical staff to learn about the best practices to reduce radiation exposure, it can be difficult to keep them in mind while performing the procedure at hand, which requires their full attention.

2.2.2.2 Virtual training systems

Since training with real radiation is dangerous and thereby prohibited, current radiation safety teaching is usually based on courses, videos, lectures and presentations of theoretical aspects rather than hands-on training [Katz 2017a]. A review about simulation-based training in radiology [Desser 2007] concluded that it will play an increasingly important role in procedural training in the future and that IR promises to be the radiologic subspecialty in which simulators will have the biggest impact. Several computer-based training systems have been introduced since, looking to help improving education on C-arm operation and minimizing radiation exposure on interventional procedures. Two relevant examples of such systems are discussed below.

VirtX [Bott 2009, Bott 2011] is a computer-based training system designed to teach trainees the skills needed to obtain X-ray images of sufficient quality for the surgical

situation in as short a time as possible and with a minimal level of radiation exposure. The system's user interface (shown in figure 2.4a) presents the trainee a 3D scene of an OR, where he/she can set the positioning/adjustment of interactive models of a C-arm, patient, and table. Simulated digitally reconstructed radiographs (DRR) are displayed to provide visual feedback about the image which would be obtained in such a scenario. This offers trainees the opportunity to practice different C-arm adjustment tasks from the daily operation workflow in a virtual environment with no X-ray exposure. By using an electromagnetic tracking system with sensors mounted on the radiation source of a real C-arm and on a patient manikin, the system can also be used to train inside an OR [Bott 2011]. Moreover, the corresponding intensity and distribution of scattered radiation can also be displayed through a color-coded visualization, which is visible in figure 2.4a. This enables the trainee to understand the effect that altering the room configuration has on the behavior of scattered radiation. MC methods are applied to simulate the propagation of scattered radiation. The initial approach, described in [Wagner 2009], relied on the Geant 4 toolkit [Agostinelli 2003] to simulate the X-ray particles' propagation and interaction on a simplified modelization of a user-defined OR scene. While in [Wagner 2009] the simulation times were too long for an application during interactive lectures (up to several minutes), an extension applying GPU-accelerated calculations was presented in [Wagner 2012]. Such an approach enabled to reduce the simulation times up to a few seconds, which was deemed acceptable for an interactive course. The virtX system was evaluated amongst OR personnel in [Bott 2009], where 75 % of the 77 participants agreed that their understanding of the effect of the position of the image intensifier on scattered radiation was improved thanks to the qualitative visualization of X-ray distribution. However, to the best of our knowledge, the results of the simulation framework and the visualizations have not been validated experimentally yet. Also, the position of the physician is not taken into account and the system is rather designed to be used as an offline training tool. Even if the possibility of training inside the room using sensors is mentioned in [Bott 2011], it would be challenging and unpractical to track by means of sensors every operator and medical equipment in the room that could have an effect on radiation propagation, and then incorporate this information into the radiation simulation.

Recently, [Katz 2017a,Katz 2017b] introduced a different kind of simulator for teaching good practices to interventional cardiologists for reducing their exposure to ionizing radiation. A low-fidelity simulator built around the "Wizard of Oz" concept is proposed, namely where a human trainer controlling and supplying online feedback is incorporated into the training process. Through a user interface (shown in figure 2.4b), the user chooses among different pre-set C-arm configurations and acquisition parameters, and the information console then displays current and cumulative radiation exposure dose values of patient and operator (dose to the head and torso). Such estimations are computed using data obtained beforehand from multiple dose measurements using phantoms. Prediction models are calculated from the experimental data, which are later applied by the simulator to compute the displayed dose values. The system is evaluated by means of a knowledge

exam given to 20 interventional cardiologists in [Katz 2017a, Katz 2017b], and the results suggest that their knowledge on radiation exposure improves after simulator training. The authors highlight that simulator training improves knowledge on the distribution and behavior of scattered radiation and teaches the users methods to reduce radiation scatter during a procedure.

(a) User interface of the virtX training system [Wagner 2012]. The simulated scattered radiation for the current user-defined imaging and scene configuration is shown.

(b) Simulator training system proposed by [Katz 2017b]. The patient and staff dose are displayed for several pre-set C-arm configurations.

Figure 2.4: Examples of computer-based training systems to teach about C-arm operation and radiation exposure.

Simulators are an interesting alternative to teach about radiation safety since they provide an engaging game-like learning environment and are risk free for both patients and doctors. Additionally, simulations enable immediate feedback to maximize learning and minimize the introduction of errors. However, virtual simulators are meant to be used outside the operating room and they cannot cover every possible scenario that could take place during a real intervention. In this thesis, we propose instead to use AR to teach about radiation protection in order to bring the training inside the operating room, allowing trainees to learn in real clinical conditions. Providing *in-situ* visual feedback about current exposure can have a stronger impact on increasing clinicians' awareness and understanding of scattered radiation.

2.2.2.3 Computational systems for increasing radiation awareness

Studies evaluating radiation awareness have reported a considerable proportion of unnecessary exposure and risk underestimation resulting from a lack of awareness and poor knowledge on radiation behavior [Katz 2017a]. [Picano 2013] highlights the fact that the practice of IC is sometimes accompanied by a sub-optimal perception of radiation risk and by negligent use of radiation protection tools. This is partially due to the invisible nature and complex behavior of ionizing radiation. However, an appropriate feedback of the current distribution of scattered radiation can increase the awareness of clinical staff and reduce the risk of overexposure. To this end, computer-based systems

combining radiation simulation, person tracking and visualization of radiation in virtual environments have been developed. We hereby present some examples of such systems which have settled the foundations for the work performed in this thesis.

[Ladikos 2010] presents a system to sensitize physicians and allow them to review their radiation exposure after a procedure. A radiation simulation framework using Geant 4 [Agostinelli 2003] is used to simulate scattered radiation and the results are displayed as a color-coded heat map overlaid over a 3D mesh representation of a person's shape. 16 optical cameras mounted on the ceiling are used together with a background subtraction and shape-from-silhouette approach to reconstruct and track the 3D mesh of a person. The position of the C-arm is determined offline and the distribution of radiation in the environment is computed by placing detector spheres around the scene in the simulation and registering the energy of the particles which fall onto them. Such an irradiation volume is pre-computed and is later composed with the tracked physician's mesh in order to accumulate the radiation received by each vertex and, by interpolation, the radiation received by the whole mesh. As shown in figure 2.5a, the exposure of a person moving around the room can be visualized this way. While this work has introduced the concept of visualizing the radiation risk overlaid on a person, the simulations neither take all parameters of the scattered radiation production nor the room configuration into account. For instance, the simulation model does not include the operating table which also affects the scattered radiation distribution. The real X-ray source parameters (peak kilovoltage, filtration, field-of-view) are not fully considered, and results are shown for a single C-arm configuration only. The validity of the proposed visualizations is also not verified experimentally. Moreover, the system is not designed for intraoperative use. Such a tracking approach based only on color images would not always be possible in a real interventional scenario since many procedures are carried out with the lights off for a better visibility of the X-ray images displayed on the screen. The dynamic nature of that environment along with the possible multiple occlusions would also be a challenge for the background subtraction approach and for the precise mesh tracking required by the proposed visualization.

Similarly [Badal 2013] propose a patient/staff dose monitoring system combining GPU-accelerated Monte Carlo simulations along with person tracking using a single depth camera. Tracking is performed with the OpenNI library [OpenNI 2013]. The MC-GPU [Badal 2009] simulation code is used to estimate the dose distribution on the skin and the internal organs of both the patient and the medical staff, modeled as computational phantoms. The imaging parameters (kVp, filtration, collimation, gantry position and angulation) are manually input by a user to the system's interface, and the depth-camera tracking provides the centroid and orientation of the tracked person. A generic phantom of a standing human is introduced at that location within the simulation model. Then, the simulations are launched and the patient and operator's dose are computed in a few seconds (when simulating in parallel on 14 GPUs). The paper describes the underlying computer architecture and communication protocols that enable fast parallel computations, but without providing details about the radiation simulation

model and the parameters used. Furthermore, it shows only a single tracking result from OpenNI for a person standing in an office. Therefore, it is unclear whether the results, computed for four different locations of the person in a room, are obtained in a real interventional room with a camera or solely in a virtual environment by adjusting the phantom's positions in the simulation model. The presented results are similar in nature to the simulations using virtual phantoms placed at femoral and radial access from the ORAMED project [Koukorava 2011]. These are displayed offline overlaid to a phantom in a virtual visualization. The simulation considers realistic irradiation parameters, yet, the results have not been validated with real dose measurements and the system has not been demonstrated in a real interventional environment.

More recently, [Leucht 2015] applied a similar pipeline with the aim of providing a visualization of the staff body-part radiation exposure by means of AR. The proposed approach relies on two RGBD cameras physically mounted to a mobile C-arm, which are used to capture and model the scene. One of the cameras is facing the table for modeling the patient's size and shape as a volume. The second camera, which faces the scene and has a better view of the surgeon, is used to approximate the surgeon's shape through a background subtraction approach. A simulation built using Geant 4 [Agostinelli 2003] is applied to compute the 3D radiation distribution, by incorporating the scene information provided by the cameras. As shown in figure 2.5b, the simulation results are shown by coloring the surgeon's tracked shape on the point cloud obtained from the RGBD data. The skeleton tracking approach from OpenNI [OpenNI 2013] is used to accumulate the simulated dose at the estimated surgeon's body-joints positions (shown as pink spheres in figure 2.5b). The simulation results are verified experimentally by comparing them to measurements obtained from a dosimeter. However, such an experimental validation was performed for a single configuration of the C-arm, namely no angulation or imaging parameters were changed. Furthermore, mounting cameras to the C-arm's detector for tracking the patient and operator only works for a PA configuration, namely when the source is under the table. A rotation of the C-arm would render the scene invisible for the cameras. Moreover, in clinical practice, the view of such cameras may be occluded by medical equipment or ceiling-suspended shields.

2.3 Thesis positioning

Exposure to ionizing radiation is accompanied by an inherent risk of negative biological effects that can lead to the appearance of cancers. As reviewed in this chapter, large-scale efforts have been made to improve current radiation safety standards, to increase the understanding of radiation behavior, to optimize the use of radiation monitoring systems, and to develop new systems to reduce the exposure of patient and staff. Indeed, we have listed a large variety of commercially available systems and works from the research community, all aiming at improving the overall radiation safety during procedures involving X-ray radiation. We summarize below several key points from this review that should be highlighted to illustrate the relevance of the work presented in this thesis.

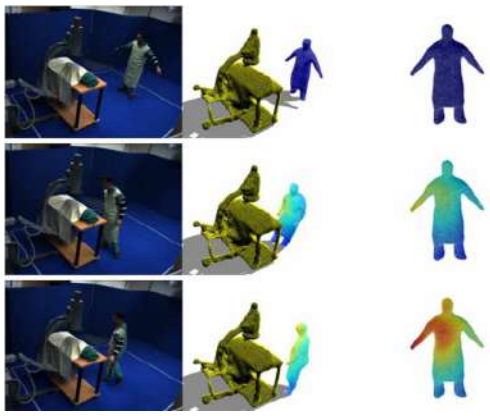

(a) System proposed by [Ladikos 2010] to visualize radiation exposure overlaid over a 3D mesh representation of a person's shape.

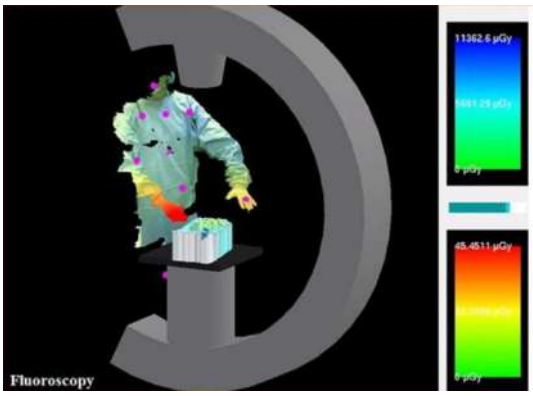

(b) Visualization of a surgeon's body radiation exposure from the system proposed in [Leucht 2015].

Figure 2.5: Systems for providing feedback of radiation exposure for increasing clinicians' awareness.

Current monitoring of the patient's and staff's radiation exposure is either based on dose metrics provided by the X-ray imaging device (*e.g.* DAP), or on the use of dosimeters to measure radiation dose. However, the accuracy of the estimations provided by the imaging device are limited since they are based on assumptions such as the position of the patient, and are measured free-in-air. Hence, they do not take into account attenuation and/or scattering effects. Furthermore, since the exposure per body-part of a clinician can significantly vary, especially for the parts closer to the irradiated area, assessing a person's full-body exposure by means of dosimeters is hard. In this thesis we propose to simulate the X-ray propagation by considering the real OR context, namely the device's configuration along with the patient and clinicians' positions. If a preoperative patient model is available, our radiation simulation approach allows the computation of precise organ and tissue dose values, which can complement the information provided by current patient dose monitoring systems. On the staff's side, we propose to combine our radiation simulation with a clinician tracking approach to assess a person's full-body exposure, thereby complementing the information provided by the dosimeter worn at chest level.

We also reviewed in this chapter systems enabling to actively reduce radiation exposure. Several tele-operated robotized assistance devices now allow surgical staff to perform an X-ray guided gesture removed from the patient (thus far from scattered radiation). However, these are designed for specific surgical gestures and even if the research community is actively working on this topic, devices for performing other more complex fluoroscopy-guided tasks in a tele-operated manner have not yet been developed. Furthermore, we also listed systems allowing to reduce the needed amount of X-ray acquisitions or fluoroscopy time (hence radiation exposure) by enhancing surgical guidance and/or navigation. Indeed, having an influence on the imaging parameters (in this case imaging time) is a good alternative to reduce radiation doses. Acting on other

imaging parameters such as the device configuration also has an impact on radiation propagation. Yet, to the best of our knowledge, no system for proposing a device's configuration safer in terms of exposure to X-ray radiation can be found. In this thesis, we propose an approach to assist the C-arm's manipulator by recommending an imaging projection enabling to reduce radiation exposure of patient and staff, while maintaining the visibility of the target in the output image.

Moreover, as discussed in section 2.2.2.2, computer-based training and simulation systems have proven to be useful to improve education on C-arm operation and on minimizing radiation exposure. Such systems incorporate simulations of scattered radiation computed for a set of user-defined parameters. Visualization of radiation color maps are then provided over a virtual operating room scenario to illustrate the effects that altering parameters such as the imaging device's angulation can have on scatter. Virtual simulators are a good step for moving from the theory to the practice, yet, these are meant to be used outside of the operating room. Moreover, it is not possible to simulate every possible scenario that could take place during a real intervention. We rather propose to make use of AR to provide a direct feedback about the behavior of radiation for the current room configuration and staff positioning. This could be applied to teach about radiation protection and bring the training inside the operating room, allowing trainees to learn in real clinical conditions. Indeed, an AR based teaching tool could be used in conjunction with interventional surgery training courses or during surgical training involving animals, for trainees to learn *in-situ* the effects of the parameters affecting radiation propagation.

As unnecessary exposure to radiation can result from a lack of awareness, poor knowledge on radiation behavior and underestimation of the risks, computer-based systems have been developed to improve the monitoring of patient/staff radiation dose. These combine radiation simulations, person tracking, and visualization to show the 3D dose distribution or the staff's exposure. However, no system has yet been designed for intraoperative use since they all consider either laboratory setups or virtual interventional environments. Even when Monte Carlo-based simulations are used for computing radiation propagation, these systems neither consider all parameters affecting radiation production nor the room layout into account. Furthermore, previous works do not give any experimental validation of the simulated scattered radiation and person exposure values[2]. To the best of our knowledge, we were the first to propose a radiation awareness system relying on MC-based simulations and AR visualizations of radiation, where the simulations were validated in clinical conditions using dosimeters.

[2]Works published subsequently such as [Leucht 2015] and [Alnewaini 2017] evaluate the accuracy of Monte Carlo simulation models using dosimeters, citing our works [Loy Rodas 2014, Loy Rodas 2015b] as reference.

Part II

Context-aware radiation monitoring

3 OR context perception through a multi-RGBD camera system

There are things known and there are things unknown,
and in between are the doors of perception.
– Aldous Huxley

Figure 3.1: Views from a multi-RGBD camera system installed in an experimental interventional room at IHU Strasbourg, featuring an Artis Zeego X-ray imaging device (Siemens Healthcare, Forchheim, Germany).

Chapter Summary

3.1 Camera setup and calibration 45
3.1.1 RGBD sensors 45
3.1.2 Camera calibration 46
3.1.3 Multi-camera system registration 47
3.2 Visual perception of the room environment 48
3.2.1 Room layout tracking 49
3.2.2 Patient registration 49
3.2.3 Clinicians tracking 49
3.3 X-ray device configuration detection 52
3.4 Conclusion 54

As outlined in section 1.2.2, the propagation of X-rays and their interactions with matter are complex phenomena affected by several factors. The exposure values of patient and staff not only depend on the imaging parameters (tube voltage (kV), current (mA), fluoroscopy time, etc...), but also on the room layout. In particular, clinicians are exposed to the photons scattered by patient, table and/or equipment, with an energy attenuated by the particles' interactions with matter in their trajectories [Nikodemová 2011, Koukorava 2011]. Such an exposure increases when standing close to the X-ray source, as the levels of scattered radiation are inversely proportional to the squared distance [Picano 2013] and the highest rate of scatter is always produced between the X-ray source and the patient [Carinou 2011]. Therefore, a global radiation awareness system, capable of properly monitoring the propagation of scattered radiation propagation and the full-body exposure of staff and patient must keep track of the current OR context and imaging parameters. Because of the strict sterilization requirements of medical environments and of the fact that the surgical workflow should not be disrupted, cameras are currently one of the least intrusive options that can be conveniently installed in the room to sense the environment.

One of the contributions of this thesis is the development of an intraoperative system for estimating and providing feedback about the propagation of scattered radiation in the current 3D environment. Such a system relies on a registered multi-RGBD camera system for tracking the layout of an interventional room. The cameras are mounted on the ceiling of the room using articulated arms in a configuration allowing them to capture key views around the operating table. After a one-time installation, such a setup can be used to keep an up-to-date picture of the room layout in a non-disruptive manner. Figure 3.1 shows an example of the views captured from one of the multi-camera systems we have installed in an interventional room at IHU Strasbourg [IHU 2017]. In this chapter we first describe such a setup along with the calibration/registration approaches involved. Then, we discuss the approaches we have explored to track the OR's layout and clinicians'

positions as required for an up-to-date simulation of the current radiation behavior.

Acknowledgments: The setup and approaches described below were developed in collaboration with fellow colleagues from Research Group CAMMA [Research Group CAMMA 2017]. Therefore, I would like to acknowledge and give proper credit to:

- Laurent Goffin and Dr. Antonio De Donno for contributing to the core software used for streaming and merging the images from the multi-RGBD system.
- Dr. Fernando Barrera for proposing and developing the approaches for the multi-camera system calibration and fusion.
- Dr. Abdolrahim Kadkhodamohammadi for proposing and developing the approaches used for human pose estimation.

3.1 Camera setup and calibration

We use consumer-grade RGBD cameras in our setup since this type of camera allows to capture an environment simultaneously through both color and depth sensors. In this section, we first provide a short description of these cameras. Then, we describe the different calibration and registration procedures enabling to reconstruct the 3D environment from the multi-camera system's images.

3.1.1 RGBD sensors

RGBD sensors combine a color camera and a depth sensor. A color image represents the color intensity on the objects' surfaces while a depth image encodes surface distances with respect to the sensor. These devices provide direct depth sensing and video capture, thereby delivering rich information about the scene structure without intensive processing. Not surprisingly, many researchers have taken advantage of this opportunity and we have seen a proliferation of research projects that rely on this technology [Badal 2013, Leucht 2015, Seitel 2016, Fotouhi 2017]. Two types of such sensors were available at the time when we were first designing our setup: the Kinect for Xbox 360 (Microsoft Corp., Redmond WA) and ASUS XtionPRO (ASUSTEK Computer Inc., Taipei, Taiwan). Both cameras use the depth sensor and processing chip developed by PrimeSense LTD (Tel-Aviv, Israel). A continuous infrared structured light is projected in the scene and captured by the sensor in order to generate textured depth maps. This depth-sensing technology is based on the use of an infrared laser and a holographic filter to project a known pattern towards the room. A video camera with an optical filter to block visible light is used to record the scene in the infrared range. A microprocessor chip in the camera post-processes the infrared image to estimate the distance of the objects in front of each pixel. Therefore, the lack of texture on the surfaces, color similarities between the surfaces or illumination changes do not affect the depth image computation. According to the sensor's technical sheet, objects must be located at a distance of between

0.5 and 5 meters approximately from the camera for their depth to be accurately sensed. However, studies have reported that the depth resolution degrades dramatically above a 3 m distance [Sturm 2012]. Also, the sensor fails on reflective and transparent surfaces. The depth data is transmitted to the computer as a 640×480 pixel image (VGA resolution) at a frequency of 30 Hz, where each pixel value corresponds to the distance of the object behind that pixel. The depth value is computed with 11-bit precision (2048 levels) and it can be observed that the depth estimations have a noticeable level of noise (jitter) of the order of ± 1 mm [Badal 2013]. The main advantages of these two consumer-grade cameras are the price and the fact that there is a large community of developers creating freely-available libraries and applications that simplify the programming of new tools. In our setup, we use the ASUS camera instead of the Kinect because of the smaller physical size, lightweight and the lack of an external power supply requirement. These properties make such cameras convenient to be fixed at the ceiling to capture a global view of an interventional room.

3.1.2 Camera calibration

The camera parameters (focal length, principal point offsets, skew value and lens distortion coefficients) of each color camera in our setup are computed by applying Zhang's method [Zhang 2011] on a set of images capturing several views of a known checkerboard pattern being moved in front of the camera. Such a dataset is also used to compute correction factors to reduce the inaccuracies of the depth measurements similarly to [Sturm 2012]. In [Sturm 2012], a unique factor is applied to every pixel. We decide to estimate a pair of linear coefficients $\alpha_{\{0,1\}}$ per pixel instead, since this provides improved results in our experiments. For each raw depth measurement d we compute its corrected value d_c as:

$$d_c = d \cdot \alpha_0 + \alpha_1 \tag{3.1}$$

The coefficients $\alpha_{\{0,1\}}$ are computed by applying a linear regression between a set of measured points d^i and their correspondences on a known plane d_p^i. The initial depth measurement errors estimated from this dataset are shown in Figure 3.2a. As expected, we observe that the error increases with the camera-to-plane distance. Indeed, as in [Sturm 2012], we measure errors of 5 cm for distances to the camera d beyond 3 m. The evaluation of the proposed depth correction approach on a different set of images, presented in figure 3.2b, shows a higher improvement of the depth measurement errors than when a unique correction factor is applied as in [Sturm 2012]. Indeed, measurement inaccuracies are reduced up to 3 cm with our method when d is close to 3 m. This is relevant to our application since the ceiling cameras are approximately positioned at such a distance from the scene. Besides this depth correction approach, no further depth camera calibration is performed.

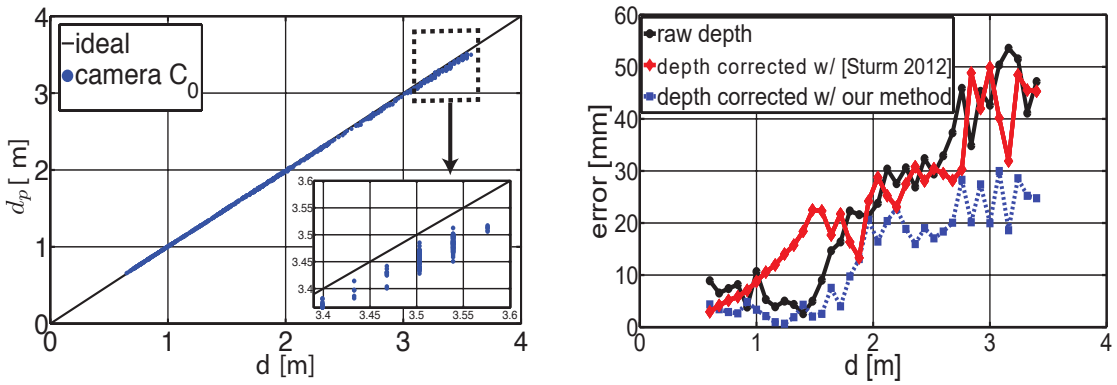

(a) Camera-to-plane distance d_p with respect to the depth measured d.

(b) Comparison of depth measurement errors before and after depth corrections.

Figure 3.2: Evaluation of the depth measurement error and of depth correction approaches.

3.1.3 Multi-camera system registration

While a single camera can be limited in terms of field of view, multiple ones can be placed around an object or a scene to improve the coverage. Therefore, we fix three cameras to the ceiling of the OR and register them to the same global room coordinate system R. This enables to merge the 3D scene information coming from each of the cameras into the same reference frame. The positions of the cameras from one of our setups in an experimental interventional room at IHU Strasbourg [IHU 2017] are visible in figure 3.3a.

The rigid transformations $\mathbf{T}^{\mathbf{R}}_{\mathbf{C}_{\{1,\dots,3\}}}$ between the cameras $C_{\{1,\dots,3\}}$ and the coordinate system R are obtained in a two-step calibration procedure. In a first step, inspired by [Svoboda 2005], the extrinsic parameters are computed from a calibration dataset recorded in the room using a laser pointer. A ping-pong ball is attached to the tip of the laser to make it more visible from the different camera viewpoints. A first sequence is acquired while continuously moving the laser pointer inside the room in the dark. Correspondences across views are obtained from this sequence, which are used for computing an initialization up to a scale factor of the camera poses using an 8-point algorithm. These poses are refined using bundle adjustment. Then, a second sequence is recorded while moving two lasers fixed to a rig at a known distance one from the other, which enables the estimation of the scale factor. This method was better suited than standard calibration methods using a checkerboard, due to the challenge of simultaneously capturing a given pattern or marker with all three cameras inside the room. The extrinsics are computed with respect to an arbitrary point in space; therefore, an extra calibration step is necessary for registering the multi-camera system to the room coordinate frame. It was decided to use the operating table as room reference. Hence, in a second step, the transformation from each camera to the left corner of the table is computed by clicking in the 3D model or by using a pattern seen by one camera. We then update the extrinsics of the other cameras accordingly. This calibration procedure is performed once per camera setup since the position of the motorized table can be

(a) Positions of the ceiling-mounted RGBD cameras installed at an experimental interventional room at IHU Strasbourg marked in red.

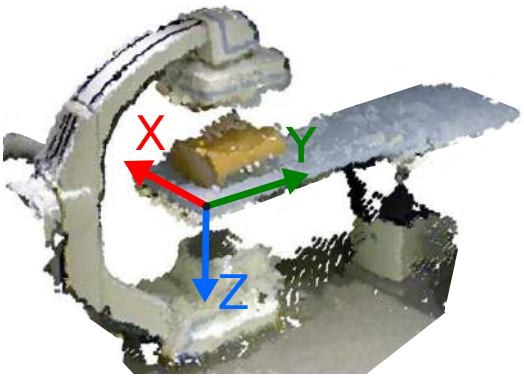

(b) 3D reconstructed model obtained by fusing the point clouds from each RGBD camera. The global room reference frame R is shown.

Figure 3.3: Registered multi-camera system for performing a 3D reconstruction of an interventional room.

re-obtained from the X-ray imaging device system and the cameras remain fixed to the ceiling of the room. The reconstructed room model is obtained by fusing the colored point clouds from all the cameras as shown in Figure 3.3b.

3.2 Visual perception of the room environment

A recording system developed within our research group [Research Group CAMMA 2017] using the OpenNI framework [OpenNI 2013], is applied to stream synchronized RGBD data from the cameras in real-time. We obtain a 3D point cloud reconstruction of the environment by merging the color and depth images from all cameras while applying the registration parameters computed with the aforementioned approach. Such a 3D reconstructed model is exploited by a radiation simulation framework (described in chapter 4) to compute the propagation of radiation for the current room context and device parameters. Also, as explained in chapter 5, it is used for providing visual feedback about the current behavior of radiation by coloring the points according the dose at that location.

In this thesis, we define room layout as the 3D positions of the bed, patient/phantom representing the patient, clinicians, wireless dosimeters[1] (if present in the scene), and of the X-ray imaging device. In this section we first describe how the room layout is modeled from the reconstructed 3D point cloud. Second, we discuss three approaches investigated for detecting clinicians and monitoring their full-body radiation exposure. Third, we describe an approach applied in this thesis to detect the imaging device's pose from the images.

[1] In the case when dosimeters are used for validation purposes as for the scenarios discussed in Chapter 4.

3.2.1 Room layout tracking

The positions and orientations of the X-ray tube and detector/image intensifier (II) can either be detected from the 3D reconstruction, read from the operating screen or obtained automatically from the application programming interface (API) of the imaging system, if available. Currently, ceiling-suspended screens, table-mounted lead curtains and medical equipment in the scene are not considered because of the difficulty of tracking them using purely vision-based approaches. On the one hand, ceiling-suspended lead shields are usually transparent for clinicians to be able to see through them when used for upper-body protection. Hence, they are invisible to structured light depth cameras. On the other hand, medical equipment such as respiratory or endoscopy towers are subject to occlusions in the ceiling views. Yet, such kind of equipment is rarely present during interventional procedures. Still, a tracking system could be used to accurately track the positions of lead protective walls, ceiling-suspended shields and medical equipment using markers. Also, instrumenting the arms holding the shields with optical encoders could allow to obtain their 3D positions. Tracking the positions of lead protective shields would be necessary for an intraoperative radiation monitoring system since their positioning has a significant impact in the diffusion of ionizing radiation. As discussed in section 8.2, tracking the lead shields is one of the perspectives of this thesis.

3.2.2 Patient registration

Registering a patient/phantom model into the room layout model is important for simulating the propagation of scattered radiation and also the patient/staff dose. To achieve this, if a 3D model of the patient/phantom involved in the study is available, its pose can be computed by applying an Iterative Closest Point (ICP) approach between the virtual model and the room's 3D point cloud. Knowledge of the table's position is applied in that case to initialize the ICP algorithm by coarsely placing the patient's model over the bed in the 3D reconstruction. If a 3D model is not available, the patient's shape can be approximated as a volume coarsely positioned in the point cloud. The table's position is known by the calibration of the multi-camera system since the global room reference system R is attached to it. If the table is displaced or rotated during a procedure, its pose can be re-obtained from the X-ray imaging device system.

3.2.3 Clinicians tracking

The monitoring of occupational radiation exposure requires to detect the positions of clinicians in the room during the irradiation process, and incorporate this information into the radiation simulation framework. Moreover, the tracking of clinicians is also necessary to provide visual feedback about their current radiation exposure. In this thesis, we have explored three different approaches for this purpose, which are described below.

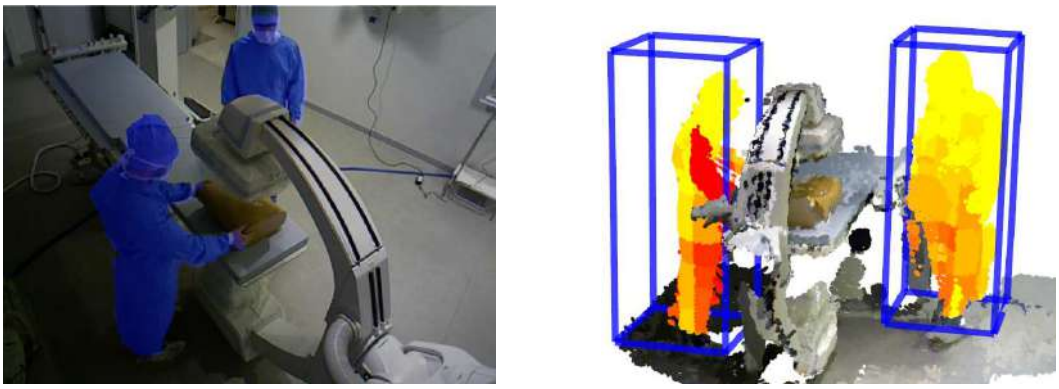

(a) Foreground mask obtained with a background subtraction approach applied on the depth image.

(b) Color-coded radiation map overlaid over the tracked clinicians' bodies in the fused point cloud.

Figure 3.4: Background subtraction approach to track the 3D positions of clinicians in an interventional room and provide a visualization of their current full-body exposure.

Bounding-box tracking

In [Loy Rodas 2015b], the positions of the clinicians are tracked with an implementation of the Gaussian mixture model for background subtraction, applied on the depth images. A foreground mask (shown in figure 3.4a) is computed on each of the multi-camera system's views, and the positions of each person in the scene is approximated by the centroid of the corresponding blob in the foreground map. The results are averaged over all views to obtain the mean 3D position of each operator per frame. As opposed to [Ladikos 2010], this method can work even when the room lights are off since the tracking is carried out on the depth images. Furthermore, this approach enables to track a bounding-box around a clinician and to show an estimation of the scattered radiation values inside that box. As discussed in chapter 4, this bounding-box is used to model the clinicians in the radiation simulation. Then, the points of the fused point cloud corresponding to the tracked person's shape, are colored according to the simulated radiation exposure value at each of its 3D locations. As it can be observed in figure 3.4b, this allows a qualitative visualization of the whole-body clinician's exposure. However, tracking the centroid of a person in the images does not provide the position of each individual body joint, which is required to compute the accumulated radiation exposure per body-part.

Multi-view human pose estimation

Results have been presented in [Kadkhodamohammadi 2017b] of the combination of a multi-view human pose estimation approach with our radiation simulation framework to compute and visualize the exposure of a clinician's body parts on RGBD frames obtained with the same multi-camera setup. A body part detector combined with a 3D pairwise deformation model is used to recover body poses in each view. These detections

Figure 3.5: Courtesy of [Kadkhodamohammadi 2017b]: (left) the detected clinician's upper-body poses on an image from an interventional room at Strasbourg's University Hospital and (right) the simulated radiation exposure per body joint (modeled as water spheres), where red indicates higher dose.

are then back-projected to 3D and merged across views with an optimization approach [Kadkhodamohammadi 2017a]. The body-part pose information can be included in the radiation simulation to compute the dose deposited. In figure 3.5 we show an example of the detected upper-body poses with the approach from [Kadkhodamohammadi 2017a], and the corresponding body-part exposure represented as color-coded spheres overlaid over a generic clinician's model. The exposure values were computed with the simulation approach described in section 4.3. Each detected body-joint is modeled in the simulation model as a sphere of water. The lower body-parts are not detected by this approach, but these can be approximated by projecting the 3D positions of the hips on the direction pointing to the floor. In figure 3.5, we show the normalized simulated exposure per body-joint. It can be observed that the person's left arm is highly exposed since it is being moved close from the irradiated area on the considered frame. Such an approach provides a clear visualization of the fact that staff receives higher doses at the left side extremities during interventional procedures (section 1.3.3). However, this multi-view human pose estimation approach is not real-time and cannot be used in an intraoperative application yet. Still, such an approach can be useful for monitoring offline and generate reports of the accumulated dose per body-part of clinical staff, by using recordings of an interventional procedure performed with our multi-RGBD camera system.

Real-time person pose estimation

We have included an open-source implementation of the approach from [Cao 2017] in our radiation awareness demonstrator system evaluated in an interventional room at IHU Strasbourg [IHU 2017] (see Chapter 7). Such an approach enables to estimate in real-time the pose of multiple persons in individual RGBD frames by simultaneously predicting

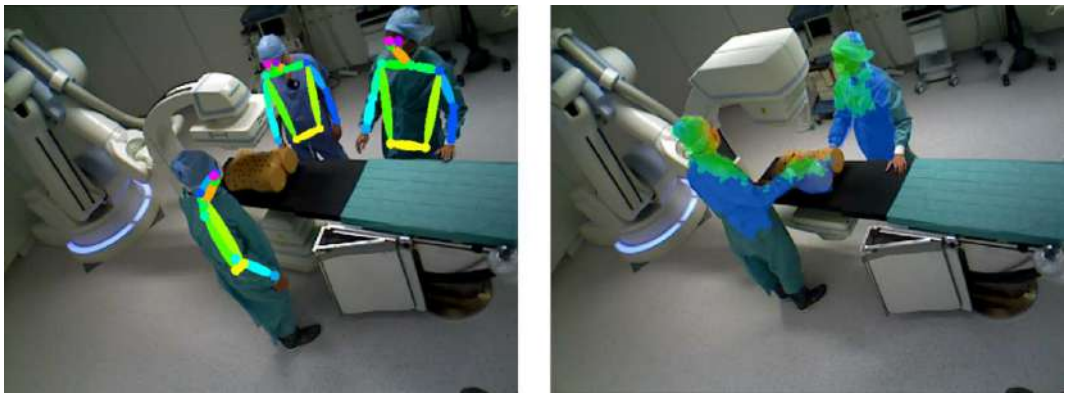

Figure 3.6: (Left) Real-time person pose estimation using the approach from [Cao 2017], and its usage for the visualization of the body radiation exposure of clinicians (right).

detection confidence maps and affinity fields that encode part-to-part association using deep convolutional neural networks. It has shown state-of-the-art accuracy on multiple public benchmarks, and we have applied it to detect in real-time person poses in a single view of a camera from our setup. In our real-time implementation, the detections are used to compute a foreground mask corresponding to the tracked clinicians' shapes. Then, we color the pixels inside the mask according to the simulated radiation value at that 3D location. In figure 3.6, we show captures from our real-time radiation awareness demonstrator system, depicting the body-part tracking of a group of clinicians in an experimental setup. We also show the visualization of the body exposure of clinicians at a different moment. This is a promising approach also to compute the accumulated dose per body-part of clinicians and provide dose data for reporting purposes. While it is prone to be affected by occlusions since it is designed for single view detection, an extension to multiple views may be possible.

3.3 X-ray device configuration detection

The imaging parameters (tube tension, filtration, FOV...) and angulation have a major influence on the patient/staff radiation dose. Hence, these parameters must be updated in the radiation simulation framework to compute the ongoing dose values. While they can be read directly from the DICOM images or obtained automatically via the device's API, access to either of them may not always be available. Moreover, a direct communication with the imaging device through software is not always feasible, as for mobile C-arms for instance. This is why in this thesis we also investigated an approach to detect the pose of the imaging device from our ceiling-mounted cameras, to automatically obtain the current C-arm angulation from it.

We presented in [Loy Rodas 2017a] an approach to perform 3D pose estimation of medical equipment using RGBD cameras. This estimation is not only necessary to correctly simulate the propagation of radiation, but it can also be useful for context-aware systems to have a full understanding of the 3D position of equipment in the OR.

Moreover, surgical activity recognition systems such as [Twinanda 2015, Twinanda 2016] can benefit from the knowledge of the interactions between clinicians and equipment. In the same way, medical equipment's 3D pose estimation can be applied for collision avoidance with automated devices in an interventional room [Ladikos 2008]. For our radiation monitoring application, we need to detect an X-ray imaging device which is large. Therefore, among the spectrum of methods available for object detection in RGBD images, we apply a template matching approach from [Hinterstoisser 2012b] and adapt it to our needs. Coined LineMOD, this method has proven to be fast and efficient when dealing with poorly textured objects [Hinterstoisser 2012a] and it can deal with large-sized objects as required for our application.

LineMOD relies on matching templates generated from a multitude of synthetic renderings from a 3D model of the object, which cover for all the possible views that can be encountered at test time. For our application, if a 3D model of the X-ray imaging device is not available, it can be generated by scanning it with an RGBD camera and using a reconstruction software such as [RecFusion 2015]. Then, using such a model, we apply the same viewpoint sampling scheme as in [Hinterstoisser 2012b] in order to equally sample a set of virtual camera viewpoints around it. This is achieved by dividing the space into a polyhedron, where each vertex represents a viewpoint from where synthetic color and depth images are generated. By repeating this process for polyhedrons of different sizes, we obtain images at different scales. This process is illustrated in figure 3.7a, where each virtual camera viewpoint around the model is represented by a red pyramid. A LineMOD template is then generated per image pair by densely computing color gradients and surface normals. Color gradients are uniformly computed only on the silhouette of the object since this method has been designed for objects with little texture. In contrast, surface normal features are computed on the interior of the object's silhouette and are discretized according to their orientation. We refer the reader to [Hinterstoisser 2012b] and [Hinterstoisser 2012a] for more information about the feature computation and encoding. Each template is labeled with the corresponding relative camera-to-object transformation. Therefore, when a template is matched at test time, it provides a coarse estimation of the object's pose, which is further refined using ICP. The registration of the ceiling cameras to the room reference system R described in section 3.1.3, provides the approximate distance of the cameras to the scene. From this information, we select the parameters and range of scales to consider in the viewpoint sampling scheme for the template generation. At the training stage, each template is also labeled with the X-ray imaging device projection angle it corresponds to. Hence, at test time, when a template is detected by one of the ceiling views, the information about the current C-arm projection can be recovered directly. From this, the position of the X-ray source and of the detector are computed and updated in the radiation simulation model. In figure 3.7b, we show an example of the detection of the imaging device's angulation from one of the ceiling-camera views, where the device's 3D model is overlaid over the color image, projected using the detected pose. Whenever the imaging device is occluded in one side of the operating table, another view from one of the remaining cameras of the system

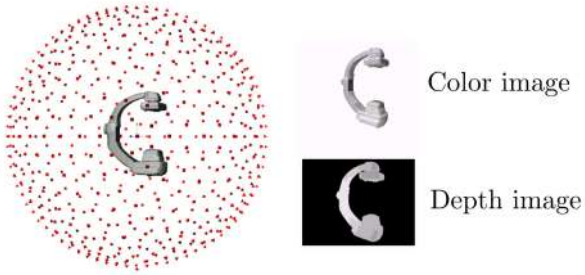

(a) Synthetic color and depth images generated by equally sampling a set of virtual camera viewpoints (in red) around a 3D model of the imaging device.

(b) Detection of the X-ray device's pose in one of the ceiling camera views: the 3D model is overlaid on the image to the detected pose.

Figure 3.7: Automatic detection of the X-ray imaging device configuration from views of the ceiling-mounted multi-camera system.

can be used to perform the detection.

Our equipment detection approach was also applied to perform camera relocalization for mobile AR visualization purposes as presented in [Loy Rodas 2017a], where its performance was evaluated on large and challenging RGBD dataset recorded in an OR. A detailed description of such a dataset is included in appendix B. Furthermore, a summary of the evaluation results of the detection of the X-ray imaging device's pose with our equipment detection approach on this dataset is provided in appendix C.4.1. From such an evaluation, the pose of imaging device could be recovered with a mean rotation error (averaged over all axis) of 4.71°. This is the mean error over all sequences, namely including those featuring rotations of the imaging device and partial occlusions in the camera view. For the sequences where the X-ray device is static, the rotation error is reduced to $1.3° \pm 0.3°$. Hence, for situations where the imaging device's pose cannot be obtained automatically from its API, an equipment detection approach on the images from our multi-camera setup yields an acceptable precision for the sake of the application.

3.4 Conclusion

In this chapter, we describe a registered multi-RGBD camera setup used for perceiving the layout of an interventional room. Such a system is a core part of the intraoperative radiation awareness system developed during this thesis. The cameras are mounted on the ceiling of the room using articulated arms in a configuration allowing them to capture key views around the operating table. We describe the calibration and registration procedures enabling us to obtain a 3D reconstruction of the scene by merging the color and depth images from each camera. Furthermore, we discuss the use of ceiling cameras for keeping an up-to-date picture of the room layout. This information is then exploited by a radiation simulation framework (described in chapter 4) to compute the propagation of radiation for the current room context and device parameters. Furthermore, we presented

several vision-based approaches for tracking the positions and body pose of clinicians, enabling our system to provide feedback about their current full-body radiation exposure. Also, in cases where the X-ray device's API is not available, an equipment detection approach applied on the images from the multi-camera system allows to estimate the C-arm's angulation, as needed to simulate radiation.

4 Radiation simulation

Essentially, all models are wrong, but some are useful.
– George E. P. Box

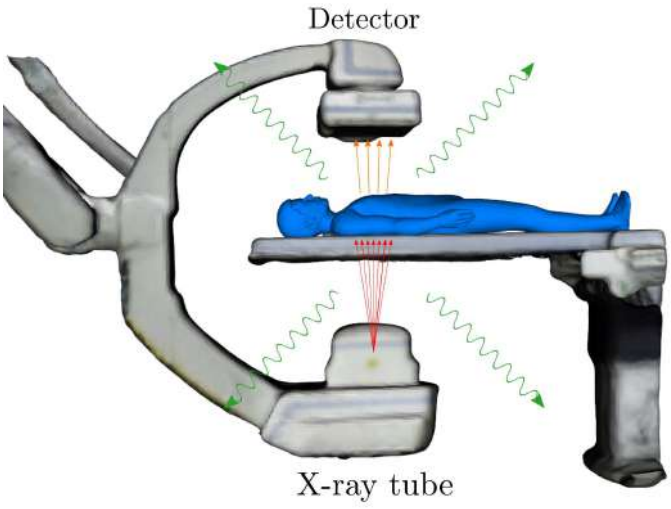

(a) Representation of the X-ray imaging process: primary X-ray cone beam (red), photons reaching the detector (orange) and scattered rays (green).

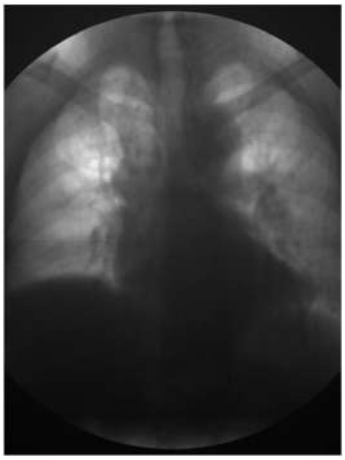

(b) Digitally reconstructed radiography (DRR), simulated using Monte Carlo methods.

Figure 4.1: Representation of the X-ray imaging process and simulated output radiography.

Chapter Summary

4.1 X-ray imaging modeling 59
4.1.1 Imaging process 59
4.1.2 X-ray energy spectrum 61
4.2 Monte Carlo simulations of X-ray transport with Geant4 62
4.2.1 Simulation approach 62
4.2.2 Visualization of simulated radiation risk maps 64
4.2.3 Experimental validation using dosimeters 65
4.2.3.1 Validation methodology 65
4.2.3.2 Results and discussion 67
4.3 GPU-accelerated radiation simulation 70
4.3.1 Simulation approach 71
4.3.1.1 Patient exposure 71
4.3.1.2 Staff exposure 74
4.3.1.3 Scattered radiation propagation 77
4.3.2 Experimental validation 77
4.3.2.1 Clinician exposure validation 77
4.3.2.2 Evaluation with experimental measurements 79
4.4 Conclusions 80

Modeling of X-ray photon propagation and interaction with matter is heavily complex and not possible to fully achieve analytically (see section 2.2.2.1). However, computer-based calculations allow to simulate these processes in an inexpensive manner. Monte Carlo methods have become the gold standard for these purposes and have been widely applied in the literature to simulate the behavior of ionizing radiation [Ladikos 2010, Koukorava 2011, Zhang 2014, Santos 2015, Leucht 2015, Principi 2016]. They are based on random sampling and can be made arbitrarily accurate by increasing the number of simulated samples.

In this chapter, we describe two simulation approaches developed in this thesis for the simulation of X-ray radiation propagation and patient/staff dose. The first approach, presented in [Loy Rodas 2014, Loy Rodas 2015b], was built using the Geant 4 library [Agostinelli 2003], and is described in section 4.2. We also present in section 4.2.3 the results of its experimental validation performed using dose measurements acquired in an OR. The second, presented in [Loy Rodas 2017b], relies on GPU-accelerated Monte Carlo calculations to compute X-ray transport in near real-time. It was developed through a collaboration with the LaTIM laboratory [LaTIM 2017] and makes use of the GGEMS library [GGEMS 2017]. Such an approach along with its experimental evaluation is presented in section 4.3. Before discussing our radiation simulation framework, we briefly describe the X-ray imaging process in section 4.1, to familiarize the reader with the

parameters and physics effects which are involved. It also allows us to explain concepts common to the two simulation approaches developed in the context of this thesis.

4.1 X-ray imaging modeling

4.1.1 Imaging process

Both fluoroscopy and CT utilize X-rays for the image acquisition process. X-rays are generated inside what is known as the X-ray tube, by accelerating electrons and directing them towards a metal target. The electrons rapidly decelerate upon encountering this material, and X-rays are created from the conversion of their kinetic energy into electromagnetic radiation [Bushberg 2011]. Depending on the elemental composition of the target electrode and the applied X-ray tube voltage, two types of X-rays are created: *bremsstrahlung* (braking radiation) and characteristic X-rays.

Primary X-ray photons, represented in red in figure 4.1a, travel in straight lines from the X-ray source. Given the typical particles' energies involved in fluoroscopy and CT, they interact with the patient through three main physics effects: photoelectric effect, Rayleigh and Compton scattering. These mechanisms are dependent on the X-ray energy, the elemental composition of the tissue and the tissue density. Due to these effects, human body structures with a higher content of calcium and phosphorus (such as bones) will be more attenuating than soft tissues. Similarly, tissues with low density (such as lungs) will be less attenuating than fat or muscle [Wong 2008]. This can be observed in the radiograph shown in figure 4.1b, where the lungs look brighter than the bones and other surrounding structures. As shown schematically in orange in figure 4.1a, only a part of the photons output by the source reach the detector. When the detector is struck, different intensity patterns or images are produced corresponding to the materials penetrated in the photons' trajectories. These patterns are then converted into light and then into electric signal, and this is why X-ray images are often described as shadowgrams or projection images (an example is shown in figure 4.1b).

Photons interacting through the photoelectric effect are absorbed inside the patient and do not reach the detector. They consume all of their energy to eject an electron from an atom and then, these ejected electrons will move around and ionize neighboring atoms. Each time an atom is ionized by ejected electrons, free radicals that can damage DNA are created. Compton scattered photons ionize atoms but do not consume all of their energy and are thereby scattered in any direction with an attenuated energy [Bushberg 2011]. Rayleigh scattering occurs when a low-energy X-ray photon is scattered from an atom without any energy loss, namely there is no energy exchange from the X-ray to the medium. Photons scattered through these effects (represented in green in figure 4.1a) are responsible for most of the medical staff's radiation exposure.

In this thesis, we focus on modeling the radiation generated during X-ray radiography or fluoroscopy since these imaging techniques are largely used for guidance during

interventional procedures (see section 1.1.3). A 3D model of a fluoroscopy system[1] is shown in figure 4.1a. In such systems, the X-ray source and detector are mounted facing each other on a C-shaped arm. This is why they are commonly known as C-arms. The operating table lies between the source and the detector, and the arm can be rotated around it in order to acquire X-ray images from any angle. Mobile C-arms are manually operated and positioned, whereas robotized ones can be programmed to follow complex trajectories and even to generate CT-like 3D images. The X-ray beam projection in a C-arm imaging device is defined using two rotation angles: the left/right anterior oblique (LAO/RAO) and the caudal/cranial (CAUD/CRAN) angles [Wang 2014] (also referred to in the literature respectively as angular and orbital rotation angles [Wang 2012]). During a procedure, the operator adjusts their values to obtain different image projections, enabling to capture X-ray images in both the transverse and the sagittal plane. These projections, named based on the location of the detector with respect to the patient, are shown in figure 4.2. The tube-to-isocenter and the tube-to-detector distances can also be modified to alter the magnification coefficient of the output image.

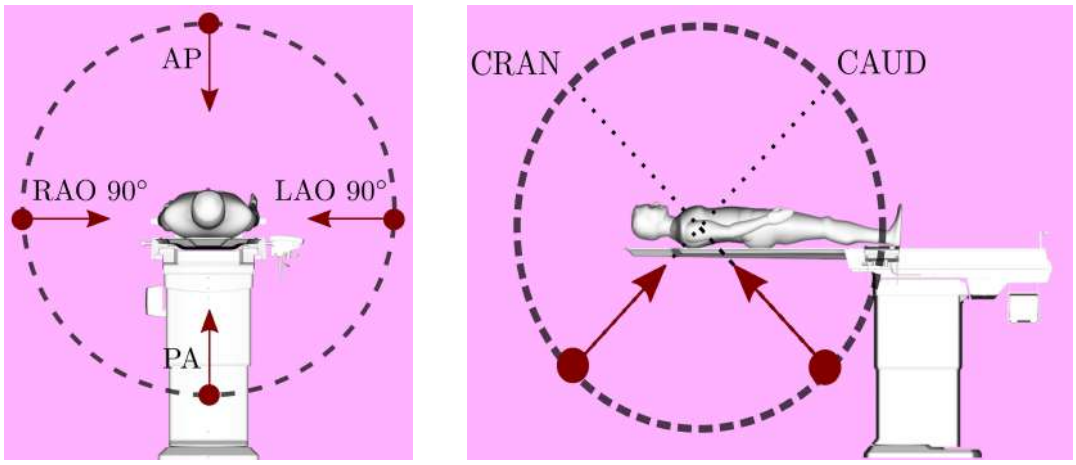

(a) Angulations in the transverse plane: PA, LAO at 90° , AP and RAO at 90°

(b) Angulations in the sagittal plane: CAUD and CRAN.

Figure 4.2: Visualization of the X-ray source position and nomenclature for imaging projections in the transverse plane (left) and in the sagittal plane (right). The position of the source is represented by the red circle with an arrow pointing in the direction of the X-ray beam.

The simulation of the X-ray imaging process and of radiation transport involves physical and geometrical operations. The first includes the computation of distances between particle interactions and the sampling of particle states after such interactions. In the second, the interface crossings and particle displacements inside a volume are calculated. These processes are performed by simulating the aforementioned physics effects (photoelectric effect, Compton and Rayleigh scattering) and by taking into consideration the patient's organ/tissue composition and imaging parameters.

[1] Artis Zeego from Siemens Healthcare, Forchheim, Germany.

The energy spectrum of the generated X-ray particles depends on the simulated imaging parameters, which can incur in lower or higher energy photons absorbed and/or scattered by the patient. We further discuss the impact of the X-ray energy spectrum in our simulation approaches in the section below.

4.1.2 X-ray energy spectrum

The quality of the obtained projection image, along with the patient/staff dose depend on several imaging parameters that influence the characteristics of the generated X-rays. There are two primary means by which the X-ray beam produced by the tube can be changed: altering the current (mA) or altering the voltage (kV). The current across the tube determines how many electrons are released to strike the anode, with a consequent linear increase in the number of photons produced. The voltage across the X-ray tube affects the velocity of the electrons as they strike the anode and this affects the energy of the photons produced by the tube [Bushberg 2011]. It is important to note that, in clinical practice, these parameters are automatically altered according to the thickness of the examined region of the patient by the X-ray device's AEC. Higher energy particles are more prone to reach the detector, therefore, tube voltage is usually automatically increased in order to compensate for the increase of beam attenuation by the patient's body to produce a clinically useful image [Santos 2015]. As dose is energy per mass of tissue, higher energy photons can incur in higher dose. Also, the higher the energy, the more X-rays undergo Compton scattering, which means that more photons may be scattered into the environment during the imaging process [Bushberg 2011]. Furthermore, thin metal filters placed in the beam are used to remove low-energy (soft) X-rays, since these have a higher probability to be absorbed by the patient and have no effect on the diagnostic quality of the image. Depending on the application, layers of aluminum, copper, or other materials can be added to the beam to allow more or less of the low-energy photons to reach the patient [Wong 2008]. Also, some imaging devices are built with inherent permanent filters.

For the sake of simplicity and also since the technology of the X-ray tubes of commercial imaging devices is often private, we do not simulate the generation of X-rays. Instead, we model the X-ray beam as a primary generator producing a user-defined number of photons from a fixed point with the shape of a collimated cone beam. Still, to account for the influence of the imaging parameters, the energies of the simulated photons are randomly sampled from an energy spectrum computed beforehand. Such a spectrum is generated from the peak tube voltage and filtration conditions from the considered imaging protocol. In figure 4.3 we show an example of a spectrum corresponding to a tube tension of 85 kV and a 0.4 mm layer of Aluminum filtering. There are several tools applying physics models and attenuation data to generate such spectra. We rely on [Siemens Healthcare 2017b] for this purpose.

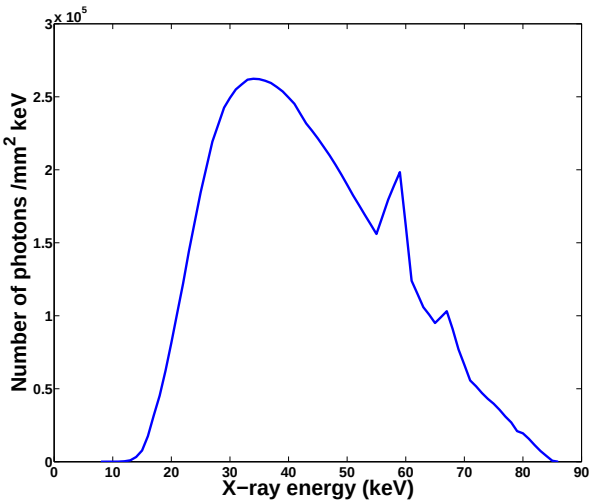

Figure 4.3: Simulated X-ray spectrum (85 kV - 0.4 mm Al filtration) using the online X-ray spectra simulator from Siemens [Siemens Healthcare 2017b].

4.2 Monte Carlo simulations of X-ray transport with Geant4

In this section, we describe the first simulation approach explored in this thesis. Such a simulation framework was developed using Geant 4 [Agostinelli 2003] to estimate the propagation of scattered radiation for the current operating room layout. Geant 4 is a C++ based toolkit initially developed at CERN, which is widely used for simulating the passage of particles through matter using Monte Carlo methods. We rely on the multi-RGBD camera system described in chapter 3 to obtain a 3D point cloud reconstruction of the current room layout. The positions of the clinicians, patient, table and C-arm are obtained as previously described and are used to build a coarse simulation model for the computation of the 3D dose distribution in the room. To compensate for the approximations introduced in the simulation model, we propose to use real-time wireless dosimeters placed at key locations in the room to provide dose measurements used both for calibrating the simulations and for evaluating the results' accuracy. We herein describe the simulation approach and its experimental evaluation in an operating room.

4.2.1 Simulation approach

A Geant 4 simulation requires the definition of the geometry of the simulation environment, namely the physical layout for the experiment. Within this geometry, the framework iteratively computes the trajectories and interactions between a given set of particles and the atoms from the materials defined in the scene. Using the information provided by our multi-camera system, we build a coarse simulation model representing the OR (see chapter 3). An example can be seen in figure 4.4a. To reduce computational time, we model each of the considered objects with a rectangular geometry, by adding rectangular volumes having the same material composition and pose with reference to the room coordinate

system as in the real-world setup. Areas of these geometries are defined as sensitive to every interaction with impacting particles and the energy deposition is measured during a simulation. Similar to [Wagner 2009], the interventional room is modeled by a volume filled with the material *air*. The X-ray tube and detector are represented as iron volumes since this has the effect to block radiation above the detector and below the source [Ladikos 2010]. Their position and orientation are adapted according to the simulated beam projection. A carbon parallelepiped is added for the operating table and a cubic volume filled with water is included to represent the phantom used for the experiments. As in [Wagner 2009] and for decreasing the calculation time, water is used to simulate the scatter factor of a human body. Hence, if clinicians are present in the room, they are modeled as $0.4 \times 0.4 \times 2$ m^3 water-filled boxes placed in the positions obtained from the tracking performed in the ceiling views (section 3.2.3).

To reduce potential errors introduced by the approximations in the simulation, the simulation results are calibrated using measurements from a subset of the dosimeters placed in the room. We refer to them as *calibration* dosimeters. A correction factor defined as the mean ratio between the measured and simulated doses from such dosimeters is applied to all simulation results. As shown in section 4.2.3, this linear correction is effective enough for obtaining low simulation errors. We use active personal dosimeters (previously described in section 2.1.2.1) for this purpose. These are calibrated in $H_p(10)$ namely the personal dose equivalent in soft tissue at a 10 mm depth below the position where it is worn, with a resolution of one measurement per second. Despite the possible imprecision in the measurements and the limited angular resolution, their portability and real-time sampling capability make them the best available solution for our system. Figure 4.4b shows an example of a real OR setup where the C-arm is set for a posterior-anterior (PA) beam projection (0° rotation angle), a water-filled slab phantom is placed over the table and eight dosimeters are distributed around the table. The corresponding simulation model is shown in figure 4.4a where the material of each solid is specified.

The dosimeters are modeled as $45 \times 45 \times 20$ mm^3 volumes of ICRU [ICRU 1980] soft tissue equivalent material (1 $g.cm^{-3}$ density and mass composition: 76.2 % oxygen, 11.1 % carbon, 10.1 % hydrogen and 2.6 % nitrogen). These are placed inside the main volume in the same positions as in the real-world setup. The $H_p(10)$ values are then evaluated by placing sensitive cells of $45 \times 45 \times 0.5$ mm^3 inside the dosimeters' models at a 10 mm depth from the outer surface. The total energy deposited in these cells after a simulation run is divided by the volume's mass (obtained from the material's definition), for estimating the personal dose equivalent. The simulated dosimeters are sensitive to any incident particle since we do not model the angular resolution of the real dosimetric system we use.

As mentioned in section 4.1.2, the energies of the simulated photons are randomly sampled from spectra generated for the considered imaging parameters. Their moment direction is randomly sampled inside a cone having the studied X-ray FOV as diameter, thus approximating the angular distribution of the particles as isotropic. The aforementioned physics effects leading to the generation of scattered radiation are also modeled.

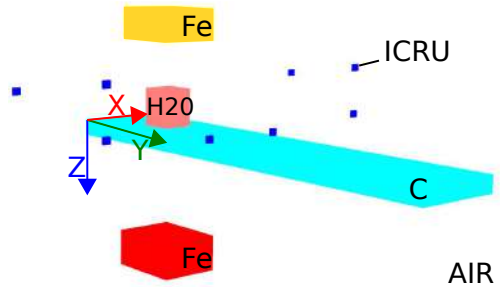

(a) Simulation model of the current OR layout considering the physical properties of each object.

(b) Real-world setup: robotized C-arm, water-filled phantom and dosimeters sparsely distributed around the table.

Figure 4.4: Simulation model and setup of the experimental validation.

The room model is divided into cubic voxels forming a 3D grid and, during a simulation run, the dose deposited in each one of them is computed. Hence, it is possible to estimate the spatial dissemination of scattered radiation during the irradiation process by checking the accumulated dose in the corresponding voxels. The material from each voxel is adjusted according to the solid it intersects with. The resolution and the coverage of the simulated radiation map depends respectively on the size of each voxel and on the number of considered voxels. The radiation shields are not modeled, therefore, the system will provide an estimate of the maximum dose that could be received in a worst-case scenario irradiation.

Simulations are performed for a large number of particles n. The number of simulated particles has an impact only on the statistical error since the computed doses are normalized by n at the end of each run. The particles are grouped into several batches and executed in parallel on different computing kernels on a multiprocessor computer. The results yielded by the independent runs of the same code are combined a posteriori to obtain a single final result with a reduced statistical uncertainty.

4.2.2 Visualization of simulated radiation risk maps

The simulation module computes the 3D dissemination of scattered radiation inside a voxelized representation of the room for a given set of irradiation parameters and layout. This information can be combined with the generated room 3D model for showing the amount and distribution of scattered radiation in an augmented reality manner. This novel visualization of ionizing radiation is further described in chapter 5, where several qualitative visualizations of the simulated radiation maps and exposure of patient/staff are provided. In the same way, other visualizations useful for teaching about the diffusion of scattered radiation can be generated with this simulation approach. In figure 4.5, we provide two examples of 2D radiation isomaps generated from simulations where the

C-arm was positioned for a PA and AP projections. The position of the X-ray source for each of these configurations can be observed in figure 4.2. Each of the proposed results was generated by simulating the deposited dose in a voxel grid of $28 \times 28 \times 18$ voxels of side length 150 mm namely covering a volume of $4.2 \times 4.2 \times 2.7$ m^3. Then, we sum the computed 3D risk maps along the x-axis (same reference frame as in figure 4.4a) to generate the isomaps. One can clearly observe how the scatter is concentrated under or over the bed depending on the case. These results suggest that blocking the radiation coming from the surroundings of the X-ray source is a good method to reduce the dose to the operators. The results also show that increasing the distance between the operator and the X-ray source is an effective method to reduce the radiation exposure.

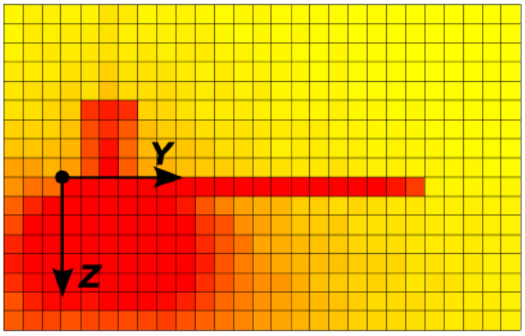

(a) Radiation isomap for an PA imaging projection (X-ray source under the bed).

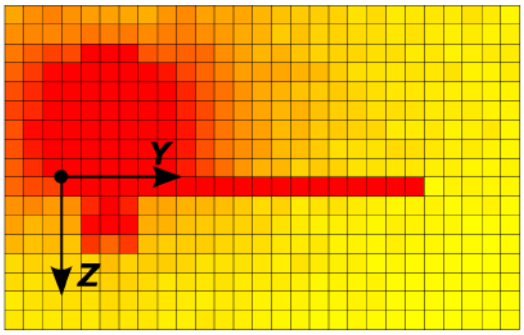

(b) Radiation isomap for a AP imaging projection (X-ray source over the bed).

Figure 4.5: 2D Isomaps obtained by summing the radiation risk maps along the x-axis for two imaging configurations (red indicates higher dose).

4.2.3 Experimental validation using dosimeters

The performance of a new Monte Carlo code is typically evaluated by simulating cases that are reproduced with laboratory experiments [Leucht 2015, Alnewaini 2017]. To validate the simulation approach herein presented, a set of experiments were performed in an interventional room using an Artis Zeego robotized X-ray imaging device, a calibrated multi-RGBD camera system and a set of RaySafe wireless active personal dosimeters [RaySafe 2017]. We hereby present the methodology and setup for these experiments along with the results obtained.

4.2.3.1 Validation methodology

Nobody was irradiated in any of the performed experiments. Instead, a phantom of $20 \times 20 \times 24$ cm^3, with 10 mm thick plexiglas walls and filled with water was irradiated under different imaging protocols for the generation of scattered radiation. Dosimeters were either placed over the operating table or taped to drip rods and placed around the work area at different positions depending on the experiment. The experimental setup is shown in figure 4.4b. Various clinical imaging conditions typical of interventional

procedures were reproduced and the generated scattered radiation levels were measured by the dosimeters at sparse locations around the work area. The same scenarios were simulated and the simulations corrected using the measurements from the calibration dosimeters. The relative errors between the computed dose values and the ones measured by the validation dosimeters were computed to verify the accuracy of the simulated dose distribution. As explained in section 2.1.2.1, the intrinsic response error from this kind of dosimeters can go up to 30 % [Struelens 2011], hence, we consider a simulation as correct when the obtained error is close or inferior to that value. Five runs of 500 million X-ray particles were simulated per test and the results were normalized by that number. The statistical uncertainty of the simulated dose values was below 1 % in all the simulation runs. Two complementary sets of experiments are hereby presented: in the first one, referred to as *configuration test*, the imaging parameters were kept constant while the positions of the dosimeters were modified. In the second set, called *tube parameters' test*, the position of the dosimeters was kept constant, while a large number of images for different tube voltages, filtration conditions, field-of-views and beam projections was acquired.

Configuration test: seven configurations of six dosimeters placed around the source were tested. The initial one is shown in Fig. 4.6a; after each irradiation, the radii r1 and r3 along with the distances d2 were increased of 30 cm, thus increasing progressively the distance of the dosimeters to the source of scattered radiation. At each tested distance, three PA projections using a 82 kV peak tube voltage, 0.4 mm Al filtration and 42 cm field size were acquired, making a total of 21 irradiations. The same conditions were simulated and the $H_p(10)$ doses at the positions of the dosimeters were computed for the different tests. Measurements from a single dosimeter were used for calibrating the simulations; the computed correction factor was applied to the rest of the simulation results and compared to the five other dosimeters' measurements.

Tube parameters' test: it aimed at testing the simulation's accuracy when changing the X-ray tube parameters and projection angle for a single configuration of calibration/validation dosimeters (shown in Fig. 4.6b). Four beam projections were examined: PA, LAO at a 90° angle, AP and RAO at a 90° angle. The position of the X-ray source for each of these projections is shown in figure 4.2a. For each angulation, the tube voltage was chosen between 80 and 117 kV, the amount of copper spectral beam filtration between 0.0 and 0.9 mm and the FOV between 11 and 42 cm, for a total of 32 tested irradiations, namely 8 per beam projection. The detailed imaging parameters that were tested are given in table 4.3. We used eight wireless dosimeters for measuring the scattered radiation at different points of the room. These were disposed symmetrically with respect to the operating bed in order to obtain measurements for every tested beam projection while also covering the entire workspace. The simulation was calibrated by computing a correction factor using measurements from two dosimeters. The error was then computed by comparing the results with the other six. To cope with the angular

resolution of the dosimeters, each one of them was oriented towards the phantom and placed at least at table height or higher. This way, we attempt to maximize the number of incident particles that are inside their measurement range for every configuration. Figure 4.6b shows the configuration of the dosimeters for this set of experiments, where the z value denotes the height with respect to the table, which is null if not specified. One dosimeter per table side is used for calibration in order to equally consider the entire work area. All sixteen possible pairs of combinations of dosimeters 1, 3, 5 and 6 (right side) with 2, 4, 7 and 8 (left side) were tested for calibration purposes while evaluating the accuracy of the results with the remaining six measurements.

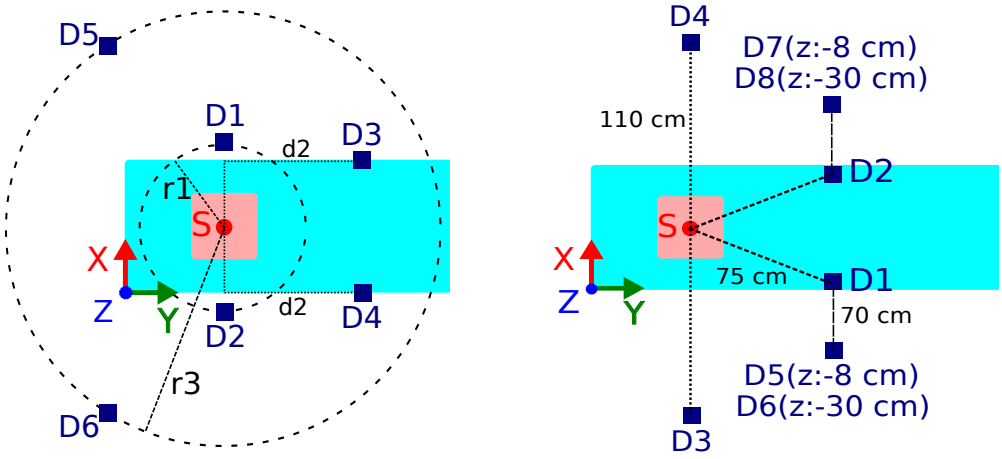

(a) *Configuration test*: radii r1 and r3 along with distance d2 were increased by 30cm after each set of irradiations.

(b) *Tube parameters' test*: irradiations with different exposure parameters and beam projections were carried out.

Figure 4.6: Position of the dosimeters with respect to the C-arm isocenter (S) for the two sets of experiments presented.

4.2.3.2 Results and discussion

Configuration test: A mean simulation error of 19.3 % ± 4.3 % was obtained when testing all combinations of one calibration dosimeter against five others. The lowest error of 14.7 % ± 5.5 % is obtained when calibrating with dosimeter 1. A summary of the mean testing errors for that case is presented in table 4.1. No apparent relationship between the simulation error and the dosimeters' distance to the source can be found. The errors remain low for a constant set of default imaging parameters when the positions of the measuring dosimeters are changed. Indeed, the simulation results remain close to the measured values even further than 2 meters away from the isocenter of the imaging device.

Tube parameters' test: A mean error of 37.4 % ± 7.4 % was obtained for all tested irradiation protocols and possible combinations of calibration/validation dosimeters. The lowest mean error, 29.2 % ± 4.1 %, was obtained when calibrating with number 6 and 8.

Table 4.1: Simulation errors for the *configuration test* when using dosimeter 1 for calibration.

Distance(m)			**Error per dosimeter (%)**					
r1	d2	r3	2	3	4	5	6	**Mean**
0.5	0.4	0.6	03.1	01.1	10.9	31.6	29.6	15.3
0.8	0.7	0.9	10.7	46.2	23.5	25.6	19.7	25.1
1.1	1.0	1.2	10.7	16.7	04.6	16.5	25.9	14.9
1.4	1.3	1.5	0.35	48.5	01.1	06.7	18.2	15.6
1.7	1.6	1.8	18.8	07.3	09.7	03.5	01.1	08.1
2.0	1.9	2.1	03.9	15.9	13.3	03.7	36.4	14.6
2.3	2.2	2.4	06.3	14.3	04.9	04.6	16.1	09.3
			08.2	**21.4**	**09.7**	**13.2**	**21.0**	**14.7**

These were consequently considered the best positioned for measuring correct scattered radiation doses at every configuration. The dosimetric system we use has been calibrated during manufacturing for usage at chest level height, which, interestingly, is close to the height of the aforementioned dosimeters (1.30 m from the floor). Table 4.2 shows error values for each beam projection and test dosimeter when calibrating with dosimeters 6 and 8. It can be observed that higher errors are obtained for the lateral projections (LAO and RAO). For these angulations, the accuracy of the measurements could have been affected by the spatial distribution of the dosimeters used for this set of experiments. Moreover, the orientation of the dosimeters was kept constant during the experiments and it is possible that the precision of the measurements could have been influenced by the dosimeters' angular resolution. Table 4.3 provides the mean test error for each of the irradiation protocols that were evaluated.

Table 4.2: Mean simulation errors per validation dosimeter and per configuration for the *tube parameters' test*, when calibrating with dosimeter 6 and 8.

	Error per dosimeter (%)						
Projection	1	2	3	4	5	7	**Mean**
PA	19.2	39.2	33.0	14.4	12.3	24.5	23.8
LAO 90°	20.7	21.9	35.3	40.4	30.6	52.7	33.6
AP	18.2	12.7	16.1	16.9	17.4	19.7	16.8
RAO 90°	59.0	11.8	43.9	51.4	55.7	34.0	42.7
	29.3	**21.4**	**32.1**	**30.8**	**29.0**	**32.7**	**29.2**

The results herein presented show that our system can be used to simulate the global propagation and intensity of scattered radiation for different X-ray tube configurations. Such an extensive evaluation of our simulation framework against experimental data, is a major difference with respect to previous works applying MC methods to simulate

Table 4.3: Mean simulation errors per irradiation protocol when calibrating with dosimeter 6 and 8 in the *tube parameters' test*.

Projection	**FOV (cm)**	**kVp (kV)**	**mm Cu**	**Error (%)**
PA	42	81	0.0	29.2
	42	96	0.0	23.0
	42	117	0.0	24.5
	42	86	0.3	25.2
	42	95	0.6	20.0
	42	102	0.9	23.3
	22	92	0.0	25.1
	11	91	0.0	19.9
LAO 90°	42	81	0.0	40.2
	42	96	0.0	32.0
	42	117	0.0	53.8
	42	81	0.3	32.3
	42	81	0.6	19.3
	42	86	0.9	21.6
	22	81	0.0	42.1
	11	92	0.0	27.5
AP	42	81	0.0	19.1
	42	96	0.0	20.1
	42	117	0.0	20.6
	42	84	0.3	15.1
	42	93	0.6	09.2
	42	100	0.9	12.0
	22	94	0.0	17.8
	11	92	0.0	20.8
RAO 90°	42	81	0.0	45.3
	42	96	0.0	53.3
	42	117	0.0	50.9
	42	81	0.3	36.5
	42	81	0.6	28.1
	42	87	0.9	40.5
	22	81	0.0	45.8
	11	91	0.0	40.7

radiation. We obtain simulation errors which are in agreement with the technical error of the dosimeters when testing the results for different room layouts and X-ray tube parameters. The obtained errors can be mostly explained by the dosimetric system used for correcting our simulation results: APDs have proven to be at least ±30 % less precise

than TLDs because of their internal semiconductor based construction [Struelens 2011], required to generate instantaneous measurements. The use of an approximated X-ray source model in the simulation framework can also introduce errors to the results. Indeed, we model the X-ray tube as a collimated source of photons due to restricted access to the actual geometry and parameters of the imaging device used in our experiments.

Currently, all results are computed offline after recording synchronized data from dosimeters and RGBD cameras. Our simulation framework is based on CPU computations hence long computational times that go up to several hours are required to compute a full 3D radiation map of the room. Pre-computing such simulation maps may be acceptable for a radiation awareness system applied for training or teaching purposes. Yet, this becomes unpractical when many imaging and/or room parameters are altered since a new simulation is required each time. For a clinical application, the simulations of radiation should be performed in real-time while considering the real room conditions and imaging parameters. Furthermore, a fast radiation simulation would also be useful for a radiation awareness training system showing radiation exposure for several clinical scenarios. In the following section, we describe the work we performed to make our radiation simulation faster by incorporating GPU-accelerated MC methods and by proposing approximations enabling to reduce computation time, while maintaining the results' accuracy.

4.3 GPU-accelerated radiation simulation

Monte Carlo methods are associated with long execution times, which is one of the major issues preventing their use in routine clinical practice. A potential solution to the intensive computational issues is the use of computer clusters, although this solution may be less realistic within a routine clinical environment given the associated cost and logistics issues. Recently, graphics processing units (GPU) have become in many different domains a low cost alternative solution for the acquisition of high computation power. Their architecture is able to provide any conventional computer with the computation power of a small cluster. This power has been exploited to speed-up Monte Carlo simulations and one can now find in the literature various MC codes implemented on GPU such as [Badal 2009, Wagner 2012, Bert 2013]. In this thesis, we also propose a simulation approach for computing in quasi real-time the exposure of patient and staff during an X-ray imaging procedure, and also for simulating the 3D propagation of scattered radiation for the current room and imaging conditions. To achieve this, we rely on an implementation of MC methods on GPU architectures *i.e.* the GGEMS library [GGEMS 2017]. Written in the CUDA language, such a framework has been validated in [Bert 2013], showing equivalence with the reference MC library Geant 4 [Agostinelli 2003], with a speed-up factor in simulation time of up to 90. It is developed and maintained by the LaTIM laboratory [LaTIM 2017], having radiotherapy and patient dosimetry as main target applications [Bert 2013, Lemaréchal 2015]. We herein propose extensions to this framework that benefit from its fast MC computation capabilities to simulate the exposure of clinicians at their current position with respect to the patient,

along with the 3D dissemination of scattered radiation in quasi real-time. Furthermore, since we were among the first external users of the framework, we also contribute with testing, providing feedback and assisting in the documentation writing of this toolkit intended to be released soon. In this section, we first describe the proposed approaches for speeding-up our radiation simulations, along with a set of experiments carried out to evaluate its performances. All results and experiments henceforth presented were obtained using an Nvidia GeForce GTX Titan X GPU card.

4.3.1 Simulation approach

In implementations of Monte Carlo simulations on GPU, the simulation is typically divided into different kernels representing specific processes that will be performed in parallel by all the particles tracked within a voxelized geometry. Indeed, such an implementation strategy is particularly adapted to the specifications and constraints of a GPU's architecture. GGEMS is based on a similar strategy where one computing thread is used per particle, *i.e.* a thread handles a given particle from its 'birth' to its 'death' [Bert 2013]. Therefore, using thousands of processing units, thousands of particles can be simulated in parallel by executing the same code on the GPU. This is equivalent to processing in parallel a stack of particles. For an efficient implementation, particles are simulated in different stages of processing stacks. These stages are associated with particle generation, navigation, physics interaction and extraction. The simulation executes all these stages in a loop until it simulates the total number of particles specified by the user. The computational codes involved in the estimation of the physical interactions of photons with matter along with the particle tracking have been extracted from Geant 4 and adapted for the GPU environment in [GGEMS 2017]. By including the models from Geant 4, this framework is flexible in terms of the applications that can be developed with it.

In Geant 4, the simulation is initialized by defining the geometry of the simulation environment and of a set of volumes sensitive to impacting particles. However, in GGEMS the structure of the simulation has only three main components: a source, a phantom and a detector. Every element of the simulation is positioned with respect to the simulated isocenter. The source is the source of photons in the simulation, and the phantom is a voxelized volume where the materials' composition of each voxel is defined. The detector is a sensitive volume which records the information of the particles striking it. The parameters of these three elements are defined according to the application to simulate. We describe below the proposed strategies to simulate patient/staff dose and the 3D propagation of scattered radiation with GGEMS.

4.3.1.1 Patient exposure

Initially, applications making use of the GGEMS library were targeting radiotherapy procedures [Lemaréchal 2015]. As required by these applications, efficient approaches adapted to GPU architectures for simulating the particle navigation/interaction inside

voxelized structures were included in the library. Indeed, these allow to accurately simulate the dose deposited inside each voxel of a voxelized phantom, as needed to simulate the correct positioning of radioactive seeds and its effects on the surrounding tissues for radiotherapy procedures. We benefit from these features to accurately compute a patient's organs dose maps when simulating an X-ray projection.

An X-ray spectrum is generated as described in section 4.1.2 from the tube voltage and filtration conditions of the considered imaging protocol. In the simulation environment, the 3D location of the X-ray source is determined according to the imaging projection to simulate (defined as in figure 4.2) and to the tube-to-isocenter distance. A first stage of the simulation handles the particles generation and photon physics effects. A photon cone beam emits particles with energies randomly sampled from the spectrum with an aperture angle α. By altering the value of α and the tube-to-detector distance, one can modify the size of the X-ray beam impacting the patient. A patient-equivalent voxelized phantom is included, centered at the simulation's isocenter. For the experiments presented in this thesis, we use a phantom generated from a generic thoracic patient CT by transforming Hounsfield units into density values of the materials in each voxel. The resulting phantom is composed of $288 \times 241 \times 164$ voxels of 41 materials (human skeleton and organs surrounded by tissue-equivalent material), with a spacing of $1.27 \times 1.27 \times 2.0$ mm^3. In a real clinical scenario, if a patient's preoperative CT volume is available, it can be used to generate the phantom for the simulation. A second phase of the simulation concerns the transportation of the emitted particles within the voxelized patient phantom and the recording of the energies deposited on each of the phantom's voxels. From the energy deposition map, the dose to each organ can be estimated using its material properties. A flat detector in front of the phantom placed at the tube-to-detector distance is also included. Such a detector enables to measure the energies of the particles exiting the phantom in order to reconstruct the obtained 2D projection images (*e.g.* figure 4.1b).

We show in figure 4.7 several color-coded visualizations of the simulation results of a patient exposure during an X-ray image acquisition. These are generated with a volume rendering approach, by mapping the simulated energy/dose to color and transparency values through pre-defined transfer functions (see section 5.1.2.2 for more information about patient dose map rendered visualization). With such a visualization approach, one can observe clearly in 3D the exposure of the internal organs and soft tissues of a patient. Figure 4.7a shows the energy deposited in each voxel of the voxelized thoracic phantom previously described. These values are converted to dose units by dividing the energy by the mass of each voxel (computed from the volume and density of each of the voxels' materials). The results were computed for an AP X-ray image, by applying the following imaging parameters: 70 kV tube tension, 0.4 mm Al filtration and 8° of aperture angle. It can be observed in figures 4.7 that highly irradiated areas correspond to where the X-ray beam strikes the phantom's chest. Bones absorb high energy values, thus, the spine is colored in red in both figures. However, soft tissues struck by the beam absorb high dose values. This can be depicted in figure 4.7b: the lungs are rather colored in yellow and light green, while they appear as dark green in the energy map.

These patient exposure maps were obtained from a simulation of 10^8 particles. The simulation time was of 2 minutes and 15 s (with revision 420 of GGEMS), and the statistical uncertainty for the peak skin organ doses was 2 %. As opposed to the commercial systems for visualizing a patient exposure described in section 2.1.1, this approach enables to see the dose to the organs and internal structures of a patient. Furthermore, while commercial systems depend on radiation metrics approximated by the imaging device or on calibration files obtained via dose measurements, our approach relies on Monte Carlo simulations of X-ray transport, which take into account the real patient anatomy, imaging parameters and physics effects. For clinical procedures where the device positioning is not constantly changed, such visualizations could be computed in a couple of minutes, providing an insight of the current patient organ dose.

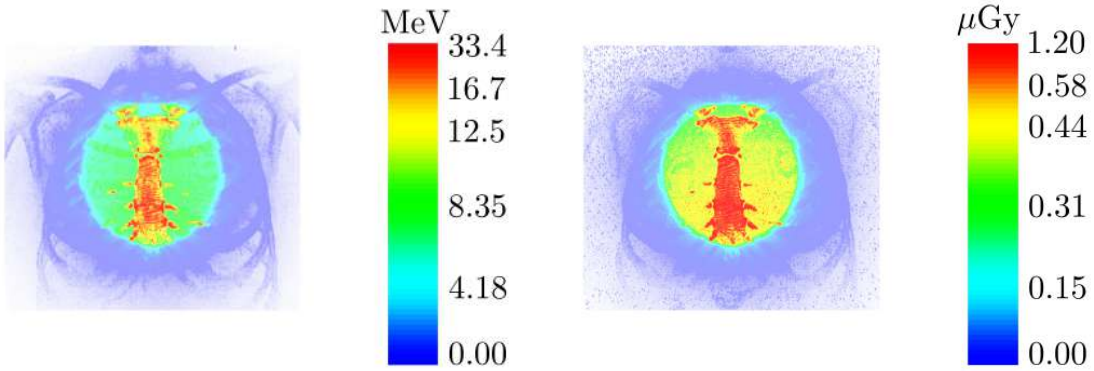

(a) Patient energy map.

(b) Patient dose map.

Figure 4.7: Patient's energy and dose maps simulated for an AP X-ray projection, 70 kV tube tension, 0.4 mm Al spectrum 8° of aperture angle.

As a consequence of the stochastic nature of Monte Carlo methods, the results have an associated statistical uncertainty σ. Yet, for sufficiently large number of simulated histories, the MC simulation can approximate the exact solution. This logically comes with a trade-off in computation time. The number of simulated particles also has an impact on the quality of the visualization. When more particles are simulated, more voxels are impacted, thus more data per voxel is recorded. We show in table 4.4, for different amounts of simulated particles, the corresponding simulation times and mean statistical uncertainty. In our experiments, 10^8 simulated particles yields an acceptable trade-off between simulation time and uncertainty. The resulting quality of the volume rendered visualization is also good (*e.g.* figures 4.7). The simulation time can be further reduced if more GPU cards are used in parallel. In clinical practice, for procedures where the device's angulation values are standard and known beforehand, a database of procedure-specific patient exposure maps can be pre-computed for default imaging parameters using a patient-specific model if available, or a generic patient-equivalent phantom otherwise. These maps could then be loaded and displayed intraoperatively for the current imaging parameters.

Table 4.4: Patient radiation exposure maps: simulation times and mean statistical uncertainty in function of the number of particles emitted.

Number of particles	**Simulation time**	**Statistical uncertainty σ (%)**
10^6	1 s 370 ms	48.6
10^7	13 s 473 ms	13.1
10^8	2 min 15 s	2.1
10^9	22 min 57 s	0.81
10^{10}	3 h 50 min	0.25

4.3.1.2 Staff exposure

Computing staff's radiation exposure requires to simulate an X-ray acquisition (as described above) and to measure the exposure of a clinician at his/her current position to the particles scattered by the patient. Particles scattered by the patient's body after each image acquisition travel with a given energy and momentum depending on their previous interactions with matter (determined by the MC simulation). Since simulating the complete trajectories and interactions of each particle emitted from the source to the patient can be time-consuming (*e.g.* table 4.4), we propose instead to save the information of the particles after they are scattered. Indeed, we can assume that the 3D dissemination and magnitude of scattered radiation will be the same if the imaging parameters and patient are not changed. Thus, there is no need to simulate the full image acquisition for each new position of a clinician. Approaches where the information about scattered particles are saved for speeding up subsequent calculations can be found in the literature [Badal 2013, Alnewaini 2017]. Usually, information such as the energy, position and direction of scattered particles are saved into what is known as phase-space files (PSF). However, since these files contain information about millions of particles, they can be significantly large in size (up to several GB), which makes them slow to load and memory-consuming. When exposure maps for different imaging parameters and patient-models have to be pre-computed, the storage of these PSF also becomes an issue. Instead, we propose an approach to characterize the "behavior" of the particles scattered by the patient for a given X-ray image acquisition and save it in a compact manner, which we define as *scatter maps*. As described below, such maps can then be rapidly loaded to compute online a clinician's exposure to the scattered particles at his/her current position in quasi real-time.

Scatter maps generation When simulating an X-ray projection, the scattered particles are projected onto a sphere of radius r, centered at the device's isocenter and enclosing the patient (as shown in figure 4.8a). Inspired by [Kläser 2008], we cluster the particles intersecting the sphere by dividing its surface into a n-sized regular polyhedron where each of its faces is considered as a bin. The number of particles intersecting each

bin (hits) along with their energies, positions and directions are stored. Instead of saving the data of millions of particles into a PSF, we propose to smartly compress the scatter information before saving it as a *scatter map*. First, by assuming that the particles clustered together have similar energies and momentum, we compute the mean energy, position and momentum per bin. Second, similarly to [Zhang 2014], we "parametrize" the dissemination of the scattered particles with a probability distribution computed using the number of hits per bin. A *scatter map* is then built by saving only the mean information along with the corresponding probability value per bin. In the end, the size of the *scatter map* file depends on the number of bins considered and not on the number of simulated particles. Therefore, a higher number of histories can be simulated (thus achieving lower statistical uncertainty), without affecting the size of the file. In a clinical application, a set of *scatter maps* can be pre-computed simultaneously to the patient exposure maps during surgery planning, by considering the different device angulations and imaging parameters that will be applied in the upcoming procedure.

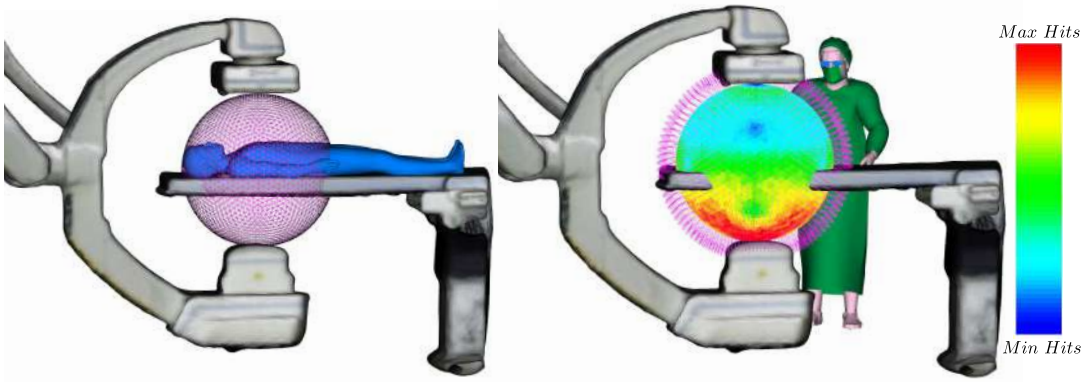

(a) Scattered particles' information saved in a spherical detector during simulation the simulation of X-ray imaging.

(b) The exposure of a clinician at his/her 3D position estimated by loading the corresponding pre-computed *scatter map*.

Figure 4.8: Generation of *scatter maps* and their use for a fast computation of a clinicians' radiation exposure.

Online computation of a clinician's exposure Tracking of the clinical staff operating near the patient can be performed with ceiling-mounted cameras as described in section 3.2.3. Such an approach enables to estimate online the 3D position of a bounding-box surrounding a tracked clinician as in [Loy Rodas 2015b], or the 3D position of the body-parts with human pose estimation methods [Kadkhodamohammadi 2017a,Cao 2017]. A clinician is represented as a voxelized slab phantom in the simulation environment. At run-time, the *scatter map* corresponding to the considered imaging parameters is loaded. Then, the pseudo-random number generator from GGEMS and the probability distribution of the *scatter map* are used to randomly sample the locations, energies and momentum of the particles to simulate. The particles are projected into the slab's surface with a ray casting approach and the clinician's exposure is approximated by

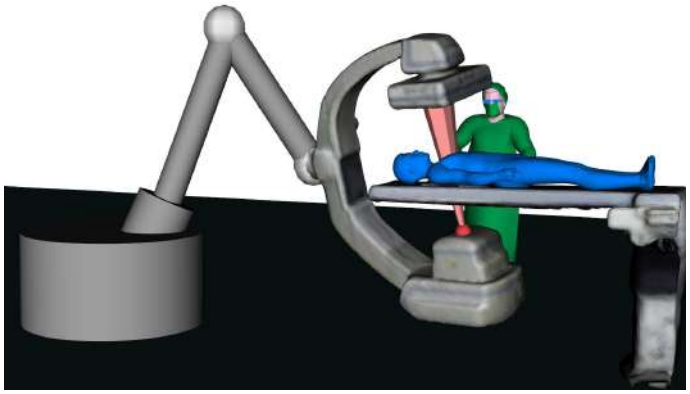

(a) X-ray device's pose for the current position of a clinician in a virtual setup.

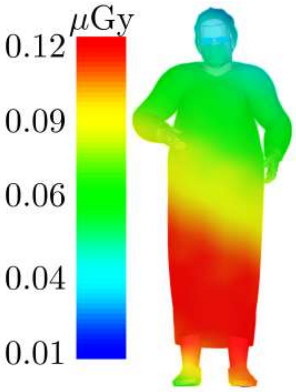

(b) Simulated dose to the clinician's body, modeled as composed by water.

Figure 4.9: Generation of *scatter maps* and their use for a fast computation of a clinicians' radiation exposure.

summing the deposited energies at each voxel. An approximation of the clinician's dose is calculated by dividing the energy values by the voxels material composition (in this case approximated as water). This process is illustrated in figure 4.8b, where we show a representation of the *scatter map* for the current device configuration and the mean direction of the particles per bin. The colors of the sphere denote the amount of particles clustered in each bin. For this configuration, a particle has a high probability to be projected under the bed, as depicted by the red/yellow bins on the lower side of the sphere. These visualizations along with the rest of the results presented in the following sections were computed by using a sphere of 500 mm of radius divided into a polyhedron with $n = 40960$ faces. Indeed, these parameters, determined empirically, yielded a good trade-off between simulation time and accuracy.

Figure 4.9 shows an example of the online computation of a clinician's exposure. First, figure 4.9a depicts a clinical scenario, where the C-arm is placed for an RAO at 10° projection, and an operator is standing 50 cm away from the table in front of the patient. The primary X-ray beam generated for this acquisition is also represented as a red cone. Then, we provide in figure 4.9b, the corresponding exposure map for the operator in this scenario. One can observe than in this case, his/her lower-body is more exposed due to backscattering. Therefore, it would be recommended for him/her to position the table mounted lead shield accordingly for protection.

Since this approach is a deterministic one, *i.e.* not based on MC techniques, it allows to compute the exposure of an operator at his/her current position in quasi real-time. However, it relies on an approximation of the behavior of scattered radiation. The effect that these approximations have on the simulation results and times are evaluated in section 4.3.2.1.

4.3.1.3 Scattered radiation propagation

The 3D propagation of scattered radiation is calculated similarly as described in section 4.2.1. When simulating an X-ray image acquisition, we place a voxelized volume in the simulation model, which is centered at the isocenter of the device and covers the space around the table. Once the simulated particles are emitted from the X-ray source, we track the path of the ones which are scattered by the patient and we keep a score of the voxels crossed in their trajectory. For each voxel, we accumulate the particles' energies which traversed it in order to obtain a 3D fluence map corresponding to the current imaging/patient parameters. To achieve this, we implemented a GPU kernel function for performing the particle navigation inside a voxelized structure efficiently. As opposed to our previous implementation on CPU, the use of a GPU architecture enables us to simulate larger voxelized grids with smaller voxels in a few minutes. These finer scattered radiation maps result in a more aesthetic visualization of the 3D dissemination of scattered radiation when applying volume rendering (see section 5.1.2).

4.3.2 Experimental validation

We evaluate our GPU-accelerated simulation framework in a twofold manner. As the patient exposure computation involves mainly the physics processes implemented in the GGEMS library and these were thoroughly validated in [Bert 2013, Lemaréchal 2015], we focus henceforth on the validation of the staff exposure and scattered radiation computation approaches. First, in order to assess the impact of the approximations we propose for a fast computation of an operator's exposure, we compare our simulations to standard methods, namely to simulations without approximations and to the use of PSF. Second, similarly to section 4.2.3, we compare our simulation results to measurements performed in an OR using dosimeters.

4.3.2.1 Clinician exposure validation

We herein evaluate the impact on simulation time and accuracy when approximating scattered radiation as *scatter maps* as proposed in section 4.3.1.2. We compare our approach to estimating an operator's exposure using a full Monte Carlo simulation, namely by simulating the complete X-ray imaging process and tracking the resulting scattered particles which impact the operator at his/her current position. As expected, this approach results in longer simulation times, yet, since no approximations are performed, it yields more accurate results. Moreover, we also compute an operator's exposure with a common approach from the literature [Badal 2013, Alnewaini 2017], where the information of the scattered particles is saved in the form of PSF. These files are pre-computed for different imaging parameters and are then loaded for computing a person's exposure at his/her current position.

First, we evaluate the simulation time and the practicality of each approach for a single set of imaging parameters and a single position of a clinician. The results were computed with the same computer and are summarized in table 4.5. For the approaches

relying on PSF and *scatter maps*, we report the time required to pre-compute each kind of file (Simulation), and the time it takes to load the pre-computed data, project the particles and compute online the clinician's exposure (Casting). We also provide, for increasing amounts of simulated particles, the respective size of a PSF and *scatter map* file per set of imaging parameters. For the full Monte Carlo method (MC in table 4.5), only one simulation time is reported since the results are obtained in a single simulation run. Relying on pre-computed phase-space files is actually equivalent to perform a full MC simulation in a two-step manner, thus, the accuracy is maintained. However, as we can observe from table 4.5, both the size (without any compression) and the computation time for each PSF increase importantly with the number of simulated particles. In our approach, since we smartly compress the scattered particles' information directly in the simulation, the size of each file remains constant for any amount of simulated particles. Indeed, the *scatter maps*' size depends only on the number of faces of the polyhedron placed around the patient during their computation. Also, since less data is loaded into the GPU, the casting process takes less time than when loading a large PSF. With all three approaches, the uncertainty in the exposure values is below 1 % when simulating 10^6 histories or more. Using our approach, the clinician exposure can be updated every 378 ms in that case. Therefore, our simulation approach enables to simulate a clinician's exposure at his/her current position at a rate of almost 3 frames-per-second. Even on GPU, a full MC simulation takes a few seconds for this task. The use of pre-computed data seems to be an appropriate approach for reaching near real-time performances for a staff dose simulation approach. Since for a clinical application it would be necessary to pre-compute patient-specific scattered particles' data for a large set of imaging protocols, the use of *scatter maps* to smartly compress these files seems to be an appropriate solution in terms of practicality and speed.

Table 4.5: Simulation times of clinician exposure with the three approaches evaluated: a full Monte Carlo simulation (MC) without approximations, with pre-computed PSF and *scatter maps*.

Particles	**MC**	**Phase-space files**			***Scatter maps***		
		Casting	Simulation	Size	Casting	Simulation	Size
10^6	3.4 s	2 s	4 s	40 MB	**378 ms**	3 s	3.1 MB
10^7	34 s	15 s	1 min 40 s	400 MB	**3 s**	41 s	3.1 MB
10^8	6 min 30 s	3 min 20 s	12 min 30 s	4.3 GB	**35 s**	7 min	3.1 MB
10^9	58 min 3 s	41 min 38 s	2 h 30 min	45 GB	**6 min 2s**	1 h 15 min	3.1 MB

Whereas *scatter maps* can be convenient in terms of speed and file size, they are based on approximations of the scattered particles' behavior. Hence, we also evaluated the loss in simulation accuracy caused by these approximations. To do so, we performed extensive simulations considering different C-arm angulations and positions of an operator with all the three approaches and compared the obtained operator's exposure values. We considered a full C-arm rotation in the LAO/RAO plane, simulating an X-ray projection every 5° rotation. For each angulation, we simulated the exposure of a virtual clinician for

a total of 16 positions on one side of the table. These positions were equally distributed in a 0.4×0.4 m^2 surface. This way, we evaluate the accuracy of the clinician's exposure computation when the X-ray source is on the same side as him/her and also when it is on the opposite side of the table. Taking the complete Monte Carlo simulation approach (with no approximations) as reference, we compute the mean relative error between the energy values obtained for each of the 1168 simulated experiments with both the PSF and our approach. These results were computed for 10^8 particles and are summarized in table 4.6. As expected, the exposure values yielded by the MC simulation and the approach using pre-computed phase space files are close. The 0.7 % difference may be explained by the different random seeds used on each simulation and by the statistical uncertainty of the simulations. Approximately, an 8 % difference in the simulation results is obtained when using *scatter maps*. Figure 4.10a shows a plot of the mean simulated energy per C-arm rotation angle computed with the three approaches. When the rotation angle is above 180° the X-ray source is on the clinician's side, thus, the exposure values are higher. Interestingly, the errors introduced by the approximations from the *scatter maps* are higher for these cases too, as depicted in the graph. Still, a mean 8 % difference is acceptable since these approximations enable a faster computation of a clinician's exposure (35 s with our approach for 10^8 particles against 3 and 6 min respectively for the PSF and MC methods).

Table 4.6: Mean relative difference of a clinician's exposure obtained with the PSF and *scatter maps* methods, compared with a full MC simulation and pre-computed PSF as references.

Method \ Reference	**Monte Carlo**	**Phase-space files**
Phase-space files	0.7 %	-
Scatter maps	8.2 %	8.0 %

4.3.2.2 Evaluation with experimental measurements

We also performed a set of dose measurements in an interventional room using an Artis Zeego robotized X-ray imaging device, a calibrated multi-RGBD camera system and a set of RaySafe wireless active personal dosimeters [RaySafe 2017] for evaluation purposes. A plexiglas phantom of $20 \times 20 \times 24$ cm^3, with 10 mm thick plexiglas walls and filled with water was irradiated under different imaging protocols. Eight dosimeters were either placed over the operating table or taped to drip rods and placed around the work area. This setup is shown in figure 4.10b. The main goal of this measurements campaign was to obtain dose data to evaluate our C-arm pose optimization approach presented in chapter 6. Therefore, the imaging protocols performed were chosen accordingly, as it is further explained in section 6.4. Indeed, the tube tension and filtration were kept constant (100 kVp and 0.4 mm Al respectively), but the C-arm projection angles were varied in the two rotation planes *i.e.* LAO/RAO and CAUD/CRAN (represented in

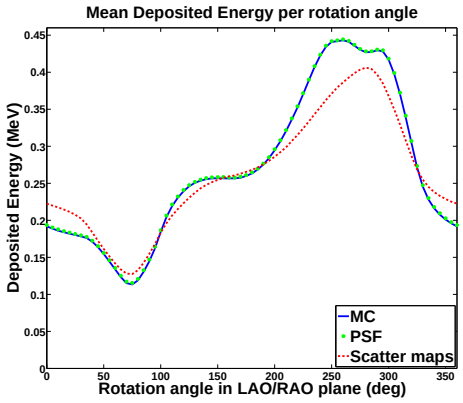

(a) Deposited energy per rotation angle computed with the three approaches: full MC simulation, pre-computing PSF and *scatter maps*.

(b) Setup for experimental validation performed at IHU Strasbourg: PA imaging projection, water-filled slab phantom and wireless dosimeters.

Figure 4.10: (Left) Results of the simulation of a clinician's energy for a full rotation of a C-arm in the LAO/RAO plane computed with a MC simulation, using pre-computed PSF or using *scatter maps*. (Right) Experimental setup for the experimental validation with measurements from dosimeters in an OR.

figure 4.2). The same experimental conditions were simulated with our GPU-accelerated approach and the results were corrected using the measurements from two calibration dosimeters. The relative errors between the simulated dose values and the ones measured by the validation dosimeters were computed to verify the accuracy of the simulated dose distribution. A total of 15 C-arm configurations were considered for this experiment. A simulation with 10^8 particles was performed for each of them, and the energy values at the dosimeters' positions could be simulated in approximately 30 s with our GPU-accelerated approach. The errors calculated using the measurements from the 6 remaining dosimeters are reported in table 4.7. The mean error obtained for all experiments was of 18.7 %. As in section 4.2.3.2, we consider this error acceptable since it is within the range of possible measurement inaccuracies from the type of dosimeters we use. Moreover, approximations in the X-ray source model in the simulation framework may introduce further errors to the results. Hence, the simulation approach presents promising performances in terms of simulation time while remaining accurate when compared to real dose measurements.

4.4 Conclusions

In this chapter, we presented two radiation simulation approaches developed during this thesis. Both of them enable to compute the 3D propagation of scattered radiation along with the patient and staff dose, by taking into account the current imaging parameters and room layout. As further explained in chapter 5, displaying the simulated dose distribution maps through augmented reality enables to provide in-situ visual feedback about the current radiation exposure in an intuitive fashion. Both radiation simulation approaches

Table 4.7: Mean simulation errors per irradiation protocol with two calibration dosimeters.

X-ray device angulation		**Error (%)**
LAO/RAO	CAUD/CRAN	
30	30	19.9
40	36	20.3
35	0	29.8
8	0	27.6
6	-10	22.1
185	0	18.6
190	7	13.8
27	29	19
37	35	20.7
88	0	14.2
98	-2	13.2
45	-25	11.8
-47	-35	14
-37	-24	16
-41	-34	19.7
Mean		**18.7**

were validated through extensive experiments performed in an interventional room using a robotized X-ray imaging device. The results have shown that the error between the simulated and measured dose values is in agreement with the intrinsic error of the dosimetric system we use, for different irradiation parameters and setups. Furthermore, both approaches have been crucial to the development of the two targeted applications of this thesis, which were discussed afore in section 1.4.2. Our GPU-accelerated approach, introduced in section 4.3, presents promising performances in terms of simulation speed and accuracy. As presented in chapter 7, such an approach has been incorporated into a radiation awareness system demonstrated in a hybrid room. Additionally, novel simulation strategies have been introduced to enable a quasi real-time simulation, as necessary for a clinical application. For instance, an intraoperative system for monitoring occupational exposure requires a fast simulation as clinicians are moving during a procedure and the system has to update accordingly the simulation model. Moreover, simulations for a large amount of varying imaging parameters and room configurations can be pre-computed fast with our approach, and the results can be conveniently compressed and saved as *scatter maps*. Such data can be used by a training system to teach about radiation exposure on standard clinical scenarios. As it is further discussed in chapter 6, our simulation approach is also well suited to be applied in an optimization loop. A cost function modeling radiation exposure can be repeatedly evaluated for many parameters and the optimization can converge to an answer in a reasonable time thanks to the fast

computation capabilities granted by our GPU-accelerated approach.

5 Intuitive visual feedback of ionizing radiation

Blessed are those who have not seen and yet have believed.
– John 20:29, The Bible

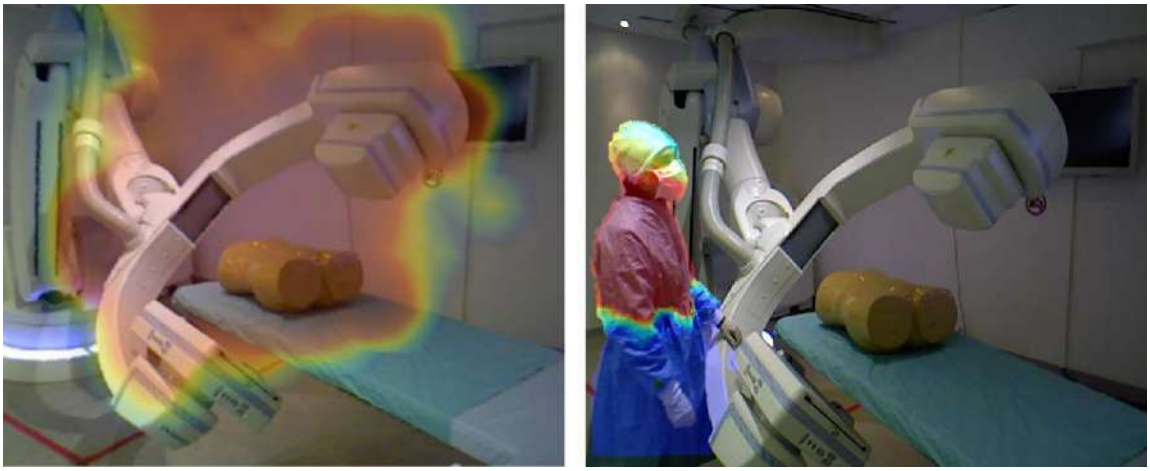

Figure 5.1: AR visualization of the 3D propagation of scattered radiation (left) and of a clinician's full-body exposure (right), during a RAO at 135° X-ray imaging projection.

Chapter Summary

5.1 Augmented reality visualization of ionizing radiation 85
5.1.1 Benefits of X-ray radiation's AR visualization 85
5.1.2 Visualization methods 86
5.1.2.1 3D propagation of scattered radiation 86
5.1.2.2 Patient exposure visualization 89
5.1.2.3 Staff exposure visualization 89
5.2 Augmented Reality visualization approaches 90
5.2.1 Ceiling-view AR visualization 91
5.2.2 Mobile AR using a hand-held screen 91
5.2.3 Mobile AR using a HoloLens 92
5.3 Conclusions 96

The invisible nature of ionizing radiation and the lack of immediate effects of exposure lead to reduced awareness and hinder the optimal use of the available protective equipment during a procedure. Radiation simulation approaches provide quantitative dose estimations that are useful for monitoring the exposure of patient and staff and/or for generating dose statistics and reports. However, the impact they can have on increasing awareness to radiation depends on how these results are presented to the clinical staff. In this thesis we propose to provide an intuitive visual feedback of the simulated radiation exposure corresponding to the current room conditions by means of augmented reality. Through AR, ionizing radiation can be rendered visible, which can have a major visual impact on the person looking at it. This can contribute not only to increase awareness to ionizing radiation but also to improve the understanding about its behavior. For instance, the use of AR can provide a clear understanding of the 3D dissemination of scattered radiation and show intuitively how highly irradiated areas on and around the patient change according to the imaging device's positioning. To the best of our knowledge, we were the first to demonstrate an AR visualization system for improving radiation safety in [Loy Rodas 2014, Loy Rodas 2015b].

We dedicate this chapter to describing our approaches for providing intuitive visualizations of X-ray radiation. We begin by discussing in section 5.1.1 the benefits and motivations behind the use of AR visualization. Then, in section 5.1.2, we introduce the different visualization modes that we propose. The next sections describe different AR approaches that were investigated. Indeed, AR visualization is achieved by overlaying virtual objects over images of the world. For our application, the appearance and colors of these virtual objects should convey relevant information concerning the current behavior of ionizing radiation and the dose values. Hence, we have explored different alternatives concerning the origin of the support images employed for the visualization. First, we have made use of the stream of images from our ceiling-mounted RGBD cameras to provide a

global visualization of the OR from a fixed point-of-view. This approach, presented in section 5.2.1, is the one we implemented in our radiation awareness prototype system demonstrated in an interventional room (see section 7.1). Second, we have proposed an approach relying on a hand-held screen to display directly in the user's view information related to radiation safety in a mobile AR manner. This is further discussed in section 5.2.2. Third, we have also worked with a commercial optical see-through head-mounted display (OST-HMD), as a different mean to show relevant information regarding radiation exposure to the user. This approach, presented in [Loy Rodas 2018a], is further discussed in section 5.2.3. For each of the presented visualizations, we provide several examples enabling a qualitative assessment of their clinical relevance for our application.

5.1 Augmented reality visualization of ionizing radiation

The last decades have seen numerous medical augmented reality systems looking to facilitate the visualization and integration of all the information available during a procedure by displaying it intuitively to the user. Nowadays, AR medical environments have successfully been applied for diagnosis [Berlage 1997], interventional planning and surgical navigation [Feuerstein 2008], and for in-situ visualization of intraoperative imaging data [Navab 2010, Chen 2013]. In this thesis, we propose to make use of AR for a different kind of medical application besides assisting the surgeon in the immediate execution of a procedure. We refer to the use of AR to increase awareness to radiation and to reduce the exposure to ionizing radiation of clinical staff and patient during surgical procedures involving X-rays. We discuss below several benefits of using AR for this purpose, followed by a description of the three modes of visualization we propose.

5.1.1 Benefits of X-ray radiation's AR visualization

Studies evaluating radiation awareness have reported a considerable proportion of unnecessary exposure and risk underestimation resulting from a lack of awareness and poor knowledge of radiation behavior [Katz 2017b]. This is partially due to the invisible nature and complex behavior of ionizing radiation. However, appropriate feedback of the current distribution of scattered radiation can increase the awareness of clinical staff and reduce the risk of overexposure. As described in section 2.2.2, several computer-based systems combining radiation simulation and visualizations of radiation in virtual environments have been developed to cope with these challenges [Bott 2009, Ladikos 2010, Badal 2013]. Following this line, we apply AR as a mean to render intraoperative ionizing radiation visible. AR enables to provide the user with an *in-situ* visual feedback about the current radiation diffusion in an intuitive and non-disruptive fashion. We provide two examples of such a visualization in figure 5.1 for an RAO at 135° angulation of a C-arm. In this configuration, the X-ray source is positioned over the bed (overcouch). We show in the left figure a visualization of the 3D distribution of scattered radiation. Such a direct visualization enables a clear understanding of the highly irradiated areas around the operating table and can help optimizing the use of protective measures to avoid overexposure.

In the right image, we show an example of an AR visualization of the full-body radiation exposure of an attendee. The highest exposure to scattered radiation can be depicted in the person's upper-body, especially in the chest and thyroid. As reported in the literature, overcouch configurations can generate up to six times more exposure to highly sensitive body-parts such as thyroid and head, and should be avoided [Koukorava 2011]. This kind of visualizations provide an intuitive way to apprehend an otherwise purely theoretical safety recommendation. Also, by looking at any of these two images, a user would be more inclined to place a ceiling-mounted shielding screen in front of his/her chest for a better protection.

Standard radiation protection reports teach about the behavior of irradiation fields with isodose or floor graphs. We provided in figure 1.3 (chapter 1) an example of the kind of images one can find in the literature for learning about the propagation of scattered radiation for different clinical conditions. However, these 2D figures can severely change when any of the factors affecting radiation propagation is modified (see section 1.2.2). The examination's complexity makes it also difficult for clinicians to keep such figures in mind and to be aware of their exposure while they are busy performing a surgical task. An intraoperative system capable of estimating and displaying the propagation of scattered radiation for the current OR configuration in an intuitive and non-disruptive fashion can therefore importantly increase the awareness of physicians to radiation risks. This could also be particularly interesting for novices since the system could also be used as a teaching tool to impart knowledge regarding scattered radiation behavior.

5.1.2 Visualization methods

AR visualization facilitates the understanding of the behavior of ionizing radiation by making its propagation visible to the user's eyes. Since such a behavior is heavily affected by various factors, the different visualizations must be updated according to the current imaging and patient parameters. As described in chapter 4, parameters such as the X-ray tube voltage, the patient model or the positions of clinicians are input to our radiation simulation approach. This way, the generated visualizations can also convey information about the effects that variations in the imaging parameters have on radiation exposure. As explained in section 3.1.3, we register our multi-RGBD camera system to a global room reference frame placed at a known position over the operating table. Such a reference frame is used for correctly positioning virtual elements with respect to the imaging device. We present below three visualization methods applied to intuitively display the results from the simulations to a user.

5.1.2.1 3D propagation of scattered radiation

It concerns the visualization of the 3D dissemination and intensity of the radiation scattered by the patient during an X-ray image acquisition. As described in chapter 4, we first compute 3D radiation distribution maps by recording the energy deposited at each voxel of a 3D grid placed around the patient when simulating an X-ray projection.

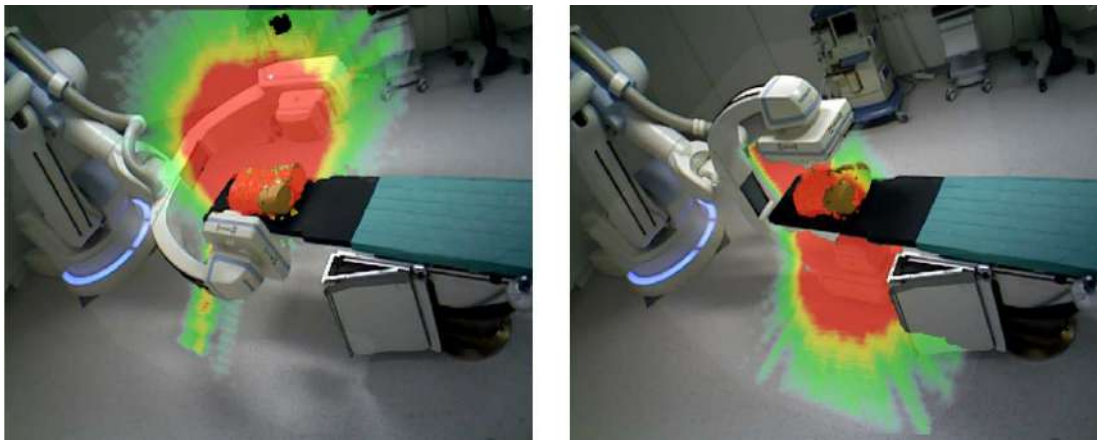

Figure 5.2: AR visualization of the 3D diffusion of scattered radiation for two imaging projections: an RAO at 120° projection (left) and a PA projection (right). Red indicates higher dose.

Next, color and transparency transfer functions are applied to map the simulated dose values inside each voxel element into RGB and opacity values. The obtained colored volume is then visualized with a volume rendering approach. We provide an example of this visualization in figure 5.2, showing rendered 3D isosurfaces overlaid over images from ceiling-mounted cameras for two different C-arm angulations. Depth data from the cameras is used to detect and filter out occlusions in the visualization for a consistent display of the virtual elements. Such a visualization provides a clear understanding of the 3D dissemination of scattered radiation and shows intuitively how highly irradiated areas around the patient change according to the device's positioning. As explained in section 1.2.2, the highest rate of scatter is always produced in the entrance surface side of the patient, namely closest to the X-ray source (*i.e.* backscattering effect) [Carinou 2011]. In the left image, which corresponds to a RAO at 120° projection, most of the scatter propagates above the table. In the right one, corresponding to an undercouch configuration, the scatter is mostly diffused under the bed, showing why undercouch configurations are preferred in clinical practice. Additionally, these visualizations suggest that standing without protection close to the X-ray source should be avoided, which also matches the radiation safety recommendations from the literature [Koukorava 2011].

In case the poses of the table- or the ceiling-suspended lead screens are known, they can be included in the simulation model and the effect they have on stopping scattered radiation can be visualized. Examples illustrating the use of protective shields for protection against scattered radiation are provided in figures 5.3 and 5.4. The 3D dose maps for these figures were computed by manually positioning the lead shields in the simulation, according to their positions in the scenarios depicted. These maps are then displayed by applying the aforedescribed AR visualization approach. In figure 5.3, one can observe for two over-couch C-arm configurations (LAO at 90° and AP), how the ceiling-suspended shields stop the propagation of scattered radiation, which would

otherwise be directed to the person's upper-body. The shape of the scatter field is also affected since X-ray particles are refracted by the shields. For both angulations depicted in figure 5.3, radiation is rather scattered towards the ceiling of the room when the shields are present. We also show an example of this visualization on images captured with our camera setup installed at Strasbourg's University Hospital IR department. Figure 5.4 shows the scattered radiation that would be generated in the scenarios depicted. One can also observe how the use of table- and ceiling-suspended shields blocks the scatter in the right image, when compared to a scenario without shielding (left image).

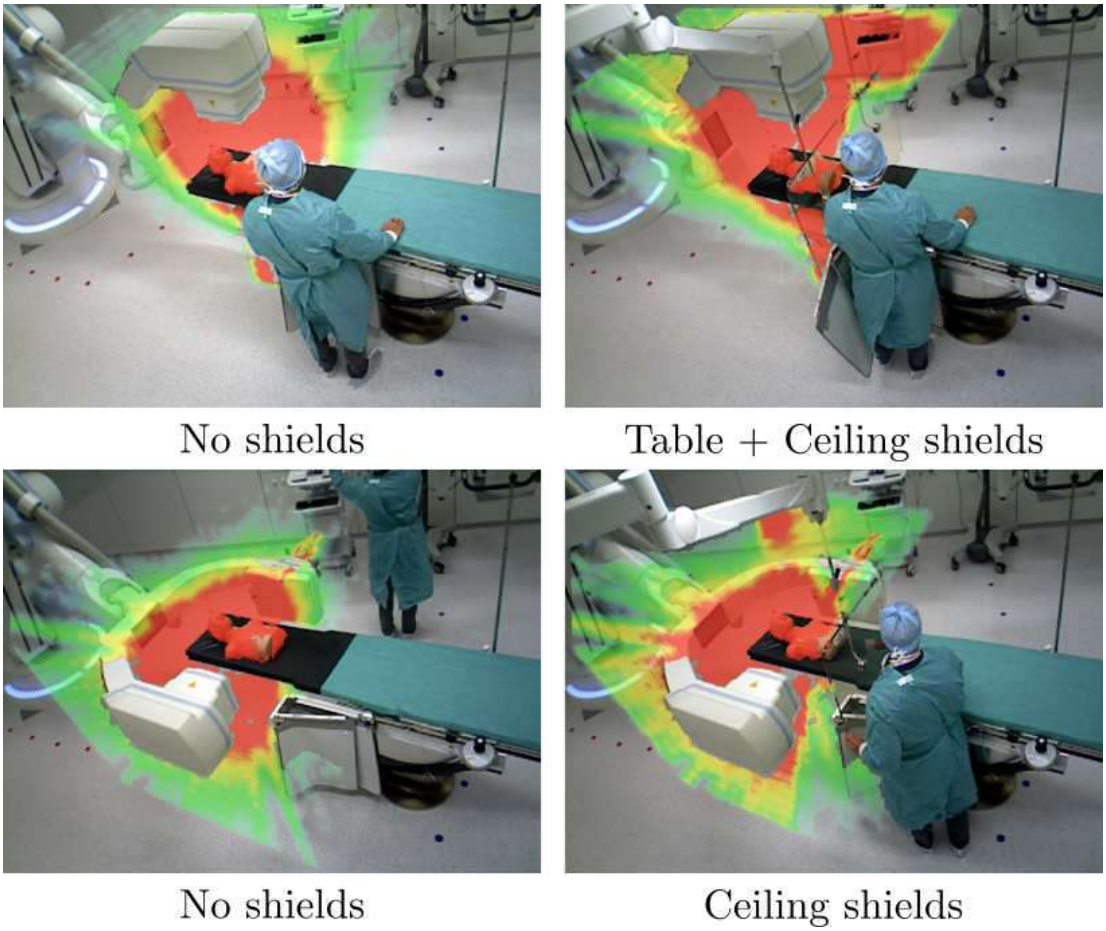

Figure 5.3: AR visualization of the propagation/intensities of scattered radiation for two C-arm angulations (AP and LAO at 90°), illustrating the effect of table- and ceiling-suspended protective shields for radiation protection.

AR visualization provides useful knowledge about the variations of the 3D distribution of the highly irradiated areas for the current C-arm configuration and room layout. Hence, it can have a strong impact on increasing clinicians' understanding and awareness of scattered radiation. It can also help trainees to learn intuitively about radiation's diffusion effects and about the best safety practices. Our collaborating clinicians have shown a strong interest in such visualizations because of the immediate visual feedback about

high-risk areas they grant and also since most of them have never seen scattered radiation in 3D before.

Figure 5.4: AR visualization overlaid a posteriori for visualization purposes, to show the scattered radiation that would be generated if the X-ray device was used in such a situation: no lead protective shields (left) and with a ceiling-suspended shield (right) (Strasbourg's University Hospital).

5.1.2.2 Patient exposure visualization

The patient exposure maps obtained from our radiation simulation approach contain clinically relevant information such as the dose to the skin and to each organ deposited after each irradiation. Similarly to the previous visualization mode, we apply volume rendering to show a patient's 3D dose map in a virtual environment. As shown in figure 5.5a, this visualization enables to see the trajectory of the X-ray primary beam inside a patient's internal structures and also provides information about the dose deposited in each organ/tissue. We also apply color and opacity transfer functions to color the surface of a generic patient model using the dose values simulated at the patient' skin. This permits to see the location of the peak skin dose for the current C-arm angulation. The example provided in figure 5.5a was simulated for an RAO at 135° radiography. We can observe the left side of the model's chest is colored in red, indicating higher exposure in the areas corresponding to the X-ray beam's entry point. In clinical practice, this kind of visualizations can be useful to avoid overexposing certain skin areas and/or to sensitize clinicians about the ongoing patient's exposure. The irradiated patient's model can also be shown in an AR manner over an image of the operating scene. This is achieved by registering the model to the viewer's point-of-view and projecting it accordingly in 2D. We show an example of this visualization in figure 5.5b, corresponding to a visualization with our mobile AR approach described in section 5.2.2.

5.1.2.3 Staff exposure visualization

This visualization mode relies on the clinician tracking approaches described earlier in section 3.2.3. These approaches are applied to track the position of clinical staff in the

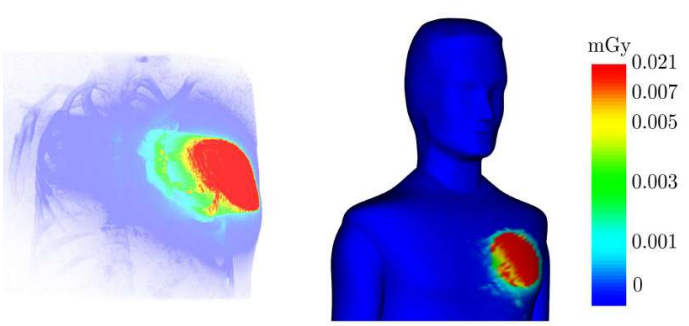

(a) Organs and peak skin dose respectively visualized over a patient's CT and over a generic model.

(b) AR visualization of a patient's skin exposure.

Figure 5.5: Visualization of a patient radiation exposure (to skin and organs) on a virtual environment (left) or through a mobile AR (right), for an RAO at 135° C-arm projection.

room, to then compute and display an estimation of the current full-body radiation exposure of each attendee. The points corresponding to the tracked person's shape are colored according to the simulated exposure value at each of its 3D locations. We discussed earlier an example of this visualization shown in figure 5.1. Two additional examples of the staff exposure visualized using AR are provided in figure 5.6. The left image corresponds to a mobile AR visualization, where the C-arm is positioned for a PA projection. Therefore, the clinician's lower-body is more exposed since radiation is majorly diffused under the operating table (*i.e.* backscattering effect). The right image is obtained by coloring the clinicians' shapes in the images' stream from the ceiling-mounted cameras. In this case, the C-arm is positioned for an AP projection and it is the clinicians' upper-body which is the most exposed. Thus, this kind of visualization enables to see clearly how the highest irradiated parts of the body change according to the position of the person with respect to the source of scatter and to the orientation of the imaging device. Moreover, while dosimeters are limited to measure the dose absorbed at the point of placement, this visualization is able to provide a full picture of the complete body exposure.

5.2 Augmented Reality visualization approaches

As clinicians can already be overwhelmed by the large amount of data and information available during a surgery, key questions to be asked are what would be the best way to present the information for radiation safety while least affecting the clinical workflow, and to whom it should be shown (operators, assistant personnel, radiation protection officers ...). As an attempt to answer the first of these questions, we have explored three different AR visualization approaches presented in this section. Since precision is not a critical factor for our clinical application, we do not present results of an evaluation[1]

[1] An extensive quantitative evaluation of our marker-less mobile AR approach (section 5.2.2) was performed and is presented in appendix C.

Figure 5.6: (Left) Mobile AR visualization of a clinician's exposure during a PA projection. (Right) Ceiling-view AR visualization of the exposure of two clinicians for an AP projection.

of the registration accuracy of the virtual elements overlaid in the images. We rather provide qualitative results to illustrate the potential in improving radiation safety of these visualizations.

5.2.1 Ceiling-view AR visualization

In this visualization approach, the virtual elements are overlaid over the color images from the RGBD cameras mounted to the ceiling. The depth maps from the camera are used to filter out occlusions in the visualization for a proper display of the virtual information. Any of the three visualization modes described in section 5.1.2 can be displayed with this approach on a screen inside the OR. This enables clinicians or trainees (if the visualizations are used for training purposes) to have an overview of the current propagation/intensity of radiation in the room and also to select the viewpoint from where to look at the scene. Moreover, this approach is convenient for an intraoperative application since it does not require a user to manipulate the screen or the device used to show the augmented images. Figures 5.2, 5.4 and 5.6 (right) are examples of the ceiling-view AR visualization.

5.2.2 Mobile AR using a hand-held screen

We also developed an approach[2] where a hand-held screen is used to display directly in the user's view information related to radiation safety in a mobile augmented reality manner. As shown in figure 5.7, this enables the user to move freely around the table and to see the 3D propagation of radiation, the medical staff's exposure and/or the doses deposited on the patient's surface "as seen through her/his own eyes". To achieve this, we attached an RGBD camera to the screen and proposed a marker-less camera tracking/relocalization

[2]I thank Dr. Fernando Barrera for collaborating with me in the development and evaluation of our mobile AR approach.

approach. Since in this chapter we focus on visualization approaches to improve radiation safety, we present the technical details of the tracking/relocalization pipeline in appendix C.2. Still, we provide below a brief description of this AR approach below.

Our approach computes the pose of the camera attached to the screen with respect to the global room coordinate system at each time step. Instead of using markers, we propose to track the observer's viewpoint with an approach relying on the use of multiple RGBD cameras, combining equipment detection for tracking initialization with a KinectFusion-like approach [Newcombe 2011] for frame-to-frame tracking. We use two of the ceiling-mounted cameras from our setup described in chapter 3 and a third one which is attached to the hand-held screen. The ceiling cameras keep an updated model of the room's layout, which is applied to exploit context information and improve the relocalization procedure. Our approach allows the system to recover from tracking failure caused by vast motion or changes in the scene just by looking at an equipment. Also, it enables the user to benefit from a large AR visualization area. We performed an extensive evaluation of our camera relocalization approach in [Loy Rodas 2017a], with a multi-camera dataset generated inside an operating room and containing ground-truth poses of the hand-held screen. The results of such an evaluation can be found in appendix C.4. To the best of our knowledge, such a dataset is the first multi-RGBD camera dataset recorded in an OR with a robotized X-ray imaging device for evaluation of SLAM/AR systems. It includes a wide variety of sequences with different scene configurations, occlusions, motion in the scene and abrupt viewpoint changes and it is representative of the challenges a tracking system could encounter in a medical environment. A complete description of this dataset[3] is provided in appendix B.

We show in figures 5.1, 5.5b and 5.6 (left) qualitative results of the different visualization modes displayed through a hand-held screen. Visualizing the patient's skin dose with this approach is more convenient than through the ceiling views since it allows the user to stand close to the patient/phantom and to benefit of a detailed visualization of the skin dose values. Furthermore, enabling the user to move freely around the operating table and see these kinds of visualizations from the perspective of a hand-held screen can be useful specially for radiation safety training sessions. Trainees can learn in an intuitive way about the effects that different orientations of the imaging device have on the diffusion of scattered radiation or can visualize the exposure of the colleague standing next to them (*e.g.* figure 5.6). For an intraoperative application, the hand-held screen can be replaced with a screen fixed to an articulated arm. An operator could then adjust the visualization perspective by displacing the articulated arm.

5.2.3 Mobile AR using a HoloLens

The development of robust algorithms for facing the challenges encountered by mobile AR technologies (indoor mapping, tracking, relocalization...), along with the advances in optics designs and embedded computational power have enabled the advent of commercial

[3]The xawAR16 dataset has been made publicly available online and can be found here: http://camma.u-strasbg.fr/xawar16-dataset

Figure 5.7: Mobile AR visualization for radiation awareness using a hand-held screen. The user visualizes the propagation of scattered radiation for the current device configuration directly in his own view.

head-mounted displays (HMD) suitable for medical applications. Indeed, the attempts to deploy HMD in the operating room have been under continuous investigation for years. Yet, nowadays we see more off-the-shelf devices with an increasing number of applications in clinical scenarios. A recent study showed that displays such as Microsoft's HoloLens are now suitable enough in terms of contrast perception, task load and frame rate, for mixed reality surgical interventions [Qian 2017]. Furthermore, another commercial device, the ODG-R7, has been used at Johns Hopkins Hospital to augment fluoroscopic images directly into the surgeon's view for some types of orthopedics procedures [Qian 2017].

An optical see-through head-mounted display (OST-HMD) is a kind of HMD capable of displaying virtual elements over an unhindered view of the scene. This is particularly adapted to clinical scenarios where even if the display malfunctions, a direct vision of reality would not be affected allowing the surgeon to safely continue the operation. We have investigated the use of an OST-HMD, namely Microsoft's HoloLens, to display information related to radiation safety to the user[4]. As opposed to a visualization over a screen (static or mobile) where the user's attention must switch back and forth between the scene and the screen, here the virtual elements are visually aligned to the scene when the user is wearing the device.

[4]We acknowledge Pamir Ghimire for developing during an internship the applications herein presented.

We have implemented the three visualization modes described in section 5.1.2 as HoloLens applications. To visualize virtual information related to the room context, an initial registration of the OST-HMD is achieved by placing a marker at a known position in the scene at detecting it in the application. Figure 5.8a shows a user wearing a HoloLens in an operating room to visualize radiation safety information. We show in figure 5.8b what the user is seeing through the HoloLens in this scenario, namely a phantom model colored according to the skin dose values and registered over the real phantom in the table. In this patient exposure application, the user can select the model to be displayed from a database simulated for a large set of imaging parameters and C-arm angulations. Similarly, an application enabling the visualization of volume rendered scattered radiation maps was implemented. An example is shown in figure 5.8c. The user also selects from a database of pre-computed 3D radiation maps the one corresponding to the current C-arm angulation. For a third application targeting the visualization of staff body-part exposure, we rely on a wireless communication between the HoloLens and a computer streaming/processing the images from our ceiling-mounted multi-RGBD camera setup. The current pose of an operator is detected on one of the ceiling cameras with the real-time human pose estimation approach described in section 3.2.3. The pose information is then transmitted to the device and a colored skeleton is overlaid over the tracked person in the HoloLens view. A short sequence of qualitative results of this visualization is shown in figures 5.9. The person seen in figure 5.9a is a few steps away from the irradiated area and his skeleton is mostly colored in blue. However, in figure 5.9b, the person is closer to the patient and his right arm is positioned directly in the X-ray primary beam's path. One can observe how the exposed parts are colored in red in the skeleton displayed by the HoloLens (indicating higher exposure), while the rest of the body remains blue.

An OST-HMD can be a useful tool for teaching radiation safety in an engaging, game-like and risk-free learning environment. With the aforementioned visualization approaches, teaching can be performed in real clinical conditions inside an OR. However, the use of an HMD also enables to train anywhere (hospital, school or even at home). Therefore, we also worked on Virtual Reality (VR) applications enabling to show virtual color-coded radiation safety information using a HoloLens, that a user can use for learning at any location. First, a virtual surgical scene composed by models of the X-ray imaging device, patient and clinicians, is displayed. Then, the user interacts with the scene to set the C-arm angulation and imaging parameters. Virtual patient and clinicians' models colored according to their ongoing exposure levels or the 3D propagation of scattered radiation for the current scene configuration are shown. Such models are pre-computed for a large set of imaging parameters with our radiation simulation approach. We show in figure 5.10 visualization examples of this VR training application. In figure 5.10a one can observe a virtual C-arm positioned for a PA projection. A clinician model in the scene is colored in red mainly in his lower-body, showing that radiation is being scattered under the table in this configuration. Figure 5.10b shows a visualization of irradiated virtual patient models: the user can select different imaging parameters (aperture angles,

(a) User wearing a HoloLens inside an experimental OR at IHU Strasbourg.

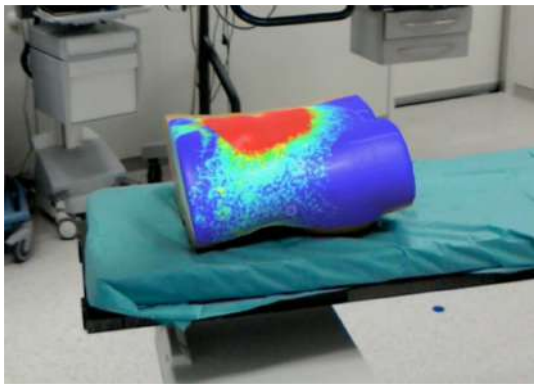

(b) Visualization of a phantom's skin exposure as seen through a HoloLens.

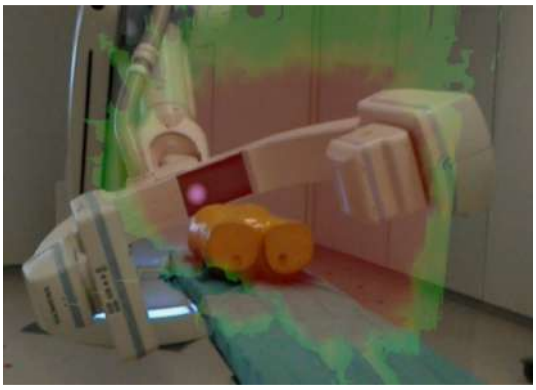

(c) Visualization of the 3D propagation of scattered radiation.

Figure 5.8: Using Microsoft's HoloLens to display radiation exposure information.

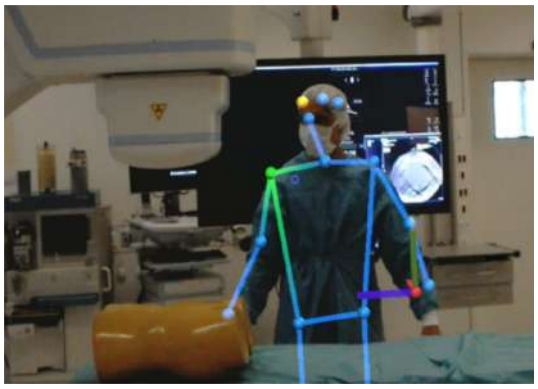

(a) The person's exposure is low (blue skeleton) when standing a few steps away from the patient.

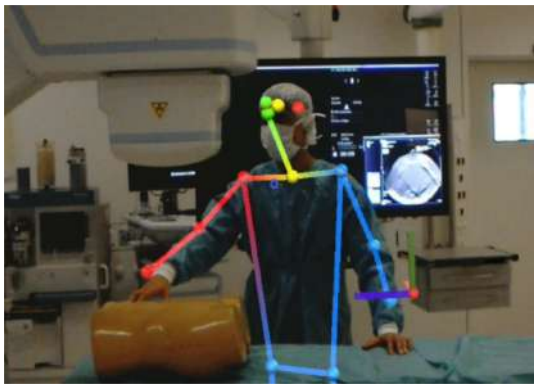

(b) The person's right side of the body is highly irradiated (red skeleton) when approaching the patient.

Figure 5.9: HoloLens visualization of a clinician's body-part exposure: the person's pose is computed in images from a ceiling-camera and transmitted wirelessly.

tube voltage, filtration...) and the corresponding skin dose is shown color-coded over the model's surface. These VR radiation safety training applications provide an immediate feedback to maximize learning about the effects that altering imaging parameters can have on radiation exposure.

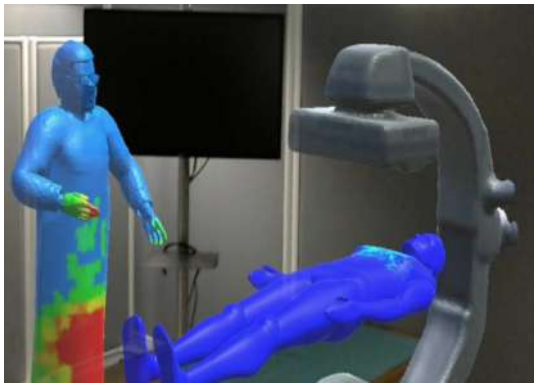

(a) A virtual C-arm (PA projection) is shown: the clinician and patient models are colored according to their current exposure.

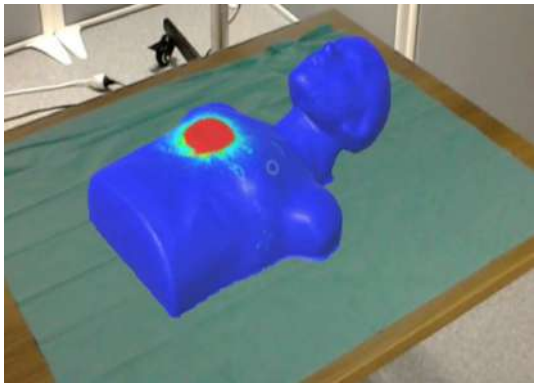

(b) Visualization of an irradiated virtual patient model: the position of the peak skin dose values for an AP projection are visible.

Figure 5.10: VR radiation training application: a virtual interventional scene is displayed to the user with information related to radiation safety through a HoloLens for learning purposes.

HMDs are valuable tools for medical AR applications and are starting to make their way into the operating theater. We have investigated the use of a HoloLens to display information related to radiation safety to the user[5]. While such a device may be too heavy for a clinician to wear during a long procedure (579g as reported in [Qian 2017]), it can still be used as a tool to teach radiation safety to trainees. Other lighter commercial HMD devices such as the ODG-R7 or Moverio's BT-200 are available which may be more adapted for intraoperative usage. Furthermore, since protective eyewear is commonly used in interventional radiology/cardiology procedures, a light OST-HMD could be designed in the future specifically to simultaneously protect the eyes while also providing an enhanced AR visualization for radiation awareness.

5.3 Conclusions

We have presented in this chapter approaches for improving radiation safety by making ionizing radiation visible through different visualization modes. These approaches rely on the multi-camera setup and the tracking/registration methods described in chapter 3, and also on the radiation simulation approaches presented in chapter 4. Through AR, a user can visualize the current patient and staff dose, along with the 3D distribution and intensity of scattered radiation. Intraoperatively, this can contribute to increase radiation

[5]A video of our applications for radiation safety training using a HoloLens can be found at: https://youtu.be/lflbEWC5VsA.

awareness and reduce overexposure risks for both patients and staff. Also, clinicians can adapt their positioning and the disposition of the protective equipment with the provided visual feedback. Preoperatively, it has the potential to be applied as an intuitive training tool to teach about radiation behavior and about the best safety practices. Besides AR visualization, other means to provide feedback about radiation exposure such as light patterns projected on the floor, holograms or acoustic signals could be envisaged. The technical feasibility and smooth integration into the clinical workflow were the criteria we considered in our work to choose visual feedback as the more adapted solution for a radiation awareness system.

Moreover, a key question we could ask ourselves is to which actor involved in the procedure should the visualizations be addressed to. Indeed, they could either be shown directly to clinicians/surgeons, so they can adapt their positioning and/or the positioning of the room shielding to better protect themselves during the execution of fluoroscopy-guided gestures. Also, since clinicians may be busy performing the procedure at hand, the visualizations could be displayed only to radiographers who are in charge of maneuvering the X-ray imaging device. Then, they could make suggestions to optimize radiation protection during the procedure or adjustments to the imaging device configuration. In the same way, recordings of procedures with radiation information overlaid in an AR manner could be examined postoperatively by the hospital's radiation safety officers. This way, they could identify steps of the surgery where potential risks of overexposure occurred. The use of AR to provide feedback about ionizing radiation opens up possibilities for several clinical applications. We discuss more about such potential applications in section 7.2.

6 Optimization of an X-ray imaging device's pose

The day before something is truly a breakthrough, it's a crazy idea.
– Peter Diamandis

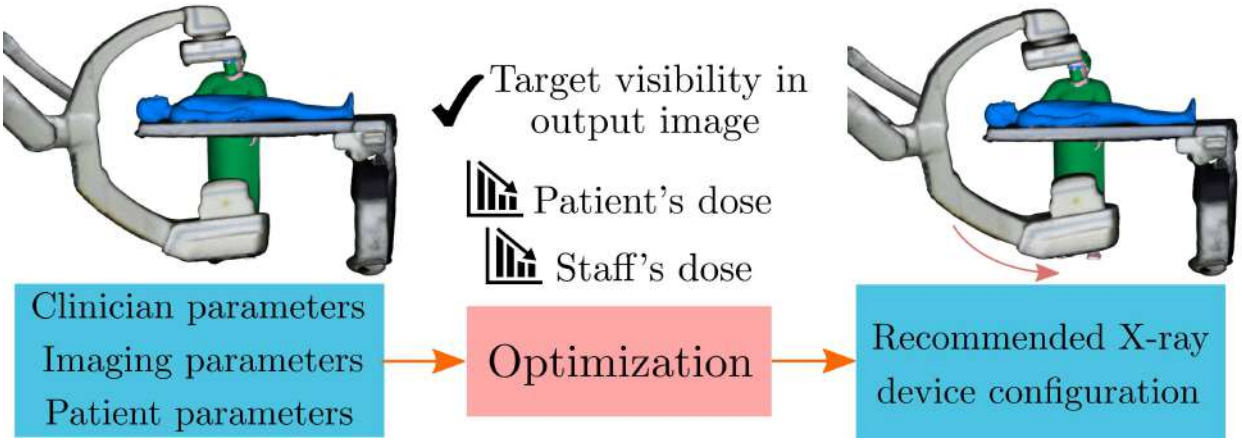

Figure 6.1: X-ray imaging device's pose optimization concept: from an initial configuration, considering clinician, imaging and patient parameters, a recommended device's pose lowering patient/staff radiation exposure and maintaining the visibility of the targeted anatomical structure in the output image is computed through an optimization loop.

Chapter Summary

6.1 C-arm positioning assistance . . . 101
6.1.1 Context . . . 101
6.1.2 Related work . . . 102
6.2 Imaging device's pose optimization . . . 103
6.2.1 Problem statement . . . 104
6.2.2 Fast computation of cost function . . . 105
6.2.2.1 Patient exposure term v . . . 106
6.2.2.2 Clinical staff exposure term h . . . 106
6.2.3 Optimization approach . . . 107
6.2.4 Imaging device's re-positioning in clinical application . . . 107
6.3 Experiments in a simulated environment . . . 109
6.3.1 Experimental setup . . . 110
6.3.2 Optimization algorithm evaluation . . . 111
6.3.3 Cost function weights trade-off analysis . . . 113
6.3.4 Evaluation of the cost function computation approach . . . 115
6.4 Evaluation with dose measurements . . . 117
6.4.1 Experimental setup . . . 117
6.4.2 Evaluation results . . . 119
6.5 Discussion and conclusions . . . 120

As discussed in section 2.2, one can find in the literature several systems for assessing and/or decreasing medical ionizing radiation either in a passive or an active manner. Reducing radiation exposure in a passive way can be achieved by improving medical staff awareness and/or the understanding of radiation propagation. Lowering the doses by having an actual influence on the imaging process is considered as an active way to achieve it. Up until now, we have presented approaches using cameras and radiation simulations to provide intuitive visual feedback about radiation behavior, with the aim of increasing awareness and improving radiation safety. Now, in this chapter, we investigate a new approach aiming to reduce radiation dose by having an *active* influence on the X-ray imaging device configuration. Our concept was first presented in [Loy Rodas 2017b] and is summarized in figure 6.1. Such an approach focuses on the optimization of a C-arm's pose for recommending a configuration which minimizes the dose to both patient and clinical staff, while also maintaining the visibility of the targeted anatomical structure in the output image. This is a complex problem where several factors must be considered (patient dose, staff dose, X-ray image quality, clinical workflow, C-arm kinematics...). Some of these factors can even be inherently conflicting with one another and this hinders the finding of an optimal solution. We herein propose an approach to model such a complex problem and approximations to make it computationally tractable.

In this chapter, we first motivate the need for C-arm maneuvering assistance systems in section 6.1 and present several related works from the literature (since this topic was not addressed in the Related Work chapter). Then, in 6.2, we describe our pose optimization approach and our modeling of this problem as the minimization of a cost function. In section 6.3, we present a set of experiments performed on simulated clinical setups for evaluating the potential and the limitations of the proposed approach. An evaluation with real dose measurements is then described in section 6.4. Finally, the conclusions of this chapter are presented in 6.5.

6.1 C-arm positioning assistance

6.1.1 Context

Last decades have witnessed significant developments in medical robotics and imaging systems. These were driven by a combination of technological improvements, advances in medical imaging and an increase in the surgeon/patient acceptance of robotized devices within the OR [Beasley 2012]. Minimally invasive procedures are now routinely performed thanks to the integration of such devices into the interventional suite. Despite the numerous benefits of MIS (see section 1.1.1), the exposure to harmful ionizing radiation still remains an issue in procedures employing X-ray based medical imaging systems. The adverse effects of radiation exposure, reviewed in section 1.2, are a major concern for health-care providers. Substantial efforts are directed towards improving the current radiation protection practices, albeit further actions to *actively* reduce exposure in the context of the procedure should be taken.

Particularly, fluoroscopy-guided interventions generate the highest radiation exposure to clinicians [Roguin 2013]. These procedures are generally performed using mobile or robotized angiographic C-arms, which can be seen as a C-shaped end-effector (X-ray source and flat detector) mounted at the end of a kinematic chain. Such a known articulated construction is exploited for positioning the X-ray source and freely acquire images of a patient from different projection angles and planes. Also, in the case of robotized C-arms, it allows to program complex trajectories in order to generate CT-like 3D-images. The maneuvering of a mobile (or robotic) C-arm into the surgeon's desired position is performed today in an open-loop manner, where the aim is to acquire the right picture for navigation or for therapy delivery [Fallavollita 2014]. Moving the C-arm into the best viewing projection is sometimes based on a mental mapping to pre-operative data, which can be complex to achieve. Moreover, manually maneuvering the C-arm can also be difficult due to the complex kinematic chain defining mobile/robotic C-arms and the complexity to find the best viewing projection in regard to the patient's anatomy. All these factors can lead to the acquisition of unnecessary images and thereby to higher radiation exposure to patient and medical staff [Navab 2006].

Whereas the imaging device's positioning is performed today by the operator in an open-loop manner and hence requires time, skill and additional radiation, the integrated C-arm kinematic chain can also be exploited to achieve a semi-automatic re-positioning.

Therefore, we propose to take advantage of these robotic capabilities to design an approach to optimize the pose of an angiographic C-arm for imaging a targeted anatomical structure, while simultaneously reducing the exposure to ionizing radiation of both patient and staff.

6.1.2 Related work

Several systems providing automatic assistance to operators in the positioning of angiographic C-arms can be found in the literature [Navab 2006, Wang 2012, Wang 2014, Fallavollita 2014]. [Navab 2006] presents an approach for speeding-up and facilitating the positioning of an imaging device by means of a camera augmented C-arm (the CamC previously described section 2.2.1.2) and CT visible markers placed on the patient's skin. A visual servoing algorithm is applied to compute the C-arm pose and the joints' displacements required to align the CamC's optical camera view to a target image. The system then provides step-by-step guidance to surgical staff until the final position is achieved. This way, the C-arm repositioning can be performed without the need of additional X-ray acquisitions. Similarly, [Wang 2012] propose an approach based on closed-form inverse kinematics for obtaining the C-arm's joint displacements in order to facilitate the positioning of the device at a desired pose. In [Fallavollita 2014], a system to assist an operator with the maneuvering of an angiographic C-arm is introduced. The user selects through a tablet PC the desired image outcome from a set of simulated X-ray images and the system automatically computes the device's positioning relative to the patient's anatomy through inverse kinematics and CT-to-patient registration. A virtual C-arm displayed on the screen shows the resulting configuration along with the device control parameters enabling to reach the desired position. The full pipeline of the approach presented in [Fallavollita 2014] is shown in figure 6.2. Furthermore, [Wang 2014] presents a method for determining the optimal viewing angle to observe topological vasculature information in angiography images. A CT volume with vessel data is used to simulate 2D angiograms under different viewing angles, and an optimization approach is applied to estimate the projection which maximizes the visibility of a given vessel structure. The aim of [Wang 2014] is to facilitate the diagnosis of coronary diseases, hence, purely geometrical constraints such as the avoidance of foreshortening and overlapping of vessel structures in the images are considered in the optimization.

The aforementioned works enable the reduction of the number of acquired X-ray images by facilitating the C-arm positioning and/or recommending an optimal configuration for a particular clinical need. However, the clinical staff and patient's radiation exposure are factors that are not taken into account when determining such an optimal configuration. These approaches are solely directed towards obtaining the best visibility of a target for surgical navigation. The approach we herein present aims at assisting the C-arm's manipulator not only by recommending an optimal viewing projection, but also by recommending one which is safer in terms of exposure to X-ray radiation.

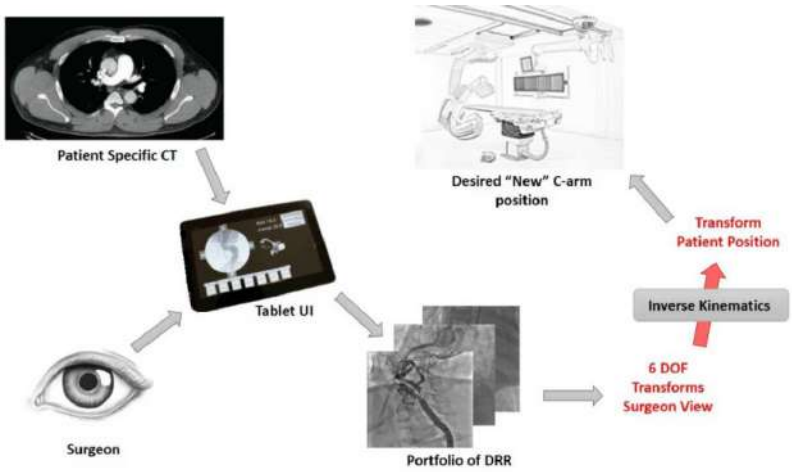

Figure 6.2: "Desired View" pipeline from [Fallavollita 2014]: the user chooses the desired outcome image and, based on simulated X-rays from pre-operative CT data, the system computes the required positioning of the imaging device.

6.2 Imaging device's pose optimization

There are currently no means to intraoperatively estimate radiation exposure for an upcoming X-ray acquisition [Kirkwood 2014]. An operator cannot know if a small change in the device's pose, for which the target visibility would be maintained, can in fact reduce the exposure of the people in the room. Hence, a system capable of estimating the overall radiation exposure for the current device's pose and finding the optimum in a neighborhood of close configurations, can assist the radiologist in choosing a less irradiating projection and thereby contribute to reduce the dose delivered to patient and clinical staff. This is not a trivial task because such a system has to keep track of the context and lay-out of the room, while also considering all parameters affecting radiation propagation. Still, recommending an imaging configuration resulting even in a small reduction of the exposure per image acquisition can make a difference for clinicians attending several procedures on a daily basis. Also, it can contribute to reduce the probability of stochastic effects manifesting in the long term for patients and medical staff.

We describe below our pose optimization approach. We propose to formulate this problem as the search for a configuration that minimizes a cost function modeling the different radiation exposures. This cost function relies on the current OR context and estimates the exposure of patient and clinicians by simulating X-ray propagation using our quasi real-time radiation simulation approach (presented in section 4.3). When applied in an optimization loop, our approach converges to a solution in a reasonable time for the sake of the application. The recommended configuration can either be suggested on a screen or the device's inverse kinematics can be used to compute the corresponding joint displacements for its automatic re-positioning.

6.2.1 Problem statement

The X-ray beam projection in an angiographic imaging device is defined using two rotation angles, which we note as the couple $C = (\theta, \phi)$. These are illustrated in figure 6.3 and are respectively defined as the left/right anterior oblique (LAO/RAO) and the caudal/cranial (CAUD/CRAN) angles [Wang 2014] (also referred to in the literature respectively as angular and orbital rotation angles [Wang 2012, Fallavollita 2014]). During a procedure, the operator adjusts their values to obtain different image projections. We also refer the reader to figures 4.2a and 4.2b for a clear representation of both LAO/RAO and CAUD/CRAN rotation planes with respect to the patient. The tube-to-isocenter and the tube-to-detector distances (respectively TID and TDD in figure 6.3) determine the magnification coefficient and are usually kept constant during image acquisition. In the rest of the chapter, all values are referred to the coordinate system centered at the device's isocenter shown in figure 6.3.

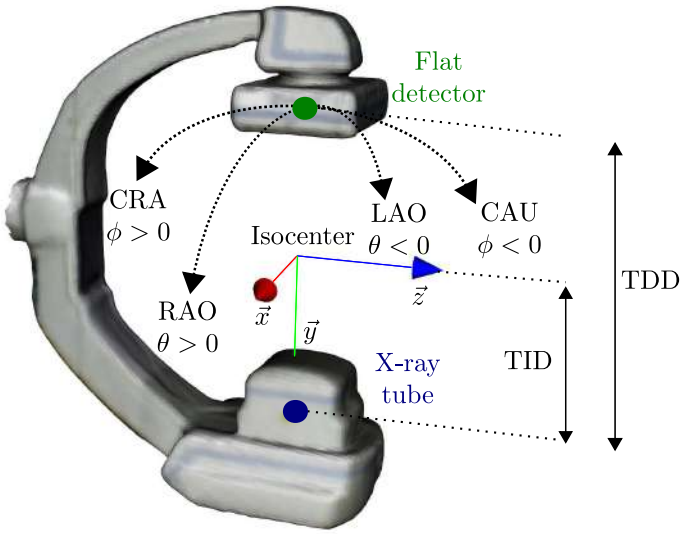

Figure 6.3: Parametrization of an angiographic C-arm: a projection is determined by the angles θ (right/left anterior oblique) and ϕ (caudal/cranial). TID (tube-to-isocenter distance) and TDD (tube-to-detector distance) determine the image's magnification.

We can assume that the image obtained with the configuration $C_\epsilon = (\theta + \epsilon_\theta, \phi + \epsilon_\phi)$ will be similar to the one from the initial nominal projection C_{nom} if ϵ_θ and ϵ_ϕ are small variations of θ and ϕ. However, the device's configuration C_ϵ may generate less exposure to radiation for staff and patient. In that case, it would be recommended for the operator to switch to such a configuration in order to keep the doses *As Low As Reasonably Achievable* (and follow the common ALARA radiation protection principle [NCRP 1990]). Therefore, we want to determine the projection angles $C_{opt} = (\theta_{opt}, \phi_{opt})$ which enable to preserve the visibility of the targeted structure while minimizing the radiation exposure of both patient and clinical staff. Such an optimal configuration is obtained by searching

$C \in S$ which minimizes the cost function defined as:

$$f(C,T,K,P) = \alpha \cdot v(C,K,P) + \beta \cdot h(C,T,K,P) \tag{6.1}$$

Where:

- C is the evaluated imaging device configuration.
- S is the range of close angles generating similar views to the nominal one, referred to as *visibility range*.
- $T = [T_x, T_y, T_z]^T$ is the 3D position of a clinician in the scene with respect to the device's isocenter.
- $K = [TID, TDD, E]^T$ corresponds to the imaging parameters: tube-to-isocenter, tube-to-detector distance and energy spectrum of the emitted X-ray particles (computed from the tube voltage and filtration values).
- P represents the patient parameters, such as the composition and pose of the patient model.
- v is the term computing the patient's exposure.
- h estimates the exposure of a clinician in the scene.
- α and β are respectively the weight coefficients applied to the patient and clinician exposure in the final cost.

The visibility of the targeted anatomical structure is here guaranteed by constraining C_{opt} to be in the vicinity of C_{nom}, in other words within the *visibility range* S: $C_{opt} \in S$. However, it would also be possible to replace such a constraint by adding a geometric term into the cost function for assessing the target visibility in the outcome image as in [Wang 2014].

We describe below how the terms h and v are defined and propose an effective solution for their fast computation in an optimization loop, which takes the current OR context and device parameters into account.

6.2.2 Fast computation of cost function

We apply our GPU-accelerated radiation simulation approach previously described in section 4.3 to compute the terms modeling radiation exposure in the cost function 6.1. Optimizing the pose of the imaging device is challenging since the context, the imaging parameters, the patient and the staff's positioning must be considered in the simulations. Even running on GPU, our simulation approach can take from several minutes up to hours depending on the level of granularity considered (see table 4.4), which would be too slow to be computed within an optimization loop. Indeed, the C-arm operator may not

be willing to wait for several minutes before obtaining a recommended device's angles. Hence, we introduce several approximations to keep the optimization computationally tractable and we also propose a novel approach to compute function 6.1 in quasi-real-time. These concepts are further described below and the benefits of such approximations are evaluated in section 6.3.

6.2.2.1 Patient exposure term v

A simulation of an X-ray image acquisition is performed to compute the term $v(C, K, P)$ of function 6.1. For this, we apply the patient exposure simulation approach described in section 4.3.1.1. An X-ray photon cone beam source in configuration C and with parameters K is placed in a simulation environment, along with a patient-equivalent voxelized phantom of parameters P and centered at the device's isocenter. Particles with energies sampled from a spectrum computed from K are emitted from the X-ray source's position and the energies deposited on each of the phantom's voxels are saved. As a result, we obtain an energy deposition map from which the dose to each organ can be estimated using its material properties. However, an accurate computation of a patient's exposure, which takes all real parameters into account, is challenging to perform and would be too time-consuming for an online optimization loop. Therefore, we propose instead to pre-compute $v(C, K, P)$ for a set of values of $C \in S$ and for fixed imaging and patient parameters. Since for a given examination the device's angulation values are standard and known beforehand, a database V of procedure-specific patient exposure maps can be pre-computed for default imaging parameters K using a patient-specific model with properties P if available, or a generic patient-equivalent phantom otherwise.

6.2.2.2 Clinical staff exposure term h

Similarly, computing $h(C, T, K, P)$ requires simulating an X-ray acquisition (as described above) and to measure the exposure of a clinician at position T to the particles scattered by the patient. However, in this case, pre-computing h for all possible positions of a person in the room and for all considered imaging device's configurations would be impractical. Also, as opposed to the patient, it is not possible to assume a constant staff positioning during an interventional procedure or to know beforehand the number of persons standing around the patient. However, as explained in section 4.3.1.2, we can assume that the 3D dissemination and magnitude of scattered radiation will be the same if the imaging parameters and patient are not changed. Thus, there is no need to simulate the full image acquisition for each new position of a clinician. Instead, we apply our approach described in 4.3.1.2 to characterize the "behavior" of the particles scattered by the patient for a given X-ray image acquisition and save it in a compact manner as *scatter maps*. As described in section 4.3.1.2, such maps can then be rapidly loaded to compute online a clinician's exposure to the scattered particles at his/her current position. Therefore, for a given procedure, a set of *scatter maps* M is pre-computed at the same time as the patient exposure maps V for the considered *visibility range* S.

Tracking of the clinical staff operating near the patient can be performed with ceiling-mounted cameras as described in section 3.2.3. Such an approach enables to estimate online the 3D position T of a bounding-box surrounding a tracked clinician, which is represented as a voxelized water slab phantom in the simulation environment. At run-time, the *scatter map* for parameters (C, K, P) is loaded and used to compute the term h in quasi real-time for the current clinician's position.

6.2.3 Optimization approach

Due to the complex nature of radiation propagation and the use of Monte Carlo simulations to approximate its behavior, function 6.1 is not convex and an analytical expression of it is difficult to obtain. Exhaustive search strategies, where all possible solution combinations are evaluated, may be too slow for a clinical application because of the high number of computations of the cost function that must be performed at each iteration. Local optimization approaches may not be able to always find a global minimum, yet they can provide a solution in a reasonable time, which guarantees to reduce the radiation exposure. Hence, for comparison purposes, we have implemented two optimization algorithms: greedy first search and gradient descent. Starting from the nominal C-arm pose C_{nom}, on the one hand, the greedy best-first search approach iteratively explores all possible neighboring configurations to find the one which reduces the cost. A summary can be found in algorithm 1. On the other hand, the gradient descent algorithm relies on a numerical differentiation of function 6.1 to decide the next best configuration reducing the cost. The general steps of such a process can be found in algorithm 2. The optimization loop stops when the relative exposure reduction Δ_f reaches a threshold th, if the evaluated pose reaches the boundaries of the allowed search space S, or after a maximum number of iterations ($iter_{max}$).

6.2.4 Imaging device's re-positioning in clinical application

We propose in figure 6.4 a pipeline for the potential clinical application of the approach herein described. The visibility of the targeted anatomical structure in the output image is considered to be maintained by constraining the optimization to look only for close C-arm configurations. In addition to this, after the optimization approach converges to a recommended device configuration, we propose to display a digitally reconstructed X-ray image obtained with C_{opt} to the operator. Such an image can be simulated in a few milliseconds with a conventional ray casting approach on GPU [Tornai 2012], either using preoperative CT volume data as in [Fallavollita 2014] or a with a generic phantom model registered to the patient. Also, the statistics regarding the estimated radiation exposure reduction achieved with such a configuration are displayed to the operator. This way, he/she can evaluate the target visibility with the recommended pose along with the benefits it would bring to the people in the room in terms of delivered dose. The recommended projection angles are displayed on the screen for the operator to manually maneuver the C-arm in case it is decided to adopt such a configuration. If

Algorithm 1: Greedy best-first pose optimization approach for a C-arm imaging device

Input: Nominal X-ray device projection C_{nom}, visibility range S, exposure reduction threshold th, maximum number of iterations $iter_{max}$

Data: Patient exposure maps V and scatter maps M pre-computed for all $C \in S$, and for P and K

Output: Recommended device configuration C_{opt}, relative radiation exposure reduction Δ_f

begin

Compute cost function for the initial configuration:
$f_{nom} \leftarrow f(C_{nom}, T, K, P)$
$min_f = f_{nom}$
$C_{min} = C_{nom}$
while $\Delta_f < th$ *and* $C_k \in S$ *and* $iter < iter_{max}$ **do**
Exhaustive list of all n_C neighboring configurations to the current one :
$N = \{C_0, C_1, ..., C_{n_C}\}$ where $C_i = C_{nom} \pm 1°$
for $C_i \leftarrow C_0$ **to** C_{n_C} **do**
Compute cost: $f_{C_i} \leftarrow f(C_i, T, K, P)$
if $min_f < f_{C_i}$ **then**
$min_f = f_{C_i}$
$C_{min} = C_i$
end
end
New cost: $f_{C_k} \leftarrow f(C_{min}, T, K, P)$
$\Delta_f \leftarrow (f_{nom} - f_{C_k})/f_{nom}$
$iter \leftarrow iter + 1$
end
$C_{opt} \leftarrow C_k$

end

Algorithm 2: Gradient descent pose optimization approach for a C-arm imaging device

Input: Nominal X-ray device projection C_{nom}, visibility range S, exposure reduction threshold th, convergence rate α, maximum number of iterations $iter_{max}$

Data: Patient exposure maps V and scatter maps M pre-computed for all $C \in S$, and for P and K

Output: Recommended device configuration C_{opt}, relative radiation exposure reduction Δ_f

begin

Compute cost function for the initial configuration:
$f_{nom} \leftarrow f(C_{nom}, T, K, P)$
while $\Delta_f < th$ *and* $C_k \in S$ *and* $iter < iter_{max}$ **do**
Numerical differentiation of cost function:
$\frac{df}{dC} \approx (f(C_k + \epsilon, T, K, P) - f(C_k, T, K, P))/\epsilon$
$C_k \leftarrow C_k - \alpha \times \frac{df}{dC}$
New cost: $f_{C_k} \leftarrow f(C_k, T, K, P)$
$\Delta_f \leftarrow (f_{nom} - f_{C_k})/f_{nom}$
$iter \leftarrow iter + 1$
end
$C_{opt} \leftarrow C_k$

end

available, closed-form inverse kinematics solutions [Wang 2012] can be applied to obtain the required C-arm joints' displacements for reaching the recommended angulation. If not, these can also be approximated numerically [Farzan 2013]. In case the angiographic C-arm is robotized and its API is connected to the system, inverse kinematics also enable to automatically re-position the device.

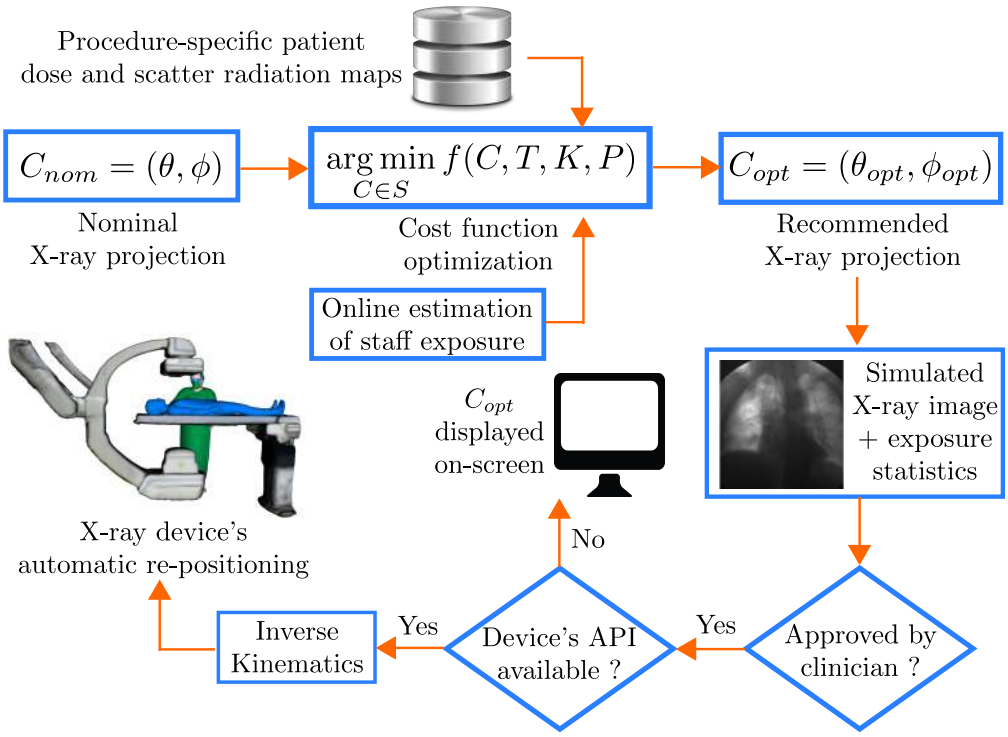

Figure 6.4: Pose optimization pipeline: from an initial nominal projection C_{nom}, our approach suggests a close configuration C_{opt} for which the radiation exposure of staff and patient is reduced. A simulated X-ray image along with exposure reduction statistics are displayed to the operator for him/her to decide to adopt or not the recommendation. If the device's API is available, its re-positioning can be performed automatically through inverse kinematics.

6.3 Experiments in a simulated environment

We evaluate different aspects of our approach in a virtual setup by simulating clinically relevant imaging conditions from interventional procedures. The aim of such an evaluation is to assess the relative exposure reduction that can be achieved with the proposed approach along with the execution times. We consider a Siemens Artis Zeego robotized C-arm as imaging system since it is the device used in our project. However, our approach can also be applied to mobile or other robotized C-arms.

6.3.1 Experimental setup

We evaluate our system on six standard imaging device's configurations (C_{nom}) specific to interventional radiology procedures performed on a C-arm angiographic system (presented in table 6.1). For each of them, a set of close imaging projections is considered in the optimization process, defined as $S = \{C_{nom} \pm 10°\}$ as advised by our collaborating radiologists. The **PA**, **AP** and **Lat** are angulation sets close respectively to the posterior-anterior, anterior-posterior and lateral C-arm configurations. **V1** and **V2** correspond to projections typically employed during vascular intervention procedures. **Ver** is a projection set used during Vertebroplasty procedures. The cost function is computed as described in section 6.2. A set of patient exposure maps V is simulated per imaging angles, using a phantom generated from a generic thoracic patient CT by transforming Hounsfield units into materials' density values. The resulting phantom is composed of $288 \times 241 \times 164$ voxels of 41 materials (human skeleton and organs surrounded by tissue-equivalent material), with a spacing of $1.27 \times 1.27 \times 2.0$ mm^3. The patient parameters P are in this case the phantom's composition and pose, which we assume aligned and centered at the device's isocenter. In a real scenario, if a patient's preoperative CT volume is available, it can be used to generate the phantom for the simulations. Concerning the imaging parameters K, we set the tube-to-isocenter and tube-to-detector distances to 70 and 120 cm respectively. Particles sampled from an energy spectrum simulated for a tube voltage of 120 kVp and a 2 mm Al (0 mm Cu) filtration are emitted in order to mimic a typical clinical configuration.

We pre-compute $v(C, K, P)$ for all configurations $C \in S$ as presented in table 6.1. A one degree spacing is considered between each configuration since this is the minimum rotation step of most mobile and robotized C-arms. Each X-ray image acquisition is simulated by emitting 10^8 photons. The simultaneous computation of the patient's exposure and the generation of the *scatter map* per configuration takes around six minutes on a Titan X GPU card for the considered parameters. The latter are computed with a sphere of 500 mm of radius divided into $n = 40960$ faces. With these parameters, the mean statistical uncertainty measured per bin in the scatter maps is below 1.5 % and of 2 % for the peak skin patient organ dose (as described in section 4.3.1.1). As mentioned earlier, all $v(C, K, P)$ and *scatter maps* from S can be pre-computed before a given procedure. However, the computation of the staff's exposure and the optimization of the device's pose is performed online by using the pre-simulated databases V and M. A tracked clinician is approximated with a voxelized bounding box of $1000 \times 2000 \times 1000$ mm^3, with voxels of $100 \times 100 \times 100$ mm^3 size. Using the simulation approach described in section 4.3.1.2, a person's current exposure for a given device's configuration can be simulated in a few milliseconds for 10^6 photons, with less than 1 % of uncertainty per voxel. All results are normalized by the number of photons simulated. All coordinates are referred to the frame depicted in figure 6.3.

We present below the results of four different experiments. For each, since we are looking to assess the potential of our approach to reduce radiation exposure, the maximum allowed number of iterations ($iter_{max}$) in the optimization loop was the only

Table 6.1: Imaging configurations typical in interventional radiology procedures evaluated with our approach along with the considered ranges for the sets S.

Projection	$C_{nom} = (\theta, \phi)$	$S = \{C_{min}, C_{max}\}$
Posterior-Anterior (PA)	$(0, 0)$	$(-10, 10, -10, 10)$
Anterior-Posterior (AP)	$(180, 0)$	$(170, 190, -10, 10)$
Vascular 1 (V1)	$(30, 30)$	$(20, 40, 20, 40)$
Vascular 2 (V2)	$(-45, -25)$	$(-55, -35, -35, -15)$
Vertebroplasty (Ver)	$(35, 0)$	$(25, 45, -10, 10)$
Lateral (Lat)	$(90, 0)$	$(80, 100, -10, 10)$

stop criteria considered. Namely, the optimization loop is not stopped after reaching a given exposure reduction threshold th, but only after a maximum of $iter_{max} = 10$ iterations or after reaching the limits of the configurations range S. First of all, we compare the performances of the two optimization algorithms described in section 6.2.3. Second, we perform a trade-off analysis of the potential increase/decrease of patient/staff radiation exposure when varying the weights (α, β). Third, we compare our approach based on approximations allowing a fast computation of cost function 6.1, against computing it with a full Monte Carlo simulation (without approximations). Finally, we evaluate our optimization approach's potential to reduce the exposure to sensitive body-parts of clinical staff on a fourth experiment.

6.3.2 Optimization algorithm evaluation

To compare the performances of the two optimization algorithms described in section 6.2.3, we consider a virtual scene with a patient and two clinicians (each standing on opposite sides of the table). A first clinician is standing 1 m away from the patient and aligned with the device's isocenter ($T_1 = [-1000, 0, 0]^T$). A second one is placed at the opposite side of the operating table at $T_2 = [700, 0, 500]^T$, to mimic an operator positioned for right femoral access. This scenario is depicted in figure 6.5. For this experiment, we set the cost function coefficients (α, β) to $(1, 1)$ to give the same weight to both patient and staff exposure terms. We consider each of the angulation sets from table 6.1. Starting from the same nominal C-arm configuration, we provide the suggested C-arm's pose C_{opt} yielded by each optimization algorithm. The results are summarized in table 6.2. For each configuration, the achieved relative radiation exposure reduction for the patient (Δ_v) and for both clinicians (Δ_h), along with the optimization time is provided.

As expected, the greedy best-first search algorithm is able to converge to recommended configurations yielding a higher exposure reduction for patient and clinicians. However, this comes at the expense of the optimization time which is consistently higher since the cost function has to be computed more times when evaluating all possible neighboring configurations. In most cases, the gradient descent approach converges to configurations which are close but for which the exposure reduction is slightly inferior. Still, the

algorithm yields a solution in half the time than when using the greedy approach. In table 6.2, the results for projection **V1** are highlighted to illustrate this fact. Indeed, the configuration output by the greedy best-first search respectively reduces of 2.31 % and 1.49 % the patient and clinicians' dose. Gradient descent is two minutes faster in yielding a close configuration which spares the patient 2.54 % less dose and 1.04 % for the clinicians. The results for the **Ver** projection are also highlighted since they illustrate the complexity of this multi-objective optimization problem, where reducing the exposure of the patient can be in conflict with reducing the staff's. Specially in the scenario we consider (figure 6.5) where clinicians stand on both sides of the table, the one closer to the X-ray source will always be the most exposed to scattered radiation. This is the case for the **Ver** projection, where both optimization algorithms converge to configurations increasing clinicians' exposure (-2.53 % and -3.32 %). Still, both output C_{opt} achieve high patient's exposure reductions (3.49 % and 3.86 %) which enable to have a reduction in the final cost function value. These experiments not only allow us to compare the performances of the two optimization algorithms, but they also illustrate the possible intricacies of this problem that hinder the finding of a C-arm pose to recommend. We refer to the trade-off between either reducing patient dose or staff dose, when it is not possible to achieve both.

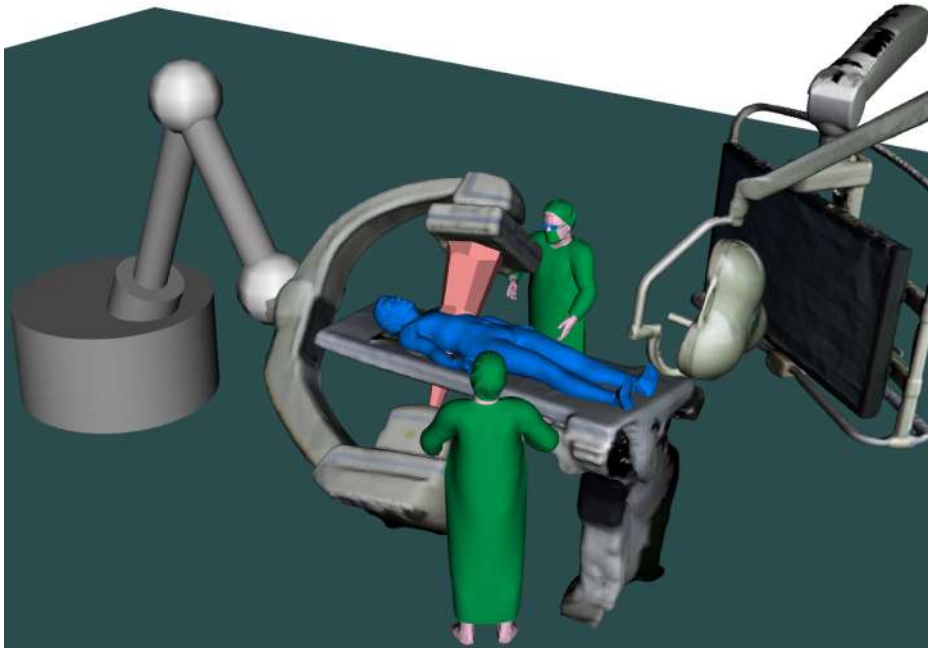

Figure 6.5: Virtual setup illustrating the two clinicians' scenario for the experiments presented in sections 6.3.2 and 6.3.3.

Even if the gradient descent approach may converge to a local minimum, it still guarantees that the recommended configuration reduces the overall radiation exposure with respect to the initial one. Moreover, the optimization is performed in significantly less time. For a potential clinical application, we favor optimization time since it is

Table 6.2: Optimization of the X-ray device's pose with two algorithms: greedy best-first search and gradient descent. A scenario with two clinicians is considered, where clinician #1 is at position $T_1 = [-1000, 0, 0]^T$ and #2 at $T_2 = [700, 0, 500]^T$. The recommended configuration C_{opt}, the relative exposure reduction of the patient (Δ_v) and of both clinicians (Δ_h), along with the optimization time are given.

Proj.	C_{nom}	**Greedy best-first**				**Gradient descent**			
		C_{opt}	$\Delta_v(\%)$	$\Delta_h(\%)$	Time(s)	C_{opt}	$\Delta_v(\%)$	$\Delta_h(\%)$	Time(s)
PA	$(2, 0)$	$(1, -10)$	0.63	0	255	$(2, -10)$	0.6	0	107
AP	$(181, 3)$	$(190, 10)$	1.64	2.03	219	$(188, 10)$	1.49	1.75	92
V1	$(31, 29)$	$(28, 39)$	**2.31**	**1.49**	255	$(29, 39)$	**2.54**	**1.04**	121
V2	$(-43, -27)$	$(-42, -35)$	2.15	0.17	230	$(-43, -35)$	2.15	0	100
Ver	$(33, 0)$	$(38, -10)$	**3.49**	**-2.53**	230	$(39, -10)$	**3.86**	**-3.23**	101
Lat	$(88, 0)$	$(98, 3)$	3.58	1.38	249	$(98, -2)$	3.53	1.38	110

preferable that the time an operator has to wait for the system to output a recommended device configuration is as low as possible. Therefore, for the rest of the experiments we apply the gradient descent based optimization algorithm.

6.3.3 Cost function weights trade-off analysis

In essence, the problem herein studied is a multi-objective optimization where we wish to minimize both the patient and the staff dose while not affecting the clinical relevance of the output X-ray image. Each of these objectives may be conflicting with each other depending on the considered scenario. We transform the problem into a single objective optimization by aggregating the first two objectives into a weighted cost function (6.1) and by transforming the third one into a constraint. However, the drawback of this approach is that the solution found will only be as good as the selection of the weights in the cost function [Ngatchou 2005] (α and β in function 6.1). In general, a priori information about the objectives to minimize is required to set the weights. For our application, choosing the weights can be complex due to the ethical issues it implies. On the one hand, one can think about giving a higher priority to reduce staff dose since clinicians can be exposed to radiation daily. On the other hand, one can also privilege reducing patient dose since patients are exposed to higher dose values, which can cause radio-induced skin injuries.

In this section, we study the impact that the weights (α, β) have on the recommended C-arm configuration and on reducing the exposure of patient/staff with the recommended device configuration. For this experiment, we consider two clinically relevant C-arm projection sets S from table 6.1, corresponding respectively to angulations typically used for vascular (**V1**) and for vertebroplasty (**Ver**) procedures. The same scenario with two clinicians at opposite sides of the operating table (*i.e.* figure 6.5) is simulated. We randomly set an initial C-arm angle pair C_{nom} from each set, and apply our optimization approach with three different pairs of (α, β) coefficients: $(10, 1)$, $(1, 1)$ and $(1, 10)$. This way, we evaluate the results when giving more or the same weigh to either of the cost

function terms. We carried out this experiment for ten different C_{nom} in each angulation set. The results are represented through the graphs in figure 6.6, which are plots of the radiation exposure reduction for the patient (Δ_v) and for the two clinicians (Δ_h) achieved for each of the configurations output by the optimization approach. These graphs illustrate the trade-off that occurs between the terms of cost function 6.1. First, for both the **V1** and **Ver** sets, the exposure of the two clinicians is actually increased with the recommended C-arm configuration when more weight is given to the patient term. This is illustrated by the negative Δ_h obtained when $\alpha > \beta$ (red circles in plots 6.6). However, the dose delivered to the patient is importantly reduced with this setup (almost up to 6 %). Second, when $\alpha = \beta$, Δ_h is still negative for some recommended configurations for the **Ver** set, which means that the optimization still does not converge to a solution reducing clinicians' dose (blue asterisks in graphs 6.6b). Yet, for the **V1** set, the dose for patient/staff is consistently reduced with this configuration. Third, when $\alpha < \beta$, the dose to clinicians is almost always reduced, but with a trade-off on the patient's dose. Negative Δ_v are yielded by some of the output configurations for the **Ver** projections set. Still, these remain inferior to the potential staff's exposure decreases that can be obtained when $\alpha < \beta$ (magenta points in graphs 6.6). For the graph 6.6a corresponding to the **V1** angulations, the patient's exposure is consistently reduced with the optimization approach for all evaluated weight values, and staff's exposure when $\alpha <= \beta$.

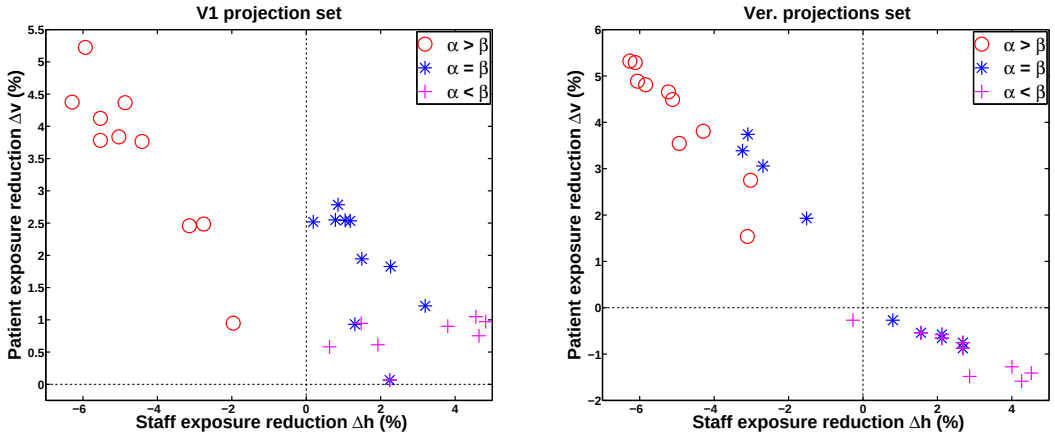

(a) Results for the vascular 1 projections sets.

(b) Results for the vertebroplasty projections sets.

Figure 6.6: Trade-off analysis when varying the weights (α, β) from cost function 6.1.

In the case of multi-objective optimization problems, these kinds of graphs are typically used to identify the Pareto optimal solutions (Pareto front) [Ngatchou 2005], namely the solutions for which no better compromise can be found for conflicting objectives. These optimal solutions should appear as points in the top right corner of the plots, *i.e.* configurations yielding high exposure reductions for both patient and clinicians. From this trade-off analysis, we can observe that no weights guarantee to obtain points on

this area of the plot. Furthermore, this problem is affected by several simultaneously changing factors that would have to be considered in such an analysis. The graphs from figures 6.6 correspond to a single set of clinicians' positions (T), patient (P) and imaging parameters (K). Variations in any of these parameters would affect the trade-off between the cost function terms. Still, the results from this trade-off analysis, when combined with a priori knowledge from radiation safety recommendations, can justify our hypothesis that clinical staff's exposure is more affected to variations of the C-arm angulations. While a patient will always be exposed up to some degree during an X-ray image acquisition, a few degrees of rotation may make a difference between an operator fully avoiding being irradiated or not. Since no optimal weights set-up can be easily be found, for the rest of our experiments we set (α, β) to $(1, 10)$ to give a higher weight to reducing clinicians' dose in the cost function.

6.3.4 Evaluation of the cost function computation approach

We herein evaluate the impact that the approximations enabling a fast computation of the cost function can have on the recommended C-arm configuration. For this, we consider a simple scenario with one clinician standing 1 m away from the patient and aligned with the device's isocenter ($T = [-1000, 0, 0]^T$). We compare computing the terms h and v with our fast simulation approach against using a full Monte Carlo simulation of 10^8 particles, namely without any of the approximations or without using pre-computed *scatter maps*. In table 6.3, we present the results obtained with both approaches on each of the studied configuration sets. We provide the suggested C-arm's pose C_{opt}, the obtained relative overall radiation exposure reduction Δ_f (computed as described in algorithm 2) and the corresponding optimization times. We assess the accuracy of the results obtained with our approach by computing the absolute difference between the normalized values of the cost computed with each method (*Diff* in table 6.3).

The results show that our approach is able to converge on each considered scenario to a recommended pose in a few seconds, for which the overall delivered dose (patient and clinician) can be reduced from 4 % to 19 %. Moreover, a difference below 5 % is obtained between the computed dose values across both simulation approaches for the studied parameters. Even if both approaches perform the same number of computations of the cost function in the optimization loop, the simulation without approximations consistently takes more than four hours to converge to a solution and achieves similar exposure reduction ratios. This is consistent with the results presented in section 4.3.2.1 where the use of pre-computed *scatter maps* enables to importantly reduce the simulation time while having a relatively low impact on accuracy. This approach enabling an accurate radiation exposure computation in quasi real-time is thereby suitable for to be applied in an optimization loop. Indeed, as shown in table 6.3, important exposure reductions are achieved after a few seconds, which can be promising for a potential intraoperative use of the system.

In table 6.4 we present results of a different study where two clinicians are considered in the same configuration as for the evaluations from sections 6.3.2 and 6.3.3. However,

Table 6.3: Results of the optimized C-arm's pose for each S and comparison with the computation of function (6.1) with no approximations (*Full MC*). The absolute difference of *Ours* and *Full MC* (*Diff*), the recommended configuration C_{opt}, the achieved relative exposure reduction Δ_f and the execution times are provided.

Projection	C_{nom}	C_{opt}	Diff (%)	Method	Δ_f (%)	Time (s)
PA	$(0, 0)$	$(-10, -10)$	1.3	Full MC	5.9	15017
				Ours	**4.1**	**41**
AP	$(180, 0)$	$(190, 10)$	2.3	Full MC	2.6	15745
				Ours	**4.5**	**40**
V1	$(30, 30)$	$(20, 40)$	3.6	Full MC	18.2	15837
				Ours	**11.1**	**39**
V2	$(-45, -25)$	$(-55, -35)$	0.5	Full MC	17.9	15557
				Ours	**19.6**	**41**
Ver	$(35, 0)$	$(25, -10)$	2.8	Full MC	18.1	15486
				Ours	**10.5**	**38**
Lat	$(90, 0)$	$(100, 0)$	4.4	Full MC	3.1	15478
				Ours	**6.5**	**37**

for this experiment we consider only the clinicians' head exposure when computing the term h, since this sensitive body-part usually remains un-protected during a procedure. Besides Δ_f, we also provide the achieved relative reduction of the patient's exposure Δ_v and of each clinician separately, respectively Δ_{h_1} and Δ_{h_2}. We observe that the patient's exposure is less affected by small changes in the device's pose, which is consistent with the results from section 6.3.3. Nevertheless, the patient's dose can still be reduced up to 5 % for some cases. Higher reductions of the dose deposited to the clinicians' heads are obtained, which can go up to 20 % as for the configurations **V2** and **Lat**. Interventional practitioners can be exposed on a daily basis and studies have shown that there is a high risk for them to develop radiation-induced brain cancers [Roguin 2013]. Lowering the dose delivered to the head is therefore important to reduce the likelihood of such negative effects. The fact that reducing patient and staff dose can conflict with each other is also illustrated in these experiments since for some cases the optimal pose was more beneficial for the patient or for one of the clinicians. For the **Ver** setup for instance, the optimal configuration generates an increase in the exposure of the clinician standing in the opposite side ($\Delta_{h2} = -0.9$ %). Yet, the absolute dose values simulated at such positions are low when compared to ones on the side closest to the X-ray source and have therefore a lower weight on the total cost. This is why the final overall exposure reduction Δ_f is still positive for the pose suggested by our approach.

In our experiments, we were looking for the highest exposure reduction achievable from the evaluated set of parameters. Yet, in practice, the convergence rates can be set for the algorithm to provide a recommended configuration in a few seconds, for instance by stopping once $\Delta_f \geq 5$ %. Such computation times are suitable for an intraoperative use of the system since, during an intervention, the C-arm may be kept

Table 6.4: Device's pose optimization with two clinicians in the scene, where clinician #1 is at position $T_1 = [-1000, 0, 0]^T$ and #2 at $T_2 = [700, 0, 500]^T$. The recommended configuration C_{opt}, the relative exposure reduction of the patient ($\Delta_v(\%)$) and of both of the clinicians' heads (Δ_{h_1} and Δ_{h_2}) are provided.

Projection	C_{nom}	C_{opt}	Δ_v (%)	Δ_{h_1} (%)	Δ_{h_2} (%)	Δ_f (%)
PA	$(8, 0)$	$(1, -8)$	0.5	1.3	0.6	0.5
AP	$(185, 0)$	$(190, 5)$	1.1	10.7	6.6	6.3
V1	$(27, 29)$	$(36, 39)$	4.9	2.4	13.9	8.2
V2	$(-37, -24)$	$(-48, -34)$	3.8	21.5	5.7	11.3
Ver	$(40, 0)$	$(38, -9)$	0.3	4.5	-0.9	1.2
Lat	$(88, 0)$	$(98, -2)$	3.5	15.9	20.4	15.1

in the same position for several minutes while a surgical task is performed or an X-ray image is observed. Furthermore, depending on the considered projection, we obtain exposure reductions of up to 11 %. The highest ones are achieved for the vascular projections **V1** and **V2**, for which the X-ray source is tilted diagonally with respect to the patient. In these configurations, the clinician can be closer to the X-ray source and small angulation changes can have a higher influence on his/her body exposure. As expected, the optimization algorithm attempts to drive the X-ray source away as far as possible from the clinician, since the scattered radiation is always higher on the source's side [Schueler 2006]. This is why for some of the evaluated projections when a single operator is considered, the recommended angulations yield higher exposure reductions since they are consistently close or in the limits of S, namely corresponding to configurations where the X-ray source is on the opposite side of the table.

6.4 Evaluation with dose measurements

The previous evaluations were performed with simulated data in a virtual environment mimicking a clinical scenario. In this section, we evaluate our optimization approach with real data gathered through a dose measurement campaign performed in an experimental hybrid OR at IHU Strasbourg. The aim of this evaluation is, first, to assess experimentally the impact that a few degrees of change in the X-ray device's angulation can have on radiation exposure and, second, to evaluate the exposure reduction achieved with the poses recommended by our algorithm.

6.4.1 Experimental setup

A setup similar to the ones described in sections 4.2.3 and 4.3.2.2 was used. A phantom of $20 \times 20 \times 24$ cm^3 with 10 mm thick plexiglas walls and filled with water was irradiated under different imaging protocols with an Artis Zeego robotized X-ray imaging device. RaySafe wireless active personal dosimeters [RaySafe 2017] were used to record dose data during the different image acquisitions. Such a setup is shown in figure 6.7. To simulate a clinician's radiation exposure, four dosimeters were taped over a drip rod at

different heights as shown in the right picture of figure 6.7. This "dummy" clinician was positioned next to the operating table at position $T = [-1000, 0, 0]^T$. Several pairs of X-ray image acquisitions were performed and the doses at the clinician's position were recorded with the dosimeters. Each pair consisted first of one acquisition with the C-arm positioned at a given nominal pose (C_{nom}) and second, of one with the pose recommended by our optimization approach (C_{opt}). Each acquisition was carried out twice and the measurements from the four dosimeters were averaged to obtain a single measure per C-arm configuration. The relative radiation exposure change (Δ_h (measured)) was computed from the mean dose measured at C_{nom} and at C_{opt}. As explained below, the list of C-arm configuration pairs executed during the measurement campaign were determined beforehand with our optimization approach. A total of forty X-ray image acquisitions was performed, all with the same nominal tube tension and filtration respectively 100 kVp and 0.4 mm Al/0.0 mm Cu.

Figure 6.7: (Left) Setup for the dose measurements performed in a hybrid OR at IHU Strasbourg using a Siemens' Artis Zeego X-ray imaging device and RaySafe dosimeters. (Right) Four dosimeters taped to a drip rod used to obtain dose measurements over a "dummy" clinician's body.

Our cost function computation approach described in section 6.2.2 was slightly modified for the considered experimental scenario. First, a cubic water-filled phantom was considered for the computation of the patient exposure term v. Second, the clinician was replaced by four voxelized volumes with the same dimensions as a RaySafe dosimeter, each one placed in the simulation at the same height as in their real positioning on the drip rod. The staff exposure term h was then computed by summing the dose simulated at each of these volumes. The nominal C-arm poses were randomly selected from each of the projections sets S from table 6.1. Our optimization approach was executed for each considered configuration in order to determine the recommended pose C_{opt}. These

C-arm configurations were then reproduced in the real OR. Figure 6.8 shows an example of images captured from our ceiling-mounted multi-camera system showing the position of the X-ray imaging device for a pair of (C_{nom}, C_{opt}) configurations. One can observe that a few degrees of rotation on each of the (θ, ϕ) planes are barely visible in the images. Yet, as it will be presented below, it can actually have a considerable impact on the measured/simulated dose.

6.4.2 Evaluation results

Figure 6.8: Images captured by our ceiling-mounted multi-camera system during the dose measurements performed at IHU Strasbourg. The nominal configuration (C_{nom}) and the one recommended by our C-arm pose optimization approach (C_{opt}) are shown.

The results of this evaluation are summarized in table 6.5. The angles for the evaluated C-arm configuration pairs (C_{nom}, C_{opt}) are listed, along with the relative clinician exposure reduction as computed from the dose measurements (Δ_h (measured)) and as predicted by the optimization approach (Δ_h (simulated)). One can observe from the measured Δ_h values that a small C-arm angulation shift can in fact decrease the exposure of a clinician standing next to the table. We also provide in table 6.5 the absolute difference between the percentages of exposure reduction predicted by our optimization approach and the measured ones. No calibration dosimeters were used to correct the simulations since Δ_h is a relative metric independent of the absolute difference between the simulated and the measured dose values. For all experiments, a mean 6.9 % absolute difference between the predicted and measured exposure reduction percentages is obtained. The lowest differences (highlighted in the table) are obtained for configurations where the X-ray source is close or on the same side as the drip rod, namely exposing the dosimeters to higher scatter radiation intensities. The highest errors are produced for poses positioning the X-ray source on the opposite side of the table, for which the dosimeters may measure low dose values. Indeed, APDs have a given angular resolution beyond which no measurements are possible. Such a resolution is not considered in the simulations and this may also explain the fact that the simulations tend to predict higher exposure reduction ratios. Indeed, incident particles striking the simulated dosimeters from any angle are considered in the Monte Carlo simulations, while these are not captured by these semiconductor-based dosimeters.

This experimental evaluation enabled us to verify experimentally that a few degrees

Table 6.5: Evaluation of the C-arm pose optimization approach with real dose measurements: the evaluated configuration pairs (C_{nom}, C_{opt}), the relative clinician exposure reduction as computed from the dose measurements (Δ_h (measured)) and as predicted by the optimization approach (Δ_h (simulated)) along with the absolute difference (Diff.) between them are provided.

Proj.	C_{nom}	C_{opt}	Δ_h (measured)(%)	Δ_h (simulated) (%)	Diff. (%)
PA	$(-1, -8)$	$(-8, 0)$	1.47	12.1	10.6
	$(6, -10)$	$(8, 0)$	1.16	7.15	5.99
AP	$(180, -1)$	$(190, -5)$	6.14	5.21	**0.93**
	$(185, 0)$	$(190, 7)$	4.94	15.2	10.2
V1	$(30, 30)$	$(40, 40)$	1.86	5.50	**3.64**
	$(27, 29)$	$(37, 35)$	13.4	2.52	10.8
V2	$(-27, 29)$	$(-36, 33)$	14.7	6.12	8.58
	$(-47, -35)$	$(-45, -25)$	0.34	7.48	7.14
Vert	$(40, 0)$	$(38, 9)$	4.80	14.9	10.1
Lat	$(88, 0)$	$(98, 2)$	0.12	0.82	**0.7**
				Mean	**6.97**

of change in the X-ray device's pose can actually contribute to reduce the exposure of operators. This information is promising for approaches aiming at reducing staff dose by acting on the C-arm's configuration. We can also conclude from the results that the poses recommended by our optimization approach achieve a real decrease in the potential exposure of a clinician in the scene. For the considered scenario and imaging protocols, a 7 % difference between the dose reduction percentages predicted by our approach and the ones measured with the dosimeters is obtained.

6.5 Discussion and conclusions

Modern imaging devices are nowadays essential to the performance of minimally-invasive procedures. Yet, despite their articulated construction and kinematic properties, they are still positioned in an open-loop manner by an operator looking to capture the best view of a targeted anatomical structure. As improving radiation safety during X-ray guided interventional procedures is now becoming a priority for healthcare providers, we propose an approach to actively reduce radiation exposure by exploiting the articulated construction of mobile/robotized C-arms and perform an optimization of their pose. Such an approach is able to suggest a less irradiating device's pose while preserving the visibility of the target in the image outcome. It can also provide useful radiation exposure statistics in near real-time during a procedure, which are related to the immediate OR's context, imaging device's configuration and staff positioning. These statistics can assist the attending personnel in adapting the use of radiation protection measures accordingly.

This is a complex problem, aiming at minimizing several objectives which can be

conflicting with each other in some scenarios. Several relevant approximations and hypotheses were carried out in the scope of this work since at this stage the goal is to assess the potential of a C-arm pose optimization approach. This is a first attempt to address such a complex problem which has room for further improvements. Indeed, additional terms can be added to the cost function 6.1 for a more detailed optimization. For instance, the 3D position of equipment in the scene can be included to avoid collisions with the suggested configuration. This can be particularly interesting for automated imaging devices. Also, the algorithm can be set to minimize the dose received at a specific organ or skin area of the patient, which can be beneficial specially to patients that have been previously irradiated at some body locations. Similarly, for tasks requiring long exposure times with the same X-ray source positioning, our approach can be applied to optimize the 3D position of a clinician around the patient to reduce his/her exposure to scattered radiation. An additional term applying geometrical constraints to quantitatively assess the target visibility in the outcome X-ray image can also be included. This would allow to also optimize the visibility of the targeted anatomical structure in the outcome image at the same time. Moreover, even if for now a clinician in the scene is approximated as a voxelized water slab, an articulated human detection approach, such as the ones presented in section 3.2.3, could be applied to accurately track his/her body-parts. This would allow not only to simulate more accurately a person's exposure, but it could also be used in the optimization algorithm to suggest a pose which minimizes the dose delivered specifically to sensitive and/or unprotected operators' body-parts. Furthermore, the positioning of the lead protective shields should be included in the computation of radiation exposure. Such information could also be incorporated and considered in the optimization loop.

The potential of our approach was evaluated through two types of experimentation. First, experiments considering a simulated clinical environment enabled to evaluate its capabilities to suggest a less irradiating configuration in a few seconds, and to assess the impact that the approximations allowing a fast computation of the cost function have on the simulated values. Second, a study with real dose measurements acquired in an OR was performed to verify that the dose reduction ratios predicted by our approach are close to the real ones. It also enabled us to confirm the fact that even a small change in a C-arm pose can contribute to decrease the dose to a clinician.

In this chapter, we propose an approach to optimize the pose of an angiographic C-arm, where we focus on the task of reducing the overall exposure to harmful ionizing radiation during X-ray guided interventional procedures. Our method takes into account the OR's context, the imaging parameters and the clinical staff's positioning to estimate the exposure to radiation of the persons in the room. It is then able to suggest a configuration preserving the visibility in the image outcome while reducing the dose delivered to patient and staff. Our optimization algorithm applies Monte Carlo simulations to compute in near real-time radiation exposure statistics at each iteration, which correspond to the current room lay-out and acquisition parameters. We envision two potential clinical applications of this approach. First, as proposed in figure 6.4, it could be used intraoperatively

to suggest a less irradiating C-arm pose for the current room context. Second, the optimization approach could also be applied to develop a tool for the preoperative planning of a procedure. Such a tool, further discussed in section 7.2.2, could determine the optimal C-arm configurations and imaging protocols that would minimize the dose delivered to the patient for the upcoming procedure.

Part III

Applications, conclusions and perspectives

7 Clinical applications

If you are not embarrassed by the product when you launch, you've launched too late.
– Reid Hoffman

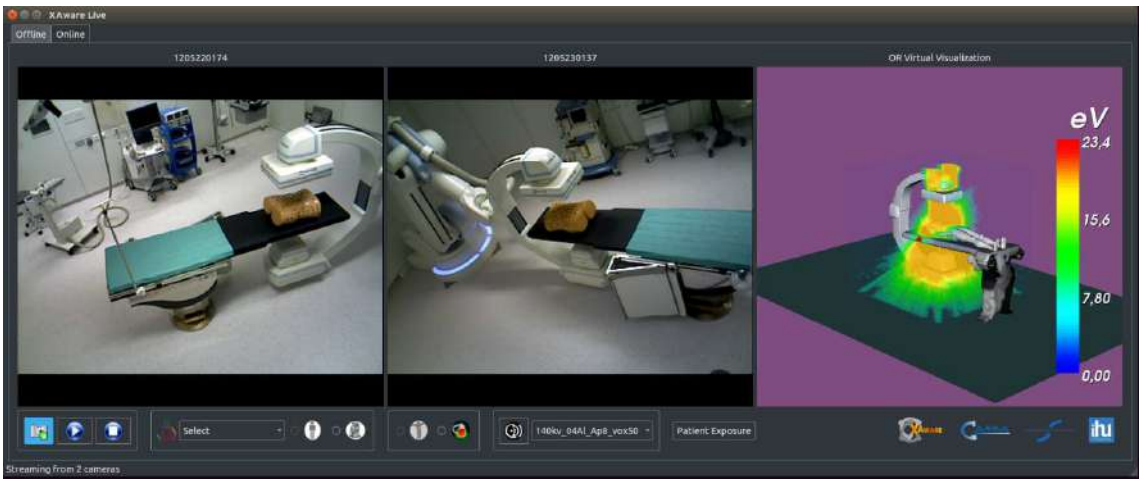

Figure 7.1: Graphical User Interface (GUI) of our radiation awareness prototype system *XAware-Live*.

Chapter Summary

7.1 XAware-Live: a global radiation awareness system 126
7.1.1 General description of the system 126
7.1.2 System's features and visualizations modes 128
7.1.3 Demonstrations and feedback about the system 129
7.1.4 Future developments 130
7.2 Potential clinical applications 131
7.2.1 Intraoperative radiation awareness 131
7.2.2 Clinical applications of a C-arm pose optimization approach 133
7.3 Conclusions 134

In this chapter, we discuss existing and potential clinical applications of the methods proposed in this thesis. We first present a radiation awareness prototype system we have developed, coined *XAware-Live*. Such a system, described in section 7.1, has been installed in an experimental hybrid OR at IHU Strasbourg and has been successfully demonstrated to several of our clinical and industrial partners. Its graphical user interface (GUI) is shown in figure 7.1. Then, in section 7.2, we discuss concepts for several potential clinical applications which can be made possible thanks to the approaches proposed in this thesis.

7.1 XAware-Live: a global radiation awareness system

XAware-Live[1] is the culmination of the approaches presented in chapters 3, 4 and 5 into a single clinical application. A working prototype capable of providing *in-situ* visual feedback about radiation exposure in the surgical room has been developed[2] and installed in an experimental hybrid room at IHU Strasbourg. We herein describe the features of the system and we present screen captures of its GUI acquired during its real usage as means to qualitatively assess its performances.

7.1.1 General description of the system

The system relies on a registered multi-RGBD camera setup (as described in chapter 3) installed in an experimental OR at IHU Strasbourg. Such a setup was shown earlier in figure 3.3a. Its GUI, depicted in figure 7.1, is divided in two main parts. The left part shows the live feed from the ceiling-mounted cameras, and the right one shows a virtual representation of the OR lay-out. A direct communication with the angiographic C-arm's (Siemens' Artis Zeego) API, enables the system to have access to the device's current kinematic parameters. These are applied to update the pose of the displayed virtual

[1] A video demonstrating *XAware-Live* can be found in: https://youtu.be/JpATPDrXvu8

[2] I thank Dr. Abdolrahim Kadkhodamohammadi for collaborating with me on the development of *XAware-Live*.

C-arm model accordingly and also to display radiation safety information corresponding to the actual C-arm configuration. In a typical usage of the system, its GUI is shown on a surgical screen inside the OR for the user to interact with it and be able to choose among the different proposed features through the icons located on its lower part.

The views from the ceiling-mounted cameras are employed to perceive the current environment; this information is then applied by the system for providing consistent visualizations. As mentioned in section 3.2.3, we have included an open-source implementation of the approach from [Cao 2017] for a real-time human pose estimation in one of the ceiling cameras' view. The upper-body joints' poses from the people in the room are displayed in 2D over the color image and their current 3D position is also shown in the virtual visualization (see figure 7.2). As explained below in section 7.1.2, this information is used for providing feedback of the attending persons' radiation exposure. However, such a 3D understanding of the current persons' positions can also potentially be applied for other clinically relevant applications such as the detection of potential collisions with the robotized imaging device.

Figure 7.2: Clinician tracking in *XAware-Live*: the 2D body-joints' positions are overlaid over the color image (left) and the persons' 3D positions are shown in a virtual environment (right).

Our GPU-accelerated simulation approach described in section 4.3 is applied to compute the 3D scattered radiation distribution maps and patient's organs/skin dose maps (*i.e.* section 4.3.1.1) displayed by the system. In its current version, these simulation maps are pre-computed for different sets of imaging parameters and angulations, and are loaded upon the initialization of the system. They are computed for several standard X-ray particles' energy spectrums (*i.e.* from X-ray tube voltage and filtration values), for every 5° projection in a full C-arm rotation in both LAO/RAO and CAUD/CRAN planes. Online, the current C-arm angulation is obtained directly from its API and the corresponding radiation map to display is loaded. Since for now only kinematic information is provided by the current API's version, the user selects through the GUI the X-ray imaging parameters to visualize.

7.1.2 System's features and visualizations modes

Several of the visualization modes described in chapter 5 have been implemented into the system to intuitively display the simulated radiation maps to the user. These are updated in quasi real-time as the C-arm parameters change to illustrate the effects that altering the projection angles and/or the imaging protocol have on the behavior of radiation. Two types of visualizations are provided: a visualization of color-coded information shown over a virtual representation of the room (right part of the GUI) and an AR visualization achieved by overlaying registered virtual elements over the color images from the ceiling-mounted cameras (left part).

Visualization in a virtual environment

Relevant information related to the current radiation propagation is shown in a virtual environment. This enables the system to be also applied in rooms without ceiling-mounted cameras if access to the imaging device's API is available. The point-of-view of the virtual visualization can be modified by the user for looking at the scene from different perspectives. As it can be seen in figures 7.1 and 7.2, 3D models of the C-arm and operating table, the 3D propagation of scattered radiation and the 3D position of the persons in the room are displayed. Furthermore, the 3D dose deposition over the patient's organs and skin is shown in an additional virtual visualization window. As depicted in figure 7.3, the user can open such a visualization through the system's GUI and the displayed patient exposure map is updated according to current imaging projection and protocol. The approach described in section 5.1.2.2 is applied for an intuitive display of the simulated dose maps as color-coded rendered volumes.

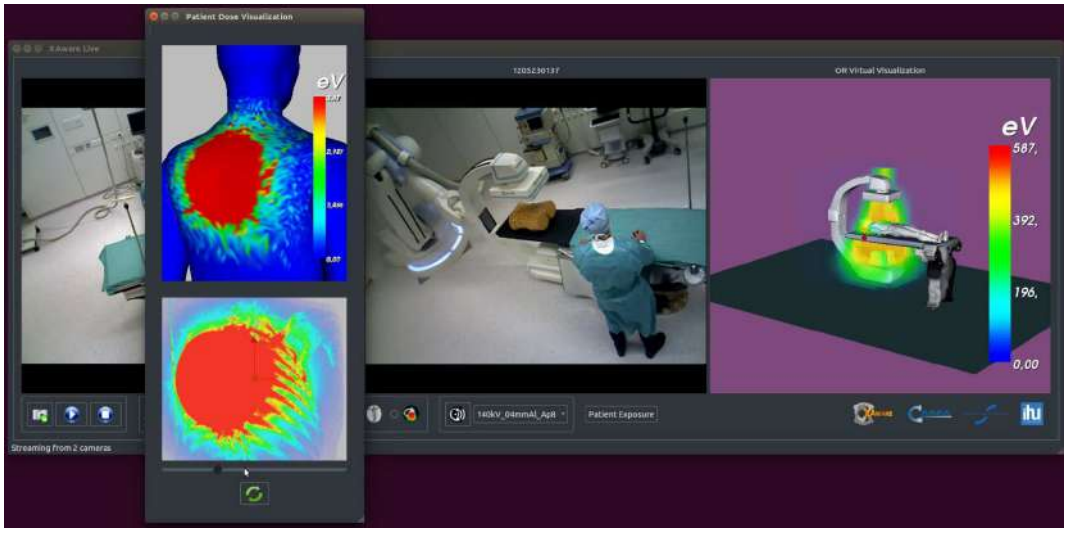

Figure 7.3: Visualization of the patient's dose to the internal structures and to the skin for the current X-ray imaging device's projection and imaging protocol on *XAware-Live*.

AR visualization

The 3D scattered radiation propagation for the current C-arm angulation is shown in an AR manner over the ceiling cameras' color images. The approach presented in 5.1.2.1 is applied to register rendered volumes over the images for this visualization mode. As illustrated in figure 7.4, such a visualization provides the user with a direct feedback of the highly irradiated areas for the current C-arm angulation and imaging parameters.

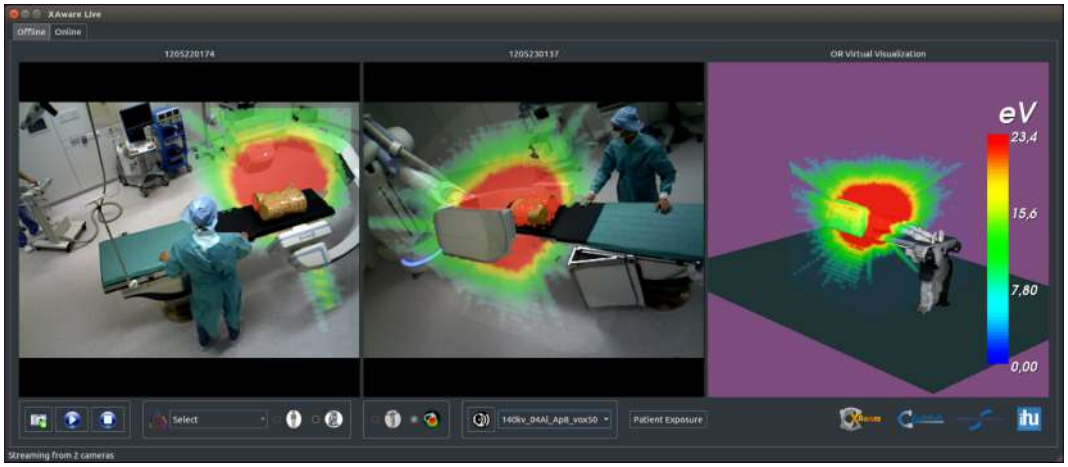

Figure 7.4: AR visualization of the intensities and of the 3D propagation of scattered radiation for the current C-arm projection with *XAware-Live*.

Similarly, the human poses' information is applied to segment the attending persons' shapes on the color images. The obtained foreground masks are then colored according to the simulated radiation intensity at each 3D location to provide feedback about the exposure to the persons' body-parts. An example is shown in figure 7.5, where it can be observed that the clinician standing on the X-ray source's side is more exposed to scattered radiation. His left arm, which is positioned directly on the beam's path, is colored in orange/red.

7.1.3 Demonstrations and feedback about the system

Demonstrations[3] of *XAware-Live* have been performed to our collaborating clinical and industrial partners. Initial feedback has been positive since the system provides *in-situ* feedback about radiation exposure in an OR in an intuitive manner. We show in figures 7.6 pictures of two of these demonstrations: one to representatives of our industrial partner Siemens Healthcare, and the other to a group of medical fellows from IHU Strasbourg. The potential of the system to be employed as a tool to teach about radiation's diffusion effects has also been acknowledged in the demonstrations. Indeed, using *XAware-Live* would enable to teach trainees intuitively in real clinical conditions. We also presented

[3]We thank Dr. Konstanze Gunzert and Dr. Bruno Mutet for kindly helping us organizing the demonstrations of *XAware-Live*, along with Mourad Bouhadjar and all radiology staff from IHU for their assistance.

Figure 7.5: AR visualization of the current personnel's body radiation exposure with *XAware-Live*.

the system to one of the radiation safety officers[4] from Strasbourg's University Hospital. He was also enthusiastic about the fact that visual feedback can render more intuitive the current training sessions, as these are based on students gathering and comparing measurements from dosimeters for different room lay-outs and C-arm configurations. He suggested that educational videos featuring our system in practice could be distributed and shown to students during training lectures.

Figure 7.6: Demonstrations of *XAware-Live* to our industrial partners (left) and to IHU Strasbourg's medical fellow staff (right).

7.1.4 Future developments

As discussed before, our system has the potential to become a teaching tool that could be used in conjunction with interventional surgery training courses or during surgical training involving animals. This would allow trainees to learn *in-situ* the effects of the parameters affecting radiation propagation. However, to fulfill the full potential of *XAware-Live*, further technical improvements have yet to be performed. First of all, the system currently shows the worst-case scenario of radiation propagation, namely when no

[4]We thank Dr. Nicolas Clauss for his feedback about the system.

lead protective shields are present. Yet, to teach about the proper use of lead protection, such screens should be tracked and be included in the simulations and visualizations. For a teaching system, it would be acceptable to place markers on the lead screens for their tracking. This would allow the system to provide visualizations of the room shielding's effect on scattered radiation during training sessions, such as the ones previously shown in figure 5.3. Second, the simulations of the scattered radiation propagation should be performed online while considering the current room lay-out and lead equipment disposition. As explained in section 4.3.1.2, such simulations can be performed in a few milliseconds with our GPU-accelerated approach. Nevertheless, for this to be feasible, the system should be able to obtain the imaging protocol information directly from the device, which is not possible through the API's license we currently have access to. Third, in the current prototype, the clinician tracking and the AR visualizations have a framerate of 4 fps. Increasing such a framerate can be possible by re-implementing several of the current approaches on GPGPU and by executing them in parallel on multiple GPUs. Fourth, integrating an OST-HMD (*e.g.* HoloLens) to the system to provide visual feedback directly in the user's view can be a promising step to make the training sessions more intuitive and engaging.

7.2 Potential clinical applications

The approaches presented in this thesis have set the foundations to potential clinical applications for reducing radiation exposure in medical environments. We dedicate this section to present concepts for several applications. Note that the potential lines of research spawn from the work of this thesis are presented in section 8.2. Following the same paradigm of reducing radiation exposure either in an "active or passive" manner, we first present applications for increasing intraoperative awareness to radiation and, second, for optimizing the C-arm poses within or before a procedure.

7.2.1 Intraoperative radiation awareness

We hereby outline three potential clinical applications we can foresee, which are based on the approaches presented in chapters 3, 4 and 5.

Virtual dose visualization tool

As raised by one of our industrial partners, fixing cameras to the ceiling of an OR may not always be convenient or even permitted. As a possible alternative, an intraoperative system could show in real-time the patient's dose along with the scattered radiation around the patient in a virtual environment. This would provide useful information to raise awareness to patient exposure and inform about the irradiated areas around the patient. A radiation simulation would incorporate data from the current C-arm configuration, imaging protocol and patient parameters for simulating in real-time the dose maps to display. We show in figure 7.7 a concept for a GUI for this application. Such a system would allow clinicians and radiographers to visualize intraoperatively and in real-time the

current scattered radiation along with the instantaneous and/or accumulated dose to the patient's organs and skin. This tool could be directly integrated to modern X-ray imaging devices for them to give a more complete and accurate radiation dose feedback during the imaging process than the metrics currently provided (see section 2.1.1). However, for such a system to present accurate patient dose and scatter information, it would be necessary to use a patient-specific preoperative model in the Monte Carlo simulations. Such a model would have to be registered to the real patient's pose, which could either be performed manually, using information from the robotized table's pose or by using an X-ray image acquired in the beginning of the procedure.

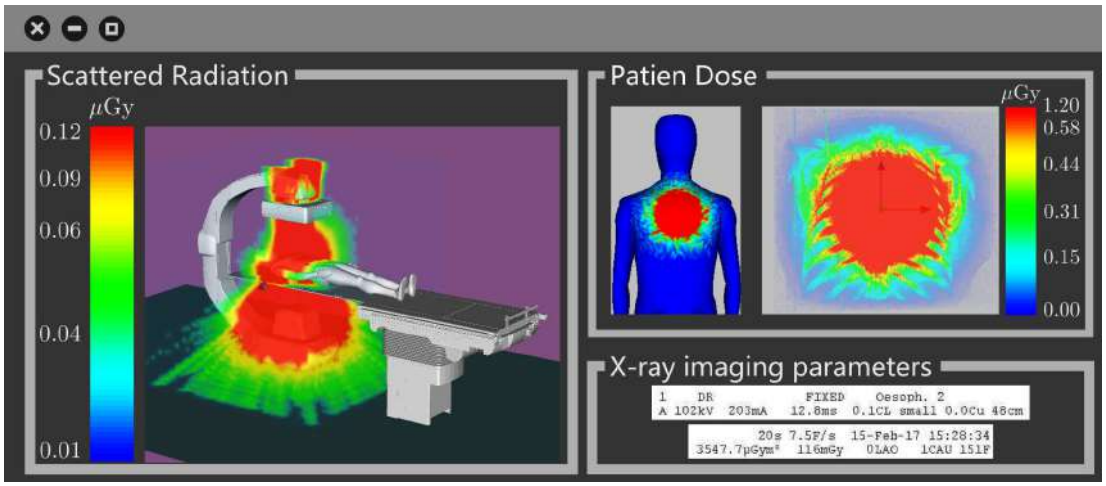

Figure 7.7: Concept of a GUI for an intraoperative tool displaying the current scattered radiation and patient dose in a virtual environment.

Postoperative radiation exposure review tool

A setup of multiple RGBD cameras installed in an interventional room could be used to obtain recordings of X-ray guided procedures, synchronized with data from the imaging device and from the active personal dosimeters worn by the medical staff during the procedure. A postoperative radiation exposure review system could process this data to provide objective statistics about radiation events. It would help verifying that the safety guidelines such as the disposition of protective equipment, the personnel's positioning during the irradiations, and the dose protocols are properly respected. Indeed, as illustrated in figure 7.8, this tool would be particularly useful for the hospital's radiation safety officer to easily identify potential radiation safety risks and to visualize moments where atypical dose values were registered by the staff's dosimeters. Surgical activity recognition approaches [Twinanda 2016] could be integrated to precisely assess the dose generated at each step of a procedure or exam. Statistics could be generated to compare practices among personnel, procedures, protocols and hospitals regarding radiation safety. Hence, such a system could contribute to devise safer surgical workflows and to determine the best practices for reducing radiation exposure while obtaining high-quality images.

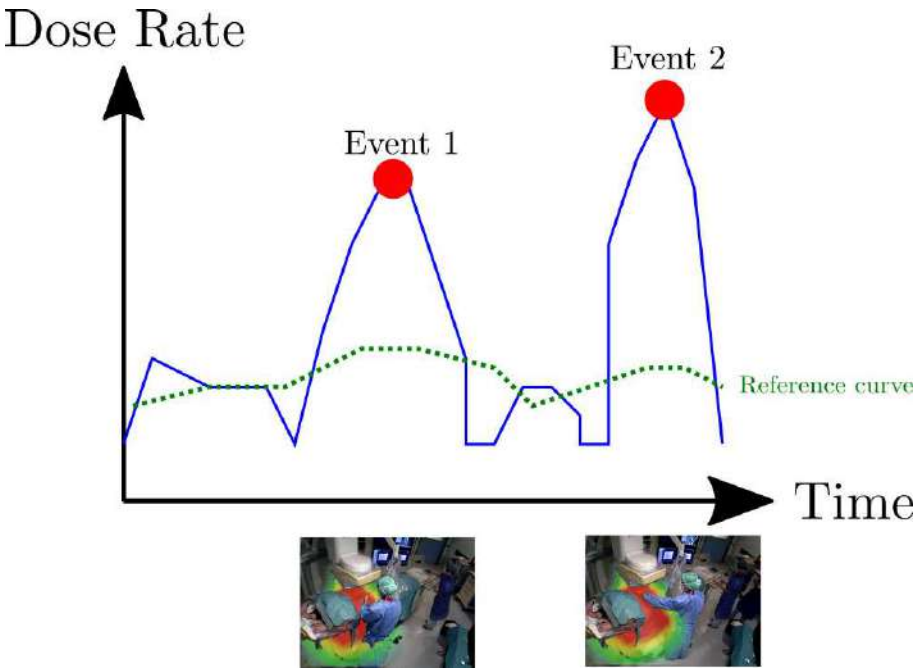

Figure 7.8: Postoperative review of atypical dose events recorded by dosimeters during an X-ray guided procedure, with an AR visualization of the propagation of scattered radiation during such events.

Intraoperative context-aware radiation monitoring

A version of *XAware-Live* suitable for intraoperative use could assist medical staff in remaining aware to ongoing radiation exposure levels. Such a context-aware system would have to integrate information about the current positions of the lead protective shields, medical equipment and attending personnel into real-time radiation simulation and visualization frameworks. If a preoperative model if not available, the patient's shape could be reconstructed with cameras, as required for the simulation of scattered radiation and of the patient skin and organ dose.

7.2.2 Clinical applications of a C-arm pose optimization approach

We presented in chapter 6 an optimization approach to estimate a C-arm pose reducing radiation exposure while maintaining the clinical quality of the output X-ray image. In section 6.2.4 we described a potential workflow (summarized in figure 6.4) of how it could be applied intraoperatively to recommend optimal X-ray angulations minimizing the patient and staff exposure in the current context. However, since such an approach enables to explore several close C-arm configurations and determine the one which causes the least radiation exposure, it could also be incorporated into a preoperative planning tool. Such a tool could assist clinicians in defining an optimal planning in terms of C-arm angles and parameters minimizing patient dose for an upcoming procedure. This would be similar to existing systems in radiotherapy applications, which are used for planning

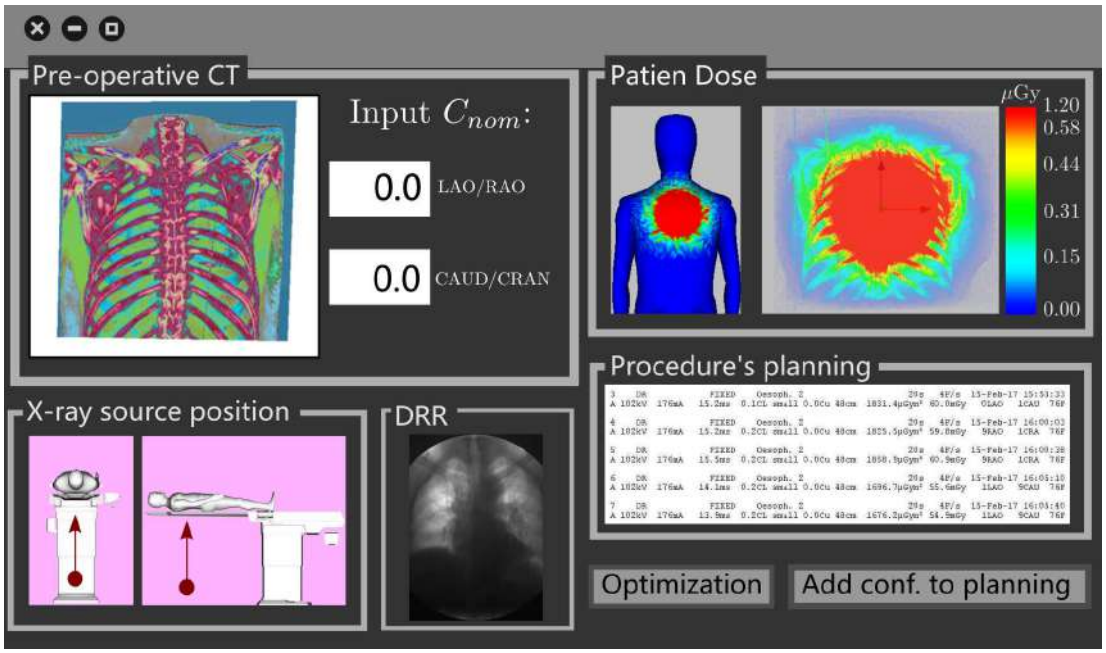

Figure 7.9: Concept for a preoperative procedure planning application to determine the optimal C-arm poses yielding the lowest dose to the patient in an upcoming procedure.

the optimal positioning of radioactive seeds using simulations [Lemaréchal 2015].

We present in figure 7.9 a conceptual GUI for such a preoperative C-arm pose planning system. For each step of the procedure, the user inputs the standard/nominal C-arm pose and the system recommends through an optimization approach a configuration enabling to reduce patient dose. For each recommended pose, a simulated digital radiography is displayed along with patient dose statistics computed in real-time. With this information, the user could decide whether to include the recommended pose to the planning or to keep the standard one. Moreover, information about previously irradiated body-areas of the patient could be integrated into the optimization. Indeed, obtaining the optimal C-arm configurations for an upcoming procedure would allow avoiding unnecessary image acquisitions and/or reducing patient overexposure risks.

7.3 Conclusions

We presented in this chapter our system *XAware-Live*, which is, to the best of our knowledge, the first radiation awareness system demonstrated in an interventional room. Such a system provides real-time feedback about the current propagation of scattered radiation along with the current patient and attending personnel dose. Moreover, we outlined in section 7.2 additional potential clinical applications of the approaches presented in this thesis, which could contribute to improve radiation safety.

8 Conclusions and perspectives

The time is gone, the song is over, thought I'd something more to say...
– *Time*, Pink Floyd (Roger Waters)

Chapter Summary

8.1 Conclusions 135
8.2 Perspectives 138

In this chapter, we conclude this dissertation by summarizing the contributions of our work. We also discuss the possible directions of future research in order to address the current limitations and improve the performance of the methods.

8.1 Conclusions

Medical imaging devices involving ionizing radiation are associated with the noxious adverse effects of radiation exposure. As the popularity of image-guided minimally invasive surgery increases, radiation exposure further becomes a concern for health care providers. There is an inherent need to improve radiation safety when X-rays are used for diagnostic or therapy delivery. Exposure to ionizing radiation can lead to negative effects such as cancers, and currently there are no means to intraoperatively depict the 3D propagation and magnitude of ionizing radiation. Indeed, several patient, equipment and/or procedure dependent factors affect the magnitude and spatial distribution of

radiation inside the OR, which render irradiated areas and the amount of radiation hard to predict. The invisible nature of X-rays and the lack of immediate effects to exposure also lead to reduced awareness and concerns about such risks. Therefore, we have presented throughout this thesis novel approaches to improve X-ray radiation safety for patients and medical staff, by acting in two complementary directions. First, we have proposed methods to improve radiation monitoring and to increase staff's awareness of radiation risk and patient dose, by providing in-situ visual feedback of the current radiation exposure. Second, we have introduced an approach to recommend X-ray device's configurations which are less irradiating for both patient and clinical staff in a given surgical task, determined through an optimization approach considering the current room context. We presented in the previous pages all the approaches and methods developed during this thesis for making the two aforementioned applications possible. In the paragraphs below, the main contributions from each chapter are recapitulated.

Our radiation monitoring approaches rely on the real-time perception of the layout of the surgical room. We described in chapter 3 the framework we developed for perceiving and modeling the OR context as required for such approaches. Our setup is composed of multiple registered ceiling-mounted RGBD cameras, which are also used for keeping track of the X-ray device configuration and/or of the positioning of equipment and clinicians in the room.

Moreover, we described in chapter 4 two radiation simulation approaches developed in this thesis. Both apply Monte Carlo methods to compute the propagation of X-rays and the deposited dose for a given imaging protocol and room lay-out. They have been crucial for the development of the two targeted applications of this thesis. Also, these approaches have been validated experimentally with measurements from dosimeters acquired in a hybrid room during several clinically relevant scenarios. The obtained results showed that the error between the simulated and measured dose values is in agreement with the intrinsic error of the dosimetric system we use. Our latest radiation simulation approach exploits the computing capabilities of GPUs to achieve quasi real-time performance in the simulation of the 3D propagation of scattered radiation and patient dose, as necessary for potential clinical applications.

We have presented in chapter 5 our approach for improving radiation safety by making ionizing radiation visible through different visualization modes. These visualizations rely on our multi-camera setup and tracking/registration methods, along with the radiation simulation approaches. We propose to use AR for giving a user the capability to visualize the current patient/staff dose and the 3D distribution and intensity of scattered radiation. Intraoperatively, this can contribute to increase radiation awareness and reduce overexposure risks for both patients and staff. Also, clinicians can adapt their positioning and the disposition of the protective equipment thanks to the provided visual feedback. Preoperatively, these visualizations have the potential to be included into training tools to teach about radiation behavior and about the best safety practices intuitively.

Furthermore, we described in chapter 6 a novel approach to actively reduce radiation exposure in the context of the OR by exploiting the articulated construction of

mobile/robotized C-arms. Such an approach takes into account the OR's context, the imaging parameters and the clinical staff's positioning to estimate the overall exposure to radiation and perform an optimization of the C-arm's pose. Indeed, our approach suggests a configuration preserving the visibility in the image outcome while reducing the dose delivered to patient and staff. It relies on an optimization algorithm applying Monte Carlo simulations to compute in near real-time radiation exposure statistics at each iteration, which correspond to the current room lay-out and acquisition parameters. Such an approach could actively participate as a decision support tool during X-ray guided procedures to suggest a less irradiating C-arm pose for the current room context. Relying on our GPU-accelerated radiation simulation methods, it can also provide useful radiation exposure statistics in near real-time that can assist the attending personnel in adapting the use of radiation protection measures accordingly. The potential of our approach was first evaluated through simulations reproducing a clinical environment. These experiments helped assessing our method's capabilities to suggest a less irradiating configuration in a few seconds. Second, a study with real dose measurements acquired in a hybrid room was performed to verify that the dose reduction ratios predicted by our approach are close to the real ones. It also enabled us to confirm the fact that even a small change in a C-arm pose can contribute to decrease the dose to a clinician.

Finally, in chapter 7 we discussed an existing and several potential clinical applications of the aforementioned approaches. We first described a real-time radiation awareness demonstrator that has been implemented in an interventional room containing a robotized X-ray imaging device. Such a system relies on our multi-camera setup along with our radiation simulation and visualization approaches to provide real-time visual feedback about the current radiation exposure. Thanks to a direct communication with the robotized imaging device's API, the system is able to show the current propagation of scattered radiation along with the patient and attending personnel dose. This prototype system has the potential to be used as a teaching tool to teach about ionizing radiation diffusion effects or to be further improved to be applied to monitor radiation exposure intraoperatively. We also laid out other exciting potential clinical applications that can be spawn from the approaches presented in this dissertation. For instance, an application relying on our C-arm pose optimization method to assist clinicians in the preoperative planning of an X-ray guided procedure. Such a tool could automatically recommend the optimal C-arm configurations reducing patient dose for the upcoming procedure.

In this thesis, we have presented novel approaches to contribute to the minimization of radiation exposure during interventional procedures, which we hope can lead to the improved health of surgeons, interventional radiologists, radiographers and patients. Indeed, these approaches can help improving medical staff's awareness to radiation exposure risks, assist them in the proper usage of protective equipment and on the optimization of the overall clinical workflow to improve radiation safety. Being able to monitor radiation exposure more precisely can also make surgeons in the hybrid operating room less apprehensive of radiation risks. Furthermore, better awareness and reduced exposure can also lead to greater acceptance of minimally invasive procedures and hybrid

rooms that heavily depend upon the use of X-ray technologies, and are planned to be routinely utilized by clinicians from a variety of disciplines. By way of consequence, improving radiation safety can facilitate greater and safer access to X-ray-based minimally invasive surgery options to a wider population.

8.2 Perspectives

With hindsight, several possible lines of research spawn from the work presented in this dissertation. These open up possibilities for exciting research problems and/or for the further development of new applications for tomorrow's OR. Several perspectives of our work are outlined below.

Radiation awareness training One of the most pertinent perspectives concerns the development of a working prototype of a radiation awareness system to be used during training sessions in a hybrid operating room. Such a tool will enable quick and effective instruction of radiation safety to untrained staff members, and also to have a visual tool to assess the radiation risks in different real situations. It will also allow to teach and to understand potential safety issues associated with a procedure by reviewing the procedure postoperatively. A prototype system has already been developed (*i.e. XAware-Live*). However, as discussed in section 7.1.4, it still is subjected to certain limitations that have to be addressed (visualization/clinicians' tracking frame-rate, pre-computed radiation maps, etc...). Moreover, the pose of the lead protective shields should be tracked and this information included in the simulations. This would allow to show in real-time during a training session the effect that the positioning of the lead shields have on the diffusion of scattered radiation, and to teach about their optimal positioning for each C-arm angulation. Educational videos recorded in centers where such a radiation awareness training system would be installed could also be diffused to trainees from other institutions or used by international radiation protection agencies. Furthermore, the use of an HMD could also be considered to teach about radiation safety in an engaging game-like manner. This would allow to immerse the user in a virtual OR environment, where he/she could learn about the best safety practices safely and anywhere.

Validation studies The impact of a radiation awareness training system should be demonstrated and evaluated during radiation safety teaching/training sessions for hybrid procedures. Experiments to collect formal feedback from clinicians and staff on the usability of the system in order to improve its interface and visualizations should be performed. The benefits of the AR/VR visualizations and the opinions of trainees and supervisors should be quantitatively and qualitatively assessed and validated.

Extensions to the radiation simulation approach One could also foresee a number of future lines of research in the context of our radiation simulation approach. First, as Monte Carlo-based radiation simulations compute dose data relative to the number

of simulated particles and to the approximations in the simulation, the best way to calibrate the simulations should be further investigated. Relative dose data may be good enough for a radiation awareness system, yet, absolute dose values would be required for other applications (*e.g.* patient/staff dose review). Using the radiation metrics provided by the X-ray imaging device (*e.g.* DAP or Kerma Air) for calibrating the simulations may be feasible, however, these measures can be prone to errors since they are based on approximations. Pre-computing calibration factors per imaging device through extensive measurement campaigns using ionization chambers may also be a less practical but more precise alternative. Second, the best approach to model a practitioner in the simulation remains an open question. As in the literature, we model staff as water-filled volumes. However, for providing feedback about the exposure per body-part for a given practitioner, it would be necessary to include an articulated human model in the simulation and deform it according to the person's current pose. This model could include the person's lead clothing too to be able to compute the dose over/under the lead apron or to simulate the particles scattered by clinicians. Further investigation could be done to determine if a generic water-filled model would be enough or a person-specific model with organ/tissue information is required. Third, a simulation strategy to simulate fluoroscopy in real-time should be further investigated. While the simulation of a patient dose map for a single radiography takes several seconds even on GPU, the simulation approach should still be further accelerated to reach the fluoroscopy rates of several frames per second. The accumulated patient dose during fluoroscopy could then be obtained directly with such an approach. Fourth, for an intraoperative radiation awareness system relying on real-time simulations computed on-the-fly, it would be interesting to investigate smart approaches to simulate only new imaging scenarios not seen before by the system. Indeed, during a procedure, a given room lay-out or imaging protocol may be repeated several times and therefore it would not be necessary to simulate it again. A dynamic lookup table could be built on-the-fly with previous patient/scatter dose maps simulated online, which would be reload when necessary.

Patient model's influence Our current radiation simulation approaches require a patient model (generic or preoperative CT) for the dose computation. For scenarios where a preoperative model of the patient may not be available, it would be interesting to determine what the actual influence of the patient model in the simulated dose values is. Indeed, the use of a generic model chosen from a discrete set of patient weight/height ranges, may possibly be enough for simulating patient dose and scattered radiation with a precision acceptable for a radiation safety application. Otherwise, it may also be interesting to investigate the feasibility of capturing the patient's 3D shape using the reconstruction from the multi-camera system and including this information in the simulation.

Monitoring of staff's accumulated dose Occupational radiation risk is primarily due to chronic exposure, whose noxious effects can take years to manifest (*e.g.* eye

cataracts and cancers). Monitoring the accumulated dose per body-part of interventional radiologists and attending personnel is thereby significantly important. Nevertheless, this requires to individually track the 3D trajectory of each person's body-parts during a procedure, which can still be challenging to achieve for vision-based approaches due to occlusions and cluttered medical environment. Still, if it is achieved, radiation simulations would provide useful information to assess the daily/monthly/yearly exposure of clinicians to unprotected body-parts for which suitable dosimeter options are still not available. This exposure data would also be useful for a hospital's radiation safety officer to review the medical staff's dose levels and recommend actions to reduce overexposure risks.

Surgical workflow and radiation exposure Surgical activity recognition approaches [Twinanda 2016] could be applied to correlate parts of the procedure's workflow to radiation exposure values, and also to precisely assess the radiation dose generated at each step of a procedure or exam. It would then be possible to identify the riskiest steps of a given procedure for the patient and the attending clinicians in terms of radiation exposure. Such information would thereby contribute to devise safer workflows for image-guided interventions and recommend optimal positioning of room shielding/lead protections. Furthermore, statistics could be generated to compare practices among personnel, procedures, protocols and hospitals regarding radiation safety. The best practices for reducing radiation exposure while achieving the required high-quality images could be determined thanks to these approaches. Moreover, this knowledge can contribute to the development of context-aware decision support tools to assist in the optimization of the layout of operating/examination rooms and/or suggest imaging device's configurations which minimize the radiation doses delivered to each of the persons involved.

X-ray pose and image optimization As discussed in section 6.5, our approach to recommend a safer X-ray imaging device's pose in terms of radiation exposure can be further extended to include additional relevant information for a more complex optimization. Indeed, the 3D position of personnel and equipment in the scene could be included to avoid collisions with the suggested configuration. This would be particularly interesting for robotized imaging devices since it would allow them to perform automated trajectories more rapidly. Also, an algorithm to minimize the dose received at a specific organ or skin area of the patient could be beneficial specially to patients that have been previously irradiated at some body locations and/or for tasks requiring long exposure times with the same X-ray source positioning. Data from a patient's previous exposures could be included in the optimization for cases when balancing the trade-off of reducing patient and staff dose is complex. Indeed, a person's dose record (staff or patient) could be applied to determine optimal weights for the patient and staff exposure terms in the cost function. Furthermore, our approach could also be extended to optimize the 3D position of a clinician around the patient to reduce his/her exposure to scattered radiation or to optimize the positioning of the lead protective shields for a given fluoroscopy-guided surgical task. Also, an additional term applying geometrical constraints to quantitatively

assess the target visibility in the outcome X-ray image could be included. This would allow to also optimize the visibility of the targeted anatomical structure in the outcome image directly in the optimization loop. A C-arm pose optimization system could not only be useful as a decision support tool in the context of the procedure, but also preoperatively to optimize a procedure's planning to minimize patient dose.

Extension to other disciplines Awareness systems can address needs from other disciplines involving exposure to noxious elements. Similar approaches could be developed for monitoring exposure coming from naturally occurring sources of radiation or from industrial applications (*e.g.* nuclear power plants). In the medical field, similar simulation and visualization approaches could be envisaged for nuclear imaging procedures or for monitoring the exposure to the electromagnetic fields generated by MRIs.

Global radiation monitoring As healthcare is changing towards adopting a personalized and predictive model, we envision that radiation safety will follow the same trend and dose monitoring will be decentralized from the OR to a person's entire life. Tomorrow, a person's radiation dose monitoring will be performed in a global way for both patients and medical staff. A personalized 3D model could be used to store the dose values received by the organs during all exposures to ionizing radiation from medical devices throughout one's lifetime. This will be possible thanks to fully context-aware operating and examination rooms where all devices are connected and their signals analyzed and interpreted by a central system acting as surgical control tower [Maier-Hein 2017]. Precise dosimetry computations will be performed by using the knowledge of the imaging device's configuration, the layout of the room and the person's pose and physiological information. Skin and organ doses delivered to both patient and personnel, respectively exposed to direct radiation and scatter, will be then accumulated in their personalized 3D irradiated model. Moreover, data analysis of a person's lifetime radiation exposure and medical records will be crucial to improve the current dose-response models. Not only it will allow to accurately predict the probabilities of occurrence of adverse effects but also to justify and optimize following exams by providing precise dose and imaging protocols. In case of risk, the use of an alternative non-irradiating modality could be suggested instead. On the personnel's side, occupational exposure will be fully assessed and the amount of interventional procedures and diagnostic exams performed by nurses, radiologists and clinicians will be automatically managed to optimize their yearly accumulated exposure.

List of Publications

Patents

Nicolas Padoy, Nicolas Loy Rodas, Michel de Mathelin, Julien Bert and Dimitris Visvikis, *Method for determining a configuration setting of a source of ionizing radiation*, EU application, January 2017.

Nicolas Padoy and Nicolas Loy Rodas, *Method for estimating the spatial distribution of the hazardousness of radiation doses*, WO2016020278 A1, 2014.

Book chapters

Nicolas Loy Rodas and Nicolas Padoy, *Augmented Reality for reducing intraoperative radiation exposure to patients and clinicians during X-ray guided procedures.* In Terry Peters, Ziv Yaniv, and Cristian Linte, editors, Mixed and Augmented Reality in Medicine, 2018.

International journals

Nicolas Loy Rodas, Fernando Barrera and Nicolas Padoy, *See It With Your Own Eyes: Marker-less Mobile Augmented Reality for Radiation Awareness in the Hybrid Room*, IEEE Transactions on Biomedical Engineering (TBME), 64(2), 429-440, 2017.
Supplementary video: https://youtu.be/rHq_5OT-Uk0

Nicolas Loy Rodas and Nicolas Padoy, *Seeing is believing: increasing intraoperative awareness to scattered radiation in interventional procedures by combining augmented reality, Monte Carlo simulations and wireless dosimeters*, International Journal of Computer Assisted Radiology and Surgery (IJCARS), 10(8), 1181-1191, 2015.

International conferences with proceedings

Nicolas Loy Rodas, Julien Bert, Dimitris Visvikis, Michel de Mathelin and Nicolas Padoy, *Pose optimization of a C-arm imaging device to reduce intraoperative radiation exposure of staff and patient during interventional procedures*, IEEE International Conference on Robotics and Automation (ICRA), 2017, **Oral presentation**.
Supplementary video: https://youtu.be/NEB782eCCRM

Nicolas Loy Rodas, Fernando Barrera and Nicolas Padoy, *Marker-Less AR in the Hybrid Room Using Equipment Detection for Camera Relocalization*, Medical Image Computing and Computer-Assisted Intervention (MICCAI), 2015, **Long oral presentation**.
Supplementary video: https://youtu.be/N5BpO6QiDic

Nicolas Loy Rodas and Nicolas Padoy, *3D Global Estimation and Augmented Reality Visualization of Intra-operative X-ray Dose*, Medical Image Computing and Computer-Assisted Intervention (MICCAI), 2014, **Long oral presentation**.
Supplementary video: https://youtu.be/pINE2gaOVOY

Abstracts presented in international conferences

Nicolas Loy Rodas, Abdolrahim Kadkhodamohammadi, Michel de Mathelin, Afshin Gangi and Nicolas Padoy, *A Global Radiation Awareness System using Augmented Reality and Monte Carlo Simulations*, European Congress of Radiology (ECR), 2018, **Cum Laude Best Poster Award**.
Supplementary video: https://youtu.be/JpATPDrXvu8

Nicolas Loy Rodas, Pamir Ghimire, Michel de Mathelin, Afshin Gangi and Nicolas Padoy, *Teaching Radiation Safety intuitively with a Head-mounted display*, European Congress of Radiology (ECR), 2018, **Oral presentation**.
Supplementary video: https://youtu.be/lflbEWC5VsA

International workshops without proceedings

Nicolas Loy Rodas and Nicolas Padoy, *Radiation safety in tomorrow's hospital*, Surgical Data Science Workshop, Heidelberg, Germany, 2016.

Appendices Part IV

A Radiation dose information

A.1 Radiation dose measurements

Radiation dose is a measure of the amount of exposure to radiation. There are three kinds of dose used in radiological protection: *absorbed dose*, *equivalent dose* and *effective dose*.

Absorbed dose is the amount of physical energy that is deposited in a unit of matter [Kaplan 2016], and the units *Gray* (Gy) and *Rad* are used to measure it. *Equivalent dose* is used to estimate the biological damage from the different types of radiation that is absorbed by tissues, and the units *Sievert* (Sv) and *Roentgen equivalent man* (Rem) are used to measure it. A given radiation dose value will have different effects depending on the type of radiation and the composition of the tissue affected. Therefore, to determine the equivalent dose (Sv), absorbed dose must be multiplied by a quality factor W that is unique to each type of radiation [Kaplan 2016]. For X-ray radiation, $W = 1$. *Effective dose* (whole-body dose) is calculated for the whole-body and is expressed in millisieverts (mSv). It is the sum of the equivalent dose to all organs, each adjusted to account for the sensitivity of the organ to radiation [ICRP 2017].

A.1.1 Conversions between radiation dose units

- 1 Gy = 1 Joule per Kg of matter
- 1 Gy = 100 Rads
- 1 Sv = 100 Rem
- 1 Sv = 1 Gy $\times W$
- For X-ray radiation: 1 mSv = 1 mGy

A.2 Radiation dose values, thresholds and occupational limits

A.2.1 Radiation dose values for common exams

Table A.1: Typical organ radiation dose from various radiologic studies, as reported in [Brenner 2007], [FDA 2010] and [Conti 2014].

Study type	Organ/Exam	Equivalent Dose (mGy)
Dental radiography	Brain	0.005
PA chest radiography	Lung	0.01
Lateral chest radiography	Lung	0.15
AP abdominal radiography	Stomach	0.25
Screening mammography	Breast	3
Adult abdominal CT	Stomach	10
Barium enema	Colon	15
CT	Coronary Angiography	16
Neonatal abdominal CT	Stomach	20
Interventional Fluoroscopy	Transjugular Intrahepatic Portosystemic Shunt Placement	70
USA natural dose (annual)		3.6

A.2.2 Radiation exposure thresholds

The X-ray beam is typically directed to a relatively small patch of skin and the length of time such a patch is exposed can be high especially when fluoroscopy is used [Miller 2005]. In some cases, the dose to the irradiated skin area can be high enough to cause damage. Table A.2 presents threshold doses for potential radiation effects with related time of onset (time it takes for the effect to manifest), as reported in [Miller 2005].

Table A.2: Threshold doses for potential radiation exposure effects, as reported in [Miller 2005].

Effects	Threshold dose (Gy)	Time of onset
Skin		
Early transient erythema	2	2-24 hours
Main erythema reaction	6	≈1.5 weeks
Temporary epilation	3	≈3 weeks
Permanent epilation	7	≈3 weeks
Dermal necrosis	>12	≈52 weeks
Eye		
Lens opacity (detectable)	>1-2	>5 years
Lens cataract	>5	>5 years

A.2.3 Dose limits as recommended by the ICRP

The following dose limits are currently recommended by the ICRP in [ICRP 2017] for both medical staff working with X-rays and the public. Exceeding a dose limit is contrary to regulations in most countries.

Table A.3: Dose Limits Recommended by the ICRP in [ICRP 2017].

Type	**Occupational exposure**	**Public exposure**
Effective Dose	20 mSv per year, averaged over 5 years, with no single year exceeding 50 mSv	1 mSv in a year
Equivalent Dose to the Lens of the Eye	20 mSv per year, averaged over 5 years, with no single year exceeding 50 mSv	15 mSv in a year
Equivalent Dose to the Skin	500 mSv in a year	50 mSv in a year
Equivalent Dose to the Hands and Feet	500 mSv in a year	-

The limits on effective dose are designed to avoid a risk of stochastic effects and the limits on equivalent dose to an organ, to prevent the occurrence of deterministic effects [ICRP 2017].

A.3 Radiation exposure metrics

The most used dosimetric indications to monitor the likely exposure of a patient during a procedure are the following:

Fluoroscopy time: measure in minutes, is the total amount of time that fluoroscopy is utilized during an imaging or interventional procedure [Kuhls-Gilcrist 2017].

Number of radiographic images: is a count of the number of digital acquisitions or cine recordings.

Air Kerma: is the energy extracted from an X-ray beam per unit mass of air in a small irradiated air volume. For diagnostic X-rays, it corresponds to the dose delivered to that volume of air [Kwon 2011].

Reference Air Kerma (RAK): also known as reference dose, cumulative dose, or cumulative dose at a reference point, is the air kerma accumulated at a specific point in space (the patient entrance reference point) relative to the fluoroscopic gantry. For C-arm fluoroscopic systems, the patient entrance reference point is a point along the central ray of the X-ray beam, 15 cm back from the isocenter toward the focal spot [Kwon 2011]. It is an actual indication of the radiation output from the X-ray tube.

Dose Area Product (DAP): also known as Kerma Air Product (KAP), is the integral of air kerma across the entire X-ray beam emitted from the X-ray tube [Kwon 2011]. It is a surrogate measurement for the entire amount of energy delivered to the patient by the X-ray beam and is most often utilized in estimating stochastic risk [Kuhls-Gilcrist 2017].

Peak Skin Dose (PSD): the greatest absorbed skin dose at any point on the patient's skin. PSD can be measured using film or dosimeters placed on the patient. However, these require prior planning and must be placed accurately at the site. Approaches for estimating PSD through regression formulas using the RAK and PSD can be found in the literature [Kwon 2011].

B xawAR16 dataset

B.1 A multi-RGBD camera dataset for camera relocalization evaluation in the operating room

Figure B.1: Sample images from the xawAR16 dataset recorded with three RGBD cameras (two ceiling-mounted and a mobile one) in an OR, with ground-truth pose information of the mobile camera.

xawAR16[1] is a large multi-RGBD camera dataset we generated inside a hybrid operating room (IHU Strasbourg, France) containing a robotized X-ray imaging device, an operating table and other medical equipment in the background. Such a dataset has been designed to evaluate the tracking/relocalization of a hand-held camera which is moved freely at both sides of the operating table under different scene configurations. It can also be used for the evaluation of SLAM or mobile AR applications inside an OR. To our knowledge, this is the first multicamera dataset of its kind, since similar existing datasets [Sturm 2012] were recorded in controlled environments such as offices or empty halls using a single RGBD camera.

The dataset is composed of 16 sequences of time-synchronized color and depth images

[1] I would like to thank Dr. Fernando Barrera and Vikram Mohanty for assisting me in recording and compiling the xawAR16 dataset.

in full sensor resolution (640×480) recorded at 25 fps, along with the ground-truth poses of the moving camera measured by the tracking device at 30 Hz. Each sequence shows different scene configurations and camera motion, including occlusions, motion in the scene and abrupt viewpoint changes. Sample frames from each camera view are shown in figure B.1. This dataset was presented in [Loy Rodas 2017a], where it was used to evaluate our marker-less mobile camera relocalization approach described in appendix C. To encourage the development of novel methods for visual odometry, 3D reconstruction and/or SLAM for medical applications, we have made this dataset publicly available[2].

B.2 Dataset description

The recording setup is shown in figure B.2. Three RGBD cameras (Asus Xtion Pro Live) were used to record this dataset. Two of them are rigidly mounted to the ceiling ($\mathbf{C_1}$ and $\mathbf{C_2}$) in a configuration allowing them to capture views from each side of the operating table. A third one is fixed to a display ($\mathbf{M}$), which is held by a user while he moves around the room. A reflective passive marker is attached to the moving camera and its ground-truth pose is obtained with a real-time optical 3D measurement system (infiniTrack system from Atracsys [Atracsys 2015]). The ceiling-mounted cameras and the optical tracking system have been registered to a global room reference frame $\mathbf{R}$ (represented in figure B.2) through a calibration procedure described in section B.3.

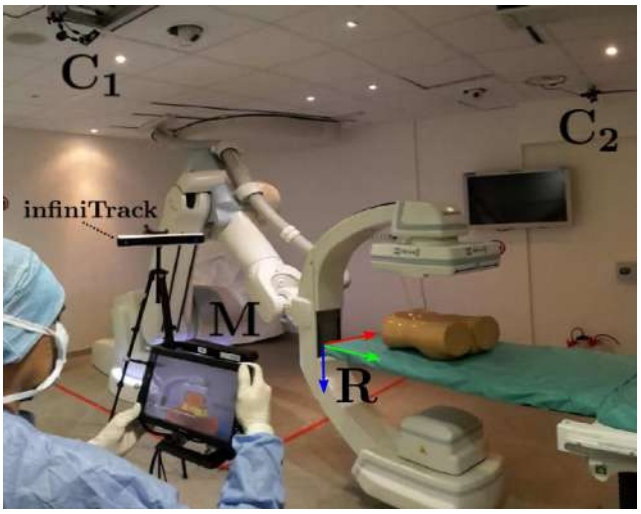

Figure B.2: xawAR16 dataset recording setup: Two RGBD cameras are rigidly mounted to the ceiling ($\mathbf{C_1}$ and $\mathbf{C_2}$), a third one is fixed to a display ($\mathbf{M}$) held by a user. A reflective passive marker is attached to the moving camera and its ground-truth pose is obtained with the infiniTrack tracking system.

The sequences from this dataset include several scenarios and challenges that can be typically encountered in a clinical environment. Four different kinds of sequences are featured in the dataset, which are divided according to the complexity for tracking the

[2]The xawAR16 dataset can be downloaded from this link: http://camma.u-strasbg.fr/xawar16-dataset

mobile display on the images:

- *Smooth:* the moving camera is moved in a smooth trajectory including several loop closures and without occlusions in the view (good for debugging purposes).
- *Clinician: Smooth* sequence with a clinician operating near the patient and therefore occluding the view of the moving camera.
- *Challenging:* sequence of type *Clinician* but in which the trajectory of the moving camera is interrupted by large motions and abrupt viewpoint changes.
- *Device rotation:* the X-ray imaging device moves during the sequence in order to change to a new image projection or to acquire a 3D image. The mobile display's trajectory can be either *Smooth* or *Challenging*.

Moreover, each type of sequence is repeated for several configurations of the X-ray imaging device. We use the standardized naming convention in interventional radiology for referring to the ongoing imaging device's angulation per sequence: PA, AP, LAO and RAO (at 45° or 135°). With this variety of scenarios, this dataset can be used to assess the performance of an SLAM/AR approach when facing various possible challenges that could be encountered in a clinical environment. The list of included sequences along with useful statistics (length, mobile camera speed of motion...) are presented in table B.1.

B.3 Optical tracking system calibration

A calibration procedure using a checkerboard pattern enabled us to obtain the registration between the infiniTrack's reference frame and our system's frame **R** for each recording setup. In a first step, the pattern was positioned in a configuration where it could be simultaneously seen by one of the ceiling cameras and by the tracking device. Then, we obtained the transformation between both systems by detecting the pattern in the color image from the camera and in the infrared images from the infiniTrack. Similarly, in a second step, the pattern was positioned to be visible by the tracking system and the camera attached to the mobile display. By considering the tracked marker's pose, we compute the transformation between the passive marker and the RGB optical frame from the moving camera. The obtained calibration matrices allowing to transform the mobile camera's ground-truth pose into reference system **R** are provided in the dataset.

B.4 Additional information

- Files for the synchronization between the color and depth images per camera are provided per sequence. Also, a file to synchronize the images of the three cameras is provided per sequence, which takes as reference the moving one and it gives the corresponding synchronized frame indices for the other two cameras.
- All calibration and pose matrices (extrinsics, moving camera pose and ground-truth registration) are provided as 4×4 homogeneous transformation matrices.

Table B.1: Evaluation dataset: each sequence is categorized according to the side of the operating table where the mobile display was held, the type of sequence (*Smooth*, *Clinician*, *Challenging* or *Device rotation*) and the ongoing X-ray device projection. The average rotation velocity (deg/s) and translation velocity (m/s) is also provided.

OR side	**Description**	**Sequence name**	**Length (s)**	**Trans. Vel. (m/s)**	**Rot. Vel. (deg/s)**
Right	Smooth	R_PA_Smooth	91.4	0.15 ± 0.07	16.9 ± 11.1
		R_AP_Smooth	41.1	0.13 ± 0.07	17.7 ± 11.3
		R_RAO135_Smooth	57.5	0.16 ± 0.07	16.8 ± 11.2
	Clinician	R_PA_Clinician	125	0.18 ± 0.10	19.7 ± 13.1
		R_AP_Clinician	27.8	0.23 ± 0.12	19.5 ± 13.2
	Device rotation	R_CT_Challenging	64.5	0.13 ± 0.07	19.5 ± 11.6
	Challenging	R_PA_Challenging	96.1	0.18 ± 0.13	20.2 ± 14.1
		R_RAO135_Challenging	107	0.24 ± 0.15	22.9 ± 15.5
Left	Smooth	L_PA_Smooth	47.5	0.13 ± 0.08	14.2 ± 9.99
		L_RAO45_Smooth	53.8	0.17 ± 0.07	14.7 ± 11.2
		L_RAO135_Smooth	60.5	0.18 ± 0.07	15.8 ± 11.2
	Clinician	L_PA_Clinician	65.7	0.21 ± 0.13	16.5 ± 12.7
		L_CT_Clinician	46.2	0.24 ± 0.15	20.0 ± 14.2
	Device rotation	L_CT_Smooth	91.9	0.12 ± 0.07	16.7 ± 11.7
	Challenging	L_PA_Challenging	83.1	0.23 ± 0.15	17.7 ± 14.3
		L_RAO45_Challenging	57.2	0.19 ± 0.17	21.1 ± 16.7

- A set of MatLab sample scripts are provided to show the correct use of the provided data: (1) sample scripts illustrating how to apply the different transformations (extrinsics, calibration. . .), which enable to register the ground-truth moving camera poses with the global room reference frame, and (2) scripts showing how to evaluate the tracking of the moving camera and the ground-truth poses with the metrics used in [Loy Rodas 2017a].

C Camera relocalization approach for a markerless mobile AR

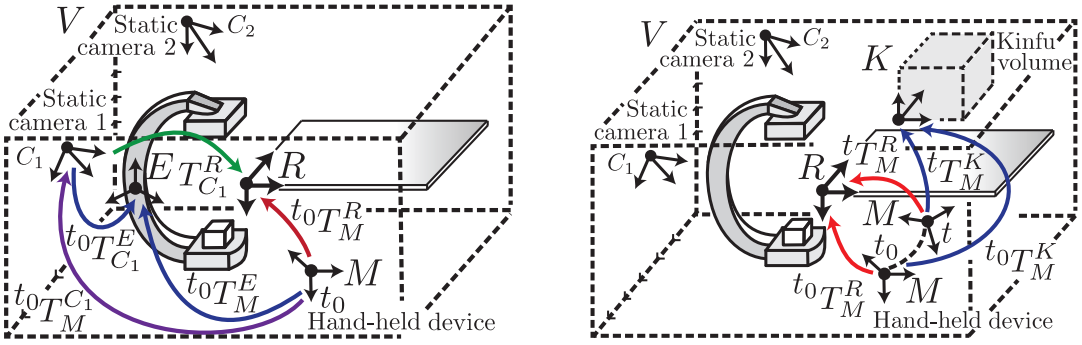

(a) Tracking initialization: estimation of the pose of M with respect to R at t_0 using a simultanous detection of equipment E in a static camera and in the moving camera.

(b) Frame-to-frame tracking: KinectFusion yields at each time step t the relative pose of M with respect to K, which is applied to estimate ${}^{\mathbf{t}}\mathbf{T}^{\mathbf{R}}_{\mathbf{M}}$.

Figure C.1: The two steps of our approach for markerless camera relocalization and tracking, applied for a mobile AR application.

C.1 Introduction

A common challenge faced by medical AR systems is how to provide an accurate registration of the viewer's point-of-view, necessary for the visualization, while interfering the least possible with the clinical workflow. To cope with this, current systems rely mostly on tracking markers placed in the scene or on the surgical tools [Sauer 2000, Sauer 2001, Das 2006, Wendler 2007]. Yet, this can be intrusive and interfere with the procedure at hand. Moreover, it requires an unobstructed line-of-sight between the markers and the tracking device, which makes such systems sensitive to occlusions and crowded scenarios. Other works also propose the estimation of the viewpoint's pose by registering a reconstructed mesh to an a priori model of the scene [Glocker 2015, Seitel 2016]. These,

however, often require precise manual initializations and are limited to static scenes and to a set of viewpoints.

To cope with the aforementioned challenges, we proposed in [Loy Rodas 2017a] a novel markerless approach for mobile AR applications. Such an approach was applied to display directly in the user's view information related to radiation safety through hand-held screen (as shown in figure 5.7). This enables the user to see the 3D propagation of radiation, the medical staff's exposure and/or the doses deposited on the patient's surface as seen through his own eyes. In this appendix, we describe a markerless camera relocalization approach we developed to make this application possible, and we present results of its evaluation on the xawAR16 multi-camera dataset introduced in appendix B.

C.2 Method

C.2.1 Overview

Our approach relies on the use of a multi-camera setup composed of three RGBD sensors as shown in figure B.2. Two of the sensors are ceiling-mounted and a third one is attached to the hand-held screen, which is used in our application as the AR display. At each time step, the mobile camera's pose with respect to the room coordinate system is computed in order to correctly overlay the virtual radiation safety information on the screen. Our approach is summarized in the figures C.1 and is explained in the sections below.

Instead of tracking external markers, we propose to combine the results of a simultaneous equipment detection in all views obtained using the state-of-the-art template matching approach LineMOD [Hinterstoisser 2012b, Hinterstoisser 2012a]. Detecting the same equipment in one static camera (registered to the room) and in the moving one, enables the estimation of the global pose of the moving device. We choose to detect the X-ray imaging device since it is large enough to be seen in all views and it is the main focus point of X-ray based interventional procedures. The camera motion is then tracked in a frame-to-frame fashion using KinectFusion [Newcombe 2011]. The use of the two ceiling cameras allows the system to keep an up-to-date picture of the room layout as needed for camera relocalization when a rapid camera motion or a change in the scene causes loss of tracking. In such cases, a new equipment detection enables a fast recovery from tracking failure. In other words, the system makes use of the equipment in the room as a "natural marker" to localize the moving device.

Our approach allows the user to move freely around the operating table and benefit from the radiation awareness AR visualization at each position while also being robust to motion in the scene and possible occlusions. The typical approaches adopted by medical AR systems can be limited when coping with these challenges. First, it is not practical to have markers placed all around the scene. Moreover, these would need to remain visible from all viewpoints and not to be occluded by the equipment or other clinicians. Second, changes in the scene, such as an X-ray device rotation, would invalidate any a priori model used by marker-less approaches. We address these particularities by proposing a marker-less approach which is non-intrusive and allows the tracking of the

mobile display in a large area. Such an approach is divided into two phases which are illustrated in the figures C.1 and are described below : tracking initialization (fig. C.1a) and frame-to-frame tracking (fig. C.1b). The overall workflow of our approach is summarized in figure C.2. We describe each stage of the pipeline in the sections below, using the naming conventions from figures C.1a, C.1b and C.2.

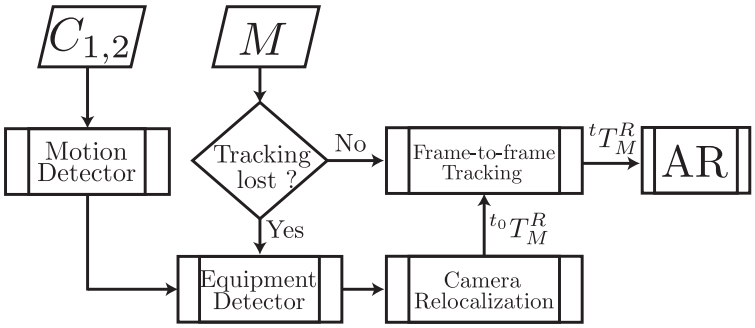

Figure C.2: Overview of our approach's workflow. In practice, the data streams from the cameras (C_1, C_2 and M) are processed simultanously by processes executed on separate threads.

C.2.2 Tracking approach

C.2.2.1 Tracking initialization/relocalization

To estimate ${}^{\mathbf{t}}\mathbf{T}_{\mathbf{M}}^{\mathbf{R}}$, namely the pose of the AR display M with respect to R at time step t, equipment detection is performed on the RGBD images from our system. Indeed, equipment detection provides a relative transformation from the detected equipment E to the camera, *i.e.* ${}^{\mathbf{t_0}}\mathbf{T}_{\mathbf{M}}^{\mathbf{E}}$ if the detection was performed at instant t_0 in M or ${}^{\mathbf{t_0}}\mathbf{T}_{\mathbf{C_1}}^{\mathbf{E}}$ for C_1. Whenever E is simultaneously detected in at least one static camera (C_1 in this case) and in the moving one, we can express the pose of M with respect to R as:

$$ {}^{\mathbf{t_0}}\mathbf{T}_{\mathbf{M}}^{\mathbf{R}} = {}^{\mathbf{t_0}}\mathbf{T}_{\mathbf{M}}^{\mathbf{E}}({}^{\mathbf{t_0}}\mathbf{T}_{\mathbf{C_1}}^{\mathbf{E}})^{-1}\mathbf{T}_{\mathbf{C_1}}^{\mathbf{R}} \tag{C.1} $$

As shown in figure C.1a, this procedure is executed to initialize the tracking or to recover from tracking failure.

C.2.2.2 Frame-to-frame tracking

Once the tracking has been initialized through the camera relocalization procedure ("Frame-to-frame tracking" in fig. C.2), we apply KinectFusion [Newcombe 2011] to track the AR display's motion. KinectFusion uses the depth stream from the camera attached to the screen to build an implicit surface model in real-time while the camera scans the room. The camera pose at time step t is then obtained by using ICP to match the current depth frame to the model. The obtained transformation ${}^{\mathbf{t}}\mathbf{T}_{\mathbf{M}}^{\mathbf{K}}$ is relative to the previous frame and referred to the reconstructed surface model K as shown in

figure C.1b. In order to compute the global pose of M at the current frame, we apply the initialization provided by the equipment detection at t_0 in the following way:

$$^{t}\mathbf{T}_{\mathbf{M}}^{\mathbf{R}} = {}^{t}\mathbf{T}_{\mathbf{M}}^{\mathbf{K}}({}^{t_0}\mathbf{T}_{\mathbf{M}}^{\mathbf{K}})^{-1}{}^{t_0}\mathbf{T}_{\mathbf{M}}^{\mathbf{R}}, \tag{C.2}$$

where $^{t_0}\mathbf{T}_{\mathbf{M}}^{\mathbf{K}}$ is a constant transformation that maps the relative initial pose of the reconstructed model to M. The system compares the ICP error to a threshold for detecting the loss of tracking. This may occur in cases of motion or changes in the scene and can cause an invalid AR visualization which would negatively affect the user experience. In such cases, looking towards an equipment with the display allows a fast tracking recovery.

C.2.3 Equipment detection in the OR

During a procedure, the attention of clinicians is focused on the imaging device and surroundings of the patient. This area is also the most irradiated when an X-ray image is acquired. Hence, we can consider that a user holding the visualization display will be looking near this region to obtain information about the potential propagation of radiation. Detecting the X-ray imaging device for localization purposes is therefore the best choice. However, the following constraints should be considered by the detection method:

(1) The equipment to detect and the camera attached to the display may be simultaneously moving.

(2) The X-ray imaging device is large, thus it might not be fully visible in every frame.

(3) Other clinicians or equipment in the view may occlude the imaging device.

To cope with these challenges, we apply LineMOD [Hinterstoisser 2012b] and adapt the training and testing stages to fit our requirements. As explained in the upcoming sections, we generate separate template databases for the ceiling cameras and the mobile display's camera. We also propose approaches to handle possible occlusions of the equipment to detect and to dynamically sub-sample the template database to accelerate the detection process.

C.2.3.1 Template databases' generation

LineMOD relies on matching templates generated from a multitude of synthetic renderings from a 3D model of the object, which cover for all the possible views that can be encountered at test time. In practice, we generate a 3D model of the X-ray imaging device by scanning it with an RGBD camera and using the software RecFusion [RecFusion 2015] to obtain a reconstructed model. Then, we apply the same viewpoint sampling scheme as in [Hinterstoisser 2012b] in order to equally sample a set of virtual camera viewpoints around the model. This is achieved by dividing the space into a polyhedron where

each vertex represents a viewpoint from where synthetic color and depth images are generated. By repeating this process for polyhedrons of different sizes, we obtain images at different scales. A LineMOD template is then generated per image pair by densely computing color gradients and surface normals. Color gradients are uniformly computed only on the silhouette of the object since this method has been designed for objects with little texture. In contrast, surface normal features are computed on the interior of the object's silhouette and are discretized according to their orientation. We refer the reader to [Hinterstoisser 2012b] and [Hinterstoisser 2012a] for more information about the feature computation and encoding. Each template is labeled with the corresponding relative camera-to-object transformation. Therefore, when a template is matched at test time, it provides a coarse estimation of the object's pose which is further refined using ICP.

C.2.3.2 Ceiling cameras template database

The parameters of the viewpoint sampling scheme are determined from the registration of the static cameras to $\mathbf{R}$. Indeed, these transformations provide the approximate distance of the cameras to the scene, from where we select the range of scales to consider.

C.2.3.3 Moving camera template database

To cope with challenge (1), the template database must consider all possible changes of the orientation of the equipment and simultaneously all possible camera viewpoints that can occur. To achieve this, we generate separate template databases for a set of orientations of the equipment. We use a priori information about the potential user's regions of motion to remove several views that would never appear at test time, and hence, reduce the size of the template database. We refer as *non-filtered* to the original sampled views and *filtered* to those which are kept for training after removing the irrelevant ones.

C.2.3.4 Occlusion handling

As opposed to the ceiling cameras which have a broader view of the scene, the view of the moving camera may often be occluded. Moreover, the imaging device is large and it will not be entirely visible on every frame. To cope with this challenge, we detect its parts instead. We split the X-ray device's 3D model by half: the bottom half including the radiation source and the top half containing the flat-panel detector. Then, we generate separate template databases for a set of orientations of each part. The full equipment can therefore be correctly detected even if it is not fully visible.

C.2.4 Dynamic template database sub-sampling

We make further use of the ceiling cameras to speed-up and improve the detection on the moving camera. First, the identified X-ray device projection from the static views is applied to load "on the fly" the subset of templates corresponding to the equipment's part which is currently visible and to its ongoing orientation. We consider that the part

located over the bed will be the most visible one for a user holding the screen at chest level or higher. Second, a coarse estimation of the user's positions in the room is obtained by applying a multi-view motion detection approach on the ceiling cameras ("Motion Detector" process in figure C.2). By this means, the number of templates to match can be reduced by searching only those which are potentially visible from such positions. To perform the motion detection, we rely on a GPU implementation of the Gaussian mixture model for background subtraction from [Pham 2010]. Motion is first segmented in the color images and the corresponding depth value is used to project the motion pixels in 3D. A discretization of the room volume V is then applied to quantify the amount of motion per voxel. We consider the 3D regions with large accumulations of motion as potential positions of the user. Using this information, the system dynamically loads only the templates which are visible from such positions, thereby, drastically reducing the search space for the template matching. In a typical usage of our system, other types of motion come from an X-ray device rotation or from another clinician in the scene. Even if the areas where these events occur are detected as potential positions of the user, the amount of templates to match is still largely reduced.

C.3 Evaluation with the xawAR16 dataset

C.3.0.1 Evaluation metrics

As proposed by [Sturm 2012], we apply the relative pose error (RPE) and the absolute pose error (APE) as evaluation metrics. For a given sequence of length n, we note the poses to evaluate as $\mathbf{P}_1, \ldots, \mathbf{P}_n \in \mathrm{SE}(3)$ and the ground-truth poses as $\mathbf{Q}_1, \ldots, \mathbf{Q}_n \in \mathrm{SE}(3)$. RPE measures the drift of a trajectory as it computes its local accuracy over a time interval Δ. It is a suitable metric to evaluate the quality of the tracking. Since it does not require both trajectories to be expressed in the same coordinate system, it is not affected by possible errors coming from the calibration stages. It is computed as follows:

$$\mathbf{E}_i := (\mathbf{Q}_i^{-1}\mathbf{Q}_{i+\Delta})^{-1}(\mathbf{P}_i^{-1}\mathbf{P}_{i+\Delta}) \tag{C.3}$$

Similarly, by applying the calibration presented in section B.3, we can also compute the absolute distances between both trajectories. If $\mathbf{S}$ is the transformation that maps the poses to the same coordinate system, APE is computed as:

$$\mathbf{F}_i := \mathbf{Q}_i^{-1}\mathbf{S}\mathbf{P}_i \tag{C.4}$$

APE is better suited to evaluate the relocalization part of our approach since this one is performed independently at time step i and does not depend on any consecutive frames. To evaluate a full sequence, we compute the mean error over all poses for the rotational and translational components of $\mathbf{E}_i$ or $\mathbf{F}_i$ depending on the considered metric.

C.3.0.2 System settings

The experiments were performed using a computer equipped with an i7-3930K 6-core processor along with a GeForce GTX Titan GPU card. The hand-held screen and all RGBD cameras are directly connected to the computer respectively through VGA and active USB extension cables. Our frame-to-frame tracking approach is based on the open-source implementation of KinectFusion *KinFu*, which is included in the PCL libraries [PCL 2015]. We apply the default parameters from *KinFu* with a TSDF volume of 8 m per side and composed of 512^3 voxels. A coarser 3D grid of same size divided in 64^3 voxels is used for the motion detection approach. Furthermore, our equipment detection approach is based on the publicly available LineMOD source code from OpenCV [OpenCV 2015]. The templates are computed using the synthetic data generated as described in C.2.3.1, using the feature extraction parameters recommended in [Hinterstoisser 2012b].

C.4 Evaluation Results

We evaluate the following aspects of our system:

- the equipment detection and the efficacy of the proposed approaches to speed-up the tracking initialization
- the overall performance of the system by looking at the tracking accuracy on all sequences of the dataset
- the accuracy of the camera relocalization

C.4.1 Equipment detection

We first study the impact of the viewpoint sampling parameters in the template generation stage. This is important to balance the trade-off between the coverage of the object for detection accuracy and the number of training views for efficiency.

We generate four template databases for each considered part of the X-ray imaging device with different viewpoint sampling parameters. For each, we keep both the *non-filtered* and the *filtered* versions. We evaluate on four sequences: two per bed side and each for a PA and AP projection. The part positioned over the bed is respectively the flat-panel detector in the PA sequences and the radiation source in the AP ones. These sequences allow us to separately evaluate the detection accuracy for each considered equipment part. We assess the relocalization performance by constantly setting the tracking as lost at each frame. Hence, we evaluate the relocalization error for different positions of the user in the room and for different views of the equipment.

The results of this evaluation are presented in table C.1. As can be expected, the best detection results are achieved when more views of the object are used for template generation. However, we show that using a priori information for filtering the template database allows us to maintain the same detection performance with a 60 % reduction of

the detection time per frame. Also, we evaluate the impact of applying the user tracking framework presented in section C.2.4 to reduce the templates to match in the moving view. The results show that this additional subsampling achieves a better relocalization accuracy while reducing by half the detection time. Hence, to dynamically subsample the templates to match using the ceiling cameras is a good action to speed-up the tracking initialization while maintaining detection robustness. In practice, the detection speed intervenes only during tracking initialization and afterwards KinectFusion runs at frame rate. Still, initialization speed is an important aspect for a smoother user experience and a faster tracking recovery.

For the reasons described above, the *filtered* version of template database #4 containing 9593 templates (cf. table C.1), in combination with the dynamic template selection approach (section C.2.4), are used for equipment detection in the rest of the experiments.

Table C.1: APE when relocalizing with different template databases. *Non-filtered*: templates generated from synthetic views covering the full sphere of viewpoints around the object. *Filtered*: sets where a priori information has been used to filter-out irrelevant views. *User tracking*: using the detected user's position to load the templates to match. The number of training views as well as the mean translation error (T) in mm, rotation error (R) in degrees, detection speed (S) in seconds and mean values for all the evaluated sequences are provided.

	Template database and number of training views																										
	Non-filtered												Filtered														
	1 (462)			2 (1782)			3 (7062)			4 (28182)			1 (169)			2 (645)			3 (2449)			4 (9593)			User tracking		
Sequence	T	R	S	T	R	S	T	R	S	T	R	S	T	R	S	T	R	S	T	R	S	T	R	S	T	R	S
R_PA_S	196	5.76	0.35	188	4.44	0.41	161	5.50	0.64	128	4.70	1.13	283	8.14	0.36	195	6.41	0.37	185	6.34	0.42	126	3.96	0.53	125	3.75	0.30
L_PA_S	166	4.15	0.31	159	4.05	0.39	139	3.62	0.62	168	3.95	1.34	210	6.72	0.27	166	4.87	0.34	151	4.21	0.42	147	3.99	0.42	134	3.77	0.27
R_AP_S	341	8.73	0.25	292	8.08	0.32	284	7.67	0.45	257	8.24	1.12	348	9.66	0.26	277	7.84	0.29	230	6.93	0.35	196	6.44	0.55	186	7.82	0.27
L_AP_S	445	9.55	0.31	261	6.15	0.38	266	6.39	0.53	257	6.54	1.19	519	11.36	0.30	274	6.34	0.33	248	6.52	0.42	176	6.19	0.54	148	3.52	0.27
Mean	287	7.05	0.30	224	5.68	0.37	212	5.79	0.56	*202*	*5.86*	*1.20*	339	8.96	0.30	227	6.36	0.33	203	6.00	0.40	*161*	*5.14*	*0.51*	**148**	**4.71**	**0.27**

C.4.2 Moving camera tracking

In this part, we evaluate in all sequences the full performance of the system to track the motion of the mobile display while performing the camera relocalization procedure whenever tracking is lost. We calculate both the RPE and the APE introduced in C.3.0.1. For estimating the RPE, we fix a Δ of 25 to evaluate the drift of the trajectory per second. Detailed results of the evaluation of all sequences are presented in table C.2. It also provides the mean errors per type of sequence (*Smooth* or *Challenging*).

From the obtained results, we conclude that our system is able to correctly track the motion of the mobile display even in the presence of occlusions and motion in the scene. We obtain in the case of the *Smooth* sequences a mean RPE of 53 mm in translation and 2.6° in rotation, and for the *Challenging* ones 86 mm and 2.8°. As mentioned in 3.1.1, depth measurement inaccuracies can be up to 50 mm with these kind of sensors so these errors are acceptable for our application where precision requirements are not particularly strict. On the sequences of type *Challenging*, *Device rotation* and *Clinician*, tracking is lost more often than in the *Smooth* sequences. Still, the difference between the measured errors is small which means that the system is able to correctly recover

from loss of tracking in challenging conditions. Higher errors are obtained for the APE metric. However, these are also affected by the multi-camera system calibration error (which we estimate to be of 33.2 mm and 3°) and by the errors from the registration of the infiniTrack to our room coordinate frame. The obtained results are good for visualization purposes and equipment detection is therefore a promising alternative to the use of markers for our application. Plots of the estimated and the ground-truth trajectories for two sequences (*Smooth* and *Challenging*) are provided in figure C.3 to offer an insight about the amplitude of the mobile display's motion on the dataset. We can observe how our tracking approach is able to follow the abrupt changes from the ground-truth trajectory which are more prominent in the *Challenging* sequence.

Setup	**Description**	**Sequence name**	**Ev. Frames**	**RPE T (mm)**	**RPE R (deg.)**	**APE T (mm)**	**APE R (deg.)**
Right	Smooth	R_PA_Smooth	1184	43.3 ± 31.1	1.37 ± 0.37	113 ± 20.9	2.16 ± 0.08
		R_AP_Smooth	858	81.8 ± 100	2.33 ± 0.48	134 ± 75.9	5.15 ± 0.78
		R_RAO135_Smooth	970	59.5 ± 79.3	2.06 ± 0.31	149 ± 51.3	4.93 ± 0.13
	Clinician	R_PA_Clinician	1481	54.9 ± 65.2	1.84 ± 0.08	148 ± 59.5	3.26 ± 0.16
		R_AP_Clinician	501	63.7 ± 63.1	1.83 ± 0.48	114 ± 46.8	4.31 ± 0.66
	Device rotation	R_CT_Challenging	1151	86.8 ± 119	2.28 ± 0.65	166 ± 95.8	3.97 ± 0.34
	Challenging	R_PA_Challenging	1141	126 ± 264	4.12 ± 0.87	124 ± 170	3.28 ± 0.73
		R_RAO135_Challenging	1953	152 ± 253	6.53 ± 1.57	146 ± 177	5.90 ± 1.40
Left	Smooth	L_PA_Smooth	882	48.8 ± 71.2	1.38 ± 0.29	184 ± 38.8	4.59 ± 0.35
		L_RAO45_Smooth	817	42.3 ± 33.8	1.48 ± 0.09	149 ± 54.6	4.71 ± 0.45
		L_RAO135_Smooth	895	45.2 ± 34.9	1.79 ± 0.78	146 ± 62.1	11.1 ± 0.45
	Clinician	L_PA_Clinician	1067	36.3 ± 45.8	1.30 ± 0.36	154 ± 73.2	4.29 ± 0.71
		L_CT_Clinician	554	117 ± 153	3.60 ± 0.40	197 ± 160	7.04 ± 0.86
	Device rotation	L_CT_Smooth	1672	44.7 ± 48.4	1.61 ± 0.15	184 ± 69.5	5.53 ± 0.28
	Challenging	L_PA_Challenging	788	89.7 ± 83.2	2.56 ± 0.24	161 ± 79.8	4.83 ± 0.18
		L_RAO45_Challenging	687	95.1 ± 136	2.74 ± 0.38	146 ± 105	4.32 ± 0.25
	Smooth	**Mean**		**53.3 ± 58.3**	**2.62 ± 0.38**	**135 ± 50.6**	**4.11 ± 0.37**
	Challenging	**Mean**		**86.6 ± 123**	**2.84 ± 0.51**	**154 ± 103**	**4.67 ± 0.55**

Table C.2: Evaluation of our full approach on all sequences from the dataset with the evaluation metrics described in C.3.0.1. The number of evaluated frames (*Ev. frames*) corresponds to the frames with ground-truth available. Mean errors per sequence type (*Smooth* AR display's trajectories or *Challenging* for sequences including occlusions, clinicians and/or large/sudden camera viewpoint changes) are provided.

C.4.3 Relocalization

Table C.3 presents the results of evaluating our approach for camera relocalization when compared to ICP. Our system waits for two simultaneous equipment detections with matching scores higher than a given threshold before initializing the tracking. Relocalization therefore succeeds when the imaging device is detected in two views. For the sake of comparison, even though ICP can provide a result on every frame, we present the error values for the frames where a relocalization was obtained with our approach and where ground-truth information is available (*Ev. Frames* on table C.3). ICP is performed between the point cloud obtained by merging the color and depth images from

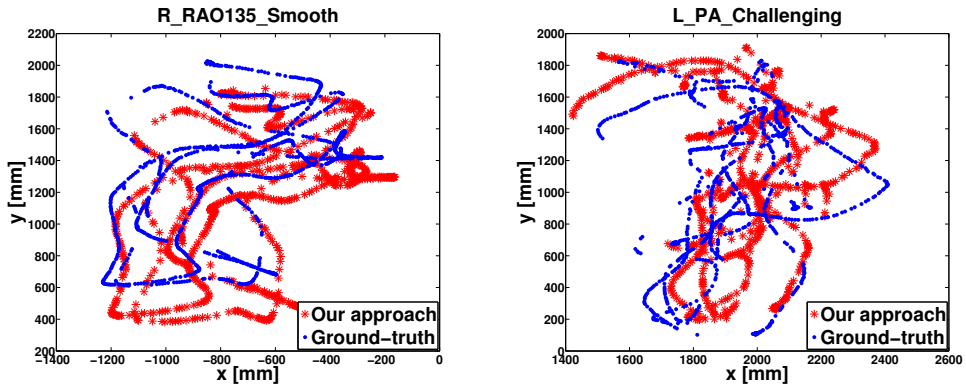

Figure C.3: Estimated mobile AR display 's trajectories with our tracking approach, compared to the ground-truth trajectories for two sequences of the dataset.

the moving camera and the registered point clouds from the static ones. Random noise is applied to the ground-truth pose (±6° and ±5 cm per axis) for initializing ICP on each frame and the maximum number of iterations is set to 500.

A mean APE of 163 mm and 5.9° is obtained with our approach against 223 mm and 6.8° when using ICP. The difficulties of the *Clinician* and *Challenging* sequences are reflected in the errors which are consistent across both approaches. To further explore the performance of our method, we also compute the percentage of frames for which tracking was successfully recovered. We consider a frame as correctly relocalized if the APE is within 15 cm in translation and 7° in rotation. We can observe from table C.3 that our approach also performs better than ICP: 41 % against 28 %. Our method fails to achieve an accurate detection if the equipment is significantly occluded or if none of its learned parts are visible. Also, false positives can be introduced in bad frames such as the ones acquired during a rapid camera motion or when the user stands closer to the area of interest than the sensor's depth measurement range. These cases were not excluded from the evaluation. However, this can be avoided in practice since, when tracking is lost, the user will point the visualization display towards the imaging device and he therefore has an influence on the frames where relocalization is performed. ICP converges in all frames, yet, it requires a large number of iterations, which is not suitable for online use. Even with an initialization derived from the ground-truth, its relocalization accuracy is not as good as the one we obtain with our equipment detection-based approach. Moreover, the success rate of ICP remains similar when evaluated in all frames (25 % of recovered frames and an APE of 228 mm and 7°).

Our method is therefore better suited for an online mobile AR application since it provides a faster and more accurate relocalization. Equipment detection can be an interesting alternative to perform automatic initial registration for mobile AR systems such as [Glocker 2015, Seitel 2016], which currently rely on a rough manual alignment as initialization of ICP.

Table C.3: Evaluation of our relocalization approach compared to ICP with initialization: *Ev. Frames* is the number of frames per sequence where a relocalization was performed and which also has ground-truth available. We evaluate by computing APE on the relocalized frames (T for the translation error in mm and R for the rotation error in degrees). *%Rel* corresponds to the percentage of recovered frames (APE within 15 cm in translation and 7° in rotation).

		ICP			**Our approach**		
Sequence	**Ev. Frames**	**T**	**R**	**% Rel.**	**T**	**R**	**% Rel.**
R_PA_Smooth	147	186	7.24	12.2	121	3.63	78.2
R_AP_Smooth	30	279	7.53	0	186	6.82	30
R_RAO135_Smooth	152	237	6.48	7.2	118	5.81	63.1
R_PA_Clinician	279	249	7.04	5.3	149	4.88	63.8
R_AP_Clinician	39	306	7.41	3.2	198	7.35	19.3
R_CT_Challenging	48	284	6.01	4.1	197	6.92	31.2
R_PA_Challenging	188	239	7.37	5.8	110	3.95	74.4
R_RAO135_Challenging	336	234	7.26	5.3	176	5.52	56.2
L_PA_Smooth	134	183	5.82	41	145	4.93	47
L_RAO45_Smooth	139	114	4.84	84	175	5.25	15.8
L_RAO135_Smooth	72	327	9.33	0	175	10.9	4.2
L_PA_Clinician	95	234	6.42	63.1	161	5.42	31.5
L_CT_Clinician	78	154	7.58	32.2	149	6.87	39.7
L_CT_Smooth	102	166	5.43	84.3	148	4.76	47
L_PA_Challenging	77	241	7.38	48	157	5.29	38.9
L_RAO45_Challenging	50	144	5.91	66	240	6.07	20
Mean		**223**	**6.81**	**28.9**	**163**	**5.90**	**41.3**

C.5 Conclusions

We herein present an approach relying on the use of commodity RGBD sensors and equipment detection to perform markerless mobile AR. We show that it is able to deal with dynamic environments and is a less invasive alternative to the use of markers. Detection of medical equipment in the OR is difficult since the objects are large and can also be moving or occluded. To cope with this challenge, we propose to use a priori information during training in combination with a part-based detection scheme. Furthermore, the use of two ceiling-mounted cameras enables the system to account for changes in the layout of the scene, allowing for a fast camera relocalization.

The evaluation of our approach on a dataset representative of the conditions that can be encountered in the surgical room shows that it can track the motion of the visualization display with a mean relative error of 7 cm in translation and 2° in rotation (mean APE of 14 cm and 4° respectively). We consider this tracking accuracy to be sufficient for AR visualization in our clinical application where precision is not a critical factor. This error is affected by noise in the depth values from the cameras which can be up to 5 cm [Sturm 2012]. Tracking accuracy can potentially be improved by using more precise

depth sensors. The highest errors are obtained in the difficult sequences containing strong motion and/or large viewpoint changes, which are reflected as deviations in the positioning of the displayed virtual information. Nevertheless, when this occurs, the overall aspect of the visualization is maintained and information such as the scattering direction is still correctly transmitted to the user. In practice, the user can also manually re-initialize tracking when the virtual elements are not properly registered in the view.

Qualitative results of the use of this approach for mobile AR visualization can be found in figures 5.1, 5.5b, 5.6(left) and 5.7. These show that the system is able to provide convincing visualizations for radiation awareness and for teaching purposes.

D Résumé en français

Méthodes de Radioprotection Réactives au Contexte pour la salle d'Opération Hybride

Chapter Summary

D.1 Introduction . . . 168
D.2 Radioprotection réactive au contexte . . . 170
D.2.1 Perception de la salle opératoire par des caméras RGBD . . . 170
D.2.2 Méthodes de simulation des radiations . . . 170
D.2.3 Visualisations des radiations par réalité augmentée . . . 172
D.3 Optimisation de la pose d'un capteur plan . . . 175
D.4 Application clinique: *XAware-Live* . . . 176
D.5 Conclusions . . . 179
D.6 Perspectives . . . 180

Abstract

L'utilisation accrue des systèmes d'imagerie interventionnelle à rayons X lors des chirurgies mini-invasives entraîne une forte augmentation de l'exposition du personnel aux radiations ionisantes. Même si les doses absorbées lors d'une procédure peuvent être faibles, l'exposition chronique aux rayons X peut causer des effets nocifs comme les cancers radio-induits. Dans cette thèse, nous avons proposé de nouvelles méthodes pour améliorer la sécurité vis-à-vis des radiations ionisantes dans la salle opératoire hybride dans deux directions complémentaires. Premièrement, nous avons développé des méthodes permettant au personnel médical d'être plus conscient de son exposition et de celle du patient, grâce à des visualisations des irradiations par réalité augmentée (AR). Deuxièmement, nous avons proposé une nouvelle méthode d'optimisation capable de suggérer une configuration de l'imageur qui minimise l'exposition aux radiations des cliniciens et du patient, tout en maintenant la visibilité de la cible dans l'image acquise. Ces deux applications ont été possibles grâce à de nouvelles approches proposées pour percevoir l'environnement 3D de la salle grâce à des caméras RGBD et pour simuler en temps-réel la propagation des radiations et la dose reçue par le patient et par les cliniciens. Ainsi, nous espérons que ces travaux puissent non seulement contribuer à la réduction des expositions aux radiations, mais aussi à améliorer la compréhension de la propagation des radiations et l'acceptation des systèmes d'imagerie à rayons X.

D.1 Introduction

L'imagerie par rayons X est aujourd'hui fondamentale pour le diagnostic des maladies ainsi que pour l'exécution de chirurgies guidées par l'image. En effet, les systèmes d'imagerie par rayons X sont largement utilisés dans plusieurs domaines de la médecine comme la radiologie/cardiologie interventionnelle, l'orthopédie, l'urologie, la neuroradiologie et la radiothérapie. Néanmoins, le patient, les chirurgiens et le personnel médical présents sont chroniquement exposés aux radiations ionisantes causées par l'utilisation de ces systèmes. De nombreuses études ont montré que toute dose de radiation reçue peut avoir des effets nocifs sur le corps telles que des brûlures cutanées, des cataractes oculaires ou même des cancers [Roguin 2013]. Même si l'exposition aux irradiations dans le cas du patient se fait de façon ponctuelle et peut être justifiée par un besoin médical, le personnel médical effectuant des procédures guidées par rayons X peut être exposé de façon répétée. Cette exposition chronique augmente le risque d'apparition d'effets négatifs sur le long terme. De plus, en chirurgie interventionnelle, une partie importante des procédures sont guidées par fluoroscopie, c'est-à-dire par l'acquisition de plusieurs clichés à des intervalles réguliers. Ceci permet au chirurgien d'observer en direct l'anatomie interne du patient mais augmente significativement la dose de radiation. Lorsque la fluoroscopie est utilisée pour guider un geste chirurgical, le chirurgien se doit de rester à côte du patient et donc son exposition ne peut pas être évitée (voir figure D.1). Ainsi, des études ont montré que, parmi les praticiens qui travaillent avec des radiations ionisantes, les chirurgiens interventionnels sont ceux qui sont exposés aux doses les plus importantes [Roguin 2013].

Malgré l'utilisation de vêtements et parois plombés pour réduire leur exposition, plusieurs parties de leurs corps (mains, tête et yeux) restent non protégées et peuvent recevoir des doses importantes [Nikodemová 2011]. Même si des dosimètres portés par le personnel médical au niveau de la poitrine sont utilisés pour monitorer les doses de radiation reçues lors d'une chirurgie, ils ne donnent pas une mesure complète de la dose perçue dans tout le corps. En effet, des études [Carinou 2011, Roguin 2013, Picano 2013] montrent des différences importantes entre les doses reçues dans les différentes parties du corps des cliniciens, notamment des doses supérieures mesurées dans la partie gauche de leur corps qui correspond à celle qui est le plus proche des zones irradiées.

Figure D.1: Chirurgie mini-invasive guidée par fluoroscopie au service de radiologie interventionnelle du Nouvel Hôpital Civil de Strasbourg.

Dans cette thèse, nous avons donc proposé des méthodes pour réduire l'exposition du patient et du personnel aux radiations ionisantes dans la salle opératoire hybride en agissant dans deux directions complémentaires. (1) Tout d'abord, nous avons développé un système capable de calculer la propagation et l'intensité des irradiations, et de donner un retour visuel par réalité augmentée (AR). Pour ceci, des approches pour simuler en temps réel les radiations ainsi que pour visualiser des cartes de dose en 3D ont été développées. En rendant les radiations visibles, ce système permet au personnel d'être plus conscient de son exposition et de celle du patient. Un prototype de ce système a été démontré dans une salle hybride à l'IHU Strasbourg. (2) Puis, nous avons proposé une méthode pour optimiser le positionnement d'un imageur à rayons X. Cette méthode est capable de recommander une pose de l'imageur qui réduit simultanément la dose du patient et du personnel, tout en conservant la qualité clinique de la radiographie obtenue.

Dans ce résumé des travaux réalisés dans le cadre de cette thèse, nous présentons

d'abord de façon synthétique les méthodes de radioprotection réactive au contexte qui ont été proposées pour la simulation des radiations et leur visualisation par AR. Ensuite, nous décrivons l'approche proposée pour optimiser la pose d'un imageur afin de réduire la dose patient/personnel. Puis, nous présentons un prototype de système de radioprotection installé dans une salle opératoire expérimentale à l'IHU Strasbourg. A la fin de ce résumé, les conclusions et perspectives de cette thèse sont présentées.

D.2 Radioprotection réactive au contexte

La nature invisible et la complexité de la propagation des radiations rendent difficile, pour les chirurgiens interventionnels, de rester conscients de leur exposition pendant une procédure. Ce manque de conscience ainsi que la sous-estimation des risques peuvent causer des expositions inutiles [Katz 2017b] et une mauvaise utilisation des moyens de radioprotection [Nikodemová 2011]. Un retour intuitif sur les zones irradiées et sur la dose actuelle permettrait aux praticiens de rester conscients de la propagation des radiations ainsi que de leur exposition et de celle du patient. Afin d'aider le personnel médical à prendre conscience de l'exposition aux rayons X, nous avons proposé des méthodes permettant de percevoir la disposition de la salle opératoire, puis de calculer et de visualiser les radiations ionisantes [Loy Rodas 2014, Loy Rodas 2015a, Loy Rodas 2015b, Loy Rodas 2017a]

D.2.1 Perception de la salle opératoire par des caméras RGBD

Un suivi global de la configuration actuelle de la salle opératoire est effectué grâce à des caméras RGBD fixées au plafond. Le positionnement des caméras est visible dans la figure D.2. Des informations comme la position 3D du personnel ou de l'imageur peuvent ainsi être déterminées à partir des images capturées par ces caméras qui fournissent une vue globale de la salle (voir figure D.3).

D.2.2 Méthodes de simulation des radiations

Des méthodes de simulation ont été proposées pour calculer la propagation des radiations dans le scénario actuel, c'est-à-dire pour la configuration de l'imageur (angle d'incidence et paramètres de l'image) et pour les positions actuelles des cliniciens dans la salle. Ces simulations appliquent des méthodes de type Monte Carlo pour calculer les trajectoires des rayons X produits par l'imageur, leurs interactions avec le patient et/ou l'environnement ainsi que les doses absorbées. Une approche de calcul sur GPU basée sur [Bert 2013, GGEMS 2017] a été conçue pour calculer la dose absorbée par les organes et la peau du patient, la diffusion en 3D des radiations et l'exposition actuelle du personnel en quasi temps réel. En utilisant un modèle du patient (CT spécifique au patient ou générique), notre approche de simulation peut calculer en quelques secondes une carte de dose aux organes de patient comme celle qui est présentée dans la figure D.4a. De plus, nous avons proposé une méthode pour caractériser le comportement des particules diffusées par le patient lors de l'acquisition. Elle permet ainsi de calculer en quelques millisecondes,

Figure D.2: Positions des trois caméras RGBD qui sont installées au plafond d'une salle opératoire expérimentale au IHU Strasbourg (en rouge).

Figure D.3: Vues du système multi-caméra utilisé pour percevoir la salle opératoire.

l'exposition des différentes parties du corps d'un clinicien et d'obtenir des cartes de dose comme celle de la figure D.4b.

Nos méthodes de simulation ont été validées expérimentalement dans une salle opératoire grâce à des mesures acquises avec des dosimètres. Après une calibration utilisant une partie des mesures, l'erreur entre les mesures et les simulations varie de 5 à 20 % pour différent scénarios cliniques. Vu qu'aujourd'hui il n'y a aucune autre estimation intraopératoire de la propagation de dose en 3D et que par ailleurs la précision des dosimètres cliniques peut varier de 5 à 30 % selon leur type [Struelens 2011], la précision de nos modèles de simulation est considérée acceptable.

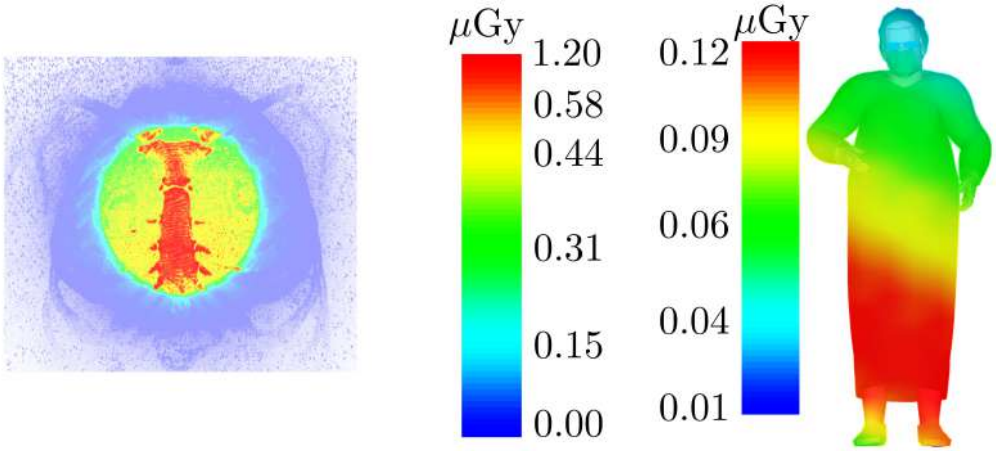

(a) Carte de dose aux organes d'un patient calculée avec notre méthode de simulation sur GPU.

(b) Exposition d'un clinicien aux radiations, calculée en temps réel avec nos méthodes de simulation.

Figure D.4: Méthodes de simulation Monte Carlo de la propagation 3D des radiations et des doses au patient et personnel médical.

D.2.3 Visualisations des radiations par réalité augmentée

Les résultats des simulations sont montrés par AR afin de donner un retour visuel intuitif aux utilisateurs. Trois types de visualisation ont ainsi été développées :

- Grâce à du rendu volumique, la propagation et les intensités du diffusé de radiation sont montrées en recalant un volume coloré aux images capturées par les caméras du plafond. Cette visualisation est mise à jour quand des paramètres comme l'angle d'incidence sont modifiés, permettant ainsi aux utilisateurs de voir l'effet du positionnement de l'imageur sur la diffusion des rayons. Deux exemples de la visualisation de la propagation du rétrodiffusé de radiation par réalité augmentée pour deux angulations de l'imageur sont proposés dans la figure D.5. On peut ainsi observer que pour des configurations où la source de rayons se trouve sur le lit, les parties supérieures du corps des cliniciens présents seront exposées à une dose plus importante. De même, en intégrant dans la simulation la position de protections, comme les suspensions plafonnières et/ou les paravents plombés, l'effet de ces dernières sur la propagation des irradiations peut être visualisé. Nous montrons dans la figure D.6 un exemple de visualisation du rétrodiffusé de radiation dans des scénarios avec ou sans protections plombées. Ces visualisations peuvent être utilisées pour enseigner de façon intuitive les bénéfices de l'utilisation de ce type de protection pour arrêter les radiations et donc des bonnes pratiques de radioprotection.

- Les informations de la position des cliniciens fournies par les caméras RGBD sont utilisées pour calculer et visualiser par AR l'exposition du staff dans tout leur corps. Ceci permet de compléter les mesures des dosimètres qui fournissent la valeur de

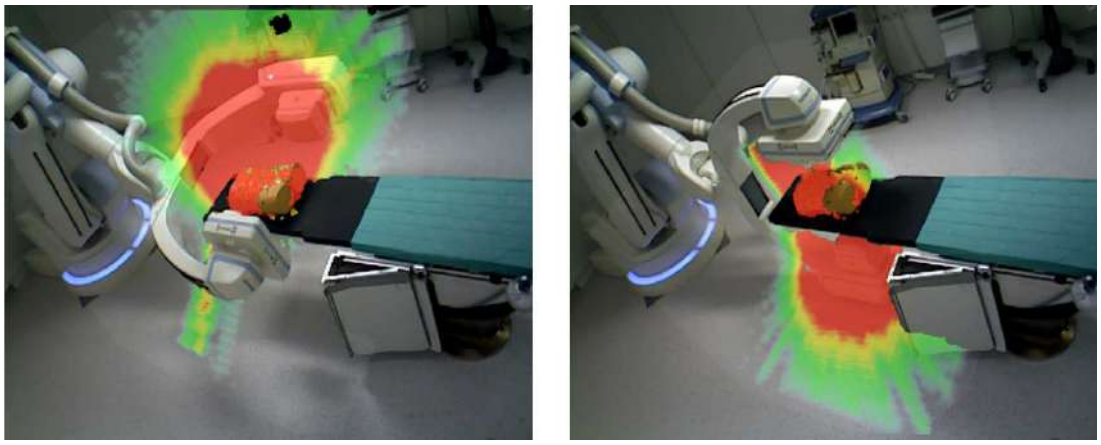

Figure D.5: Visualisation par AR de la propagation en 3D du rétrodiffusé de radiation, pour deux angulations différentes de l'imageur: pour une acquisition RAO à 120° (gauche) et une PA (droite).

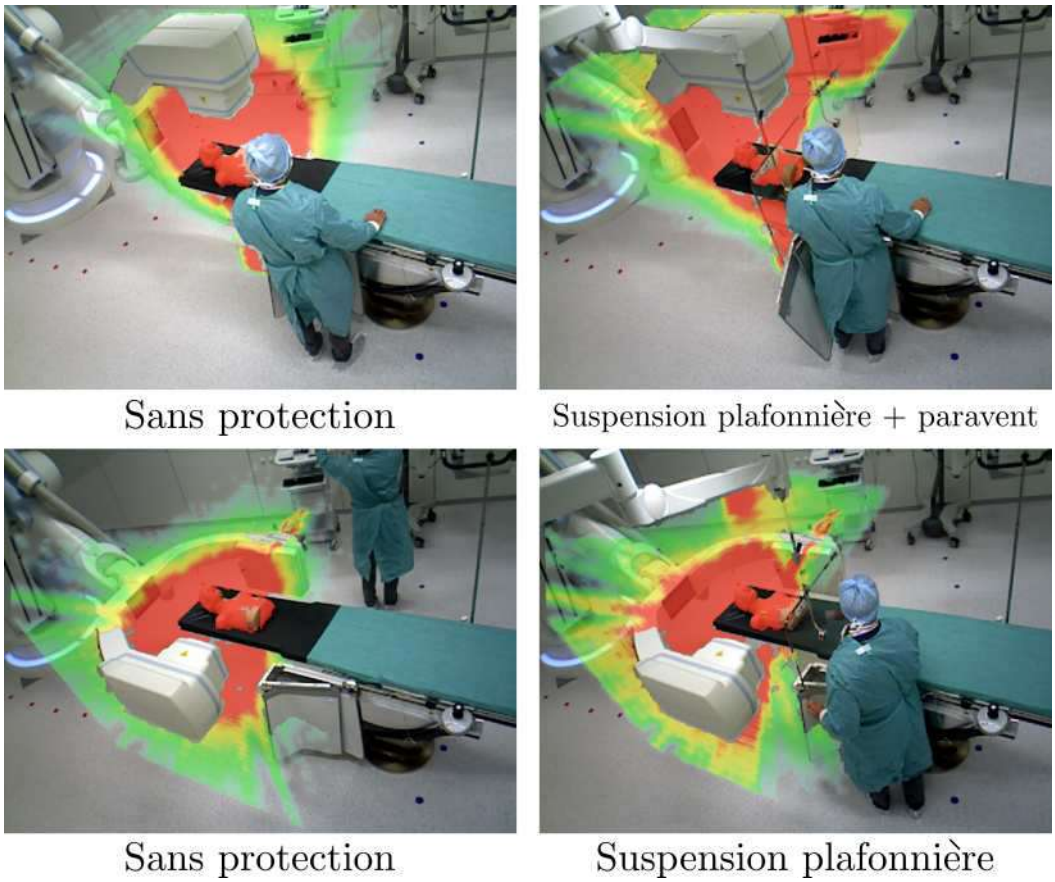

Figure D.6: Visualisation par AR de la propagation en 3D du rétrodiffusé de radiation, pour deux angulations différentes de l'imageur, avec un sans utilisation de protection plombées (suspension plafonnière et paravent plombé).

dose en un point uniquement. Deux exemples de ces visualisations sont fournis dans la figure D.7.

Figure D.7: (Gauche) Visualisation par AR mobile de l'exposition aux radiations des cliniciens lors d'une acquisition PA. (Droite) Visualisation par AR effectuée avec les vues des caméras fixées au plafond de la salle, illustrant l'exposition de deux cliniciens lors d'une acquisition AP.

- La dose absorbée par le patient est aussi montrée soit en recalant aux images un modèle 3D du patient où la peau est colorée d'après la dose simulée, soit en affichant un modèle virtuel montrant par transparence le degré d'exposition des organes. Ce type de visualisation permet de sensibiliser les cliniciens à l'exposition du patient lors d'une procédure. Des exemples de visualisations de la dose patient sont proposés dans la figure D.8.

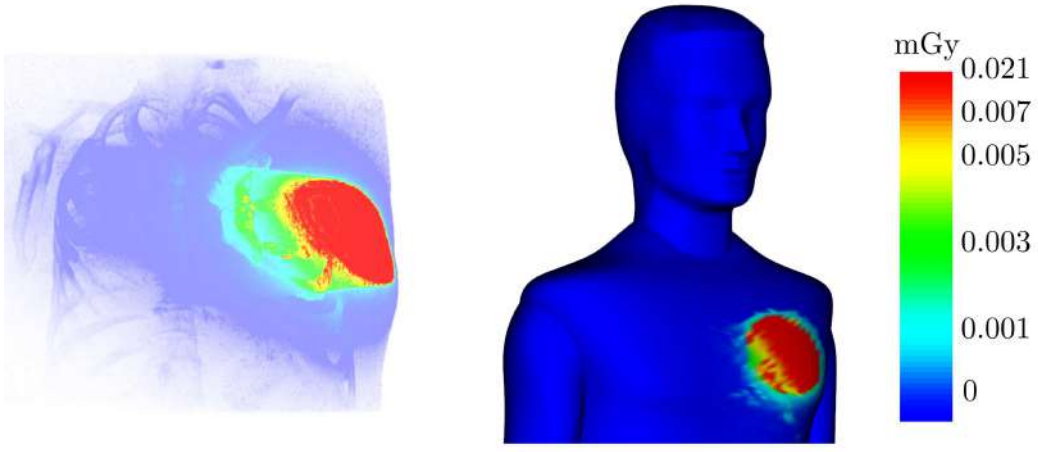

Figure D.8: Visualisation de la dose aux organes et à la peau du patient calculée avec nos méthodes de simulation Monte Carlo.

Les méthodes présentées dans cette section (perception, simulation et visualisation) ont été intégrées dans un système de radioprotection. Ce système, décrit dans la section

D.4, est actuellement installé dans une salle opératoire hybride expérimentale à l'IHU de Strasbourg.

D.3 Optimisation de la pose d'un capteur plan

La plupart des chirurgies guidées par fluoroscopie sont effectuées grâce à des systèmes de type "C-arm". Dans ces systèmes, qui peuvent être robotisés ou manuels, la source de rayons X et le détecteur sont embarqués sur un arceau en forme de C qui est monté au bout d'une chaîne articulée. Cette construction permet de modifier le positionnement de l'arceau afin de capturer des radiographies sous différents points de vue ou même d'effectuer une rotation autour du patient pour générer une image 3D. Malgré leur architecture semblable à celle d'un manipulateur robotique, le positionnement de l'arceau se fait en boucle ouverte. En effet, les radio-manipulateurs cherchent à le positionner de façon à acquérir l'image avec le meilleur point de vue dans le contexte de la procédure en cours [Fallavollita 2014]. Dans cette thèse, nous avons donc proposé une méthode pour optimiser le positionnement d'un capteur plan afin de garantir, non seulement une bonne visibilité de l'organe cible, mais aussi de réduire la dose délivrée au patient et au personnel [Loy Rodas 2017b].

Des travaux visant à optimiser le positionnement d'un C-arm pour atteindre un point de vue désiré existent [Navab 2006, Fallavollita 2014]. Néanmoins, l'exposition aux radiations n'est pas un critère qui est considéré dans ces travaux. En effet, il n'est pas possible aujourd'hui d'estimer la dose patient/personnel pour une radiographie à venir lors d'une procédure. Le radio-manipulateur ne peut donc pas savoir si un léger changement dans le positionnement de l'arceau peut réduire la dose tout en gardant une bonne visibilité d'un organe cible dans l'image obtenue. Nous avons donc proposé une méthode capable d'explorer des positionnements proches du positionnement actuel et de calculer la dose patient/personnel pour chacun d'entre eux, afin de recommander une configuration réduisant les doses.

Nous formulons ce problème comme la recherche d'une configuration de l'arceau qui minimise une fonction de coût modélisant l'exposition aux radiations du patient et du personnel dans le contexte actuel de la procédure. Ainsi, à partir d'une configuration initiale et en prenant en compte les positions actuelles du staff ainsi que les paramètres de l'acquisition et du patient, notre méthode cherche une configuration optimale en termes de dose patient/staff et de qualité clinique de l'image. Pour ceci, nous avons proposé une approche basée sur des simulations Monte Carlo sur GPU pour calculer en temps réel la fonction de coût, adaptée à son calcul itératif dans une boucle d'optimisation. L'optimisation est contrainte à chercher dans un espace de configurations proches à l'initiale pour ainsi garantir que la visibilité de l'organe cible dans l'image est maintenue. Quand une pose réduisant la dose est trouvée, le modèle géométrique inverse peut être appliqué pour repositionner automatiquement l'imageur à la pose recommandée (en cas d'un capteur plan robotisé). Notre approche est ainsi illustrée dans le schéma de la figure D.9.

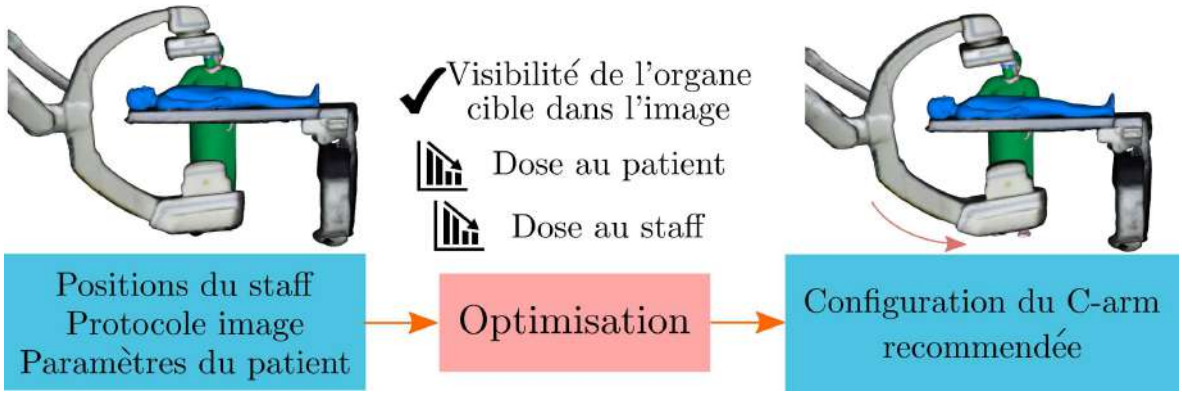

Figure D.9: Méthode d'optimisation de la pose d'un C-arm: à partir d'une configuration initiale et en prenant en compte les positions actuelles du staff, les paramètres de l'acquisition et du patient, notre méthode cherche la configuration optimale qui réduit la dose patient/staff tout en conservant la qualité clinique de l'image.

Une première évaluation sur des scénarios cliniques simulés a montré qu'en quelques secondes notre méthode est capable de recommander une pose de l'imageur qui peut réduire l'exposition du patient et des cliniciens de 5 à 15 %. Une deuxième évaluation avec des mesures de dose obtenues dans une salle opératoire a confirmé le potentiel de la méthode. Ces mesures ont été effectuées d'abord pour diverses configurations initiales, puis pour les recommandées par notre méthode. Les valeurs obtenues ont montré que des légères variations de la pose de l'imageur peuvent effectivement réduire la dose patient/personnel. De plus, une différence moyenne de 10 % entre les réductions prédites par notre méthode et celles mesurées par les dosimètres a été trouvée.

Notre méthode d'optimisation est capable de recommander une pose du capteur plan réduisant la dose patient et personnel en quelques secondes. En rajoutant des éléments additionnels à la fonction de coût, il serait possible d'adapter l'optimisation à d'autres objectifs qui peuvent être aussi pertinents (minimiser la dose à un organe du patient en particulier par exemple). Cette méthode pourrait aussi être appliquée lors du planning chirurgical pour déterminer les configurations optimales de l'imageur qui minimisent la dose absorbée par le patient dans la procédure à venir. Ainsi, nous proposons dans la figure D.10 un concept d'interface pour cette potentielle application clinique de notre méthode. Un modèle préopératoire du patient serait utilisé pour simuler les doses de radiations et les radiographies qui seraient obtenues avec les configurations recommandées par le système.

D.4 Application clinique: *XAware-Live*

Nous avons intégré nos méthodes de perception par caméras RGBD, de simulation des radiations et de visualisation par réalité augmentée dans un prototype d'application

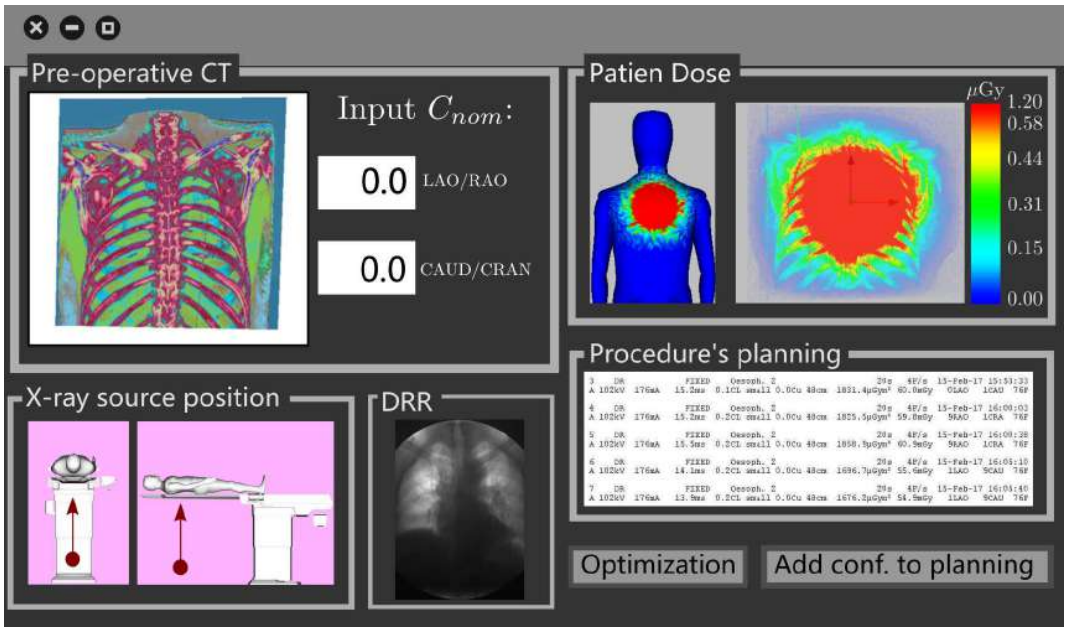

Figure D.10: Concept pour l'interface utilisateur d'une application de planning préopératoire pour déterminer les configurations optimales de l'imageur qui minimisent la dose au patient.

clinique de radioprotection. Ce système, nommé *XAware-Live*[1], a été installé dans une salle opératoire expérimentale à l'IHU de Strasbourg. Il propose des visualisations des radiations en temps réel, qui sont mises à jour d'après la configuration actuelle de l'imageur ou des positions du personnel dans la salle.

Une communication directe entre le C-arm robotisé installé dans la salle (Artis Zeego) et le système permet de mettre à jour les visualisations montrées d'après le positionnement actuel de l'imageur. L'interface utilisateur du système montre d'une part les images capturées par les caméras installées au plafond (côté gauche), et d'autre part, une visualisation virtuelle de la salle. Des cartes de dose précalculées (dose patient ou propagation 3D des radiations) pour des paramètres standard d'image et pour chaque projection obtenue tous les 5° d'une rotation complète dans chaque plan, sont chargées lors de l'initialisation du système.

Les trois types de visualisations décrits auparavant dans la section D.2 ont été intégrés dans le système pour visualiser les simulations. Nous montrons dans la figure D.11, un exemple de la visualisation par AR de la propagation du diffusé de radiation montrée par *XAware-Live*. Comme mentionné précédemment, cette visualisation est mise à jour en temps réel lorsque l'angle d'incidence de l'imageur est modifié. Ceci permet alors aux cliniciens d'avoir un retour visuel des zones les plus irradiées à tout moment. De même, la figure D.12 montre la visualisation de la dose absorbée par le patient (peau et organes) proposée par le système.

[1]Une vidéo illustrant le système et ses différentes fonctionnalités peut être trouvé à partir de ce lien: https://youtu.be/JpATPDrXvu8

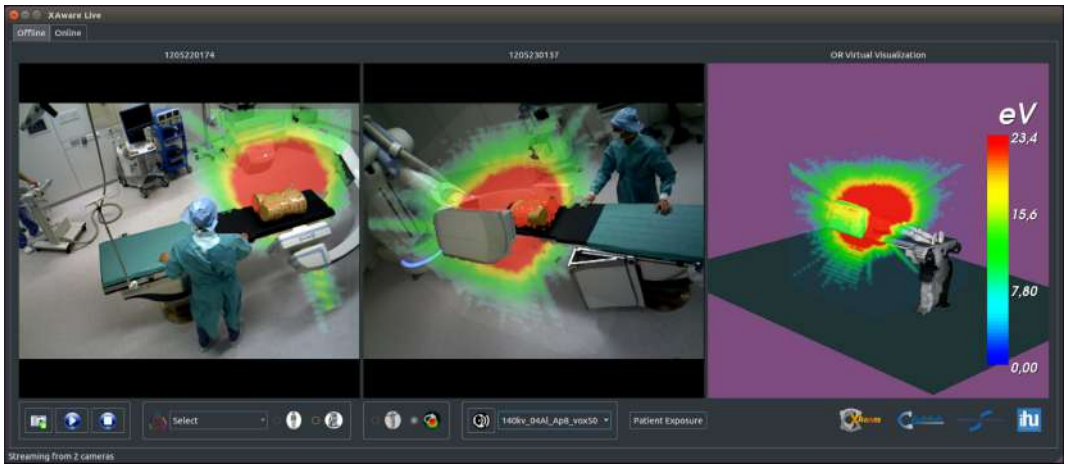

Figure D.11: Visualisation par réalité augmentée de la propagation et intensité du rétrodiffusé de radiation pour l'angle d'incidence courant du capteur plan, proposée par le système *XAware-Live*.

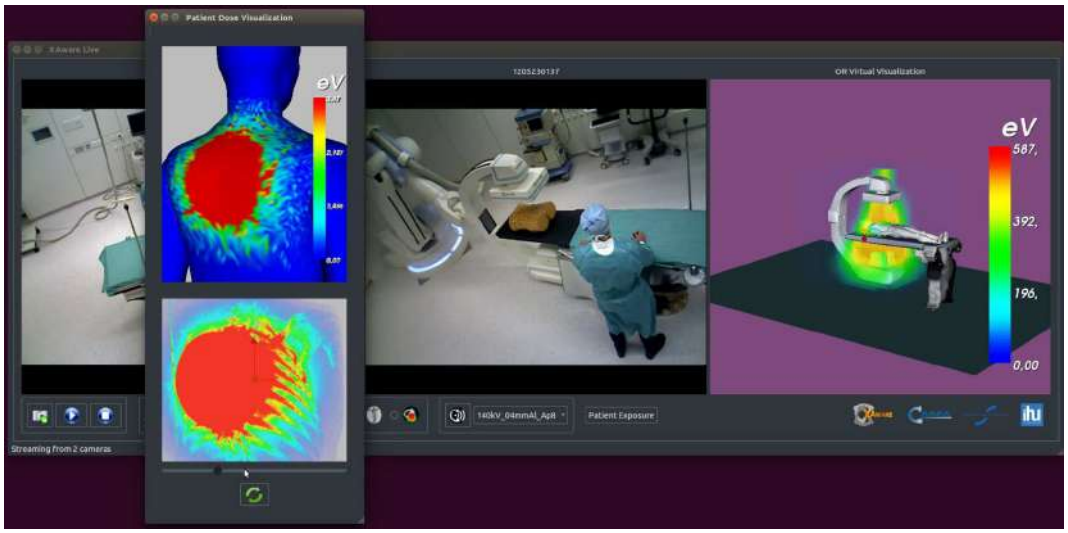

Figure D.12: Visualisation de la dose à la peau et aux organes du patient pour l'angle d'incidence courant du capteur plan, proposée par le système *XAware-Live*.

De plus, nous avons intégré l'approche de [Cao 2017] pour l'estimation en temps réel des poses des cliniciens présents dans la salle sur les images couleur des caméras du plafond. Grace à cette approche, le système peut montrer les poses des personnes sur les images couleur, ainsi qu'une représentation de la position 3D des personnes autour de la table dans la visualisation virtuelle de la salle (voir figure D.13). Le système utilise ces informations pour montrer par réalité augmentée l'exposition aux irradiations sur les différentes parties du corps des personnes présentes dans la salle pour l'angle d'incidence actuel du C-arm. La figure D.14 montre un exemple de cette visualisation, où l'on peut observer que les parties du corps qui sont les plus proches de la source des radiations et

donc exposées à une dose plus importante, sont colorées en orange/rouge.

Figure D.13: Estimation en temps réel de la pose des cliniciens présents dans la salle, grâce à l'intégration de l'approche de [Cao 2017] à *XAware-Live*.

Figure D.14: Visualisation par réalité augmentée de la dose sur les différentes parties du corps des cliniciens présents dans la salle pour l'angle d'incidence courant du capteur plan, proposée par le système *XAware-Live*.

Nos partenaires cliniques et industriels ont montré un grand intérêt pour ce système car il permet de montrer de manière intuitive les radiations dans la salle opératoire. En effet, ce système a le potentiel de servir comme outil pour enseigner intuitivement à des étudiants le comportement des radiations ainsi que les bonnes pratiques pour réduire la dose patient/personnel.

D.5 Conclusions

Nous avons proposé dans cette thèse de nouvelles méthodes pour contribuer à l'amélioration de la sécurité vis-à-vis des radiations dans des procédures guidées par rayons X. Ces méthodes ont été appliquées au développement d'un système de suivi et de visualisation

des radiations dans une salle opératoire, qui permet à des utilisateurs de voir la propagation du rayonnement en 3D dans la configuration actuelle de la salle. Ce système peut ainsi contribuer à aider les cliniciens à prendre conscience de leur exposition aux radiations, et il est aussi particulièrement adapté à l'enseignement des bonnes pratiques de radioprotection. Nous avons aussi proposé une nouvelle approche pour optimiser le positionnement d'un imageur à rayons X, afin de recommander une pose en quelques secondes qui réduit la dose du patient et du personnel présent. Nous espérons qu'en contribuant des méthodes ayant le potentiel de réduire l'exposition aux irradiations, cette thèse puisse aussi aider à rendre les bénéfices des chirurgies guidées par image accessibles à une plus grande population.

D.6 Perspectives

Parmi les perspectives de nos travaux, la plus immédiate est le développement d'un système éducatif de radioprotection à partir de nos méthodes de simulation et visualisations des radiations. Les limitations actuelles de notre prototype *XAware-Live*, comme le fait que les cartes de radiation sont précalculées ou que les protections plombées ne sont pas prises en compte actuellement, doivent être alors adressées. De plus, des études pour valider l'impact d'un système de réalité augmentée dans l'enseignement des bonnes pratiques de radioprotection doivent être réalisées. Ceci peut être accompli à travers des questionnaires qui serviraient à valider la pertinence du système. Une autre perspective de nos travaux est l'utilisation des caméras RGBD pour reconnaitre automatiquement les activités dans la salle opératoire et ainsi trouver des corrélations entre les activités chirurgicales et l'exposition aux irradiations. En effet, ceci permettrait d'identifier les étapes d'une chirurgie qui génèrent les doses de radiation les plus importantes et de recommander des workflows plus sûrs en termes d'exposition aux rayons X.

References

[Agostinelli 2003] S. Agostinelli, J. Allison and K. Amako et al. *GEANT4 - A simulation toolkit.* Nuclear Instruments and Methods in Physics Research, Section A: Accelerators, Spectrometers, Detectors and Associated Equipment, vol. 506, no. 3, pages 250–303, 2003. (Cited on pages 32, 34, 36, 37, 58, 62, and 70)

[Alnewaini 2017] Z. Alnewaini, E. Langer, P. Schaber, M. David, D. Kretz, V. Steil and J. Hesser. *Real-time, ray casting-based scatter dose estimation for C-arm X-ray system.* Journal of Applied Clinical Medical Physics, vol. 18, no. 2, pages 144–153, 2017. (Cited on pages 33, 39, 65, 74, and 77)

[Atracsys 2015] Atracsys. http://www.atracsys.com/, 2015. (Cited on page 152)

[Badal-Soler 2008] A. Badal-Soler. *Development of advanced geometric models and acceleration techniques for Monte Carlo simulation in Medical Physics.* Doctoral Dissertation, Institut de Tècniques Energètiques Universitat Politècnica de Catalunya, 2008. (Cited on page 32)

[Badal 2009] A. Badal and A. Badano. *Accelerating Monte Carlo simulations of photon transport in a voxelized geometry using a massively parallel graphics processing unit.* Medical Physics, vol. 36, no. 11, page 4878, 2009. (Cited on pages 32, 36, and 70)

[Badal 2013] A. Badal, F. Zafar, H. Dong and A. Badano. *A real-time radiation dose monitoring system for patients and staff during interventional fluoroscopy using a GPU-accelerated Monte Carlo simulator and an automatic 3D localization system based on a depth camera.* Proc. SPIE 8668, Medical Imaging, no. March, 2013. (Cited on pages 36, 45, 46, 74, 77, and 85)

[Baró 1995] J. Baró, J. Sempau, J. Fernández-Varea and F. Salvat. *PENELOPE: An algorithm for Monte Carlo simulation of the penetration and energy loss of electrons and positrons in matter.* Nuclear Instruments and Methods in Physics Research Section B: Beam Interactions with Materials and Atoms, vol. 100, no. 1, pages 31 – 46, 1995. (Cited on page 32)

[Beasley 2012] R. A. Beasley. *Medical Robots: Current Systems and Research Directions.* Journal of Robotics, 2012. (Cited on page 101)

[Berlage 1997] T. Berlage. *Augmented reality for diagnosis based on ultrasound images.* In CVRMed-MRCAS'97: First Joint Conference Computer Vision, Virtual Reality and Robotics in Medicine and Medical Robotics and Computer-Assisted Surgery, volume 1205, pages 253–262. 1997. (Cited on page 85)

[Bert 2013] J. Bert, H. Perez-Ponce, Z. E. Bitar, S. Jan, Y. Boursier, D. Vintache, A. Bonissent, C. Morel, D. Brasse and D. Visvikis. *Geant4-based Monte Carlo simulations on GPU for medical applications.* Physics in Medicine & Biology, vol. 58, no. 16, pages 5593–5611, 2013. (Cited on pages 70, 71, 77, and 170)

[Bordier 2014] C. Bordier, R. Klausz and L. Desponds. *Patient dose map indications on interventional X-ray systems and validation with gafchromic XR-RV3 film.* Radiation Protection Dosimetry, vol. 163, no. 3, pages 306–318, 2014. (Cited on page 26)

[Bott 2009] O. J. Bott, M. Wagner, C. Duwenkamp, N. Hellrung and K. Dresing. *Improving education on C-arm operation and radiation protection with a computer-based training and simulation system.* International Journal of Computer Assisted Radiology and Surgery, vol. 4, no. 4, pages 399–407, 2009. (Cited on pages 33, 34, and 85)

[Bott 2011] O. J. Bott, K. Dresing, M. Wagner, B.-W. Raab and M. Teistler. *Informatics in Radiology: Use of a C-Arm Fluoroscopy Simulator to Support Training in Intraoperative Radiography.* RadioGraphics, vol. 31, no. 3, pages E65–E75, 2011. (Cited on pages 33 and 34)

[Brenner 2007] D. J. Brenner and E. J. Hall. *Computed Tomography — An Increasing Source of Radiation Exposure.* New England Journal of Medicine, vol. 357, no. 22, pages 2277–2284, 2007. (Cited on pages xviii, 8, and 148)

[Bushberg 2011] J. Bushberg, J. Seibert, E. Leidholdt and J. Boone. The essential physics of medical imaging. Wolters Kluwer Health, 2011. (Cited on pages 59 and 61)

[Cao 2017] Z. Cao, T. Simon, S. Wei and Y. Sheikh. *Realtime Multi-Person 2D Pose Estimation using Part Affinity Fields.* In 2017 IEEE Conference on Computer Vision and Pattern Recognition (CVPR), 2017. (Cited on pages xii, xvi, 51, 52, 75, 127, 178, and 179)

[Carinou 2011] E. Carinou, P. Ferrari, C. Koukorava, S. Krim and L. Struelens. *Monte Carlo calculations on extremity and eye lens dosimetry for medical staff at interventional radiology procedures.* Radiation Protection Dosimetry, vol. 144, no. 1-4, pages 492–496, 2011. (Cited on pages 11, 14, 16, 17, 44, 87, and 169)

[Chen 2013] X. Chen, L. Wang, P. Fallavollita and N. Navab. *Precise X-ray and video overlay for augmented reality fluoroscopy.* International Journal of Computer Assisted Radiology and Surgery, vol. 8, no. 1, pages 29–38, 2013. (Cited on pages 30 and 85)

[Clairand 2011] I. Clairand, J.-M. Bordy, E. Carinou, J. Daures, J. Debroas, M. Denozière, L. Donadille, M. Ginjaume, C. Itié, C. Koukorava, S. Krim, A.-L. Lebacq, P. Martin, L. Struelens, M. Sans-Merce and F. Vanhavere. *Use of active personal dosemeters in interventional radiology and cardiology: Tests in laboratory conditions and recommendations - ORAMED project.* Radiation Measurements, vol. 46, no. 11, pages 1252 – 1257, 2011. International Workshop on Optimization of Radiation Protection of Medical Staff, ORAMED 2011. (Cited on page 27)

[Conti 2014] C. R. Conti. *Radiation awareness.* European Heart Journal, vol. 35, no. 10, pages 600–601, 2014. (Cited on pages xviii, 8, and 148)

[Corindus 2017] Corindus. *CorPath GRX Vascular Robotic System.* http://www.corindus.com/, 2017. (Cited on page 28)

[Dagnino 2017] G. Dagnino, I. Georgilas, S. Morad, P. Gibbons, P. Tarassoli, R. Atkins and S. Dogramadzi. *Intra-operative fiducial-based CT/fluoroscope image registration framework for image-guided robot-assisted joint fracture surgery.* International Journal of Computer Assisted Radiology and Surgery, pages 1–15, 2017. (Cited on page 30)

[Das 2006] M. Das, F. Sauer, U. J. Schoepf, A. Khamene, S. K. Vogt, S. Schaller, R. Kikinis, E. vanSonnenberg and S. G. Silverman. *Augmented Reality Visualization for CT-guided Interventions: System Description, Feasibility, and Initial Evaluation in an Abdominal Phantom.* Radiology, vol. 240, no. 1, pages 230–235, 2006. (Cited on page 155)

[Desser 2007] T. S. Desser. *Simulation-Based Training: The Next Revolution in Radiology Education?* Journal of the American College of Radiology, vol. 4, no. 11, pages 816–824, 2007. (Cited on page 33)

[Ertel 2012] A. Ertel, J. Nadelson, A. R. Shroff, R. Sweis, D. Ferrera and M. I. Vidovich. *Radiation Dose Reduction during Radial Cardiac Catheterization: Evaluation of a Dedicated Radial Angiography Absorption Shielding Drape.* ISRN Cardiology, 2012. (Cited on pages 14 and 17)

[Fallavollita 2014] P. Fallavollita, A. Winkler, S. Habert, P. Wucherer, P. Stefan, R. Mansour, R. Ghotbi and N. Navab. *Desired-View Controlled Positioning of Angiographic C-arms.* In Medical Image Computing and Computer-Assisted Intervention - MICCAI, pages 659–666, 2014. (Cited on pages xiii, 101, 102, 103, 104, 107, and 175)

[Fardid 2011] R. Fardid, F. Mirzadeh and H. Rezaei. *Occupational doses of cardiologists in cath labs and simulation method.* Journal of Cancer Research and Therapeutics, 2011. (Cited on page 16)

[Farzan 2013] S. Farzan and G. N. DeSouza. *From D-H to inverse kinematics: A fast numerical solution for general robotic manipulators using parallel processing.* In IEEE/RSJ International Conference on Intelligent Robots and Systems, pages 2507–2513, 2013. (Cited on page 109)

[FDA 2010] FDA. *Initiative to Reduce Unnecessary Radiation Exposure from Medical Imaging.* U.S. Food and Drug Administration - Center for Devices and Radiological Health, 2010. (Cited on pages xviii, 8, 9, 15, and 148)

[Feuerstein 2008] M. Feuerstein, T. Mussack, S.-M. Heining and N. Navab. *Intraoperative Laparoscope Augmentation for Port Placement and Resection Planning in Minimally Invasive Liver Resection.* IEEE Transactions on Medical Imaging, vol. 27, no. 3, pages 355–369, March 2008. (Cited on page 85)

[Fotouhi 2017] J. Fotouhi, B. Fuerst, W. Wein and N. Navab. *Can real-time RGBD enhance intraoperative Cone-Beam CT?* International Journal of Computer Assisted Radiology and Surgery, vol. 12, no. 7, pages 1–9, 2017. (Cited on pages 31 and 45)

[Fuchs 2002] K. H. Fuchs. *Minimally Invasive Surgery.* Endoscopy, vol. 34, no. 02, pages 154–159, 2002. (Cited on page 6)

[GGEMS 2017] GGEMS. *GPU Geant4-based Monte-Carlo Simulations, LaTIM, INSERM, CHRU Brest, France.* http://ggems.fr/, 2017. (Cited on pages 32, 58, 70, 71, and 170)

[Glocker 2015] B. Glocker, J. Shotton, A. Criminisi and S. Izadi. *Real-Time RGB-D Camera Relocalization via Randomized Ferns for Keyframe Encoding.* IEEE Transactions on Visualization and Computer Graphics, vol. 21, no. 5, pages 571–583, 2015. (Cited on pages 155 and 164)

[Hansen Medical 2017a] Hansen Medical. *Magellan Robotic System.* http://www.hansenmedical.com/us/en/vascular/magellan-robotic-system/product-overview, 2017. (Cited on page 28)

[Hansen Medical 2017b] Hansen Medical. *Sensei Robotic System.* http://www.hansenmedical.com/us/en/cardiac-arrhythmia/sensei-robotic-system/product-overview, 2017. (Cited on page 28)

[Hinterstoisser 2012a] S. Hinterstoisser, C. Cagniart, S. Ilic, P. Sturm, N. Navab, P. Fua and V. Lepetit. *Gradient Response Maps for Real-Time Detection of Textureless Objects.* IEEE Transactions on Pattern Analysis and Machine Intelligence, vol. 34, no. 5, pages 876–888, 2012. (Cited on pages 53, 156, and 159)

[Hinterstoisser 2012b] S. Hinterstoisser, V. Lepetit, S. Ilic, S. Holzer, G. Bradski, K. Konolige and N. Navab. *Model Based Training, Detection and Pose Estimation of Texture-Less 3D Objects in Heavily Cluttered Scenes*. In Asian Conference on Computer Vision - ACCV, pages 548–562. 2012. (Cited on pages 53, 156, 158, 159, and 161)

[Huang 2009] B. Huang, M. W.-M. Law and P.-L. Khong. *Whole-body PET/CT scanning: estimation of radiation dose and cancer risk*. Radiology, vol. 251, no. 1, pages 166–174, 2009. (Cited on page 15)

[ICRP 2017] ICRP. *Dose Limits Recommended by the International Commission on Radiological Protection (ICRP)*. http://www.icrp.org/icrpaedia/limits.asp, 2017. (Cited on pages xviii, 147, and 149)

[ICRU 1980] ICRU. Report no. 33. 1956-1964: National Bureau of Standards handbook. International Commission on Radiation Units and Measurements, 1980. (Cited on page 63)

[IHU 2017] IHU. *Institute of Image-Guided Surgery of Strasbourg*. http://www.ihu-strasbourg.eu/ihu/en/, 2017. (Cited on pages 18, 44, 47, and 51)

[Kadkhodamohammadi 2017a] A. Kadkhodamohammadi, A. Gangi, M. de Mathelin and N. Padoy. *A Multi-view RGB-D Approach for Human Pose Estimation in Operating Rooms*. In IEEE Winter Conference on Applications of Computer Vision (WACV), pages 363–372, 2017. (Cited on pages 51 and 75)

[Kadkhodamohammadi 2017b] A. Kadkhodamohammadi. *3D Detection and Pose Estimation of Medical Staff in Operating Rooms using RGB-D Images*. PhD thesis, University of Strasbourg, 2017. (Cited on pages xii, 50, and 51)

[Kaplan 2013] A. Kaplan. *Three-Year Experience with the Robotic Catheter System*. EP Lab Digest, 2013. (Cited on page 28)

[Kaplan 2016] D. J. Kaplan, J. N. Patel, F. A. Liporace and R. S. Yoon. *Intraoperative radiation safety in orthopaedics: a review of the ALARA (As low as reasonably achievable) principle*. Patient Safety in Surgery, vol. 10, no. 27, 2016. (Cited on pages 8, 10, 11, 17, and 147)

[Katz 2017a] A. Katz, A. Shtub and A. Roguin. *Minimizing Ionizing Radiation Exposure in Invasive Cardiology Safety Training for Medical Doctors*. Journal of Nuclear Engineering and Radiation Science, vol. 3, no. 3, 2017. (Cited on pages 18, 33, 34, and 35)

[Katz 2017b] A. Katz, A. Shtub, A. Solomonica, A. Poliakov and A. Roguin. *Simulator training to minimize ionizing radiation exposure in the catheterization laboratory*. International Journal of Cardiovascular Imaging, vol. 33, no. 3, pages 303–310, 2017. (Cited on pages 34, 35, 85, and 170)

[Kirkwood 2014] M. L. Kirkwood, G. M. Arbique, J. B. Guild, C. Timaran, R. J. Valentine and J. A. Anderson. *Radiation-induced skin injury after complex endovascular procedures.* Journal of Vascular Surgery, vol. 60, no. 3, pages 742 – 748, 2014. (Cited on pages 10, 12, 18, and 103)

[Kläser 2008] A. Kläser, M. Marszalek and C. Schmid. *A Spatio-Temporal Descriptor Based on 3D-Gradients.* In Proceedings of the British Machine Vision Conference, pages 1–10, 2008. (Cited on page 74)

[Koukorava 2011] C. Koukorava, E. Carinou, P. Ferrari, S. Krim and L. Struelens. *Study of the parameters affecting operator doses in interventional radiology using Monte Carlo simulations.* Radiation Measurements, vol. 46, no. 11, pages 1216–1222, 2011. (Cited on pages 12, 13, 14, 32, 33, 37, 44, 58, 86, and 87)

[Kuchynka 2015] P. Kuchynka, L. Lambert, V. Černý, J. Marek, D. Ambrož, B. A. Danek and A. Linhart. *Coronary CT angiography.* Cor et Vasa, vol. 57, no. 6, pages e425 – e432, 2015. Imaging in Coronary Artery Disease. (Cited on page 3)

[Kuhls-Gilcrist 2017] A. Kuhls-Gilcrist. *Dose Tracking System : A Paradigm Shift in Patient Dose Monitoring.* Toshiba Dose Tracking System Whitepaper, 2017. (Cited on pages xi, 23, 25, 26, 149, and 150)

[Kwon 2011] D. Kwon, M. P. Little and D. L. Miller. *Reference air kerma and kerma-area product as estimators of peak skin dose for fluoroscopically guided interventions.* Medical Physics, vol. 38, no. 7, pages 4196–4204, 2011. (Cited on pages 25, 149, and 150)

[Ladikos 2008] A. Ladikos, S. Benhimane and N. Navab. *Real-Time 3D Reconstruction for Collision Avoidance in Interventional Environments.* In Medical Image Computing and Computer-Assisted Intervention - MICCAI, pages 526–534, 2008. (Cited on page 53)

[Ladikos 2010] A. Ladikos, C. Cagniart, R. Ghotbi, M. Reiser and N. Navab. *Estimating Radiation Exposure in Interventional Environments.* In Medical Image Computing and Computer-Assisted Intervention - MICCAI, pages 237–244. 2010. (Cited on pages 36, 38, 50, 58, 63, and 85)

[Lakhan 2009] S. E. Lakhan, A. Kaplan, C. Laird and Y. Leiter. *The interventionalism of medicine: interventional radiology, cardiology, and neuroradiology.* International Archives of Medicine, vol. 2, no. 27, 2009. (Cited on pages 6 and 7)

[LaTIM 2017] LaTIM. *Laboratory of Medical Information Processing (LaTIM - INSERM UMR 1101), Brest, France.* http://latim.univ-brest.fr/, 2017. (Cited on pages 58 and 70)

[Lemaréchal 2015] Y. Lemaréchal, J. Bert, C. Falconnet, P. Després, A. Valeri, U. Schick, O. Pradier, M.-P. Garcia, N. Boussion and D. Visvikis. *GGEMS-Brachy: GPU*

GEant4-based Monte Carlo simulation for brachytherapy applications. Physics in Medicine and Biology, vol. 60, no. 13, pages 4987–5006, 2015. (Cited on pages 32, 70, 71, 77, and 134)

[Lepoutre 2016] N. Lepoutre, R. A. Porto, L. Meylheuc, G. I. Bara, F. Schmitt, L. Barbé and B. Bayle. *Robotically assisted injection of orthopedic cement: System design, control and modeling.* 2016 European Control Conference, ECC 2016, pages 2127–2132, 2016. (Cited on page 29)

[Leucht 2015] N. Leucht, S. Habert, P. Wucherer, S. Weidert, N. Navab and P. Fallavollita. *[POSTER] Augmented reality for radiation awareness.* Proceedings of the 2015 IEEE International Symposium on Mixed and Augmented Reality, ISMAR 2015, pages 60–63, 2015. (Cited on pages 37, 38, 39, 45, 58, and 65)

[Linton 1995] O. W. Linton. *Medical applications of X-rays.* SLAC Beam Line, vol. 25N2, page 25, 1995. (Cited on page 5)

[Loy Rodas 2014] N. Loy Rodas and N. Padoy. *3D Global Estimation and Augmented Reality Visualization of Intra-operative X-ray Dose.* In Medical Image Computing and Computer-Assisted Intervention - MICCAI, pages 415–422, 2014. (Cited on pages 21, 39, 58, 84, and 170)

[Loy Rodas 2015a] N. Loy Rodas, F. Barrera and N. Padoy. *Marker-Less AR in the Hybrid Room Using Equipment Detection for Camera Relocalization.* In Medical Image Computing and Computer-Assisted Intervention - MICCAI, pages 463–470, 2015. (Cited on pages 21 and 170)

[Loy Rodas 2015b] N. Loy Rodas and N. Padoy. *Seeing is believing: increasing intraoperative awareness to scattered radiation in interventional procedures by combining augmented reality, Monte Carlo simulations and wireless dosimeters.* International Journal of Computer Assisted Radiology and Surgery, vol. 10, no. 8, pages 1181–1191, 2015. (Cited on pages 21, 39, 50, 58, 75, 84, and 170)

[Loy Rodas 2017a] N. Loy Rodas, F. Barrera and N. Padoy. *See It With Your Own Eyes: Marker-less Mobile Augmented Reality for Radiation Awareness in the Hybrid Room.* IEEE Transactions on Biomedical Engineering, vol. 64, no. 2, pages 429–440, 2017. (Cited on pages 21, 52, 54, 92, 152, 154, 156, and 170)

[Loy Rodas 2017b] N. Loy Rodas, J. Bert, D. Visvikis, M. de Mathelin and N. Padoy. *Pose optimization of a C-arm imaging device to reduce intraoperative radiation exposure of staff and patient during interventional procedures.* In IEEE International Conference on Robotics and Automation (ICRA), pages 4200–4207, 2017. (Cited on pages 21, 58, 100, and 175)

[Loy Rodas 2018a] N. Loy Rodas, P. Ghimire, A. Gangi, M. de Mathelin and N. Padoy. *Teaching Radiation Safety intuitively with a Head-mounted display.* In European Congress of Radiology (ECR), 2018. (Cited on pages 21 and 85)

[Loy Rodas 2018b] N. Loy Rodas, A. Kadkhodamohammadi, A. Gangi, M. de Mathelin and N. Padoy. *A Global Radiation Awareness System using Augmented Reality and Monte Carlo Simulations.* In European Congress of Radiology (ECR), 2018. (Cited on page 21)

[Loy Rodas 2018c] N. Loy Rodas and N. Padoy. *Augmented Reality for reducing intraoperative radiation exposure to patients and clinicians during X-ray guided procedures.* In T. Peters, Z. Yaniv and C. Linte, editors, Augmented Reality in Medicine. 2018. (Cited on page 21)

[Maier-Hein 2017] L. Maier-Hein, S. S. Vedula, S. Speidel, N. Navab, R. Kikinis, A. Park, M. Eisenmann, H. Feussner, G. Forestier, S. Giannarou, M. Hashizume, D. Katic, H. Kenngott, M. Kranzfelder, A. Malpani, K. März, T. Neumuth, N. Padoy, C. Pugh, N. Schoch, D. Stoyanov, R. Taylor, M. Wagner, G. D. Hager and P. Jannin. *Surgical data science for next-generation interventions.* Nature Biomedical Engineering, vol. 1, no. 9, pages 691–696, 2017. (Cited on page 141)

[Maor 2017] E. Maor, M. F. Eleid, R. Gulati, A. Lerman and G. S. Sandhu. *Current and Future Use of Robotic Devices to Perform Percutaneous Coronary Interventions: A Review.* Journal of the American Heart Association, vol. 6, no. 7, 2017. (Cited on page 28)

[Miller 2005] D. Miller. *Interventional Fluoroscopy: Reducing Radiation Risks for Patients and Staff.* Journal of Radiology Nursing, vol. 24, no. 3, pages 52–56, 2005. (Cited on pages xviii, 6, 7, 9, 11, and 148)

[Morrish 2008] O. W. E. Morrish and K. E. Goldstone. *An investigation into patient and staff doses from X-ray angiography during coronary interventional procedures.* The British Journal of Radiology, vol. 81, no. 961, pages 35–45, 2008. (Cited on page 10)

[Müller 2013] M. Müller, M.-C. Rassweiler, J. Klein, A. Seitel, M. Gondan, M. Baumhauer, D. Teber, J. J. Rassweiler, H.-P. Meinzer and L. Maier-Hein. *Mobile augmented reality for computer-assisted percutaneous nephrolithotomy.* International Journal of Computer Assisted Radiology and Surgery, vol. 8, no. 4, pages 663–675, 2013. (Cited on page 30)

[Navab 2006] N. Navab, S. Wiesner, S. Benhimane, E. Euler and S. M. Heining. *Visual Servoing for Intraoperative Positioning and Repositioning of Mobile C-arms.* In Medical Image Computing and Computer-Assisted Intervention - MICCAI, pages 551–560, 2006. (Cited on pages 101, 102, and 175)

[Navab 2010] N. Navab, S. M. Heining and J. Traub. *Camera augmented mobile C-arm (CAMC): Calibration, accuracy study, and clinical applications.* IEEE Transactions on Medical Imaging, vol. 29, no. 7, pages 1412–1423, 2010. (Cited on pages 30 and 85)

[Navab 2012] N. Navab, T. Blum, L. Wang, A. Okur and T. Wendler. *First deployments of augmented reality in operating rooms*. Computer, vol. 45, no. 7, pages 48–55, 2012. (Cited on pages 30 and 31)

[NCRP 1990] NCRP. Report No. 107 - Implementation of the Principle of As Low As Reasonably Achievable (ALARA) for Medical and Dental Personnel. National Council on Radiation Protection and Measurements, 1990. (Cited on pages 15 and 104)

[Newcombe 2011] R. A. Newcombe, S. Izadi, O. Hilliges, D. Molyneaux, D. Kim, A. J. Davison, P. Kohli, J. Shotton, S. Hodges and A. W. Fitzgibbon. *KinectFusion: Real-time dense surface mapping and tracking*. In 10th IEEE International Symposium on Mixed and Augmented Reality (ISMAR), pages 127–136, 2011. (Cited on pages 92, 156, and 157)

[Ngatchou 2005] P. Ngatchou, A. Zarei and A. El-Sharkawi. *Pareto Multi Objective Optimization*. In Proceedings of the 13th International Conference on, Intelligent Systems Application to Power Systems, pages 84–91, 2005. (Cited on pages 113 and 114)

[Nguyen 2010] B. L. Nguyen, J. L. Merino and E. S. Gang. *Remote Navigation for Ablation Procedures – A New Step Forward in the Treatment of Cardiac Arrhythmias Remote Navigation for Ablation Procedures*. In European Cardiology, volume 6, pages 50–56. 2010. (Cited on pages 27 and 28)

[Nikodemová 2011] D. Nikodemová, M. Brodecki, E. Carinou, J. Domienik, L. Donadille, C. Koukorava, S. Krim, N. Ruiz-López, M. Sans-Merce, L. Struelens, F. Vanhavere and R. Zaknoune. *Staff extremity doses in interventional radiology. Results of the ORAMED measurement campaign*. Radiation Measurements, vol. 46, no. 11, pages 1210 – 1215, 2011. International Workshop on Optimization of Radiation Protection of Medical Staff, ORAMED 2011. (Cited on pages xi, 5, 6, 7, 8, 11, 12, 14, 16, 17, 27, 44, 169, and 170)

[Omar 2017] A. Omar, N. Kadesjö, C. Palmgren, M. Marteinsdottir, T. Segerdahl and A. Fransson. *Assessment of the occupational eye lens dose for clinical staff in interventional radiology, cardiology and neuroradiology*. Journal of Radiological Protection, vol. 37, no. 1, page 145, 2017. (Cited on page 12)

[OpenCV 2015] Open source Computer Vision. OpenCV. http://opencv.org/, 2015. (Cited on page 161)

[OpenNI 2013] OpenNI. *PrimeSense NiTE library*. https://structure.io/openni, 2013. (Cited on pages 36, 37, and 48)

[ORAMED 2011] ORAMED. *Optimization of RAdiation protection for MEDical staff*. http://www.oramed-fp7.eu/, 2011. (Cited on pages 12, 27, and 32)

[Padoy 2014] N. Padoy and N. Loy Rodas. *Method for estimating the spatial distribution of the hazardousness of radiation doses*, 2014. US Patent App. 15/501,319, World Patent App. PCT/EP2015/067,639. (Cited on page 21)

[Padoy 2017] N. Padoy, N. Loy Rodas, J. Bert, M. de Mathelin and D. Visvikis. *Method for determining a configuration setting of a source of ionizing radiation*, 2017. EU Patent Appplication. (Cited on page 21)

[PCL 2015] PCL. *Point Cloud Libraries*. http://www.pointclouds.org, 2015. (Cited on page 161)

[Pelowitz 2005] D. Pelowitz. *MCNPX User's Manual, Version 2.5.0, Los Alamos National Laboratory*, 2005. (Cited on pages 32 and 33)

[Pham 2010] V. Pham, P. Vo, V. T. Hung and L. H. Bac. *GPU Implementation of Extended Gaussian Mixture Model for Background Subtraction*. In Computing and Communication Technologies, Research, Innovation, and Vision for the Future (RIVF), 2010 IEEE RIVF International Conference on, pages 1–4, Nov 2010. (Cited on page 160)

[Philips 2017a] Philips. *ClarityIQ X-ray imaging technology*. http://www.philips.ng/healthcare/product/HCNOCTN163/alluraclarity-with-clarityiq-technology, 2017. (Cited on page 15)

[Philips 2017b] Philips. *DoseWise Portal radiation dose management solution*. https://www.usa.philips.com/healthcare/product/HC895001, 2017. (Cited on page 26)

[Picano 2013] E. Picano, M. G. Andreassi, E. Piccaluga, A. Cremonesi and G. Guagliumi. *Occupational Risks of Chronic Low Dose Radiation Exposure in Cardiac Catheterisation Laboratory: the Italian Healthy Cath Lab Study*. EMJ Int Cardiol, pages 50–58, 2013. (Cited on pages 6, 10, 11, 12, 13, 14, 35, 44, and 169)

[Piccin 2016] O. Piccin, J. Sieffert, F. Schmitt, L. Barbé, L. Meylheuc, F. Nageotte and B. Bayle. *Design and characterization of a novel needle insertion tool*. 2016 6th IEEE International Conference on Biomedical Robotics and Biomechatronics (BioRob), pages 266–271, 2016. (Cited on page 29)

[Principi 2016] S. Principi, J. Farah, P. Ferrari, E. Carinou, I. Clairand and M. Ginjaume. *The influence of operator position, height and body orientation on eye lens dose in interventional radiology and cardiology: Monte Carlo simulations versus realistic clinical measurements*. Physica Medica, vol. 32, no. 9, pages 1111 – 1117, 2016. (Cited on pages 12, 33, and 58)

[Proietti 2013] R. Proietti, V. Pecoraro, L. Di Biase, A. Natale, P. Santangeli, M. Viecca, A. Sagone, A. Galli, L. Moja and L. Tagliabue. *Remote magnetic with open-irrigated catheter vs. manual navigation for ablation of atrial fibrillation: A*

systematic review and meta-analysis. Europace, vol. 15, no. 9, pages 1241–1248, 2013. (Cited on pages 27 and 28)

[Qian 2017] L. Qian, A. Barthel, A. Johnson, G. Osgood, P. Kazanzides, N. Navab and B. Fuerst. *Comparison of optical see-through head-mounted displays for surgical interventions with object-anchored 2D-display*. International Journal of Computer Assisted Radiology and Surgery, vol. 12, no. 6, pages 901–910, 2017. (Cited on pages 93 and 96)

[Rana 2013] V. K. Rana, S. Rudin and D. R. Bednarek. *Updates in the real-time Dose Tracking System (DTS) to improve the accuracy in calculating the radiation dose to the patients skin during fluoroscopic procedures*. Proceedings of SPIE–The International Society for Optical Engineering, 2013. (Cited on pages xi, 23, 25, and 26)

[RaySafe 2017] RaySafe. *RaySafe i2 active dosimetry system*. http://raysafe.com/Products/Staff, 2017. (Cited on pages 26, 65, 79, and 117)

[Razani 1972] A. Razani. *A Monte Carlo Method for Radiation Transport Calculations*. Journal of Nuclear Science and Technology, vol. 9, no. 9, pages 551–554, 1972. (Cited on page 32)

[RecFusion 2015] ImFusion GmbH. RecFusion. http://http://www.recfusion.net/, 2015. (Cited on pages 53 and 158)

[Reed 2011] A. B. Reed. *The history of radiation use in medicine*. Journal of Vascular Surgery, vol. 53, no. 1, pages 3S – 5S, 2011. Radiation Safety in Vascular Surgery. (Cited on pages 3, 4, 5, and 10)

[Research Group CAMMA 2017] Research Group CAMMA. *Computational Analysis and Modeling of Medical Activities*. http://camma.u-strasbg.fr/, 2017. (Cited on pages 45 and 48)

[Roguin 2012] A. Roguin, J. Goldstein and O. Bar. *Brain tumours among interventional cardiologists: a cause for alarm?* EuroIntervention, vol. 7, pages 1081 – 1086, 2012. (Cited on pages 7, 12, 16, and 17)

[Roguin 2013] A. Roguin, J. Goldstein, O. Bar and J. A. Goldstein. *Brain and Neck Tumors Among Physicians Performing Interventional Procedures*. The American Journal of Cardiology, vol. 111, no. 9, pages 1368 – 1372, 2013. (Cited on pages 6, 7, 9, 11, 101, 116, 168, and 169)

[Roguin 2014] A. Roguin. *Radiation in cardiology: can't live without it!* European Heart Journal, vol. 35, no. 10, pages 599–600, 2014. (Cited on pages 10 and 17)

[Sailer 2017] A. M. Sailer, L. Paulis, L. Vergoossen, A. O. Kovac, G. Wijnhoven, G. W. H. Schurink, B. Mees, M. Das, J. E. Wildberger, M. W. de Haan and C. R. Jeukens.

Real-Time Patient and Staff Radiation Dose Monitoring in IR Practice. Cardio-Vascular and Interventional Radiology, vol. 40, no. 3, pages 421–429, 2017. (Cited on page 27)

[Santos 2015] W. S. Santos, L. P. Neves, A. P. Perini, W. Belinato, L. V. E. Caldas, A. B. Carvalho and A. F. Maia. *Exposures in interventional radiology using Monte Carlo simulation coupled with virtual anthropomorphic phantoms.* Physica Medica, vol. 31, no. 8, pages 929–933, 2015. (Cited on pages 12, 13, 14, 33, 58, and 61)

[Sauer 2000] F. Sauer, F. Wenzel, S. Vogt, Y. Tao, Y. Genc and A. Bani-Hashemi. *Augmented workspace: designing an AR testbed.* In Augmented Reality, 2000. (ISAR 2000). Proceedings. IEEE and ACM International Symposium on, pages 47–53, 2000. (Cited on page 155)

[Sauer 2001] F. Sauer, A. Khamene, B. Bascle and G. Rubino. *A Head-Mounted Display System for Augmented Reality Image Guidance: Towards Clinical Evaluation for iMRI-guided Neurosurgery.* In Medical Image Computing and Computer-Assisted Intervention - MICCAI, pages 707–716. 2001. (Cited on page 155)

[Schueler 2006] B. A. Schueler, T. J. Vrieze, H. Bjarnason and A. W. Stanson. *An Investigation of Operator Exposure in Interventional Radiology.* RadioGraphics, vol. 26, no. 5, pages 1533–1541, 2006. (Cited on pages xi, 11, 12, 13, and 117)

[Seitel 2016] A. Seitel, N. Bellemann, M. Hafezi, A. M. Franz, M. Servatius, A. Saffari, T. Kilgus, H. P. Schlemmer, A. Mehrabi, B. A. Radeleff and L. Maier-Hein. *Towards markerless navigation for percutaneous needle insertions.* International Journal of Computer Assisted Radiology and Surgery, vol. 11, no. 1, pages 107–117, 2016. (Cited on pages 30, 31, 45, 155, and 164)

[Siemens Healthcare 2017a] Siemens Healthcare. *Low dose solutions.* http://www.healthcare.siemens.com/medical-imaging/low-dose, 2017. (Cited on page 15)

[Siemens Healthcare 2017b] Siemens Healthcare. *Online tool for the simulation of X-ray Spectra.* https://www.oem-xray-components.siemens.com/x-ray-spectra-simulation, 2017. (Cited on pages xii, 61, and 62)

[Singer 2005] G. Singer. *Occupational radiation exposure to the surgeon.* The Journal of the American Academy of Orthopaedic Surgeons, vol. 13, page 6976, 2005. (Cited on page 15)

[Stereotaxis 2017] Stereotaxis. *Stereotaxis Niobe magnetic navigation system.* http://www.stereotaxis.com/products/niobe/, 2017. (Cited on pages 27 and 28)

[Struelens 2011] L. Struelens, E. Carinou, I. Clairand, L. Donadille, M. Ginjaume, C. Koukorava, S. Krim, H. Mol, M. Sans-Merce and F. Vanhavere. *Use of active personal dosemeters in interventional radiology and cardiology: Tests in*

hospitals - ORAMED project. Radiation Measurements, vol. 46, no. 11, pages 1258–1261, 2011. (Cited on pages 27, 66, 70, and 171)

[Sturm 2012] J. Sturm, N. Engelhard, F. Endres, W. Burgard and D. Cremers. *A benchmark for the evaluation of RGB-D SLAM systems*. In 2012 IEEE/RSJ International Conference on Intelligent Robots and Systems, pages 573–580, 2012. (Cited on pages 46, 151, 160, and 165)

[Svoboda 2005] T. Svoboda, D. Martinec and T. Pajdla. *A Convenient Multicamera Self-Calibration for Virtual Environments*. Presence, vol. 14, no. 4, pages 407–422, Aug 2005. (Cited on page 47)

[Tornai 2012] G. J. Tornai, G. Cserey and I. Pappas. *Fast DRR generation for 2D to 3D registration on GPUs*. Medical Physics, vol. 39, no. 8, pages 4795–4799, 2012. (Cited on page 107)

[Toshiba 2017] Toshiba. *Dose Tracking System*. http://www.toshibamedicalsystems.com/products/dose/lowdose_xray/fluoroscopy.html, 2017. (Cited on page 15)

[Twinanda 2015] A. P. Twinanda, E. O. Alkan, A. Gangi, M. de Mathelin and N. Padoy. *Data-driven spatio-temporal RGBD feature encoding for action recognition in operating rooms*. International Journal of Computer Assisted Radiology and Surgery, vol. 10, no. 6, pages 737–747, 2015. (Cited on page 53)

[Twinanda 2016] A. P. Twinanda, P. Winata, A. Gangi, M. de Mathelin and N. Padoy. *Multi-Stream Deep Architecture for Surgical Phase Recognition on Multi-View RGBD Videos*. In The 7th MICCAI Workshop on Modeling and Monitoring of Computer Assisted Interventions (M2CAI), 2016. (Cited on pages 53, 132, and 140)

[Vanhavere 2008] F. Vanhavere, E. Carinou, L. Donadille, M. Ginjaume, J. Jankowski, A. Rimpler and M. Sans Merce. *An overview on extremity dosimetry in medical applications*. Radiation Protection Dosimetry, vol. 129, no. 1-3, pages 350–355, 2008. (Cited on pages 9 and 16)

[Wagner 2009] M. Wagner, C. Duwenkamp, K. Dresing and O. J. Bott. *An approach to calculate and visualize intraoperative scattered radiation exposure*. Studies in Health Technology and Informatics, vol. 150, no. 0, pages 831–835, 2009. (Cited on pages 34 and 63)

[Wagner 2012] M. Wagner, K. Dresing, W. Ludwig, C. A. Ahrens and O. J. Bott. *SIScaR-GPU: Fast simulation and visualization of intraoperative scattered radiation to support radiation protection training*. Studies in Health Technology and Informatics, vol. 180, pages 968–972, 2012. (Cited on pages 34, 35, and 70)

[Wang 2012] L. Wang, P. Fallavollita, R. Zou, X. Chen, S. Weidert and N. Navab. *Closed-Form Inverse Kinematics for Interventional C-Arm X-Ray Imaging With Six*

Degrees of Freedom: Modeling and Application. IEEE Transactions on Medical Imaging, vol. 31, no. 5, pages 1086–1099, 2012. (Cited on pages 60, 102, 104, and 109)

[Wang 2014] X. Wang, J. Yang, Y. Chen, D. Ai, Y. Hu and Y. Wang. *Optimal Viewing Angle Determination for Multiple Vessel Segments in Coronary Angiographic Image.* IEEE Transactions on Nuclear Science, vol. 61, no. 3, pages 1290–1303, 2014. (Cited on pages 60, 102, 104, and 105)

[Wang 2016] X. Wang, S. Habert, C. S. zu Berge, P. Fallavollita and N. Navab. *Inverse visualization concept for RGB-D augmented C-arms.* Computers in Biology and Medicine, vol. 77, pages 135–147, 2016. (Cited on page 31)

[Wendler 2007] T. Wendler, A. Hartl, T. Lasser, J. Traub, F. Daghighian, S. I. Ziegler and N. Navab. *Towards Intra-operative 3D Nuclear Imaging: Reconstruction of 3D Radioactive Distributions Using Tracked Gamma Probes.* In Medical Image Computing and Computer-Assisted Intervention – MICCAI, pages 909–917. 2007. (Cited on page 155)

[Wong 2008] K. H. Wong. *Imaging Modalities.* In T. Peters and K. Cleary, editors, Image-Guided Interventions: Technology and Applications, pages 241–273. Springer US, Boston, MA, 2008. (Cited on pages 9, 59, and 61)

[Xu 2015] T. Xu, S. Hutfless, M. Cooper, M. Zhou, A. Massie and M. Makary. *Hospital cost implications of increased use of minimally invasive surgery.* JAMA Surgery, vol. 150, no. 5, pages 489–490, 2015. (Cited on page 6)

[Zhang 2011] C. Zhang and Z. Zhang. *Calibration between depth and color sensors for commodity depth cameras.* In IEEE International Conference on Multimedia and Expo, pages 1–6, 2011. (Cited on page 46)

[Zhang 2014] M. Zhang, W. Zou, T. Chen, L. Kim, A. Khan, B. Haffty and N. J. Yue. *Parameterization of brachytherapy source phase space file for Monte Carlo-based clinical brachytherapy dose calculation.* Physics in Medicine and Biology, vol. 59, no. 2, page 455, 2014. (Cited on pages 58 and 75)

Nicolas Loy Rodas

Context-Aware Radiation Protection for the Hybrid Operating Room

Summary

The use of X-ray based imaging technologies during minimally-invasive procedures exposes both patients and medical staff to ionizing radiation. Even if the dose absorbed during a single procedure can be low, long-term exposure can lead to noxious effects (e.g. cancer). In this thesis, we therefore propose methods to improve the overall radiation safety in the hybrid operating room by acting in two complementary directions. First, we propose approaches to make clinicians more aware of exposure by providing in-situ visual feedback of the ongoing radiation dose by means of augmented reality. Second, we propose to act on the X-ray device positioning with an optimization approach for recommending an angulation reducing the dose deposited to both patient and clinical staff, while maintaining the clinical quality of the outcome image. Both applications rely on approaches proposed to perceive the room using RGBD cameras and to simulate in real-time the propagation of radiation and the deposited dose. We hope that this thesis can contribute to the overall reduction of radiation exposure and to make the benefits of image-guided procedures available to a wider population.

Key-words: Medical Robotics, X-ray Guided Procedures, Radiation Safety, Augmented Reality, Monte Carlo Simulations, Computer-Assisted Interventions.

Résumé

L'utilisation de systèmes d'imagerie à rayons X lors de chirurgies mini-invasives expose patients et staff médical à des radiations ionisantes. Même si les doses absorbées peuvent être faibles, l'exposition chronique peut causer des effets nocifs (e.g. cancer). Dans cette thèse, nous proposons des nouvelles méthodes pour améliorer la sécurité vis-à-vis des radiations en salle opératoire hybride dans deux directions complémentaires. Premièrement, nous présentons des approches pour rendre les cliniciens conscients des irradiations grâce à des visualisations par réalité augmentée. Deuxièmement, nous proposons une méthode d'optimisation pour suggérer une pose de l'imageur réduisant la dose au personnel et patient, tout en conservant la qualité de l'image. Pour rendre ces applications possibles, des nouvelles approches pour la perception de la salle grâce à des caméras RGBD et pour la simulation en temps-réel de la propagation et doses de radiation ont été proposées. Nous espérons que cette thèse puisse contribuer à réduire l'exposition aux radiations et à rendre les bénéfices des chirurgies guidées par image accessibles à une plus grande population.

Mots-clés : Robotique Médicale, Chirurgies Guidées par Rayons X, Radioprotection, Réalité Augmentée, Simulations Monte Carlo, Chirurgie Assistée par Ordinateur.